A patient-specific CT-Mesh hybrid computational phantom and its applications in out-of-field dose, equivalent dose, and secondary cancer risk estimation in proton therapy

München 2022

A patient-specific CT-Mesh hybrid computational phantom and its applications in out-of-field dose, equivalent dose, and secondary cancer risk estimation in proton therapy

Erika Kollitz

Dissertation on Physics
of Ludwig–Maximilians–Universität München

submitted by
Erika Kollitz
from Corvallis, Oregon in the
United States of America

München, on the date January 15, 2022

First Referee: Prof. Dr. Katia Parodi
Second Referee: Prof. Dr. Wayne Newhauser
Supervision: Prof. Dr. Katia Parodi and Dr. George Dedes
Date of Oral Examination: March 16, 2022

Zusammenfassung

Eine Strahlentherapie ist bei 50% der Krebsbehandlungsschemata indiziert. Mit dem technologischen Fortschritt und der Zunahme der Krebsberlebenden rckt die Verbesserung der Lebensqualitt der Patienten nach der Behandlung in den Mittelpunkt. Die Vorbeugung einer sekundren Krebserkrankung wird durch einen Mangel an
dosimetrischen Daten auerhalb des behandelten Bereichs erschwert, der auf die begrenzten anatomischen Kenntnisse aus der Teilkrperbildgebung und die Unfhigkeit des Behandlungsplanungssystems zurckzufhren ist, die Dosis auerhalb des Behandlungsfeldes genau zu berechnen.

Das Ziel dieser Dissertation war es, zunchst eine Methodik zu entwickeln, um patientenspezifische Ganzkrper Computertomographie-Mesh (CT-Mesh) hybride Computerphantome zu erstellen, die entwickelt wurden, um die in einem klinischen Strahlentherapie-Planungs-CT fehlende Anatomie durch die eines Referenzphantoms zu ergnzen, und zweitens die Eignung des Hybrid-Phantoms fr Anwendungen bei der Vorhersage der Dosis auerhalb des Feldes und der quivalentdosis sowie der Schtzung des sekundren Krebsrisikos zu untersuchen, insbesondere im Fall der Neutronendosis in der Protonentherapie.

Das Hybridphantom ist in drei Segmente unterteilt: das Patienten-CT im Feld, das Mesh-Type Reference Computational Phantom (MRCP) auerhalb des Feldes, das auf physikalische Patientenmessungen skaliert ist, und einen gemischten bergangsbereich. Der nchste Schritt nach der Erstellung bestand darin, die Fhigkeit Hybrids zur Vorhersage der Dosis auerhalb des Feldes und der quivalentdosis zu berprfendes. Zu diesem Zweck wurden vier Protonenbehandlungsplne erstellt und an jeweils vier Patientendarstellungen simuliert: ein Ganzkrper-CT (WBCT) als Referenz, das Hybrid, das skalierte MRCP und das Default MRCP. Zwei benutzerdefinierte Bewertungsskalen wurden entwickelt, um zu testen, wie sich Definitionen von Neutronenenergiebewertungsskalen auf den Neutronengewichtungsfaktor, die geschtzte quivalentdosis und letztendlich die Risikovorhersage auswirken. Nach der Simulation wurden die Dosis und die quivalentdosis vergleichen, die von den Plnen an verschiedene Organe im Krper abgegeben wurden. Sowohl bei der Gesamtdosis als auch bei der quivalentdosis war das Hybridmodell in den Organen innerhalb des Feldes immer gleich gut oder besser als die reinen Netzphantome. In den Organen auerhalb des Feldes lieferte der Hybrid am hufigsten die der Referenz am nchsten kommende Schtzung (56%) und war am wenigsten wahrscheinlich der unterlegeneste Prdiktor (2%).

Ein hnlicher Ansatz wurde verwendet, um die Vorhersagefhigkeit des Hybrids in Bezug auf die Modellierung des sekundren Krebsrisikos zu bewerten. Basierend auf den vorheri-

gen Ergebnissen wurden hier nur die hybride, skalierte MRCP und WBCT verwendet. Sieben einzigartige WBCTs wurden verwendet, fr die alle Protonenplne erstellt wurden. Diese Plne wurden auf den drei Patientendarstellungen simuliert. Die resultierenden Organquivalentdosen wurden als Eingabe in fnf sekundre Krebsrisikomodelle verwendet (eins linear, zwei linear-exponentiell und zwei linear-plateau). Whrend die Wahl des Risikomodells das vorhergesagte absolute Risiko beeinflusste, hatte es keinen Einfluss auf die relative Vorhersagefhigkeit des Hybrids. Dies bedeutet, dass das Hybridphantom unabhngig von der Risikomodellauswahl gleich effektiv war. Die Wahl des der Bewertungsskala beeinflusste das geschtzte Risiko, aber in den meisten Regionen, insbesondere bei Organen, die >0.1 Sv erhielten, war die Unsicherheit bei der Auswahl des Scorers signifikant geringer als die inhrente Unsicherheit der Risikomodellierung. Insgesamt, hnlich wie bei der Dosis/quivalentdosis, war der Hybrid bei den Organen innerhalb des Feldes immer gleich gut oder besser als der skalierte MRCP. In den Organen auerhalb des Feldes lieferte der Hybrid am hufigsten den berlegenen Schtzwert gegenber der Referenz (52%), gefolgt von einem quivalenten Schtzwert (29%), dann einen niedrigeren Schtzwert gegenber dem skalierten MRCP (19%).

Das Hybridphantom lieferte am ehesten die Gesamtdosis, die quivalentdosis und die Schtzung des Zweitkrebsrisikos, die dem WBCT am nchsten kamen. Diese Hybridphantome finden Anwendung beider Behandlungsplanung, die das Risiko von Sekundrkrebs minimiert, whrend die klinischen Ziele eingehalten werden, oder bei der Dosisrekonstruk,on bei Patienten, die sich zur erneuten Bestrahlung vorstellen.

Abstract

Radiation therapy is indicated in 50% of cancer treatment regimens. As technology advances, an increase in the population of cancer survivors shifts the focus to improving patient quality of life post-treatment. The prevention of a secondary cancer is made difficult by a lack of dosimetric data outside the treated area due to a combination of the limited anatomical knowledge from partial-body imaging and the treatment planning system's inability to accurately calculate dose outside of the treatment field.

The goal of this thesis was to first develop a methodology to create patient-specific whole-body computed-tomography-mesh (CT-mesh) hybrid computational phantoms, designed to supplement anatomy missing from a radiation therapy clinical planning CT with that of a reference phantom, and secondly to investigate the hybrid phantom's viability for applications in out-of-field dose and equivalent dose prediction and secondary cancer risk estimation particularly in the case of neutron dose in proton therapy.

The hybrid phantom is divided into three segments: the in-field patient CT, the out-of-field mesh-type reference computational phantom (MRCP) scaled to physical patient measurements, and a blending transition region. The next step after creation was to verify the hybrid's ability to predict out-of-field dose and equivalent dose. For this purpose four proton treatment plans were created and simulated on four patient representations each: a whole-body CT (WBCT) ground truth, the hybrid, the scaled MRCP, and the default MRCP. Two custom scorers were developed to test how neutron energy scoring definitions would effect the neutron weighting factor, estimated equivalent dose, and ultimately risk prediction. After simulation, the dose and equivalent dose delivered by the plans to several organs throughout the body were compared. Overall, for both total dose and equivalent dose, in the in-field organs the hybrid was always as good as or superior to the mesh phantoms alone. In the out-of-field organs the hybrid most frequently yielded the closest estimate to the ground truth (56%) and was least likely to be the most inferior predictor (2%).

A similar approach was used to assess the hybrid's predictive ability with respect to secondary cancer risk modelling. Based on the previous results, only the hybrid, scaled MRCP, and WBCT were used here. Seven unique WBCTs were used, all of which had proton plans created for them. These plans were simulated on the three patient representations. The resulting organ equivalent doses were used as input into 5 secondary cancer risk models (1 linear, 2 linear-exponential, and 2 linear-plateau). While the choice of risk model did effect the predicted absolute risk, there was no impact on the hybrid's relative predic-

tive ability. This means the hybrid phantom was equally effective regardless of risk model selection. Choice of scorer impacted the estimated risk, but in most regions, particularly for organs receiving >0.1 Sv, the uncertainty of the scorer choice was significantly less than the inherent uncertainty in the risk modelling. Overall, similarly to the dose/equivalent dose results, in the in-field organs the hybrid was always as good as or superior to the scaled MRCP. In the out-of-field organs the hybrid yielded the superior estimate to the ground truth most frequently (52%), followed by an equivalent estimate (29%), then an inferior estimate to the scaled MRCP (19%).

The hybrid phantom was the most likely phantom to yield the total dose, equivalent dose, and second cancer risk estimate closest to the WBCT. These hybrid phantoms have applications in treatment planning that minimizes the risk of secondary cancer while maintaining clinical objectives, or in dose reconstruction in patients presenting for re-irradiation.

+

Acknowledgements

I would like to thank my two supervisors, Prof. Dr. Katia Parodi and Dr. George Dedes, for their invaluable support and guidance over the course of my doctoral work. Through their feedback, patience, and incredible dedication this work was made possible. I can confidently say I could not have asked for better supervisors. Whether it was working together to solve technical problems, in-depth discussions about project direction, or the insightful guidance for career progression and professionalism in science, your contributions to this thesis and my doctoral experience cannot be quantified.

I would also like to thank Prof. Dr. Wayne Newhauser, who recommended me for this opportunity and who provided significant scientific support over the course of this project. It is not an exaggeration to say that without him I would not where I am today. Furthermore, I would like to thank Prof. Dr. Katia Parodi once again and Prof. Dr. Franz Pfeiffer for their wonderful work as joint speakers of the Graduiertenkolleg 2274. The GRK 2274 provided a wonderful program and many opportunities to learn from some of the top researchers in the field of medical physics. The focus on collaboration and big-picture perspectives formulated the key principles which guided my project and hopefully my future career.

Of course, this work could not have been accomplished without the valued contributions of many scientific collaborators. Prof. Dr. Claus Belka, Dr. Florian Kamp, Prof. Dr. Chan Hyeong Kim, and Ms. Haegin Han, on whose research and resources this project was built. Prof. Dr. Marco Riboldi, Dr. Marco Pinto, and Dr. Marco Schwarz, who were consulted on key technical and clinical aspects of this project. And finally, Mr. Mortiz Roew, who despite having to work remotely, was not only extremely diligent and insightful, but also produced high quality work on the hybrid phantoms.

Special thanks to my colleagues in the same office, Sonja Gerlach, Ronaldo Kalunga, Pratik Dash, and Franz Englbrecht, who, for the time when working in presence was common, provided a warm and friendly environment with many lively discussions. In particular I would like to thank Sonja for always helping me with my German, and for her review of the Zusammenfassung.

Finally, I would like to express my boundless gratitude my family and my partner, who throughout my studies have been unwaveringly supportive despite the distance from home. Thank you to my parents, Kathleen, Steve, Alex, and Caryn, for their love, faith, pet pictures, and regular phone calls. And thank you to my partner, Philip, for always being by my side and for being a source of warmth and comfort throughout.

Contents

Zusammenfassung **v**

Abstract **vii**

Acknowledgements **ix**

1 Introduction and Background **1**
1.1 Treating Cancer with Radiation 1
1.1.1 Defining Dose Quantities 1
1.1.2 Radiobiological Mechanisms 3
1.2 Modern Radiation Therapy Modalities 6
1.2.1 Internal: Brachytherapy 6
1.2.2 X-Ray External Beam Radiotherapy (EBRT) 7
1.3 Proton Therapy 9
1.3.1 Physical Properties 9
1.3.2 Active Scanning vs Passive Scattering 13
1.3.3 Advantages and Disadvantages 15
1.3.4 Current Perspectives: Neutron Risk in IMRT vs. Scanning and Scattering Proton Therapy 16
1.4 Monte Carlo 17
1.5 Treatment Planning 18
1.5.1 Clinical Workflow and Treatment Planning 19
1.5.2 Limitations of Treatment Planning Systems 21
1.5.3 Advancements in Treatment Planning 22
1.6 Second Cancer Risk Modeling 23
1.6.1 Secondary Cancer Incidence 23
1.6.2 Secondary Cancer Risk Modeling 24
1.7 Computational Phantoms 25
1.7.1 Use in Therapy and Radiation Protection 26
1.7.2 Advancements in Computational Reference Phantoms 26
1.7.3 Mesh-type Computational Reference Phantoms 29
1.8 Thesis Summary and Specific Aims 30

2 Hybrid Phantom Creation **33**
2.1 Scaling the MRCP . . . 34
2.2 Voxelizing the MRCP . . . 37
2.2.1 Developing the Voxelization Code . . . 38
2.2.2 Validating MRCP Voxelization . . . 38
2.3 Creating the Transition Slices . . . 40
2.3.1 Preparing for Deformable Image Registration . . . 40
2.3.2 Deformable Registration . . . 42
2.4 First Prototype Hybrid: Voxel Geometry Only . . . 43
2.5 Creating the Out-of-Field Mesh Segments . . . 44
2.6 Completed Hybrids . . . 45

3 Computational Development **49**
3.1 Designing Geant4 to Handle Hybrid Geometry . . . 50
3.2 Custom Scorers . . . 52
3.3 Material Assignment for Voxelized Geometry . . . 54
3.4 Calibration to RayStation Stopping Powers . . . 55
3.5 Converting Treatment Plans to Geant4 . . . 58
3.5.1 MU to Number of Particles . . . 58
3.5.2 Converting Geometric Beam Qualities . . . 59

4 Validating the Hybrid Geometry **63**
4.1 Hybrids Created for Geometry Validation . . . 63
4.2 Organ Contouring and Masking . . . 65
4.2.1 Organ Contouring for Voxelized Geometry . . . 65
4.2.2 Organ Masking . . . 66
4.3 Designing and Simulating Treatment Plans . . . 67
4.3.1 Male Pelvis: Prostate . . . 67
4.3.2 Female Pelvis: Cervical Cancer . . . 67
4.3.3 Male Head and Neck: Nasopharyngeal Cancer . . . 68
4.3.4 Female Head and Neck: Meningioma . . . 69
4.3.5 Simulations . . . 71
4.4 Data Analysis . . . 71
4.4.1 Calculating Equivalent Dose . . . 72
4.4.2 Organ Dose Quantity Calculation . . . 74
4.4.3 Assessing Phantom Predictive Performance . . . 75
4.4.4 Hybrid Performance Results . . . 76
4.4.5 Considerations for the Hybrid Phantoms . . . 80

5 Risk Modelling Using Hybrid Phantoms **85**
5.1 Hybrids for Risk Model Implementation . . . 85
5.2 Treatment Planning and Organ Contouring . . . 87
5.3 Simulating the Treatment Plans . . . 90

5.4 Risk Models . . . 91
5.5 Data Analysis . . . 94
5.6 Phantom Comparison Using Equivalent Dose . . . 95
5.7 Phantom Comparison Using Risk . . . 97
5.7.1 Impact of Model Choice on Risk Prediction . . . 98
5.7.2 Impact of Neutron Energy Weighting on Risk Prediction . . . 100

6 Discussion **103**
6.1 Hybrid Creation . . . 103
6.1.1 Place in the Literature . . . 103
6.1.2 Strengths and Limitations . . . 104
6.1.3 Future Directions . . . 105
6.2 Hybrid Predictive Ability . . . 106
6.2.1 Dose and Equivalent Dose . . . 106
6.2.2 Secondary Cancer Risk . . . 109
6.2.3 Place in the Literature . . . 112
6.2.4 Strengths and Limitations . . . 113
6.2.5 Future Directions . . . 114

A **117**
A.1 Male Pelvis . . . 117
A.2 Female Pelvis . . . 120
A.3 Male Head and Neck . . . 123
A.4 Female Head and Neck . . . 126

B **129**

C **135**
C.1 Equivalent Dose Boxplots . . . 135
C.2 ERR Risk Figures . . . 143

D **145**
D.1 Equivalent Dose Tables . . . 145
D.2 Secondary Cancer Risk Tables . . . 153
D.2.1 Pat 1 . . . 153
D.2.2 Pat 2 . . . 158
D.2.3 Pat 3 . . . 163
D.2.4 Pat 4 . . . 168
D.2.5 Pat 5 . . . 173
D.2.6 Pat 6 . . . 178
D.2.7 Pat 7 . . . 183

List of Figures

1.1 High vs. Low LET DNA Damage 4
1.2 IMRT vs. 3D-CRT 8
1.3 Primary Proton Fluence with Depth 11
1.4 Percent Depth Dose Curves for photons, electrons, protons, and carbon ions 12
1.5 Spread-Out Bragg Peak 13
1.6 Passive Scattering vs Active Scanning 14
1.7 Photon vs. Proton Plans 15
1.8 Radiotherapy Clinical Workflow 19
1.9 Intro to Risk Models 25
1.10 MIRD Stylized Phantom 27
1.11 Stylized vs. Voxel Anatomy Comparison 28
1.12 Surface vs Tetrahedral Mesh Types 31

2.1 Voxel vs. Mesh ICRP Adult Reference Computational Phantoms 33
2.2 Hybrid Phantom Creation Flowchart 35
2.3 Considerations for the Scaling Factor 36
2.4 Effect of scaling on the MRCP 37
2.5 Voxelization Resolution Test 39
2.6 Transition Region Creation Diagram 41
2.7 Morphon Deformable Image Registration Example 43
2.8 Prototype Hybrid 44
2.9 Hybrids for Geometry Validation 46
2.10 Hybrids for Risk Modelling (Male) 47
2.11 Hybrids for Risk Modelling (Female) 47

3.1 Effect of Phantom Container Definition on Tetrahedral Mesh Construction 51
3.2 Impact of Energy Weighting Method on Neutron Weighting Factor 53
3.3 How Stopping Power Changes with I Value 56
3.4 Results of Geant4 I Value Calibration 57
3.5 RayStation vs Geant4 Coordinate Systems 59

4.1 Hybrids for Geometry Validation 64
4.2 Prostate Plan in the Male Pelvis 68

4.3 Cervical Cancer Plan in the Female Pelvis 69
4.4 Nasopharyngeal Carcinoma Plan in the Male Head and Neck 70
4.5 Meningioma Plan in the Female Head and Neck 70
4.6 Impact of Energy Weighting Method on Neutron Weighting Factor 73
4.7 Total Dose Boxplots for the Male Pelvis 77
4.8 Percent Difference from the WBCT for all Dose Quantities and Patient Representations for the Male Pelvis Treatment Site 78
4.9 Percent Difference from the WBCT for all Dose Quantities and Patient Representations for the Female Pelvis Treatment Site 78
4.10 Percent Difference from the WBCT for all Dose Quantities and Patient Representations for the Male Head and Neck Treatment Site 79
4.11 Percent Difference from the WBCT for all Dose Quantities and Patient Representations for the Female Head and Neck Treatment Site 79
4.12 Possibility of Out-of-Field Misalignment in Scaled MRCPs 81
4.13 Shifting Organ Mask to Match WBCT Distance to Isocenter 82
4.14 Transplanting WBCT Organ Mask into the Phantom's Organ Location . . 83

5.1 Hybrids for Risk Modelling (Male) 86
5.2 Hybrids for Risk Modelling (Female) 87
5.3 Risk Modelling Treatment Plans Patients 1-4 89
5.4 Risk Modelling Treatment Plans Patients 5-7 90
5.5 Risk Models Used in Analysis 94
5.6 KERMA-Weighted Equivalent Dose for Pat 1 96
5.7 Comparing EAR Predictions Across Risk Models for Each Patient 99
5.8 Comparing EAR Predictions Across Patients for Each Risk Model 101

A.1 Total Dose Boxplots for the Male Pelvis 117
A.2 Neutron Dose Boxplots for the Male Pelvis 118
A.3 Equivalent Dose (Fluence-weighted) Boxplots for the Male Pelvis 118
A.4 Equivalent Dose (KERMA-weighted) Boxplots for the Male Pelvis 119
A.5 Total Dose Boxplots for the Female Pelvis 120
A.6 Neutron Dose Boxplots for the Female Pelvis 121
A.7 Equivalent Dose (Fluence-weighted) Boxplots for the Female Pelvis 121
A.8 Equivalent Dose (KERMA-weighted) Boxplots for the Female Pelvis 122
A.9 Total Dose Boxplots for the Male Head and Neck 123
A.10 Neutron Dose Boxplots for the Male Head and Neck 124
A.11 Equivalent Dose (Fluence-weighted) Boxplots for the Male Head and Neck 124
A.12 Equivalent Dose (KERMA-weighted) Boxplots for the Male Head and Neck 125
A.13 Total Dose Boxplots for the Female Head and Neck 126
A.14 Neutron Dose Boxplots for the Female Head and Neck 127
A.15 Equivalent Dose (Fluence-weighted) Boxplots for the Female Head and Neck 127
A.16 Equivalent Dose (KERMA-weighted) Boxplots for the Female Head and Neck128

C.1 KERMA-Weighted Equivalent Dose for Pat 1 136
C.2 Fluence-Weighted Equivalent Dose for Pat 1 136
C.3 KERMA-Weighted Equivalent Dose for Pat 2 137
C.4 Fluence-Weighted Equivalent Dose for Pat 2 137
C.5 KERMA-Weighted Equivalent Dose for Pat 3 138
C.6 Fluence-Weighted Equivalent Dose for Pat 3 138
C.7 KERMA-Weighted Equivalent Dose for Pat 4 139
C.8 Fluence-Weighted Equivalent Dose for Pat 4 139
C.9 KERMA-Weighted Equivalent Dose for Pat 5 140
C.10 Fluence-Weighted Equivalent Dose for Pat 5 140
C.11 KERMA-Weighted Equivalent Dose for Pat 6 141
C.12 Fluence-Weighted Equivalent Dose for Pat 6 141
C.13 KERMA-Weighted Equivalent Dose for Pat 7 142
C.14 Fluence-Weighted Equivalent Dose for Pat 7 142
C.15 Comparing ERR Predictions Across Risk Models for Each Patient 143
C.16 Comparing ERR Predictions Across Patients for Each Risk Model 144

List of Tables

1.1 ICRP 92 weights 2
1.2 ICRP 103 weights 3

2.1 Voxelization Gamma Analysis 40

3.1 CT Hounsfield Units to Density Conversion Curve from RayStation for a Generic CT 54

4.1 Fraction of cases by dose quantity prediction performance for all phantoms across all treatment sites. 76
4.2 Comparison of the dose delivered to the liver and percent difference from the ground truth in the first test setup with the organ mask in its default location/geometry and in the second case after translating each phantom's organ mask to match WBCT distance from isocenter. 82
4.3 Comparison of the dose delivered to the liver and percent difference from the ground truth in the second test setup with the organ mask in its default location/geometry and in the second case after transplanting the WBCT organ mask into the phantom organ's location. 83

5.1 Table of the α values used in this thesis compared against the values from Fontenot et al 2010 [48] 93
5.2 Fraction of organs by phantom which gave the best equivalent dose prediction. In/near-field: brain, left and right eyes, thyroid. Out-of-field: lungs, liver, kidneys, bladder. 95
5.3 Equivalent dose prediction average percent difference from WBCT of organs falling under the superior/inferior performance category for both phantoms. In/near-field: brain, left and right eyes, thyroid. Out-of-field: lungs, liver, kidneys, bladder. 97
5.4 Fraction of organs by phantom which gave the best risk prediction. In/near-field: brain, left and right eyes, thyroid. Out-of-field: lungs, liver, kidneys, bladder. 97

5.5 Risk prediction average percent difference from WBCT of organs falling under the superior/inferior performance category for both phantoms. In/near-field: brain, left and right eyes, thyroid. Out-of-field: lungs, liver, kidneys, bladder. 98

B.1 Quantitative Data for the Male Pelvis 130
B.2 Quantitative Data for the Female Pelvis 131
B.3 Quantitative Data for the Male Head and Neck 132
B.4 Quantitative Data for the Female Head and Neck 133

D.1 Equivalent Dose in Pat 1 146
D.2 Equivalent Dose in Pat 2 147
D.3 Equivalent Dose in Pat 3 148
D.4 Equivalent Dose in Pat 4 149
D.5 Equivalent Dose in Pat 5 150
D.6 Equivalent Dose in Pat 6 151
D.7 Equivalent Dose in Pat 7 152
D.8 LNT Risk in Pat 1 153
D.9 Lin-Plat 10 Sv Risk in Pat 1 154
D.10 Lin-Plat 40 Sv Risk in Pat 1 155
D.11 Lin-Exp 10 Sv Risk in Pat 1 156
D.12 Lin-Exp 40 Sv Risk in Pat 1 157
D.13 LNT Risk in Pat 2 158
D.14 Lin-Plat 10 Sv Risk in Pat 2 159
D.15 Lin-Plat 40 Sv Risk in Pat 2 160
D.16 Lin-Exp 10 Sv Risk in Pat 2 161
D.17 Lin-Exp 40 Sv Risk in Pat 2 162
D.18 LNT Risk in Pat 3 163
D.19 Lin-Plat 10 Sv Risk in Pat 3 164
D.20 Lin-Plat 40 Sv Risk in Pat 3 165
D.21 Lin-Exp 10 Sv Risk in Pat 3 166
D.22 Lin-Exp 40 Sv Risk in Pat 3 167
D.23 LNT Risk in Pat 4 168
D.24 Lin-Plat 10 Sv Risk in Pat 4 169
D.25 Lin-Plat 40 Sv Risk in Pat 4 170
D.26 Lin-Exp 10 Sv Risk in Pat 4 171
D.27 Lin-Exp 40 Sv Risk in Pat 4 172
D.28 LNT Risk in Pat 5 173
D.29 Lin-Plat 10 Sv Risk in Pat 5 174
D.30 Lin-Plat 40 Sv Risk in Pat 5 175
D.31 Lin-Exp 10 Sv Risk in Pat 5 176
D.32 Lin-Exp 40 Sv Risk in Pat 5 177
D.33 LNT Risk in Pat 6 178

D.34 Lin-Plat 10 Sv Risk in Pat 6 179
D.35 Lin-Plat 40 Sv Risk in Pat 6 180
D.36 Lin-Exp 10 Sv Risk in Pat 6 181
D.37 Lin-Exp 40 Sv Risk in Pat 6 182
D.38 LNT Risk in Pat 7 183
D.39 Lin-Plat 10 Sv Risk in Pat 7 184
D.40 Lin-Plat 40 Sv Risk in Pat 7 185
D.41 Lin-Exp 10 Sv Risk in Pat 7 186
D.42 Lin-Exp 40 Sv Risk in Pat 7 187

Chapter 1

Introduction and Background

The extent of this project necessitates the significant coverage of several topics related to radiation, its applications in cancer therapy, and some techniques used to study it. The initial pages of this work seeks to provide sufficient background to understand and critically evaluate the scientific work undertaken in this project, both in terms of methodology and in the implications of the results. Additionally, this chapter covers the rationale for the project, and the questions this project aims to address, and the potential clinical impact of the proposed methods.

1.1 Treating Cancer with Radiation

Cancer is the second leading cause of death globally (WHO [5]). Estimations place the number of new cancer cases in the US alone as over 1.8 million in just the year 2021, of which more than 600,000 are expected to result in death (Siegel et al 2021 [138]). One study by Bryant et al 2017 [23] placed the percent of cancer survivors treated by radiation in the US in 2016 at 29%. While it is widely cited that radiotherapy is indicated in approximately 50% of cases, actual utilization of radiotherapy tends to be lower in both the US and European countries (Borras et al 2016 [20], Delaney et al 2005 [40]). This underutilization indicates room for growth in a field already ubiquitous in cancer treatment.

It is evident that radiation can be used as an effective treatment for cancer, especially in conjunction with surgery and/or chemotherapy. In order to provide some background for why radiation is so effective, is important to understand some of the terms used to quantify the effect of radiation on tissue and the mechanisms by which radiation acts on cells, organs, and overall health.

1.1.1 Defining Dose Quantities

Arguably the most important term to understand is absorbed dose, or simply dose. This quantity describes the amount of energy absorbed by a material for a given unit of mass. For medical physics applications, the standard unit of absorbed dose is Gray (Gy), where

Table 1.1: Weighting factors for varied incident radiation types as recommended by the International Commission on Radiological Protection (ICRP) 92
Publication to reflect each radiation type's production of stochastic effects.

Type of incident radiation	ICRP 92 weighting factor
Photons	1
Electrons	1
Protons	2
Neutrons	2.5-20 (Energy dependent)
Alpha particles, heavy ions, and fission fragments	20

1 Gy is equal to 1 Joule of ionizing energy absorbed per 1 kilogram of material mass. Absorbed dose is the metric which guides treatment planning objectives for both tumor prescription and healthy tissue limits.

However, absorbed dose alone is not enough to full quantify the effect that dose has on tissue. Due to the different radiobiological properties of different radiation types (photons, neutrons, protons, heavy ions, etc.) 5 Gy of absorbed dose from photons would result in a different amount of cell-killing and have a different biological effect compared to 5 Gy of carbon ions. To account for this difference, we have the quantity of equivalent dose. Equivalent dose is defined as the absorbed dose, multiplied by a particle-specific radiation weighting factor. This means that equivalent dose uses the same base international system (SI) unit as absorbed dose, J/kg, however to differentiate it from the purely physical absorbed dose, the standard unit is Sieverts (Sv). The commonly accepted radiation weighting factors, taken from the International Commission on Radiological Protection (ICRP) 92 recommendations [62] are given in Table 1.1. Neutrons, rather than having a single weighting factor like the others, use a fluctuating weighting factor which varies from 2.5 to 20 depending on the energy of the neutron field. While the weighting factor represents the radiation type's relative probability of inducing a stochastic effect, i.e., a statistical effect whose probability is proportional to dose but whose severity is independent of the dose level, other measures of the relative biological effect (RBE) will use for example cell killing/survival as the relevant outcome for tumor control by which the radiation types are compared. For example, the commonly accepted value for protons in RBE-based treatment planning is 1.1. However, different studies have indicated possible variations of RBE throughout the proton path, and this topic is still under scientific discussion [113] [53] [165].

Taking this concept an additional step further, not only does radiation have different radiobiological properties, but the tissues themselves have varying levels of radiosensitivity. Effective dose takes the equivalent dose and further multiplies it by a unitless weight that represents a particular tissues response to radiation. Also similar to equivalent dose, effective dose uses units of Sieverts, to differentiate it from the purely physical quantity of absorbed dose. The tissue weighting factors for the organs listed in the ICRP Publication 103 [63] are given in Table 1.2.

One final quantity that should be discussed and defined here is the concept of monitor

Table 1.2: Weighting factors for varied tissue types as recommended by the ICRP 103 Publication for the purpose of representing individual organ sensitivity to radiation-induced stochastic effects.

Tissue	ICRP 103 weighting factor
Bone-marrow (red), Colon, Lung Stomach, Breast, Remainder*	0.12
Gonads	0.08
Bladder, Esophagus, Liver, Thyroid	0.04
Bone surface, Brain, Salivary glands, Skin	0.01

* Remainder tissues include: Adrenal glands, Extrathoracic region, Gallbladder, Heart, Kidneys, Lymph nodes, Muscle, Oral mucosa, Pancreas, Prostate, Small intestine, Spleen, Thymus, and Uterus/cervix.

units (MU). Monitor units are also related to absorbed dose, but in the context of clinical treatment machine output and "beam-on" time. An ionization chamber within the head of the treatment machine called a monitor chamber keeps track of how much radiation passes through. The machine is calibrated such that when the monitor chamber reads 1 MU, a dose of 1 cGy has been delivered to a specified point inside of a water phantom for a field size of 10×10 cm. There are multiple methods depending on a given clinic's preference to define the specified point, normally related to the distance from the beam source to either its isocenter or the surface of the water phantom. For a given treatment plan, more MUs means a longer beam-on time, a longer delivery time, and a greater stray dose component from leakage and scatter.

1.1.2 Radiobiological Mechanisms

To accurately prescribe and deliver radiation therapy, it is necessary to understand the underlying biological mechanisms which impact treatment efficacy. This section will discuss about radiobiological concepts and the potential impact they have on treatment planning decisions. The primary method through which radiation kills cells is by damaging the cell's DNA via double strand breaks, which are difficult for the cell to repair and can result in an inability of the cell to replicate. Radiation therapy is effective because of the ability to localize the radiation to tumor volumes, killing the malignant cells and sparing the healthy tissue around it.

When radiation enters a cell, it can damage DNA in two ways. The first is a direct effect, which is where the radiation deposits energy directly into an atom or molecule which is part of the DNA itself to liberate an electron from its chemical bond, causing a break in the strand. The second method is an indirect effect, which is where the radiation instead ionizes an intermediate molecule, such as water, and creates one or more free radicals which then interacts with the DNA and induces a strand break. This means that, based on the energy deposition patterns of different radiation types, the same dose from two different radiation types might induce different levels of DNA damage, and therefore, different levels

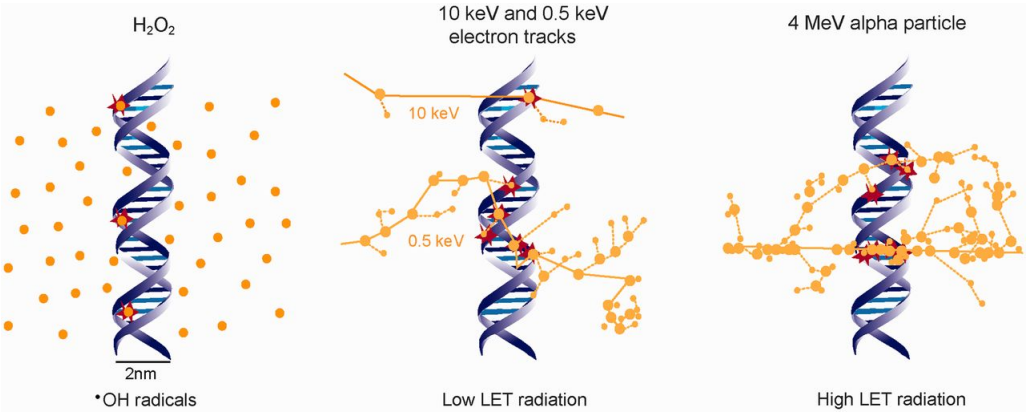

Figure 1.1: A depiction of the types and distribution of DNA damage inducing events based on the interaction probability from OH radicals, low LET ionizing radiation, and high LET ionizing radiation. The large dots represent ionizations while the smaller dots represent excitations (Schipler and Iliakis 2013 [126]).

of cell-killing. This was alluded to in the previous section when discussing the difference between absorbed dose and equivalent dose, where a unitless quantity was applied to the absorbed dose to represent a change in biological effect from the same absorbed dose. The primary governing property of radiation which dictates its biological effectiveness is its linear energy transfer (LET), which describes how much energy is deposited by a particle along a given path length. A low LET particle such as a photon will have more sporadic ionizations, and it is less likely for a single photon to cause a double strand break. Therefore, treatments using photons rely on having a large quantity of photons interacting in the same area to produce enough strand breaks to create a double strand break. On the other hand, high LET particles, such as protons, neutrons, and heavy ions, deposit more energy along a smaller path length, increasing the likelihood of inducing a double strand break. Figure 1.1 from Schipler and Iliakis (2013) [126] illustrates how a low versus high LET particle might deposit energy relative to the size of a strand of DNA.

Although double strand breaks are the key factor to cell-killing, single stand breaks are not without effect. Failure to repair single strand breaks can lead to mutagenesis and cancer induction. Therefore, a great deal of effort in radiation therapy is put into reducing the low dose exposure that healthy tissues receive during treatment, as lower doses are less likely to result in cell death, and more likely to result in mutations and chromosomal aberrations.

Besides the LET of the radiation types, there are other radiobiological factors which influence a cell population's sensitivity and response to radiation. They are often referred to as the 4 R's of radiobiology: repair, redistribution, reoxygenation, and repopulation [114]. Repair refers to the process of repairing sublethal DNA damage, where despite the DNA having been damaged via a single strand break, the cell is able to successfully recover the lost or corrupted genetic information. The second of the 4 R's refers to the redistribution of cells throughout the cell cycle. The cell is more radiosensitive leading up to and during the

stage of mitosis, where the DNA is being replicated and split into the daughter cells. When a population of cells is exposed to ionizing radiation, it is more likely that the cells currently in those radiosensitive stages will be killed. This leads to a temporarily synchronous population of cells, which might be more vulnerable to another well-timed exposure to ionizing radiation. However as more time passes, the cells begin to redistribute throughout the cycle until they return to a natural distribution. The third R, reoxygenation, refers to the oxygenation of the tumor volume. Tumor growth is maladaptive, and oftentimes the surrounding vasculature is incapable of fully saturating the tumor. This leads to tissue hypoxia (insufficient oxygenation) in some regions of the tumor. The presence of oxygen makes tissue more radio-sensitive, as the indirect effect of DNA damage is exacerbated by the presence of oxygen acting as an intermediary between the ionizing radiation and the DNA. When a solid tumor is exposed to radiation therapy, the oxygenated tissue is killed, but the radioresistant hypoxic regions remain. As time passes after initial exposure, parts of the tumor that were previously hypoxic are re-oxygenated via the newly available vasculature. Therefore, with repeated exposures to ionizing radiation, the tumor can be shrunk and killed. The final R, repopulation, refers to the replication of the surviving cells following radiation exposure, for both the healthy and cancerous tissue. All of these effects interplay with each other and drive the design of the treatment plan to maximize tumor response while minimizing healthy tissue toxicity. Typically plans are delivered in multiple routine dose deliveries over a set period of time in a process called fractionation. Conventionally fractionated radiation therapy is delivered in 1.8-2 Gy doses over a period of several weeks. For example a conventionally fractionated prostate treatment using photons might have 74 Gy delivered over the course of 37 fractions and at a rate of 5 fractions per week. Some other fractionation schemas include using higher doses per fraction with fewer total fractions (hypofractionation) or smaller doses per fraction with more total fractions delivered over the same time period as conventional fractionation (hyperfractionation).

On a larger scale, healthy organs can have different levels of tolerance for dose depending on structure, kinetics (repopulation time), and tissue radiosensitivity. With respect to structure, tissues and organs are typically categorized as either structured serially or in parallel. A single organ is split into functional sub-units (FSUs), such as the alveoli in the lung. If damage to one FSU results in no impairment to surrounding FSUs, that organ is said to be structured in parallel. Organs like this, such as the liver or lung, tend to be allowed to receive more dose than those in serial organs, as function is not overly compromised by the loss of small FSUs. Examples of serial organs would be the spinal cord or the digestive tract, where damage to one FSU impacts the ability of all downstream FSUs. Next, cell kinetics will impact the overall tolerance of an organ. If two organs, all else being equivalent, have different rates of cell repopulation, then the one with the faster kinetics will better tolerate dose as the damage to the organ can be repaired quickly. This can be a factor when planning fractionation plans to allow for the healthy tissue to recover between radiation applications. Finally, the cells of each tissue have inherent different levels of radiosensitivity which will dictate the ability of that tissue to tolerate radiation. Some examples of tissues with highly radiosensitive cells include bone marrow, reproductive organs, and gastro-intestinal lining. On the other hand, radioresistant tissues

include muscle, brain, cartilage, and nerves. The organ's ability to tolerate radiation will guide radiotherapy treatment planning by avoiding excess dose to organs at risk (OAR) that will be unable to tolerate therapeutic dose levels.

1.2 Modern Radiation Therapy Modalities

A well-developed clinic will have the equipment and staff required to deliver a variety of radiotherapeutic treatment techniques. Broadly these techniques can be broken down into external beam therapies and internal therapies. Which technique is prescribed to a patient will depend on the available facilities and the clinical indications for a particular treatment as determined by the radiation oncologist. This section will discuss the difference classifications and modalities of modern radiation therapy. The purpose of this section is not to give a comprehensive list of every application of radiation in therapy, but rather to introduce a broad overview of common modalities encountered in the clinic. For particular relevance to the topic of this thesis, the delivery mechanisms of each of these therapies leads to different effects on stray radiation and/or out-of-field dose, which is relevant to the potential applications of this thesis work.

1.2.1 Internal: Brachytherapy

Internal radiation therapy is the targeted placement of radioactive materials within the body of the patient to locally irradiate the tumor. Brachytherapy accomplishes this by the direct placement of sealed radiation sources in or next to the cancerous tissue. The radioactive material produces short-range radiation which spares the healthy tissue around the implanted area [26]. This differs from external beam radiotherapy where the radiation has to pass through the outer portion of the body before interacting with the tumor, and by necessity deposits dose in those healthy tissues. The direct implantation of the seeds into the tumor also means that if the patient moves after the radioactive material is placed, the radiation remains localized to the tumor. Again this is unlike external beam therapy, where patient movement and anatomical changes during and between treatments introduces a lot of problems in targeting the tumor. Brachytherapy can be used on its own as a cancer therapy, or in conjunction with surgery, external beam radiotherapy, or chemotherapy. Depending on the radioisotope used in the procedure, brachytherapy is either classified as high dose-rate (HDR) or low dose-rate (LDR). HDR sources are always removed after treatment, but LDR sources can either be removed or remain permanently inside the patient, depending on the treatment plan. Seed implantation for brachytherapy involves precise placement of the spatial distribution of the radioactive seeds based on a priori treatment plans, but the final dose distribution ultimately depends on needle placement at the time of implantation. Typically post-implantation, the positioning of the implanted seeds will be verified and the dose distribution calculated to ensure sufficient coverage [116]. Some common cancers which can be treated by brachytherapy include breast, prostate, and cervical cancer.

1.2.2 X-Ray External Beam Radiotherapy (EBRT)

External beam radiotherapy (EBRT) is categorized broadly as all radiation therapy which involves targeting an externally generated beam of directed radiation to kill cancer cells and shrink tumors within a patient. The varied modalities of EBRT reflect differences in planning, application techniques, and radiation type. Most of the modalities in this section typically use photons generated by a linear accelerator, however stereotactic radiosurgery (SRS) can use active Cobalt-60 sources to produce gamma rays (or, less frequently, specialized machinery with protons [13]) and stereotactic body radiotherapy (SBRT) can be used with protons in addition to photons.

Conventional and 3D Conformal Radiotherapy

Conventional radiotherapy is the simplest and oldest of the EBRT modalities here. It is rarely used in modern clinics, but forms the foundation on which many other photon linear accelerator (linac) modalities are ultimately based. In conventional radiotherapy, beam delivery is fixed, usually in 4-field laterally opposed beams facing the left, right, anterior, and posterior sides of the patient. Treatment planning was done on orthogonal x-rays taken of the patient at those two angles, and field shaping was minimal, often using simple square shaped fields. Due to the inherent simplicity and lack of knowledge of the full 3D structure of the tumor, this treatment modality often resulted in high levels of dose in the nearby healthy tissues, and possibly left the target volume underdosed.

The next step in EBRT development was 3D conformal radiotherapy (3D-CRT). This modality introduces 3D imaging techniques such as computed tomography (CT) scans to produce treatment planning images, allowing for a more nuanced planning of beam positioning and more conformal target coverage. Furthermore, 3D-CRT also utilizes beam shaping techniques, either with material blocks, usually made of cerrobend, placed on the patient to shape the beam at the skin surface, or inside the head of the linac with multi-leaf collimators (MLCs). 3D-CRT provides a marked improvement over conventional radiotherapy in terms of target coverage and increased healthy tissue sparing [52].

IMRT, VMAT, and IGRT

Intensity-modulated radiotherapy (IMRT) is a more advanced form of 3D-CRT where instead of the field consisting of a single shaped beam, it is split into smaller beamlets of which are assigned variable intensities/fluence. The size of these beamlets is determined by the physical properties of the multileaf collimator (MLC). By using the MLCs to shape the field multiple times over a single delivery, the intensity/fluence of the field can be varied to better refine conformality and organ at risk sparing. One example of how IMRT improves dose conformality in a prostate treatment is shown in Figure 1.2 from the work of Sveistrup et al (2014) [147]. Another important advancement which was critical for the widespread implementation of IMRT is the development of inverse planning. In inverse planning, a computer algorithm optimizes the intensity distribution of the beamlets, typically by minimizing an objective function [32]. The objective function describes a series of clinical

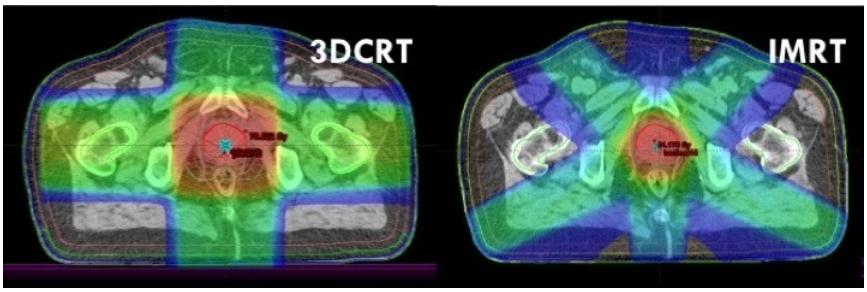

Figure 1.2: A prostate treatment plan using 3D-CRT (left) and IMRT (right) highlighting the ability of IMRT to produce more conformal plans and reduce dose to healthy tissues from Sveistrup et al (2014) [147].

goals designed to target the tumor volume and spare healthy tissue. Some downsides to IMRT is a longer time to plan, longer time to deliver the plan to the patient, increased low dose to the patient whole body (due to the machine needing to deliver more monitor units (MU) for the same treatment) and necessarily more complex computer algorithms to optimize the beamlet intensities at all the beam angles [51] [89]. IMRT is often chosen over 3D-CRT alone if the tumor has a particular complex 3D shape or in regions where sensitive OARs would receive considerable sparing over 3D-CRT.

Volumetric-modulated arc therapy (VMAT) in turn is a more advanced form of IMRT, where in addition to the beamlet intensity control, the gantry of the linac rotates around the patient up to 360°while continuously delivering the treatment. VMAT does not necessarily offer more improvement in dose conformality and tissue sparing, but it does reduce treatment time and monitor unit delivery [151].

Unlike the previous modalities, Image-guided radiotherapy (IGRT) cannot be described as a technical upgrade to a previous treatment modality. Image guidance could be used alongside 3D-CRT techniques like IMRT and VMAT and is a critical part of modern clinical radiotherapy workflow. Instead of describing a method of radiation delivery, IGRT refers to the application of advanced image guidance to verify and adjust patient positioning prior to each fraction to ensure the treatment plan correctly aligns with the target volume. In IGRT, the patient is imaged prior to each treatment session (such as with a CT simulator), and can additionally be imaged during the session (for example in lung tumors where intra-fractional motion is a large obstacle to delivering conformal plans). Based on these images, the patient positioning can be adjusted to match the planned treatment conditions. Some treatment machines have built-in imaging devices such as a cone-beam CT (CBCT) to verify patient positioning while on the treatment couch [101] [38].

SRS and SBRT

The final three modalities discussed in this section are stereotactic radiosurgery (SRS), stereotactic body radiotherapy (SBRT), and intra-operative radiotherapy (IORT). These are not usually common treatment modalities, and are generally used for special procedures.

Stereotactic radiosurgery (SRS) is the delivery of small highly precise beams of radiation to target lesions in the brain and spine. A common method of delivering SRS treatments is through a Gamma Knife machine. As opposed to linacs, which produce photons via physical interactions from an electron beam incident on a target, Gamma Knife systems produce photons via gamma emission from cobalt-60 sources within the main unit. A patient is first placed on the treatment couch and their head is very precisely positioned within the Gamma Knife machine. Then, highly collimated photons beams are delivered to the lesion in much higher doses and with much higher precision than traditional EBRT [106].

SBRT extends the concept of radiosurgery throughout the whole body. While SBRT is also delivered via a linac, some treatment machines can differ greatly from the gantries of traditional EBRT. One such machine is the CyberKnife, which places the treatment head on the end of a robotic arm, delivering small radiation beams from a variety of angles with an extremely high level of precision [8]. SBRT can be delivered with photons, protons, or even heavier ions. Proton SBRT does not have a delivery machine analogous to the CyberKnife, and instead typically uses large gantries with a separate room dedicated to proton production.

1.3 Proton Therapy

According to the Particle Therapy Co-Operative Group (PTCOG) in October of 2021, there were over 100 operational proton therapy centers across the world with another 61 currently in either construction or planning stages [3]. The growth of proton centers has been extraordinarily rapid, growing from 11 centers worldwide in the year 2000, to 24 in 2010, to 103 in 2020. This incredible amount of interest and investment in proton therapy is due primarily to the physical properties of its dose distribution and how it differs from photons, which enables highly conformal treatment plans and minimizing dose to healthy tissue.

1.3.1 Physical Properties

Protons are classified as a heavy particle with a positive charge. This sets them apart from other common types of radiation considered for therapeutic purposes such as: photons (massless and uncharged), electrons (low mass with negative charge), and carbon ions (heavy and positively charged, but with a charge of +6 instead of +1 and a mass of approximately 12 times that of the proton). Despite protons and electrons both being charged particles, the proton's mass means that they travel in much straighter lines than electrons as they are not so easily deflected by Couloumbic interactions. The charge on the protons means that, unlike photons, protons have a set stopping point after which there is no probability of any interactions from primary protons. The range of a proton beam of a given energy is defined by the point at which half of the primary protons have stopped. This range describes the beam as a whole, not for an individual proton, which

may have a slightly longer or shorter range than the beam overall due to energy straggling from fluctuations in the stochastic energy loss between particles.

The primary physical interactions in matter which dictate the properties of the proton dose distribution at clinical energies are: inelastic Coulomb interactions, elastic Coulomb scattering, and non-elastic nuclear interactions. Inelastic Coulomb interactions occur when the proton transfers energy to atomic electrons, this can lead to either an excitation or ejection of an electron and corresponding energy lost to the proton. Protons can only transfer a limited amount of energy through these interactions, so an electron ejected from this process will not be able to travel far (typically <1 mm) and it will deposit its energy locally. Due to the low mass of the electrons, these interactions do not contribute to any significant deflection of the protons. As the proton beam passes through matter, the protons will lose energy semi-continuously via frequent inelastic Couloumb interactions. Although the energy loss is not strictly continuous, for most practical calculations, use of the continuous slowing down approximation (CSDA) is sufficient. One such quantity, the CSDA range, is a common quantity used to describe a proton beam.

Because the range of a proton beam of a given energy is primarily determined by inelastic Coulombic interactions with atomic electrons, a material's ability to stop a proton beam, so-called "stopping power", is heavily influenced by that material's electron density. A more physically complete equation describing the stopping power of a material for protons >1 MeV is given by the Bethe-Bloch formula [16] [17] written below:

$$\frac{S}{\rho} = -\frac{\mathrm{dE}}{\rho \mathrm{d}x} = 4\pi N_A {r_e}^2 {m_e}^2 \mathrm{c}^2 \frac{\mathrm{Z}}{\mathrm{A}} \frac{\mathrm{z}^2}{\beta^2} [ln \frac{2{m_e}^2 \mathrm{c}^2 \gamma^2 \beta^2}{I} - \beta^2 - \frac{\delta}{2} - \frac{\mathrm{C}}{\mathrm{Z}}] \tag{1.1}$$

where $\frac{S}{\rho}$ is the mass stopping power (where S is the stopping power $\frac{dE}{dx}$, E is energy, x is distance in particle travel direction, and ρ is the material density), N_A is Avogadro's number, r_e is the electron radius, m_e is the electron mass, c is the speed of light, Z is the atomic number of the material, A is the atomic weight of the material, z is the projectile particle charge, $\beta = v/c$ where v is the particle projectile velocity, γ is the Lorentz factor ($(1-\beta^2)^{-1/2}$), I is the mean excitation potential of the material, δ is a correction to account for electrons near to the particle shielding the electrons farther from the particle track at high projectile speeds, and C is a shell correction to account for the account for invalidity of the assumption that electrons are stationary which becomes relevant at lower proton energies. Some important notes to take from this formula: 1) stopping power is not dependent on the particle's mass, 2) stopping power is proportional to the charge of the particle squared and inversely proportional to the particle velocity squared (meaning particles with stronger charge and lower speed will lose energy faster for a given material medium), and 3) for different materials, the primary dependence of linear stopping power (S) is material density and is proportional to the material's electron density ($N_A \rho \frac{Z}{A}$), although there is also a dependence on the excitation energy as $ln\frac{1}{I}$.

The second kind of interaction, elastic Coulomb scattering, occurs when the proton is deflected by a positively charged nucleus, resulting in a change of the proton's direction. This ultimately affects the sharpness of the proton beam's lateral fall-off as the protons

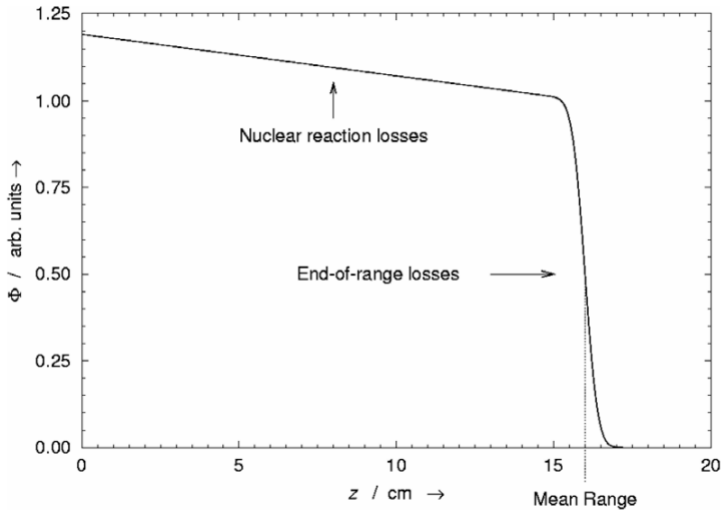

Figure 1.3: Figure from Newhauser and Zhang [104] of the fluence of the primary protons as the beam travels in depth through an absorber material. The slight decline at shallower depths is due to the slow yet steady reduction of primary protons due to their removal via non-elastic nuclear interactions. As the proton beam reaches the end of its range, the rest of the protons are removed rapidly as they run out of energy with a small fluctuation due to energy straggling.

are deflected multiple times as they traverse a material. While each individual elastic interaction results in only a small deflection, with distance these interactions will be more frequent, leading to an angular scattering pattern described by multiple Couloumb scattering (MCS). While the most physically complete description of MCS, described by Molière [97], is quite complex, the distribution of particles scattering through matter is typically approximated as a gaussian distribution. This physically results in increased blurring of the lateral penumbra with depth in material, broadening the laterally integrated Bragg peak (discussed later). The ability of a material to scatter protons is described by its scattering power, which is defined by

$$T = \frac{d < \theta^2 >}{dt} \tag{1.2}$$

where T is the scattering power, $< \theta^2 >$ is the mean squared scattering angle, and t is the thickness of the material that the particle (protons in this case) have traveled (notably different from the path length of that particle).

The final interaction type discussed here are non-elastic nuclear interactions. These, like the elastic Couloumbic interactions, also occur when the proton interacts with an atomic nucleus, but rather than a Coulombic deflection, the primary proton is lost via nuclear forces and a secondary particle is ejected from the nucleus, such as secondary protons, neutrons, alpha particle, or gamma ray. In some cases, the nucleus can break

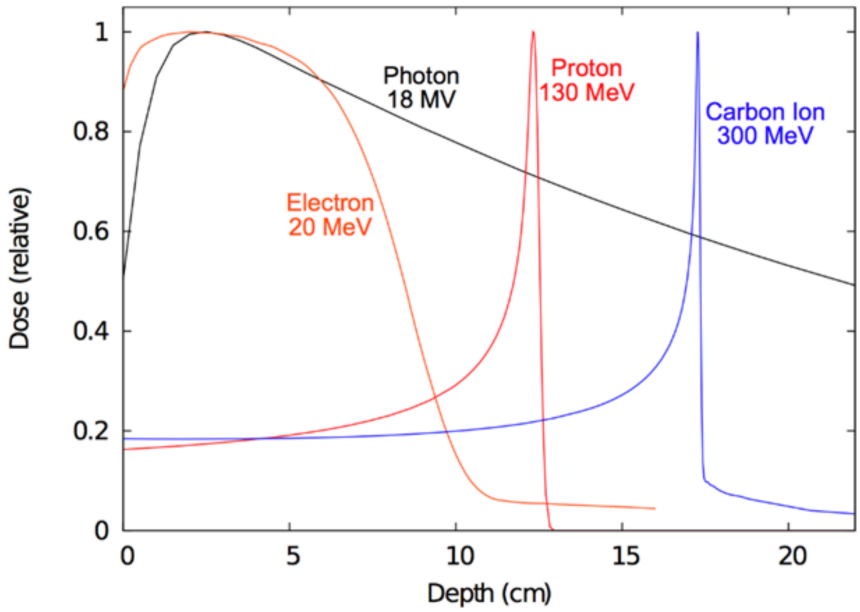

Figure 1.4: Percent depth dose curves (PDDs) for photons, electrons, protons, and carbon ions showing the ability of proton beams to reduce entrance dose and remove exit dose.

apart completely. This is a property of particle therapy because protons (and neutrons) are hadronic (containing quarks) and can interact with the nucleus of an atom via the strong nuclear force. This also applies for particle therapy using heavy ions, as the ions themselves contain protons and neutrons. The dosimetric effect of these interactions is the removal of protons from the primary beam (shown in Figure 1.3 from Newhauser and Zhang 2015 [104]) and generation of secondary particles which can effect the dose distribution. Secondary protons contribute approximately 10% of the dose from a therapeutic energy proton beam [111]. Deuterons and heavier ions do not have a large impact on the dose distribution, they deposit dose locally and consist of 1% or less of the total therapeutic dose [65]. Of more interest for this thesis are the gammas and particularly the neutrons which can deposit energy outside of the desired treatment area (or exit the patient completely).

The signature dose deposition of a proton beam with depth, the Bragg peak, results from a combination of the protons' approximately continuous loss of energy and their tendency to deposit remaining energy very quickly once the protons are under a certain energy threshold (recall the dependence on particle speed in Equation 1.1). For a monoenergetic beam, this results in a lower entrance dose than for photons, and a sharp distal fall-off which quickly converges to zero and significantly reduces exit dose. Figure 1.4 shows the differences in dose deposition with depth of photons, electrons, protons, and carbon ions (Kaiser et al 2019 [71]). As a note, while carbon ions share deposition properties with protons due to their heavy mass and particle charge, the increased mass and energy inherent to carbon ion beams also increases the frequency of nuclear reactions which result in projectile fragmentation [154]. These fragments then travel and deposit dose beyond the

Bragg peak distal fall-off, forming a fragmentation tail (visible in Figure 1.4).

Given this energy deposition pattern, proton beams with multiple energies and appropriately weighted fluence can be used to deliver an even dose distribution to a target via the spread out Bragg peak (SOBP), shown in Figure 1.5 from Jones and Schreuder (2001) [69]. Integrating these weighted beams results in even, high target coverage while sparing more healthy tissue relative to comparable target coverage from photons.

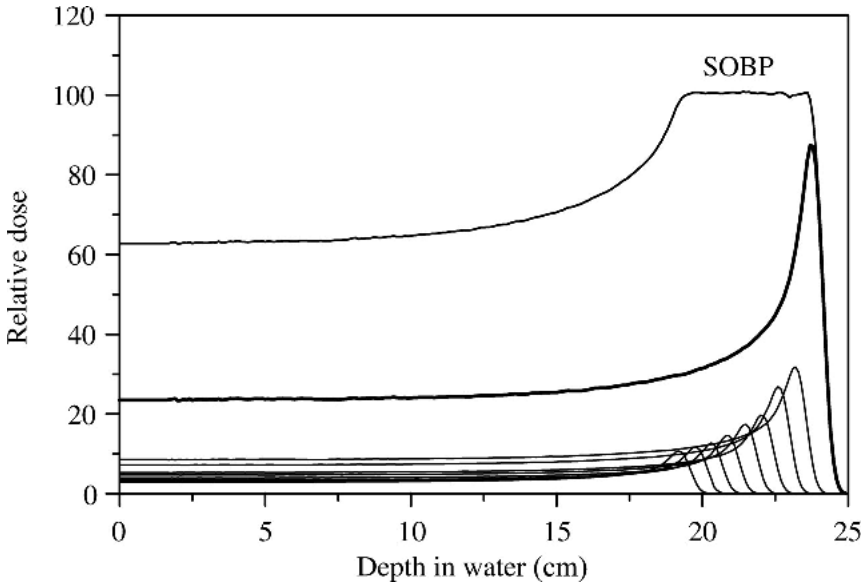

Figure 1.5: Figure of a spread-out Bragg Peak from Jones and Schreuder (2001) [69] formed by a combination of multiple individual Bragg Peaks from proton beams of differing weights and energies. This shows how protons can be used to deliver uniform dose at depth with lower entrance dose than photons and low exit dose.

1.3.2 Active Scanning vs Passive Scattering

The two primary methods of delivering proton therapy is by passive scattering or active (pencil beam) scanning. With passive scattering, the proton beam is passed through a scattering system, range modulator, and range compensator which forms a shaped field. However with active scanning systems, narrow pencil beams of protons are directed by dipole magnets to target a series of spots (with gaussian sigmas taken at isocenter in air which can range from 2.5 mm to more than 10 mm [78] [135]) that are weighted such that they deliver an even dose distribution. For a simplified illustration of the active scanning versus passive scattering systems, see Figure 1.6 (Son et al 2018 [142]). Scattering proton delivery is an older technique, and while some facilities still use scattering machines, most newer facilities and research directions use active scanning delivery for proton treatments. Due to the nature of the scattering delivery, scattering proton plans are associated with much higher levels of stray neutron radiation from high energy protons interacting within

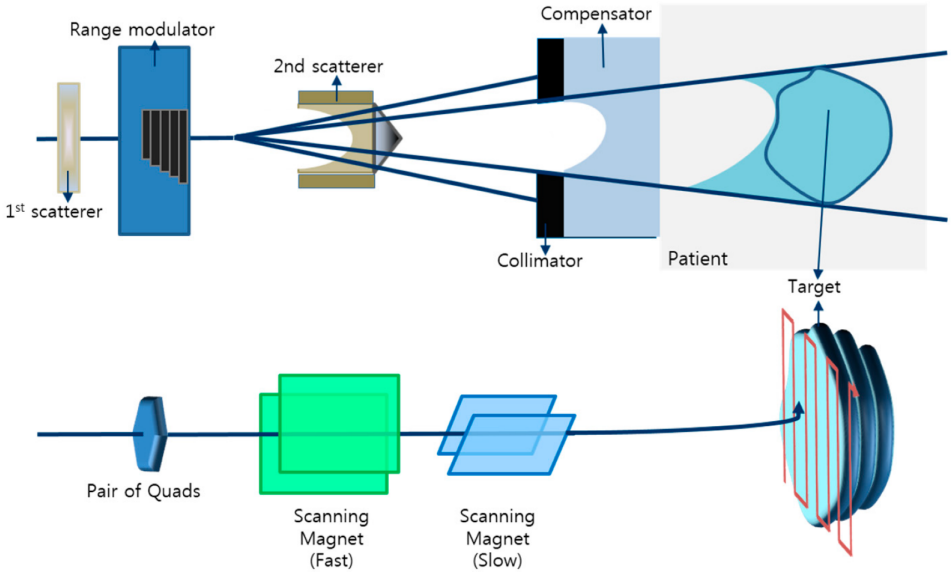

Figure 1.6: Simplified figure of the mechanisms of passive scattering and active scanning proton therapy delivery from Son et al (2018) [142].

the scatterers and compensators (Schneider et al 2002 [128]). In addition to that, it is possible with pencil beam scanning delivery to have highly conformal plans compared to passive scattering (Paganetti et al 2005 [112]) and the ability to create fluence/intensity-modulated proton plans using inverse planning similar to IMRT.

Active scanning systems "paint" the target in energy layers, where each layer consists of a series of spots that the beam targets in succession at a given energy. As the energy of the beam changes between layers, the Bragg peak shifts in depth, and delivers a highly conformal 3D dose distribution. In some treatment plans, slabs of material called range shifters are placed near the patient surface to reduce the range of the proton pencil beam to treat at shallower depths. Compared to scattering protons, motion of the patient during the delivery has a much higher impact when using pencil beam scanning systems. This is both because of the more conformal nature of the plans and because of the time-dependent nature of the beam delivery. With scattering systems, a field is delivering dose uniformly throughout the entire beam-on time. However, with active scanning systems, each spot is delivered individually as the beam scans across and down the target until the full layer has been treated, like printing a document. Because of this scanning pattern, the planned dose can only be delivered correctly to the target if target volume is stationary during the delivery of each layer. Therefore, motion-management is of much greater importance for pencil beam scanning deliveries, particularly for treatment sites experiencing respiratory motion (Grassberger et al 2013 [54], St. James et al 2018 [143]).

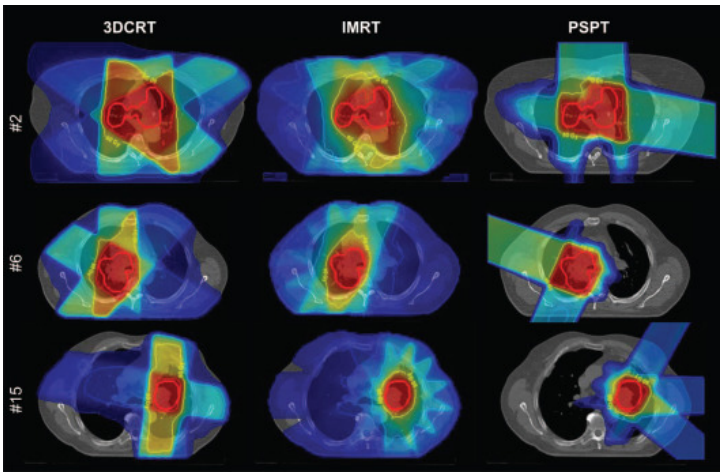

Figure 1.7: A comparison of three different treatment modalities used to treat the same anatomy, with the left and middle being photon 3DC-CRT and IMRT respectively, and the right being a passively scattered proton plan, taken from Roelofs et al (2012) [122]. From this image the healthy tissue sparing capabilities of proton therapy can clearly be seen, as much of the low-dose bath is reduced and the conformality of the high dose to the target volume is increased.

1.3.3 Advantages and Disadvantages

The primary advantage of proton therapy is increased conformality and reduced dose to healthy tissue from the low-dose bath produced in photon plans. This is of particular interest in pediatric cases, patients presenting for re-irradiation (whose organs might not be able to tolerate more dose), and patients with complex tumor volumes in close proximity to sensitive tissues. In addition to this, it is thought that a reduction of the low-dose bath would additionally lower the risk of a radiogenic secondary cancer. Since the low-dose bath is deliberately planned to reduce cell death in healthy tissues, it is more likely that mutagenic changes might survive, which leads to an increased risk for developing a secondary malignancy. Figure 1.7 shows how the the low-dose bath differs between a photon 3DCRT, photon IMRT, and a passive scattering proton plan from Roelofs et al 2012 [122].

That said, proton therapy is not without its disadvantages, and while more literature is coming out supporting the hypothesis that proton therapy reduces risk of secondary cancer, there are a lot of uncertainties in measuring these benefits, and whether it outweighs the costs (Fontenot et al 2009 [49], Chung et al 2013 [33], König et al 2020 [50]). For one thing, proton therapy is more complex and costly, both technically and from a planning perspective. Proton therapy uses a single cyclotron or synchrotron to accelerate the protons which are then funneled to individual treatment rooms, so only one proton treatment can be delivered at a time as opposed to photon treatments, which have their own self-contained units installed in each room. As technology develops, particularly regarding recent developments with compact proton therapy units, the costs will likely decrease

(Mansur 2014 [92]), but the cost-effectiveness of proton therapy is still in flux (Verma et al 2016 [157]). Additionally, treatment planning for protons is typically much more complex. The precise reason why proton therapy offers benefits over photon therapy inherently complicates the planning and delivery process. That is, the conformality. Proton therapy plans must take into account range uncertainty, where the true range of the protons in tissue is uncertain due to a combination of patient positioning, imaging, treatment planning system dose calculation algorithms, and other factors. While many of these uncertainties are also present in photon therapy, due to the sharpness of the Bragg peak, plan conformality, and the fact that protons having a definitive stopping point, range uncertainty could result in underdosing the target or overdosing OARs. Typically this is also dealt with by adding a margin to the clinical target volume (and making careful selection of treatment field angles), however the addition of all of these margins begins to reduce the benefit of having the ability to create such conformal plans.

In addition to this, any intra- or inter-fractional motion runs the risk of underdosing tumor volume and overdosing healthy tissue. In most cases, treatment planners will add a margin of several millimeters to the clinical target volume to account for some patient motion and machine calibration uncertainties and ensure that the tumor is not missed. However, in some cases that is not enough, for example in the lung. While lung motion is a problem even for photon therapy, it is compounded in proton therapy as delivery is not only designed to be highly conformal, but also the "painting" method of a scanning proton treatment delivery requires the tumor to remain motionless while the scan works its way through the volume. Minimizing this so-called interplay effect between the delivery and the patient movement is the subject of a great deal of research (De Ruysscher et al 2015 [39], Molitoris et al 2018 [98]).

1.3.4 Current Perspectives: Neutron Risk in IMRT vs. Scanning and Scattering Proton Therapy

Finally, the last point that will be discussed here is the effect of stray neutron radiation in proton vs. photon therapy. Stray neutron radiation originates from two sources: leakage from the treatment head and internal generation within the patient. The contribution of neutron dose and its effect on the patient during radiation therapy has been a richly researched subject (Brenner and Hall 2008 [21], Jarlskog and Paganetti 2008 [67], Schneider and Hälg 2015 [129]). Neutron generation is a problem because 1) neutrons have a high and variable radiation weighting factor (from 2.5-20, compared to 1 for photons and 2 for protons) due to the neutrons' biological effect and 2) as uncharged particles they can travel quite far from the treatment field and deposit dose throughout the body. For this discussion, it is important to distinguish that typically the three treatment delivery methods that are compared are IMRT (photon), passive scattering (proton), and active scanning (proton). Neutrons are not produced at any significant level in photon plans which use energies under 10 MeV. For proton therapy, scattering and scanning systems have vastly different neutron contributions due to the presence or lack of scatterers and

other material in the beamline in which neutrons can additionally be generated besides those created in the patient. A study by Schneider and Hälg 2015 [129] found that active scanning protons indicated an improved outcome for secondary cancer risk over scattering protons and equivalent outcomes compared to IMRT. Another study from Newhauser et al 2009 [103] indicated that it was possible that both methods of proton delivery reduced risk of secondary cancer compared to IMRT. On the subject of neutron dose influencing the risk of developing a secondary cancer, a review article on the state of knowledge by Hälg and Schneider 2020 [55] collated the data from eleven studies on neutron measurements from multiple proton delivery methods, angles, field sizes, and energies and concluded that while scanning provided significant reduction of stray neutron dose compared to scattering systems, it was unlikely that the neutron doses from either technique would contribute significantly to increased secondary cancer incidence for proton therapy patients, both in general and when directly compared to IMRT patients. However, they also acknowledge that the uncertainties regarding the accuracy of neutron measurements and neutron RBE with respect to cancer induction could still influence our understanding of the role of neutrons in second cancer risk.

1.4 Monte Carlo

It is important to have some background in Monte Carlo (MC) simulations, as not only were they key to this project's undertaking, but also because of the broader impact they have on the field of medical physics. An MC simulation is, in broad terms, a computational method that relies on repeated sampling of a scenario dictated by probabilistic interactions to get quantitative results. They can be used to solve a wide variety of physical and mathematical problems, but for medical physics, they are primarily used to predict radiation transport in matter for a given source and geometry. MC simulation applications in medical physics range from shielding design and radioprotection, to treatment planning system commissioning, and in patient-specific treatment planning optimization (Andreo 2018 [9]). Furthermore, there is interest in adding radiobiological models to MC codes, particularly for use in particle therapy (Mairani et al 2010 [91], Chatzipapas et al 2020 [27], Muraro et al 2020 [100]).

Multiple MC particle simulation platforms have been made for the purposes of radiation transport. Some examples of MC codes include Geant4 (C++) [7], FLUKA (Fortran) [47], and MCNPX (Fortran) [117]. Of course the implementations of each of these codes are different, but in general in order to run a simulation you need to define a radiation source, the properties of the physics processes of interest, an environment (even if its empty), and any materials used in the environment. For more complicated simulations, multiple sources may be defined, such as multiple fields of varying energy, shape, distribution, direction, and particle type. Once everything has been defined, then the user chooses the number of "events" or initiating particles to generate and process. The initially generated particle is then propagated through the environment, where the selected physics process govern the interactions that the particle undergoes based on random seeds and probability

cross-sections. The more particle events, the higher statistics, and the more likely that quantitative values derived from the simulation results will accurately represent the reality represented in the simulation. The advantage of MC simulation when applied to medical physics is that many complex scenarios can be predicted very accurately without risk of exposing humans to ionizing radiation. In terms of dose calculation, MC simulations are the gold standard. However, they are limited by the need to simulate a sufficient number of particles to draw accurate conclusions. This burden of computational power and time is a problem in a clinical setting, particularly in larger centers which can treat more than 200 patients per day (Mayo Clinic: Rochester [1], University of Pennsylvania [4]). However, there has been a lot of recent research dedicated to GPU-based MC calculations (Qin et al 2017 [118], Qin et al 2018 [119], Adam et al 2020 [6]) and developing so-called 'fast' MC codes for daily clinical use (Muraro et al 2020 [100]). Currently, MC options in clinical treatment planning software is available, but is mostly used for verification of the optimized treatment plans rather than in the optimization itself since the plan optimization relies on iterations, each of which would require additional MC simulations. That said, future researchers could see a day when MC treatment planning optimization is standard practice.

This doctoral thesis utilized the Geant4 code in the C++ programming language. Geant4 is open access, with publicly available source code and an extensive library of sample geometry and source configurations. Geant4 also is very flexible with respect to user access to particle tracking information, and because of this a large variety of quantities can be tracked and scored for post-simulation analysis. Because the work of this thesis required detailed tracking information to develop custom in-house scorers (described in detail in Section 3.2), Geant4 was an ideal choice. The base implementation of Geant4 used in this project was based on the work of Schmid et al 2015 [127], which included all the physics lists needed for simulating clinically relevant transport interactions and code to import a medical image and build voxel-based geometry in the simulated environment based on the provided image. This implementation was further developed during this thesis (Section 3.1) to be compatible with the newly developed hybrid phantoms (Chapter 2).

1.5 Treatment Planning

Treatment plans are designed to deliver therapeutic levels of dose to cancerous target volumes for the purpose of tumor control, either alone or in conjunction with surgery and/or chemotherapy. This process involves a clinical team (dosimetrists, physicists, physicians, therapists, etc.) creating and executing an appropriate radiation therapy plan to treat a patient with the joint goals of tumor control and healthy tissue sparing. This includes imaging, defining critical structures (targets, organs at risk, etc.), selecting a delivery method, designing the beam set-up and use of other equipment (motion management systems, skin collimators, wedges, etc.). Depending on the patient and the cancer stage, sometimes the only treated volume is the primary solid tumor. In other cases, lymph node

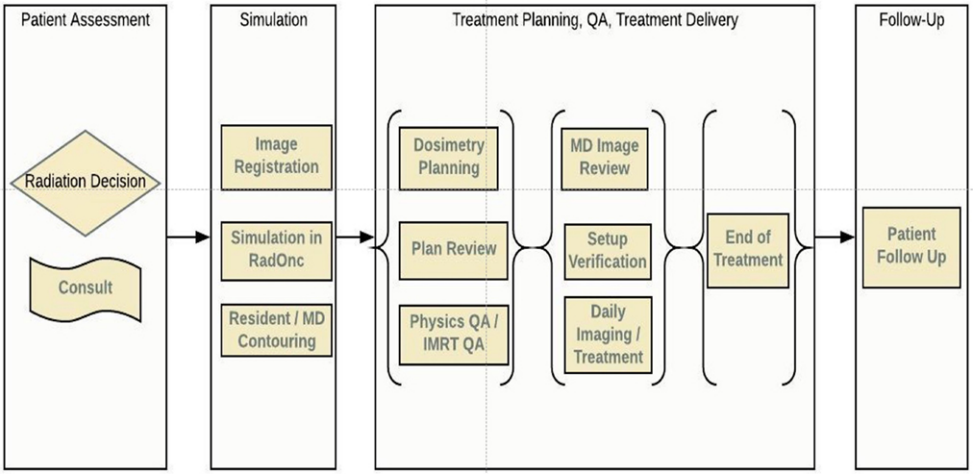

Figure 1.8: A simplified and general example of the clinical workflow for a radiation therapy patient.

volumes will also be irradiated at a lower dose to limit the spread of subclinical disease (here meaning not visible yet on imaging but suspected to be present by the physician). For this project, all of the treatment plans were created as active scanning proton beam plans with no other equipment or techniques.

1.5.1 Clinical Workflow and Treatment Planning

A general example of the radiation therapy clinical workflow, starting from initial consultation to follow up post-treatment, can be shown in Figure 1.8 (from Feng et al 2018 [46]). The patient begins with the initial diagnosis and recommendation for radiation therapy. The patient is then imaged on a CT-simulator, which yields a 3D image of the internal patient anatomy while the patient is positioned in a way which mimics their positioning during treatment delivery. This CT scan is used to contour the tumor target volumes and various organs at risk, possibly with the assistance of other image modalities (such as MRI). Using the contours and CT data, a treatment plan is designed, checked, and ultimately delivered to the patient. Of course depending on the delivery method and individual clinical protocols, there might be a high degree of fine tuning such as additional imaging prior to every treatment fraction, motion management, adaptive planning which modifies the plan after some threshold of change within the patient between fractions, and multiple stages of plan review and quality assurance (QA) prior to treatment application.

The subject of this thesis is primarily concerned with potential improvements in the planning stage, where the decisions regarding beam set-up and dose distribution design are made. Treatment planning is primarily done with clinical software called treatment planning systems which on the broadest level are capable of importing patient image information, creating structure definitions, calculating dose, and optimizing beam configurations to assist the planners to design the best treatment plan for each patient.

TPSs are typically able to handle multiple image modalities (CT, PET, MRI), which especially helps when contouring important structures. However the CT image is vital for dose calculation because it is inherently a measurement of the imaged tissue's attenuation properties which directly impacts the shape of the dose distribution. CT images are based on Hounsfield Units (HU), where each voxel (a volume element, the 3D equivalent of the 2D pixel) is assigned a HU value based on the transmission properties of the tissue that pixel is imaging. Hounsfield units are defined as:

$$HU = 1000 \times \frac{\mu - \mu_{water}}{\mu_{water} - \mu_{air}} \tag{1.3}$$

where μ is the linear attenuation coefficient of the voxel, and μ_{water} and μ_{air} are the linear attenuation coefficients of water and air respectively. HU is a measure of radiodensity represented in an image by a grayscale value gradient. If the HU of a material is <0, that material is less dense than water and will show up darker in the image. Likewise, if the HU is >0, that material is denser than water and will show up brighter. For reference, pure air is around -1000 HU, lung is between -700 and -600, soft tissues can be around -100 to 50 depending on fat content (Lamba et al 2016 [82]), and cortical bone can reach HU values >1000 (although there is a significant range to bone materials due to the different densities of cortical and trabecular bone). Since CT scans are taken using photons, CT images can be used to calculate dose from a photon plan based on the level of attentuation encoded by the HU which has an inherent connection to the relative electron density of the material. When using CT images for dose calculation in proton therapy, the HU values are used in conjunction with a calibration curve unique to the imaging machine to convert the HU values given by the patient image to material density or directly to relative stopping power (RSP) depending on the TPS and clinic. In this way the RSP for each voxel can be determined and used in the TPS dose calculation algorithms.

With the image data imported into the TPS, a trained clinical staff member (for example a dosimetrist, physicist, or physician) can contour and define structures important to treatment planning. Often these fall into two categories: organs at risk and target volumes. OARs are healthy tissues with important biological functions that should be avoided as much as possible when planning the irradiation. Target volumes can be solid tumors or other regions at risk of developing lesions or hosting cancerous cells such as tumor beds in post-mastectomy breast cancer patients or nodal volumes in later stage cancers. Other volumes may be defined to help guide the treatment planning in a specific direction or emphasize an important region which the optimization is under or over dosing. The TPS can also be used to add uniform margins around a given structure. This is often used for target volumes, where the visible solid tumor is contoured as the gross tumor volume (GTV), a margin is added to account for subclinical disease to become the clinical target volume (CTV), an optional margin can be added to account for internal patient motion for the internal target volume (ITV), and then a final margin is added to account for set-up error (imaging, positioning, range uncertainties, etc) to create the planning target volume (PTV).

Once all of the relevant volumes are contoured the planner defines a set of objectives

to guide the optimization function. These objectives can direct the optimizer to prioritize tumor coverage and high risk OARs, set hard limits on dose, and push the plan to be uniform and conformal to the target. Target coverage is dictated by the physician prescription, and typically requires the target to receive the full prescription dose to a large fraction of its volume. Organ at risk constraints are driven by dose limits set by past literature and clinical experience to avoid critical levels of toxicity. In general, if toxicity to healthy tissue can be avoided, it should, however OAR sparing cannot come at the cost of target coverage and ultimately tumor control. Once the initial objectives are defined, the TPS runs an optimization function which attempts to create a treatment plan which prioritizes the objective weighting set by the planner. This process is referred to as "inverse planning".

As part of this optimization process, and as part of the final confirmation of the treatment plan, the TPS must use dose calculation algorithms to accurately determine the optimal coverage. These dose calculation methods can be split into three types: correction-based, model-based, and Monte Carlo. Correction-based algorithms start with some base dose calculation data and then applying corrections to it. The base dose calculation data involves taking measurements in a large water phantom under the most general conditions to construct a library of dose data. Then, depending on the actual beam set-up and patient geometries, some corrections can be applied to reconstruct patient dose. Examples of these corrections include tissue heterogeneity, irregularly shaped fields, and angled field incidence on a curved surface. Model-based algorithms work by using dose kernels to calculate the dose distribution from the radiation based on its potential to physically interact inside the patient geometry at specific points or along a line [160]. The final category, Monte Carlo, uses the same principles described in Section 1.4 to predict dose for each iteration of the optimizer. These MC codes are typically very specialized and use 'fast' algorithms to make the optimization process feasible on a clinical scale. Alternatively, instead of during the optimization, MC can be used post-optimization to verify an analytically optimized plan by recalculating the dose with high accuracy. A priority for these three methods, besides being accurate, is that they must also be fast if they are to be used in the optimization process. The dose must be calculated anew for every new step the optimizer takes to improve the treatment plan, and depending on the outcome the planner might need to adjust the dose objectives and re-optimize multiple times.

1.5.2 Limitations of Treatment Planning Systems

Treatment planning systems are highly specialized to accurately represent the dosimetric properties of the treatment machines in the clinic, however, there are some limitations to their capabilities. Dose calculation algorithms at their core are using approximations of highly complex physical mechanisms, and will therefore always have some level of uncertainty (Van Dyk et al 1993 [155]). Additionally, the use of HU rather than a true characterization of tissue stopping power limits the calculations for charged particle therapy, such as with protons. However for the scope of this thesis, the most important limitation is the deterioration of TPS accuracy outside of the treatment field. Jagetic and Newhauser

2015 [66] showed that for photon therapy, TPS dose calculation algorithms start to deviate from the ground truth at anywhere from 5-10 cm away from the edge of a 5 × 5 cm field. While that is not so much of a problem for initial tumor control, if out-of-field dose and second cancer risk is to be implemented as factors in the treatment planning process, this flaw becomes much more relevant. Tied to this limitation, TPS do not actively transport neutrons, which become a much larger proportionate influence on dose outside the treatment field in proton therapy. As discussed in previous sections, these neutrons can have a significant impact on equivalent dose and therefore the potential risk of secondary cancer.

1.5.3 Advancements in Treatment Planning

Some relatively recent directions in TPS development include the use of linear energy transfer and relative biological effectiveness to inform particle therapies, outcome or risk optimized treatment planning, and developments for fast MC dose calculation. The first involves the use of both dose and LET in proton therapy to minimize the variability of the RBE uncertainties mentioned previously in Section 1.1.1. To expand on that, the biological effect of the protons within the treatment field can differ due to the variance in RBE, which is related to the LET. So by incorporating LET or more sophisticated RBE models, treatment planners could better tailor their plans to have the correct tumor control outcome and minimize healthy tissue damage in particle therapy (McMahon et al 2018 [94], Toma-Dasu et al 2020 [152]).

More relevant for this thesis is the increased interest in outcome or risk optimized treatment planning. This methodology uses not only the physical deposition of dose as an indication of treatment plan quality, but also biological outcomes such as biochemical no-evidence of disease (BNED) (Smith et al 2016 [140]) or risk of developing adverse late effects such as secondary cancer (Rechner et al 2015 [120], Lim et al 2020 [86]). These approaches to treatment planning speak to a growing interest in not only initial tumor shrinkage/control, but also in patient quality of life post-treatment. Despite the interest, there are some fundamental obstacles which make the introduction of risk-based optimizations difficult to implement clinically. The first is that risk models are inherently uncertain and much more nebulous than the physical dose that treatment plans typically rely on. Optimizing based on risk then introduces the possibility of optimizing based on inaccurate assumptions. The second is that even under the conditions of a perfectly accurate risk model, there will likely be a need to compromise between tumor control and secondary cancer risk.

One obstacle in implementing these kind of optimizations is that since they are more separated from purely physical dose they can introduce a level of uncertainty, for example what if these biological/risk optimizations indicate a plan which would, by typical standards, be underdosing the target volume? For curative therapy the priority is tumor control first and foremost, so typically these new optimization methods are constrained to plans which otherwise meet clinical standards.

Also of relevance to this thesis, as touched on in Section 1.4, is the development of more advanced MC computing methods to make fast and accurate MC dose calculation

feasible in clinical settings. While general MC codes are still mostly relegated to research, some highly specialized codes have been developed to yield fast MC dose calculations such as the one used in RayStation [18], a clinical particle therapy TPS. That said, while these 'fast' MC codes can be used for clinical dose calculation, and are typically used to verify the result of the analytical algorithms, not used in the optimization itself (Muraro et al 2020 [100]). They are also inherently limited in the amount of information they provide for the sake of speed, and the quantities needed for secondary cancer risk modeling (described in the next section) are not available from these MC codes.

1.6 Second Cancer Risk Modeling

Radiation therapy can cause damage to tissues other than the target volume, which results in a large range of negative side effects depending on treatment site such as nausea, dry mouth, shortness of breath, infertility, and fibrosis of the heart. One of the most devastating long term effects of radiation is the potential induction of a secondary cancer. The ability to predict the influencing factors of risk for secondary cancer is vital to tailoring treatments to minimize that risk. As radiation therapy carries an inherent risk for mutagenesis and thus carcinogenesis, it is doubly important to understand radiation's role in second cancer risk.

This thesis focuses on two risk quantities: excess relative risk (ERR) and excess absolute risk (EAR). To calculate both of these quantities, the rate of secondary cancer incidence in an unirradiated population is compared against the rate of incidence in an irradiated population. ERR describes the percent increase in risk for the irradiated population compared to the unirradiated, while EAR describes the absolute number of excess incidences compared to the unirradiated group.

1.6.1 Secondary Cancer Incidence

The population of cancer survivors is increasing, both due to early screening methods and to improved treatment. In the US alone, it is projected that the number of cancer survivors will increase from 14 million in 2014 to 20 million in 2024 (Miller et al 2019 [96], Howlader et al 2021 [59]). This population is at risk for developing a secondary malignant neoplasm (SMN), otherwise called a secondary primary malignancy or simply a second cancer. These are cancers which develop independently of the initial cancer (i.e. not a recurrence or metastasis). The National Cancer Institute [2] reports that 1 in 5 new cancer diagnoses are in a patient who has had a previous cancer, and that overall second cancer is a leading cause of death in cancer survivors. Another review paper from Vogt et al 2017 [158] cites several studies which, depending on location, cohort size, and definition of a second cancer, places the incidence of multiple primary cancers in a population of cancer patients between 2-17%. In any case, it is clear that a large population of cancer patients will develop a second cancer, and these cancers pose particular difficulty given that prior treatment might result in the healthy tissue having a lack of tolerance for additional

radiotherapy treatment.

There are many studies on the overall incidence of secondary cancer, but identifying what fraction of those are radiogenic is very difficult due to other influences such as patient genetics, lifestyle, and environmental factors. While it might be impossible to determine the cause of an individual case of second cancer, by examining whole populations of patients who underwent radiation therapy and comparing against those who didn't, it is possible to make some statements on the relative risk of undergoing radiation therapy. A study from Berrington de Gonzalez et al 2011 [15] collating several Surveillance, Epidemiology, and End Results (SEER) Program databases reports that in populations of adult patients (>20 years old) the risk of developing a specifically radiogenic cancer is quite low (8% of solid secondary cancers related to prior radiotherapy). Combined with the estimate of a second cancer occurring regardless of underlying cause, one could calculate an approximate 1-2% chance of developing specifically a radiogenic SMN after radiotherapy. This estimation increases to 3-4% for pediatric patients due to their long survival post treatment. Despite these relatively low percentages, the devastating nature of a second cancer combined with the large numbers of cancer survivors means that a huge emphasis in research is being placed on predicting and minimizing SMN incidence.

1.6.2 Secondary Cancer Risk Modeling

Secondary cancer risk model development relies heavily on data from the atomic bomb survivors. The Biologic Effects of Ionizing Radiation VII Report (BEIR VII) [36] is the most commonly accepted source of best practices for secondary cancer risk modelling. The BEIR VII model for solid secondary cancers is the linear no-threshold (LNT) model, which holds that any amount of radiation has a chance to induce a cancer, and the risk of that induction increases linearly with dose. The slope of that linear relationship depends on a variety of factors such as the irradiated tissue, patient gender, age at exposure, and attained age. Tables with coefficients corresponding to all those influencing factors are given in the BEIR VII report and used to calculate organ-specific risk coefficients.

An important thing to note is that the LNT model described in the BEIR VII Report is only applicable for low doses (<2.5 Sv), and even in that range the accuracy of the LNT model is hotly debated (Sykes 2020 [149], Cardarelli and Ulsh 2018 [24], Mossman 2012 [99]). Not only were the populations used to create the models inherently limited (atomic bomb survivors, select medical exposures), but even within that dataset in the time since the publication of the BEIR VII, an update to the atomic bomb mortality data yielded a dose-response curve inconsistent with the LNT model (Doss 2018 [43], Ozasa et al 2012 [110]). Furthermore, the low dose limit of <2.5 Sv means the LNT model is not applicable to any of the tissues which would be exposed to high therapeutic doses during radiotherapy.

Several alternate models have been proposed to supplement the LNT model at higher doses (Fontenot et al 2009 [49], Rechner et al [120], Dasu and Toma-Dasu 2017 [37], Stokkevåg et al 2016 [145]). Many of these models are designed to replicate the shape of the LNT model at low doses, and then shift at a proposed "inflection point" which

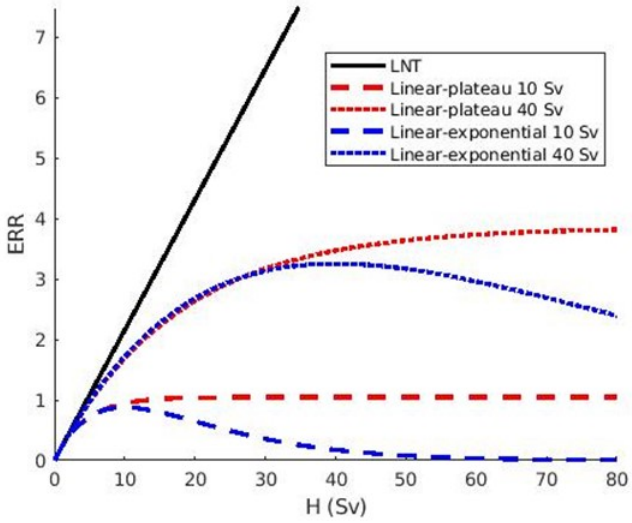

Figure 1.9: The shape of the 5 risk models used in this thesis: linear no-threshold (LNT), linear-plateau with an inflection at 10 Sv and at 40 Sv, and linear-exponential with an inflection at 10 Sv and at 40 Sv. Equivalent dose (H) is measured in Sv on the x axis and risk is calculated as the ERR. The inflection points represent different possible dose-response relationships in the region outside of the LNT's recommended use. This example uses the generic organ coefficient from the BEIR VII report for a patient with an age at exposure of 45 and an attained age of 65.

represents the dose at which the risk of cancer incidence no longer follows linearly. Two of these models are the linear-exponential and linear-plateau models. The linear-exponential model sets the risk to peak at the inflection point and then fall off to zero, while the linear-plateau model approximately levels off near the inflection point and approaches the theoretical limit of risk as dose grows to infinity. Other models attempt to model risk mechanistically (Shuryak et al 2009a [136], 2009b [137]). For this project we chose to use the LNT model, the linear-exponential model, and the linear-plateau model. Each of the latter models were used with inflection points at 10 Sv and 40 Sv, to represent a wide range of investigated dose-response relationships (Schneider et al 2011 [130], Sachs and Brenner 2005 [125], Sigurdson et al 2005 [139], Ruben et al 2008 [124]). A figure showing the shape of all tested risk models is given in Figure 1.9 when calculated using the BEIR VII organ specific risk coefficients for a non-specific organ in a patient at age 45 at exposure and attained age of 65.

1.7 Computational Phantoms

One tool used to estimate dose delivered to a patient are phantoms. Phantoms can be either physical or computational, but broadly they seek to mimic the radiation interaction

properties of human bodies. Phantoms can be used to calibrate treatment machines, to test prospective treatment plans, or to recreate a historical radiation exposure incident for retrospective dose analysis. Physical phantoms can come in varied sizes, shapes, and materials, from water tanks to anthropomorphic to patient-specific 3D prints (Halloran et al 2021 [56]. Computational phantoms can be used in computer simulations for dosimetric analysis and radiation safety assessment. As computer technology over the years has improved, these phantoms have developed from simplistic shapes and organ models to libraries of varied body types represented by complex meshes. Computational phantoms are ubiquitous in MC-based dosimetry studies, and accurate representation of the human body is essential to draw accurate conclusions from simulated geometries. This thesis is based on computational tools, and so this section will focus on the development of computational phantoms prior to the work accomplished in this thesis.

1.7.1 Use in Therapy and Radiation Protection

Phantoms provide a method of estimating the effects of radiation on a person by replicating the shape, density, and elemental composition of human tissues. For dosimetric applications, the anatomically accurate representation of the tissue-equivalent materials is essential. Human bodies are highly heterogeneous, with organic materials varying from lung to fat to dense bone, as well as inorganic materials such as tooth fillings and pacemakers or other implants. A thorough study of internal dosimetry for patients undergoing therapeutic or imaging procedures necessitates an accurate anatomical model. Furthermore, physical anthropomorphic phantoms are used to benchmark and verify the accuracy of computational dose simulations.

Computational phantoms are used in situations where it isn't feasible or is significantly easier to use than a physical phantom. For example, computational phantoms can be used in prospective shielding calculations to estimate dose to radiation workers, to predict how a treatment plan will deliver dose across the whole body, or to replicate a radiation accident for retrospective dose analysis. Often these simulations use MC codes, which can adapt to a variety of different environment geometries and radiation sources. Computational phantoms are flexible because there is a much higher level of control over the quantities that are simulated and tallied. Additionally, many modern computational phantoms are customizable, and come in a wide variety of patient body types, including stages of pregnancy and pediatric development. This gives them an advantage over physical phantoms, which can be quite expensive, although all simulations with computational phantoms should be benchmarked with physical measurements.

1.7.2 Advancements in Computational Reference Phantoms

One of the earliest computational phantoms was the Medical Internal Radiation Dose (MIRD) phantom, developed by Snyder et al initially in 1969 and further revised 1978 [141] to represent an average healthy adult male. This phantom was composed of extremely simple shapes described by geometric primitives as shown in Figure 1.10. Based

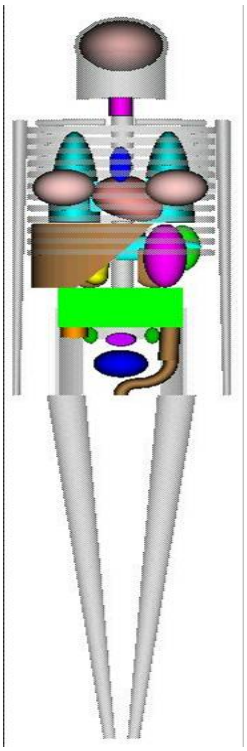

Figure 1.10: The original MIRD stylized phantom composed of geometric primitives from Snyder et al (1969) [141] at Oak Ridge National Laboratory.

on this phantom, several other phantoms were created in "families" that would share similar structures but vary in size to represent patients of different sizes or ages. However, while the model itself was already fairly geometrically simplistic, a scaled model of an adult is not accurate to the anatomical proportions of a child. Therefore another set of specifically designed pediatric phantoms were also created (Hwang et al 1976 [61], Jones et al 1976 [70], Deus and Poston et al 1976 [41]). Further advances were the development of gender specific phantoms (Kramer et al 1982 [79]), and phantoms of pregnant women (Stabin et al 1995 [144]). However, despite all of this progress, the phantom structure was still "stylized" in the form of basic geometric shapes, such as ellipsoids, cylinders, and combinations of prisms.

As computer technology developed for both modelling and simulation, there was an interest in further refining the phantoms to be more anatomically accurate. With CT scans becoming more widely available in the late 70's and early 80's, research groups were able to create voxel-based phantoms directly from the whole-body images of real people (often cadavers as they could tolerate the high levels of dose needed for a high resolution whole-body CT scan). Each slice of a 3D CT scan could be segmented into various tissues and organ structures, and once that was done for all slices, they could be stacked and combined into a voxel-based phantom. This was quite laborious, since for a whole-body phantom one would need to go slice by slice and identify each pixel as belonging to a

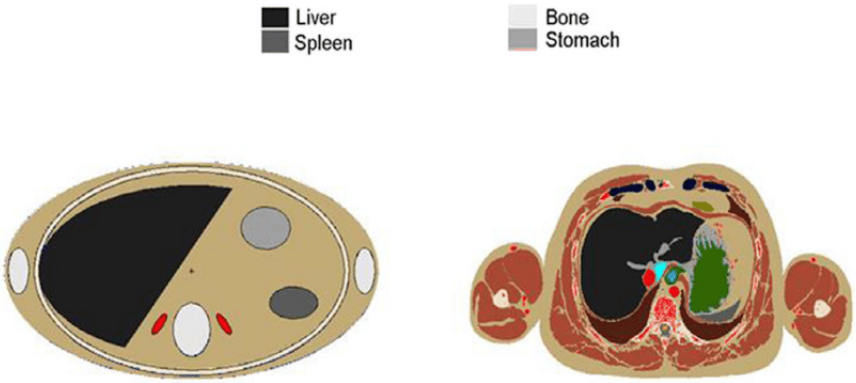

Figure 1.11: A stylized adult phantom (left) compared against a voxel phantom (Visible Photographic Man phantom, or "VIP-Man", right) from Xu 2014 [163] illustrating the increased anatomical complexity and accuracy available from advances in voxel-based phantoms.

particular tissue or structure, specify and define the density and chemical composition for each tissue or structure, and the finally convert that data into an MC compatible data format. Despite that, a huge number of new voxel phantoms were developed (Zaidi and Xu 2007 [166], Xu 2014 [163]), and the ICRP published a voxelized version of adult reference male and female phantoms (ICRP 110 [64]). A comparison from Xu 2014 [163] of the anatomical complexity available in voxel vs stylized phantoms is shown in Figure 1.11.

While the voxel phantoms were an improvement over the stylized phantoms, they are not without their limitations. It is very difficult to modify or customize a voxel phantom, and so would impact the ability to execute 4D studies involving motion. Furthermore, the coarseness of the voxel resolution could lead to incontinuities in organ structures, and an inability to precisely render small-scale organs with anatomical accuracy. The latest generation of phantoms seek to overcome these obstacles. Boundary representation (BREP) and polygon mesh based phantoms are able to be posed, deformed, and otherwise modified to allow for 4D studies in for example cardiac and lung respiration [146]. BREP phantoms have structures defined by mathematical curves such as non-uniform b-spline (NURBS) to construct complex surfaces. The flexibility of the BREP phantoms means that a relatively large number of "families" and libraries have been created, covering a range of patient body types from the same base anatomy (Zhang et al 2009 [167], Segars et al 2013 [133]). On the other hand, polygon meshes are defined by connecting a series of points in space with polygonal faces, and are commonly used in computer graphics, engineering, and visual effects in entertainment. The first polygon mesh phantom was developed by Kim et al 2011 [73] to convert the voxel-based VKH-Man phantom (based on a reference Korean adult male) into a polygon surface mesh. However, simulations using a surface mesh are significantly slower compared to voxel or tetrahedral mesh phantoms. Since then, the research group at Hanyang University in Korea has developed a method to

convert the surface meshes into a solid tetrahedral mesh and implement these phantoms into a Geant4 Monte Carlo simulation environment for a significant increase in computational speed (Yeom et al 2014 [74], Han et al 2020 [57]). As the mesh phantoms developed by the Hanyang University group were used for this thesis, the next section is dedicated entirely to a more technical background of these phantoms.

1.7.3 Mesh-type Computational Reference Phantoms

ICRP Task Group 103 under Committee 2 is dedicated to developing the next generation of computational phantoms. The new phantoms are mesh-type computational reference phantoms (MRCPs) which use 3D mesh structures to overcome voxel format limitations for dose calculations. Since polygon meshes are so common in other applications, a wide variety of commercial and free to use software is available to manipulate, deform, and customize mesh phantoms. These mesh phantoms are provided in both a triangular surface mesh, such as those 3D models used in computer graphics, and in a 3D tetrahedral volumetric mesh, which is used to build the geometry in the Monte Carlo simulations. The particular mesh phantoms used here are based on the adult reference computational voxel phantoms from the ICRP 110 publication [64], developed by the Hanyang group (Kim et al 2016 [76], Kim et al 2018 [75]). In addition to the phantoms used in this study, the Hanyang University group is working on developing pediatric mesh phantoms (Choi et al 2021 [30]), and on building a complete library with various patient body types (Choi et al 2020 [31]). The phantoms used in this study are the male and female MRCPs which were designed to replicate the voxel-based ICRP 110 adult reference computational phantoms.

The primary advantages gained by using these phantoms is the ease of manipulation (such as adapting phantom positioning or scale), more accurate anatomy in small volume organs (such as the lens of the eye), and the smoothness and continuity of mesh structures, particularly in volumes with thin sharp curves (such as layers of skin or bone). The advantage over BREP phantoms is the relative freedom of deformation, as since the models are not based on mathematical curve descriptions, they are much easier to define and edit. Furthermore, some BREP models require voxelization before implementation into MC simulations, while tetrahedral meshes can be built as meshes inside MC particle transport geometries. However, they are subject to issues of resolution, not enough polygons and the surface of a supposedly smooth organ might be bumpy and angled.

One of the main incentives for the development of these mesh phantoms is for use in radioprotection. These mesh phantoms are more easily adjusted than voxel-based phantoms, and can be posed using typical 3D modelling software to replicate the geometry of radiation accidents or other situations of interest. For this project, the only manipulation we apply to the MRCPs are scaling, translation, and cutting. Due to the mesh properties, all of the organ and structure meshes can be scaled without any loss of image data. There is no partial volume effect that would be present in resizing a voxel-based image, and the scaling factors can be accurately applied even on extremely precise scales if necessary.

The second advantage is the continuity of the phantom. In a voxel format, depending on the voxel size, there can be situations where the surface of a curved organ is not accurately

represented in the 3D structure. As an illustrative example, imagine a beam superior to the skull which points directly down on a head phantom which has been coarsely voxelized. There could be a case where, due to the curve on the apex of the skull, the first material the beam interacts with is brain, and not skin or bone. This problem is eliminated when using the mesh phantoms.

As part of the research agreement with the team at Hanyang University, the Department of Medical Physics of LMU Munich has access to the two MRCPs created from the ICRP 110 phantoms along with the organ material definitions for both. Each MRCP comes in two mesh formats, a triangular surface mesh (.obj), and a tetrahedral volumetric mesh (.ele and .node) a visual guide of which can be seen in Figure 1.12 from the development of the PSRK-Man tetrahedral mesh phantom from Yeom et al 2014 [74]. The surface mesh format consists of concentric hollow organ meshes, and this format is what is easily manipulated in 3D modelling software. The volumetric mesh is constructed of solid tetrahedral meshes, and this format is what is ultimately implemented into Geant4 for MC dose calculations. In addition to the raw phantom data, they provided their implementation of the tetrahedral meshes (also referred to here as tetmeshes) into Geant4 and the script they developed to convert a surface mesh phantom into a tetrahedral mesh. Both of these approaches have been slightly adapted for this thesis to fit into the Geant4 workflow, be compatible with a hybrid geometry format, and in general tweaked to fit the hybrid development workflow. These phantoms and codes were used in this project to create two of the three segment types in the patient-specific whole-body hybrid phantom developed in this thesis. They also function as a control against the new hybrid phantom methodology. The regions of the hybrid derived from the MRCPs provide an approximation of the patient anatomy which is missing or not included in the planning CT. The full hybrid creation process will be detailed in Chapter 2.

1.8 Thesis Summary and Specific Aims

The goal of this thesis was to take steps to fill the gap in knowledge described by Newhauser and Durante 2011 [102], where patient-specific anatomical knowledge outside the imaged area is needed to make observations on patient-specific risk of secondary cancer. With the ability to represent patient out-of-field geometries, there is a potential to tailor treatment planning not only for primary tumor control, but also to reduce late effects like secondary cancer. Without a computational phantom, the only way to get patient-specific anatomical representation would be through additional CT scans, which would expose the patient to unnecessary dose. To avoid this, the already known CT scans of a patient can be combined with a computational phantom selected and tailored to match noninvasive patient measurements (taken from physical measurements or surface scanning). With this kind of composite phantom, the integrity of the known in-field is maintained and supplemented by a "best guess" estimate of the patient anatomy outside the treatment field. While the methodology which was created for this project can be flexibly utilized with any treatment technique which can be simulated in Geant4, this project chooses to focus on active scan-

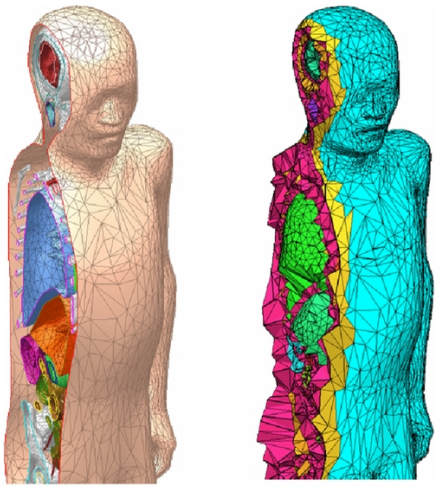

Figure 1.12: Figure from Yeom et al 2014 [74] demonstrating the structural differences between a polygonal surface mesh as a series of hollow shells (left) and a volumetric tetrahedral mesh as a series of filled layers (right)

.

ning proton treatment plans, taking into particular consideration the neutrons generated inside the patient during proton therapy. The specific aims of this project were to:

- Develop the tools and methodology needed to create a hybrid CT-Mesh whole-body phantom. Questions to answer are: Is this hybrid geometry feasible to simulate in terms of computation time? Is the methodology flexible enough to handle diverse patient geometries?

- Verify and quantify the hybrid's ability to predict dose quantities throughout the body using the mesh phantoms as a control and a whole-body CT as ground truth. Pertinent questions are: How can neutron dose, neutron energy, and equivalent dose be accurately scored and/or calculated? Is the hybrid able to offer an improvement over a mesh phantom alone? How well does the hybrid predict the dose quantities of the ground truth whole-body CT for representative proton therapy treatment sites?

- Implement multiple risk models, expand the hybrid library, and assess the impact of using risk rather than dose quantities to quantify hybrid performance. Some questions to answer are: Does a significant difference in dose prediction between two phantoms translate to a significant difference in risk prediction? How does choice of risk model effect the relative performance of the hybrid? Ultimately, are the risk predictions given by the hybrid a reasonable approximation of the ground truth?

Chapter 2

Hybrid Phantom Creation

This chapter will discuss the creation process of the hybrid computational phantom and go over the motivations for key design decisions. The starting point for any hybrid creation begins with a patient CT and a whole-body unscaled mesh reference computational phantom (MRCP), pictured on the right of Figure 2.1 from Yeom et al 2018 [164]. Using these two starting images and the tools developed during the course of this project, a hybrid phantom can be developed regardless of patient gender or treatment site. In the future, when more mesh phantoms are available from a library, hybrids could benefit from intelligent selection of closer body type, e.g. for pediatric patients, or patients at various stages of pregnancy.

A standard whole body hybrid can be composed of 3 to 5 segments depending on the location of the treatment site. These segments can be categorized into three distinct types: the in-field, the out-of-field, and the transition. The in-field is a CT image of the patient. In a clinical situation it would be the same CT used for treatment planning, but in the case of this project, the in-field was selected manually from a whole-body CT (WBCT). The hybrid will always have at least one of each of these segment types.

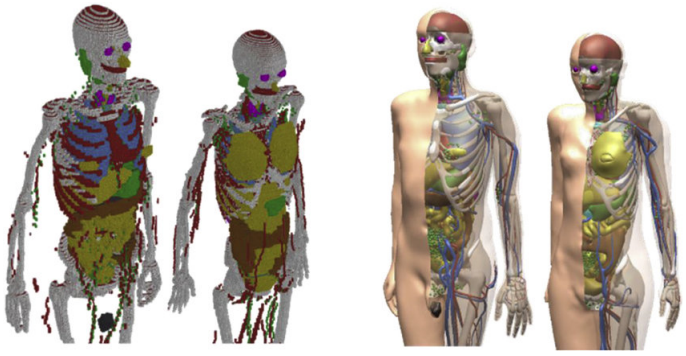

Figure 2.1: A visual comparison of the voxel-based ICRP 110 Adult Computational Reference Phantoms (left) and the new MRCPs based on the ICRP phantom anatomy (right) from Yeom et al 2018 [164]

Depending on the in-field location and extent of the patient on either side of the in-field, there might be an additional transition and out-of-field segment. By using an extraction from a WBCT, the WBCT can be used as a "ground truth" when examining whole body dose distributions from the hybrid and other phantoms. The out-of-field is represented by a mesh-type reference computational phantom (MRCP) which has been scaled to patient measurements and cut into segments which flank the in-field and transition regions. In a clinical situation the patient measurements for scaling would be taken physically in the form of sitting height and waist dimensions or by using surface scanning technology, but in the case of this project, the measurements were taken directly from the WBCT bony anatomy in the form of spine height and pelvis width/depth. Finally, the transition region is a voxel-based segment derived from the mesh phantom and deformed to blend into the patient CT. This blended region is created by voxelizing the whole body scaled MRCP, then registering the voxelized and scaled MRCP in-field anatomy to the CT in-field, and finally modifying the deformation field from that registration with an extended softening gradient which blends the in-field patient CT into the out-of-field mesh region(s) and applying the extended field back onto the whole body scaled MRCP. The final blended region smoothly transitions the anatomy of the in-field CT to that of the MRCP. A flowchart illustrating the simplified hybrid creation process is shown in Figure 2.2.

2.1 Scaling the MRCP

The scaling methodology is adapted from that of Zvereva et. al [168] and modified to account for the fact that this study utilizes WBCTs and did not have access to physical measurements. Instead, measurements were taken from both the WBCT and the default MRCP at the terminal points of the spine (inferior/superior) and of the pelvis (anterior/posterior, left/right). In addition to these base measurements, the chosen WBCT "in-field" and the section of the MRCP anatomy which most closely matched the anatomy of the chosen WBCT "in-field" was measured using the terminal points in the Z dimension (inferior/superior). The two "in-field" anatomies were taken into account in the scaling factor calculation to ensure that, after splicing the WBCT in-field into the scaled MRCP and transition regions, the completed hybrid and the WBCT would have the same pelvic and spinal dimensions. An exaggerated visual representation of this concept is shown in Figure 2.3.

Based on the described measurements, the scaling factors in X (left-right), Y (antero-posterior), and Z (craniocaudal) were calculated using the following methods:

$$X := \frac{X_{max,WBCT} - X_{min,WBCT}}{X_{max,MRCP} - X_{min,MRCP}} \tag{2.1}$$

$$Y := \frac{Y_{max,WBCT} - Y_{min,WBCT}}{Y_{max,MRCP} - Y_{min,MRCP}} \tag{2.2}$$

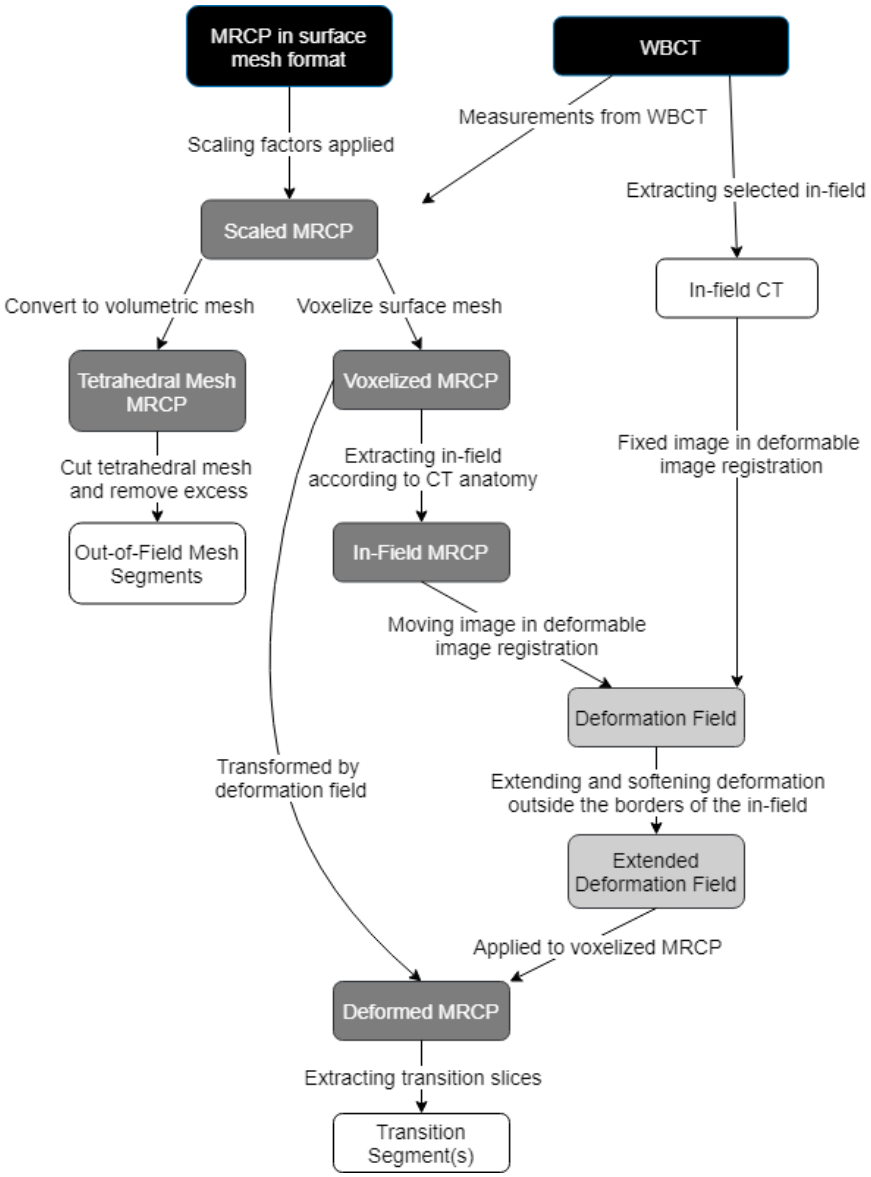

Figure 2.2: Flowchart from Kollitz et al 2022 [77] showing the creation of a hybrid phantom from starting materials (black), intermediate image components (dark gray), deformation fields (light gray), to final components which will be spliced together to make the hybrid (white).

For an in-field entirely outside the spine measurements (e.g. the skull above its base):

$$Z := \frac{Z_{max,WBCT} - Z_{min,WBCT}}{Z_{max,MRCP} - Z_{min,MRCP}} \tag{2.3}$$

For an in-field extending within and above the spine measurements (e.g. the head and

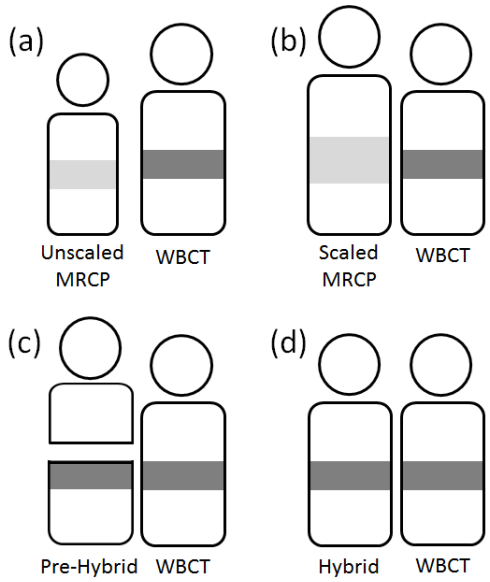

Figure 2.3: Schematic from Kollitz et al 2022 [77] showing the sequence of steps to visualize how the scaling factor takes into account the relative differences in size of the in-field after scaling, so that when the CT image supplants the reference phantom anatomy, the final size of the hybrid will match that of the patient. (a) shows the starting CT and the default mesh phantom with the in-field (light gray in the MRCP, dark gray in the WBCT) size differences exaggerated for visibility. Then the mesh is scaled in (b), the in-field anatomy replaced in (c), and the superior part of the the mesh is translated inferiorly in (d) to eliminate the gap. In a true hybrid, the in-fields from a) would undergo the registration and transition region creation, however for clarity these were omitted in the visuals. The hybrid in d) would have two transition regions flanking the transplanted dark gray in-field.

neck):

$$Z := \frac{(Z_{max,WBCT} - Z_{min,WBCT}) - (Z_{max,WBCT} - InField_{min,WBCT})}{(Z_{max,MRCP} - Z_{min,MRCP}) - (Z_{max,MRCP} - InField_{min,MRCP})} \tag{2.4}$$

For an in-field extending within and below the spine measurements (e.g. the prostate):

$$Z := \frac{(Z_{max,WBCT} - Z_{min,WBCT}) - (InField_{max,WBCT} - Z_{min,WBCT})}{(Z_{max,MRCP} - Z_{min,MRCP}) - (InField_{max,MRCP} - Z_{min,MRCP})} \tag{2.5}$$

This scaling factor calculation accounts for potential differences in the relative anatomy of the scaled MRCP in-field and the original WBCT in-field. This ensures that, at the end of the hybrid creation process, both the WBCT and the hybrid will have the same spinal height. This can be seen in Figure 2.4, which shows how the scaling factor adjusts the size of the default MRCP to more closely match the spinal dimensions of the WBCT, not necessarily the overall height of the WBCT. The leg length was not included in the height scaling since the majority of the organs of interest are contained within the torso,

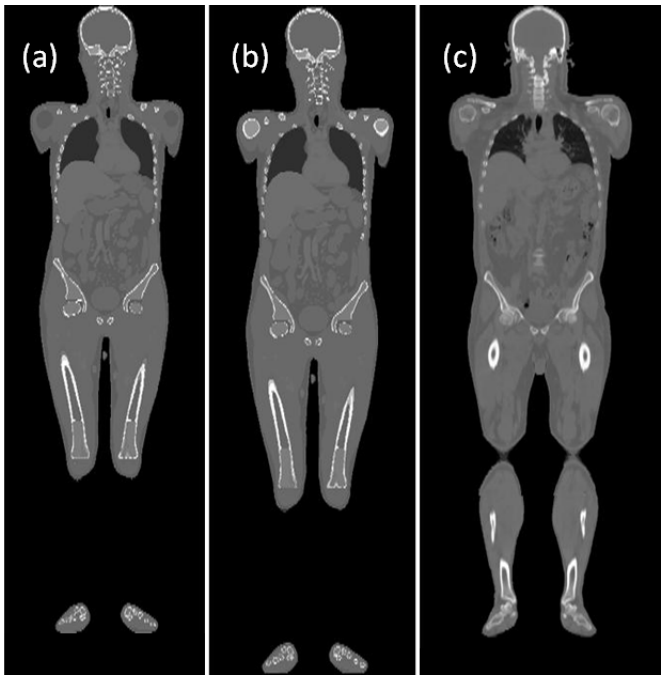

Figure 2.4: A visual comparison between (a) the unscaled MRCP, (b) the scaled MRCP, and (c) the WBCT, shown here in voxel format, which illustrates how the scaling elongates the reference phantom to match the spinal cord and pelvic dimensions of the WBCT.

so the scaling measurements were chosen to match the torso size as closely as possible. Theoretically, segmented scaling factors are possible, which can take into account the relatively different sizes of segments of patient anatomy, but to do so would require a more detailed mesh scaling implementation and additional measurements of the patient in a clinical environment. For our baseline study, it was considered sufficient to scale to a single factor in each dimension. Once calculated, the scaling factors were applied to the surface mesh format of the MRCP using Blender [35], a free to use 3D modelling software. The scaled mesh was then exported as a ".obj" surface mesh for future use in creating the transition and out-of-field mesh segments.

2.2 Voxelizing the MRCP

While the Geant4 Monte Carlo simulations utilize the MRCPs in their mesh format, a voxelized version of these phantoms (both scaled and unscaled) are needed for visualizing the complete hybrid in Matlab, for masking organs for dose analysis, and for creating the transition region. An in-house code was developed to convert MRCPs in surface mesh format into 3D Matlab voxel arrays. From there those arrays could be converted into medical image filetypes such as DICOM, .mha, or .mhd files. Those filetypes, especially DICOM, encode more information than Matlab about the image array, such as position in

3D coordinates and voxel dimensions, and can optionally include patient name (anonymized for our purposes), treatment information, and more.

As part of this process it was important to determine that the voxelization did not have a significant impact on the dose distribution. To this end, the same default male MRCP was first voxelized at multiple voxel resolutions, then a monoenergetic proton field was simulated on the default MRCP as well as all the voxelized versions. A gamma index analysis was performed to quantify the effect that different voxel resolutions had on the dose distribution compared to the original mesh (fully described in Section 2.2.2).

2.2.1 Developing the Voxelization Code

The voxelization code takes an MRCP surface mesh in .obj file format and converts it into a Matlab 3D voxel array. The user must input whether the MRCP is either male or female, the dimensions of the 3D space which fully contains the mesh, and what quantity the voxel array will represent (mesh material ID, density, or Hounsfield unit). The code first uses the Matlab Wavefront OBJ toolbox developed by D.J. Kroon [80] to read in a .obj surface mesh file into the Matlab environment. Next, the code iterates through every organ mesh present in the read-in .obj file, and voxelizes each individual organ structure along the user-defined 3D grid, and assigns it the numerical property corresponding to the selected quantity. The program then sorts all of the organ voxel arrays based on the size of the organ and then iteratively combines them into one complete array. In almost all cases in this study, the MRCP was voxelized into a 3D array using Hounsfield units (HU) to match the WBCTs. The HU for a given organ was calculated using a conversion from density based on the density/elemental composition of the mesh materials and the density-HU conversion table used in RayStation 7 (research version of a clinical treatment planning system). The densities for each organ was given as a part of the material property in the MRCP data files. One limitation for this program is that the organ meshes in the MRCP (scaled or unscaled) must adhere to a particular naming and identification schema so the code can correctly assign each organ its correct value. If the MRCPs have been updated or adapted to use a different naming convention, then this program would have to be appropriately altered.

2.2.2 Validating MRCP Voxelization

Once the MRCP was able to be voxelized, a voxel resolution needed to be determined which 1) would not disturb the mesh dose distribution via partial volume effects and 2) would not be computationally burdensome to voxelize or simulate. The first voxelization of the MRCP was completed based on the voxel dimensions of the ICRP 110 adult male reference computational phantom ($2.08 \times 2.08 \times 8$ mm). Due to the particularly coarse resolution in Z, the mesh phantom was also voxelized to have slice thicknesses of 6 and 4 mm. The voxelized MRCPs at each of the chosen resolutions is shown in Figure 2.5. The effect of the voxelization is most readily visible in areas of fine curving bony anatomy, such as the skull, vertebrae or the pelvis.

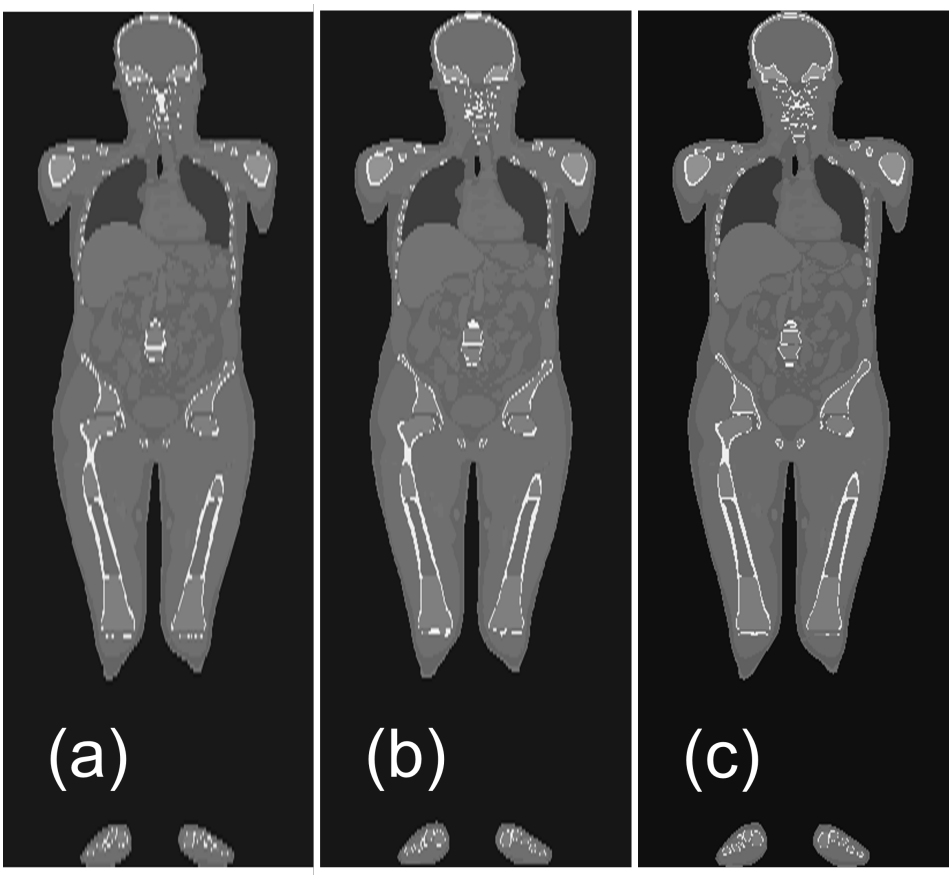

Figure 2.5: Coronal slices of the three voxelization resolutions of the default MRCP. Between the three, only the voxel size in Z (craniocaudal) was changed from (a) 8 mm to (b) 6 mm and to (c) 4 mm.

A monoenergetic proton beam was simulated impinging on the anterior surface of the body in four anatomical locations: the head, the chest, the abdomen, and the pelvis. Total absorbed dose was scored in the original MRCP and three voxelized MRCPs and an in-house code was written to assemble the scored data into a 3D array. Gamma index analysis [85] was then performed to determine to what extent the voxelization affected the dose distribution given by the original mesh phantom. Gamma index analysis measures how similar two data distributions are by using a pass-fail system for each individual voxel, given two parameters, a percent difference and a distance to agreement in units of mm, which determine the acceptable tolerance in dose distribution differences. Gamma index analysis is designed to take into account not only the difference in value between the same individual voxels in two distributions, but also the proximity to voxels of a similar value. In this way, a small offset in a region of sharp change in the distribution would not be overly punished by the algorithm. For this test, only voxels which scored at least 10% of the maximum dose were analyzed to omit the influence of statistical fluctuation outside of the primary field. The two pass parameters set for our analysis was 3% for dose difference and 3

Table 2.1: Gamma index analysis pass rates for each of the three voxel resolutions for the four tested anatomical regions

		Beam Position			
		Head	Chest	Abdomen	Pelvis
Slice Thickness (mm)	8	0.833	0.880	0.891	0.889
	6	0.944	0.965	0.971	0.975
	4	0.984	0.984	0.992	0.995

mm distance to agreement to match typical clinical conditions where two dose distributions are considered equal when there is a passing rate fraction of over 0.95 using the parameters 3%/3mm.

Table 2.1 shows the gamma pass rates for each of the three voxelizations compared against the true values of the mesh geometry. Another note is that while slice thicknesses of 4, 6, and 8 mm were chosen for the purposes of testing the voxelization process, it was determined later that the most effective way of creating and verifying the hybrid was to match the slice thickness to that of the whole-body CT, which was 5 mm. It was decided that the relatively small loss of resolution compared to 4 mm was an acceptable compromise given the results of the gamma index analysis, the fact that the voxelized segments only appear in the transition region (outside of the treatment field), and the ease and precision gained during transition slice creation by matching the slice thickness of the WBCT.

2.3 Creating the Transition Slices

This section will go over the creation process of the transition slices for the hybrid. In brief, the transition slices are short (in the Z dimension), voxelized regions created by applying a custom deformation field to the voxelized, scaled MRCP (referred to in this section as just the scaled MRCP for brevity), which extends past the in-field, softening as the distance from the border increases. The transition slices are then extracted from the deformed scaled MRCP and implemented as their own individual segments in the hybrid. The high level steps in this process were shown in the Figure 2.2 flowchart, and a little more detailed visualization is shown in Figure 2.6.

2.3.1 Preparing for Deformable Image Registration

To start, the scaled MRCP, still in mesh form, is exported as a surface mesh ".obj" file. Using an in-house code described in Section 2.2, the scaled MRCP is voxelized according to HU material assignments, using a voxel resolution of 2.08 × 2.08 × 5 mm and the dimensions of the mesh (extracted from Blender and rounded to the next largest voxel). Ultimately, the scaled MRCP and the transition slices should be in a DICOM format, since that is what is used as an input to construct the Geant4 geometry. However, due to the nature of DICOM files, the information encoded in them is difficult to edit once made.

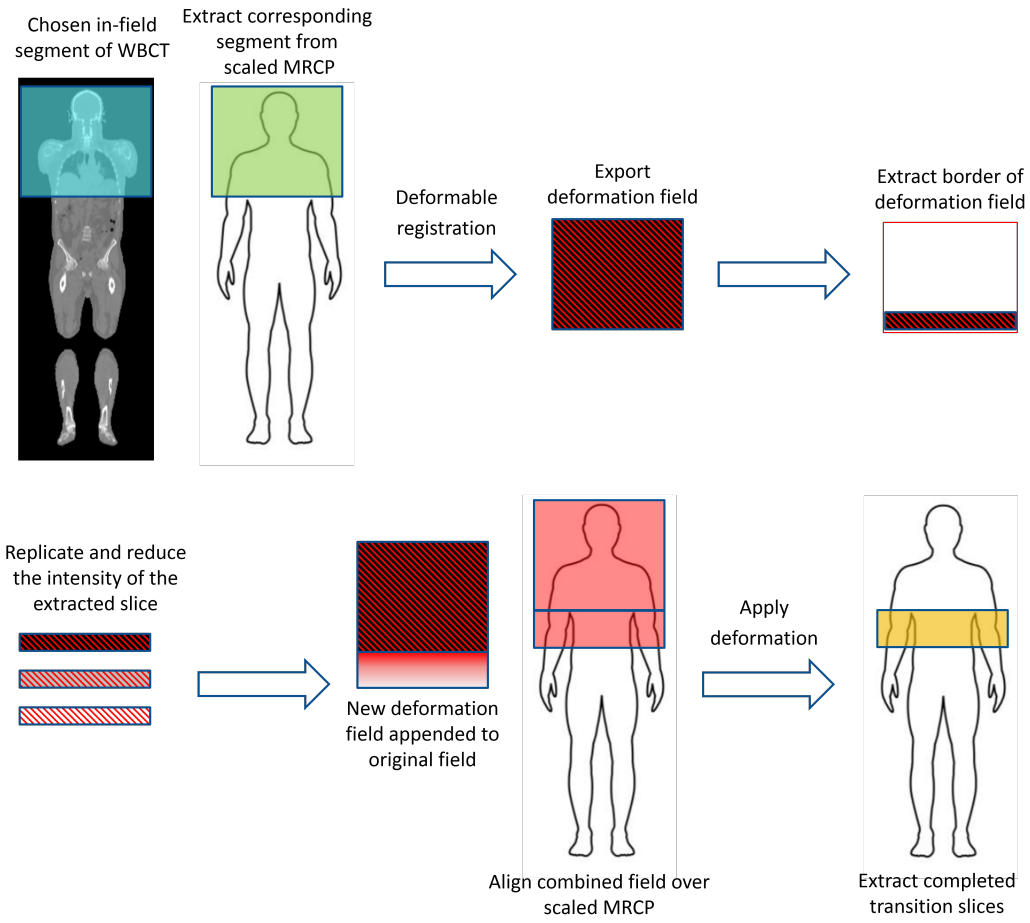

Figure 2.6: A more detailed overview of the steps taken to go from the starting WBCT in-field and scaled MRCP to completed transition slices for the hybrid phantom.

However, unlike DICOM images, .mhd files have a text editor friendly header section where some basic properties of the image can be easily edited (such as voxel resolution and 3D coordinate location). Therefore, the .mhd filetype was used as an intermediary between Matlab arrays and DICOM files.

Once voxelized, the scaled MRCP was converted into a .mhd file using the Matlab Reggui extension [109]. The appropriate spatial information was entered into the .mhd header, and then the image was converted into a DICOM format again using Reggui. At this point there are 3 versions of the voxelized scaled MRCP, the ".mhd" with spatial information encoded, ".mat" where the image slices can be easily separated, and DICOM which has both spatial information and the ability to easily separate slices. For the registration and subsequent splicing of the hybrid, the spatial information is necessary. Therefore to obtain the scaled MRCP segment which anatomically corresponded to the WBCT in-field, the selected slices were extracted from the DICOM image of the scaled MRCP by copying the relevant slices and placing them in a new file directory.

To further assist the registration algorithm, the WBCT was manually translated to align the WBCT in-field anatomy to that of the scaled MRCP. The WBCT was chosen to be translated rather than the scaled MRCP because the scaled MRCP was roughly centered around (0,0,0), while the WBCTs were all originally centered very far from the origin. While functionally this wouldn't have made much of a difference, intuitively it was easier to understand relative placement and dimensions when translating to the scaled MRCP. Once the WBCT was translated to overlay with the scaled MRCP, the WBCT in-field was extracted in DICOM format as its own file similarly to the scaled MRCP in-field. This extracted WBCT in-field also serves as the in-field segment of the completed hybrid (again reference Figure 2.2) and is the image on which all treatment planning would be performed for that patient treatment site.

Due to the simplicity of using a linear scaling factor, it is possible that even after the scaling, the size of the anatomy corresponding to the designated in-field will differ between the scaled MRCP and the original WBCT (reference part (b) of Figure 2.3). If this was the case, then the CT in-field was duplicated and the slice thickness adjusted such that the two in-fields would have the same location and dimension in height. The original in-field CT at its native dimensions was used in the hybrid and the adjusted duplicate was used only for the registration. The adjustment in the CT slice thickness was done to improve the results of the deformable image registration by removing the need of the algorithm to pull or push an image to match a different size. The reason for adjusting the WBCT in-field height rather than that of the scaled MRCP is because the deformation matrix produced by the registration would ultimately be applied to the scaled MRCP, so by orienting everything along the scaled MRCP in-field coordinates and voxel resolution, the deformation matrix output would naturally have the correct dimensions.

2.3.2 Deformable Registration

The Matlab extension Reggui's Morphon algorithm was used to execute all deformable image registration in this thesis. Reggui was already being used to convert between various image file formats (.mat, DICOM, .mhd), as well as to perform the manual translation to align the WBCT with the scaled MRCP in the region of the in-field. Furthermore, out of all the algorithms and programs tested (Plastimatch's b-spline, BRAINSTools' Demons, and Reggui's Morphon), Reggui provided the most accurate image deformation in a short time (<2 minutes). A series of images showing how the Morphon algorithm registers the scaled MRCP to the WBCT in-field is given in Figure 2.7. The deformation is not without imperfections, and there are often some skin surface discontinuities at the CT-transition boundary. Furthermore, there can be some distortion of the bony anatomy that is not biologically feasible. However, overall it provides a much closer approximation to the patient anatomy than the scaled MRCP alone, and in the soft tissue where the specific organs of interest are the discontinuities are minor.

Once the Morphons registration was completed using the WBCT as the fixed image and the scaled MRCP as the moving image, the deformation field was exported from Reggui as a Matlab file. An in-house Matlab code was used to propagate the terminal edges of

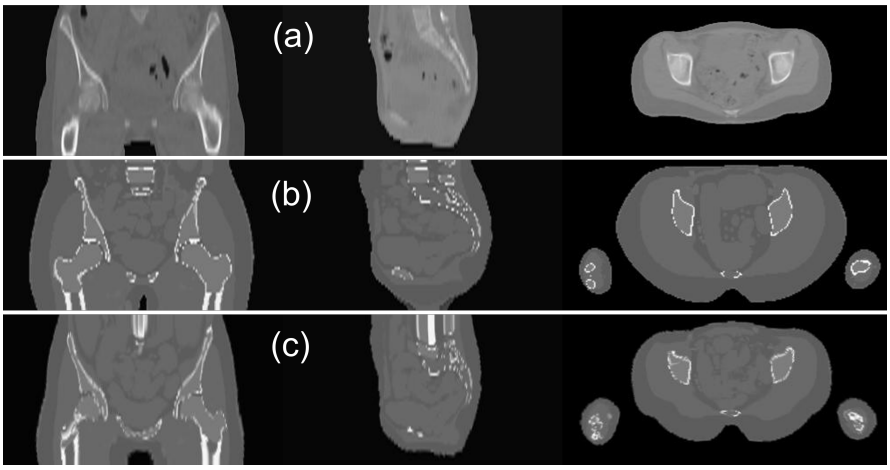

Figure 2.7: A visual representation of how the Morphon algorithm registers inter-patient anatomies (WBCT and scaled MRCP). Subfigure (a) shows the coronal, sagittal, and axial views of the excised pelvis in-field CT from a female WBCT, (b) shows the same views for the corresponding anatomy of the scaled MRCP, and (c) shows the same views from the resultant deformed image using the WBCT anatomy as a fixed image and the scaled MRCP anatomy as the moving image.

the deformation field across a distance of 10 cm (20 slices at the chosen resolution) on the inferior and superior side, decreasing the field intensity with the distance based on a sigmoid function. After modification, the blending region extensions were concatenated onto the edges of the original deformation field.

The resulting extended deformation field was then applied to the whole-body voxelized scaled MRCP in Reggui. After this, the deformed scaled MRCP was exported as a DICOM image, and the slices affected by the extended blending region were separately extracted into their own discrete images as completed transition slices. If necessary, the transition regions were translated in Z (inferior/superior) to ensure a continuous hybrid (for example, referencing the translation step illustrated in part (c,d) of Figure 2.3.

2.4 First Prototype Hybrid: Voxel Geometry Only

The first version of the hybrid phantom did not utilize the full MRCP mesh geometry in the out-of-field. At the time of initial construction the computational development had not yet been made to implement a hybrid mesh structure into our configuration of Geant4, nor had the programs been written to convert the surface mesh into a tetrahedral mesh or cut the tetrahedral mesh. Additionally, at the time of initial creation, there was only a single WBCT available for use, and this WBCT was not an ideal starting point due to the patient lying in a relaxed position (leading to head tilt and spine curvature not present in the MRCP), several metallic implants in the spine (causing difficulties in the image registration), and a body type which differed greatly from the default MRCP. In addition,

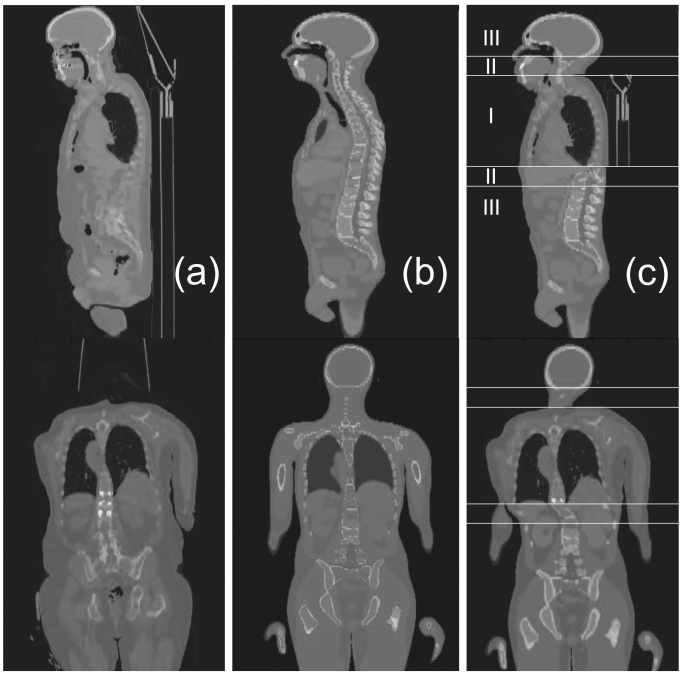

Figure 2.8: The initial (a) WBCT in sagittal and coronal views, (b) the scaled MRCP, and (c) the prototype hybrid. Subfigure (c) containing the prototype hybrid shares the chest in-field anatomy with the WBCT and has each of the segments (from top to bottom: upper out-of-field scaled MRCP (III), upper transition (II), in-field CT (I), lower transition (II), and lower out-of-field scaled MRCP (III)) demarcated by a white line.

the initial WBCT did not come with external skin contours to isolate the body from the treatment table, and therefore the prototype hybrid had a partial segment of the table included in the final image.

The final version of the prototype therefore primarily serves to demonstrate the deformation and transition region creation processes and ensure the continuity of all hybrid segments. The prototype hybrid was a necessary proof of concept until such time as the incorporation of the mesh segments was possible, and it was able to demonstrate the feasibility of creating a whole-body patient-specific hybrid phantom. The prototype hybrid is shown along with the original WBCT and the scaled MRCP in Figure 2.8. Initial testing of this prototype hybrid was designed to simply verify the construction of the hybrid in Geant4, and not geared to any comparative study or performance assessment.

2.5 Creating the Out-of-Field Mesh Segments

The final part of the hybrid which needed to be created were the out-of-field mesh segments. These consist of scaled MRCP segments which have been cut and shifted (if necessary)

to flank the transition region. Shifting was required for cases in which the scaled MRCP in-field and the WBCT in-field are different in height. If this was the case, the simplest way to approach the translation was to first translate the voxel segments to match the upper edge of the inferior mesh segment, then shift the superior mesh segment to match the upper edge of the voxel segments. If the hybrid is of the head and neck, where there is no superior mesh segment, then no mesh shift will be required, as the voxelized segments can all be adjusted independently to align with the inferior mesh. If translating a superior mesh segment was necessary, the shift was performed on the whole body scaled MRCP ".obj" file in Blender.

Once in its correct position, the scaled MRCP was exported as a ".obj" file. The POLY2TET code [57], provided by members of the ICRP Task Group 103 under Committee 2, was slightly modified to handle a different material naming schema, and used to convert the scaled MRCP into a volumetric tetrahedral mesh, capable of being built in Geant4.

To facilitate cutting the tetrahedral mesh into the hybrid's requisite segments, a rectangular prism surface mesh was created in and exported from Blender as a ".ply" file with dimensions defined such that the unwanted segment of the MRCP is contained within the prism. An in-house code was then used to cut the whole body tetrahedral mesh by the prism mesh, remove the unwanted half contained in the prism, and then re-calculate the mesh to maintain its closed, tetrahedral structure. The program's main cutting algorithm was adapted from the GitHub code from Wang et al [161] based on their mathematical algorithm to cut a tetrahedral mesh by a given surface mesh and re-convert the cut region into a tetrahedral mesh. The original code only performed the calculation to cut the tetrahedral mesh, and so further functionalities were added to remove portions of the mesh after cutting, accept multiple structures as an input (each organ in our mesh would be considered a different structure), handle material assignment for the reconstructed tetrahedra, and write out the completed cut mesh into the necessary files for implementation in Geant4.

2.6 Completed Hybrids

Over the course of this project, nine hybrid phantoms were created based on seven unique whole body CT scans. The first study used four hybrids from two WBCTs, to evaluate feasibility and predictive ability of using the hybrid to supplement missing anatomy for patient-specific whole-body dose and equivalent dose calculation. The two selected source WBCTs were the largest male and the smallest female scans of the seven WBCTs made available by the University Hospital of LMU Munich. For each of these two WBCTs, a hybrid for a pelvic treatment and a head and neck treatment were created, for a total of four hybrids. These hybrids are shown in Figure 2.9 alongside their reference WBCTs and will be discussed in more details in Chapter 4. For the second study on evaluating the hybrid's ability to provide patient-specific second cancer risk predictions, the two head and neck hybrids from the first study were used in addition to five new head and neck hybrids created from the remaining WBCTs. The gender distribution was 4 male hybrids/WBCTs,

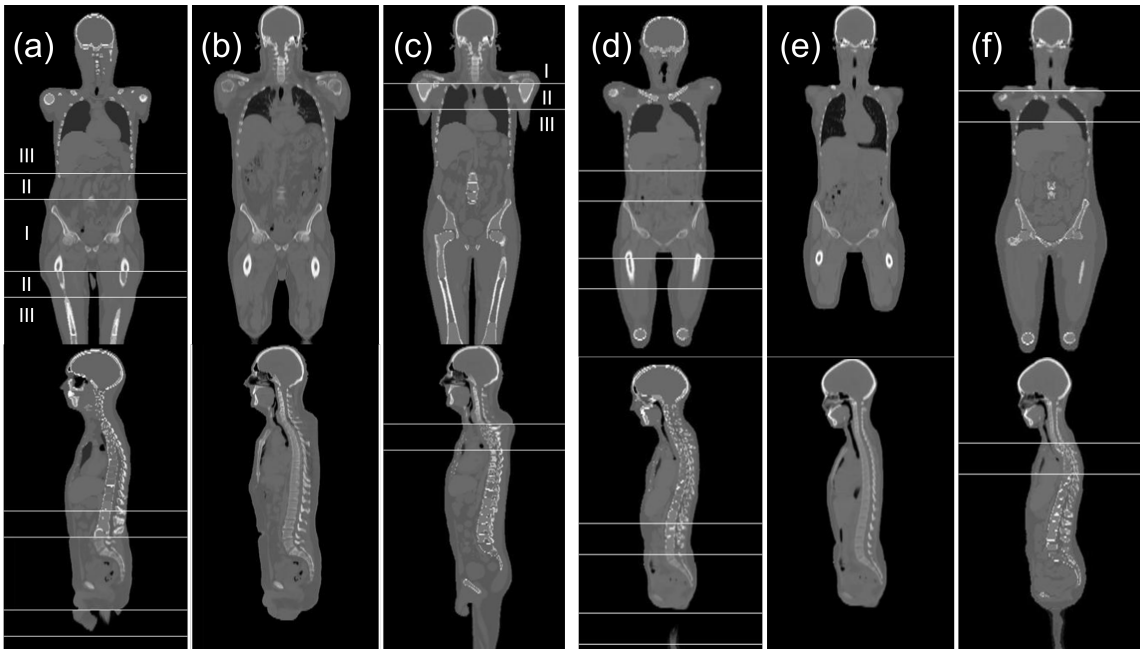

Figure 2.9: All hybrid phantoms developed for the geometry validation study side by side with their respective WBCT. Subfigures a), b), and c) show the male hybrids [pelvis in a) and head and neck in c)] flanking the male WBCT in b). Subfigures d), e), and f) show the female hybrids [pelvis in d) and head and neck in f)] flanking the female WBCT in e). The pelvic hybrids have each of the three segments demarcated by a white line and labelled in subfigure (a) from top to bottom: upper out-of-field scaled MRCP (III), upper transition (II), in-field CT (I), lower transition (II), and lower out-of-field scaled MRCP (III). The head and neck hybrids are similarly demarcated and labelled in subfigure (c) from top to bottom: in-field CT (I), transition (II), and out-of-field scaled MRCP (III).

and 3 female. These hybrids alongside their respective WBCTs are shown in Figure 2.10 for the male hybrids and Figure 2.11 for the female, these as well will be discussed further in Chapter 5.

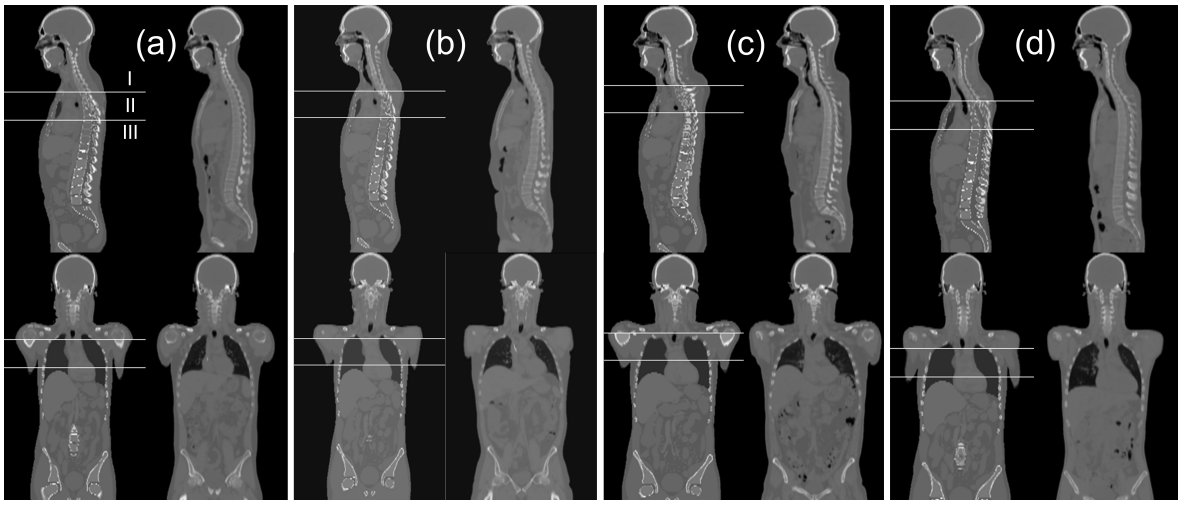

Figure 2.10: The male hybrid phantoms used in the risk modelling study side by side with their respective WBCTs. For each sub-figure a), b), c), and d), the hybrid is on the left and the WBCT is on the right. The hybrid has each of the three segments (from top to bottom in each torso: in-field CT (I), transition (II), and out-of-field scaled MRCP (III)) demarcated by a white line and labelled in subfigure (a), where the shared anatomy is the most superior segment of the head and neck.

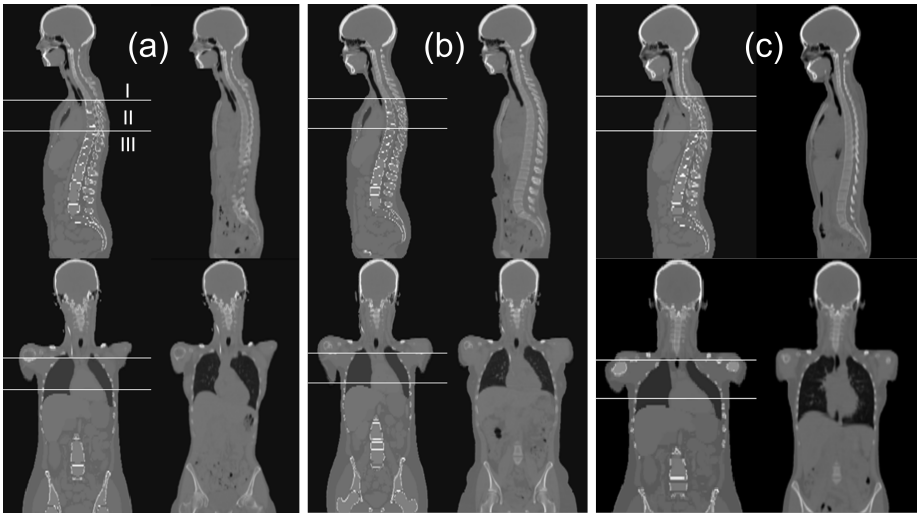

Figure 2.11: The female hybrid phantoms used in the risk modelling study side by side with their respective WBCTs. For each sub-figure a), b), c), and d), the hybrid is on the left and the WBCT is on the right. The hybrid has each of the three segments (from top to bottom in each torso: in-field CT (I), transition (II), and out-of-field scaled MRCP (III)) demarcated by a white line and labelled in subfigure (a), where the shared anatomy is the most superior segment of the head and neck.

Chapter 3

Computational Development

A significant amount of computational development was necessary to execute the designed simulations with the hybrid phantom. This section details the technical background work which enabled proper simulation physics and dose scoring, including integrating hybrid geometry, custom scorer development, stopping power calibration, and material information assignment and conversion (density, elemental composition, and HU). Besides the work for Geant4, there is also a section regarding the development of a tool to convert a RayStation treatment plan into a Geant4 beam information file which would enable a simple conversion of simulated dose to therapeutic dose.

The implementation of Geant4 used in this thesis was built on that from Schmid et al 2015 [127] which in turn was based on the Geant4 DICOM example from the extended medical category [11]. From the beginning it included the ability to build voxelized geometry from a DICOM image using the Schneider et al 2000 [131] materials and a built-in HU to density to material conversion, as well as some select dose to material and dose to water scorers. This implementation would accept a DICOM image as an input and check if there were corresponding implementation-specific ".g4dcm" files. Each slice of the DICOM image set corresponds to one ".g4dcm" file, which in plain text describes the material names used in the image slice, the number of voxels in each slice, the dimensions of the image, and then a list per voxel of the material IDs following by a list per voxel of the densities in a simple human-readable text file. If the ".g4dcm" files do not exist for the input DICOM image set, then the implementation would write them out based on the DICOM data, an HU to density conversion curve, and a density to material conversion table. Geant4 would then be able to construct, slice by slice, the voxel geometry of the DICOM image by reading the dimensions, material ID and density of each voxel from the ".g4dcm". Besides the base materials described by Schneider et al 2000 [131], there was also a "density fine-tuning" where if the density of the voxel differed from the assigned base material by a certain margin, a new material would be created of identical chemical composition with the new voxel density (described in more detail in Section 3.3).

3.1 Designing Geant4 to Handle Hybrid Geometry

For the purposes of this thesis, the geometry functionality of the Geant4 implementation needed to be expanded to build tetrahedral mesh geometries from .node, .ele, and .material files, build a geometry which incorporates both voxel and tetmesh structures, have material lists which can correctly assign HU-based materials to voxel structures and organ-based materials to mesh structures, and create additional scorers for equivalent dose calculations. This section focuses on the geometry-related developments. The scorer development is covered later in Section 3.2.

Before developing the ability to build multiple geometries in a single environment, the first step was ensuring that the tetmesh geometry alone could be accurately constructed. The source files for the tetmesh comes in a triplet: ".node" which lists the ID numbers and X, Y, and Z coordinates of a series of nodes which correspond to the points of the tetrahedra, ".ele" which lists the ID number of each tetrahedra, the IDs of each node which belongs to that tetrahedra, and the material ID assigned to that volume, and the final file is ".material" which associates each material ID number with a name, density, and elemental composition. The material files have to be present for each new mesh phantom geometry, but are all identical between meshes of the same sex. The Hanyang University research group who developed the mesh-type reference computational phantoms (MRCPs) also provided their implementation of these phantoms into Geant4. Because of this, it was not necessary to design a custom method to build the tetrahedral geometry in the Geant4 implementation used here. However some adjustments were necessary to make the two codes compatible. Key modifications were made in the phantom container definition, for integration with the currently existing classes (for example a user input option to indicate which geometry type was being constructed), and for adding and integrating the new organ-based mesh materials. Initially, there was a separate user option to indicate what material list to use (HU-based, organ-based, or both), however, later it was changed to always use a single integrated material list consisting of the base HU-based materials, the density-tuned HU-based materials, and the tetrahedral organ-based materials (described in more detail in Section 3.3).

The framework of the initial Geant4 implementation was predicated on a single geometry. In order to build multiple geometries, the implementation had to be restructured on a fundamental level to allow input from multiple image sources, regardless of geometry type. A user input was added to allow dynamic switching between a single voxelized geometry, a single mesh geometry, a hybrid voxel-mesh geometry with three segments (1 in-field, 1 transition, and 1 out-of-field, such as for head and neck anatomy), and a hybrid voxel-mesh geometry with five segments (1 in-field, 2 transition, and 2 out-of-field, such as for torso anatomy). Due to the different organ types in male and female mesh phantoms, another user switch was added to indicate patient sex.

For a hybrid geometry (using both voxel and mesh structures), some additional framework was needed to ensure that the automatically assigned phantom containers did not overlap with the voxel geometry containers and that the mesh was constructed correctly. This was a problem because the tetrahedral structures are constructed with respect to the

center of the designated container. Therefore if a container was not centered at (0,0,0), then when the mesh phantom would be constructed it would effectively be rigidly translated and it would also no longer be centered at (0,0,0). By default, the mesh container was defined as the minimum and maximum points of the mesh plus a margin of a couple millimeters. This works with no issue for a geometry with an MRCP only. However, if the mesh being constructed is cut, then the default container will be defined based on the cut mesh dimensions, likely resulting in an uncentered container and the subsequent misplacement of the mesh geometry. This effect is visualized in Figure 3.1. To fix this, the container definition had to be modified to always be based on a container centered at (0,0,0), large enough to fit the entire MRCP geometry. In this case, the dimensions of this base container was set to be excessively large as a cube with a side length of 5.4 meters. This volume was then modified with a subtraction volume designed to remove from the container the volume which would contain the voxel geometry and, if two meshes were used, the other mesh region. In this way, when the tetrahedral mesh structures are built, they will use the central coordinate of (0,0,0) to base the relative coordinates of the tetrahedra on, while also not interfering with the construction of other hybrid segments.

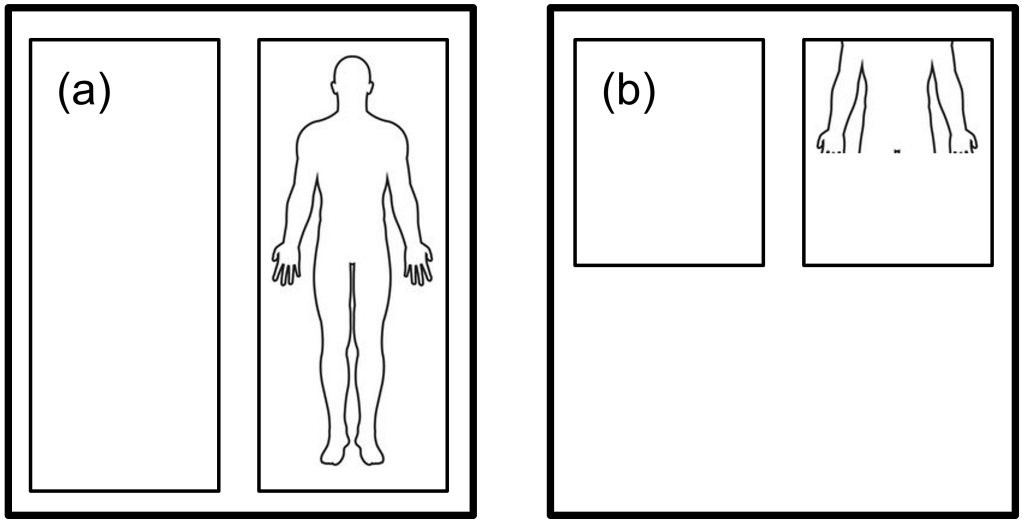

Figure 3.1: A diagram visualizing how the phantom container definition effects the construction of the tetrahedral mesh. Subfigure a) shows on the left a phantom container based on the minimum and maximum dimensions of the full MRCP and on the right how the MRCP is constructed within that container, based on the container's center. Subfigure b) shows on the left a phantom container based on the dimensions of a cut mesh which would represent the upper out-of-field segment of a hybrid phantom and on the right how the cut MRCP would be constructed within that container. Instead of the cut mesh perfectly fitting within the container based on its dimensions, it is mis-constructed about the center of the new container.

3.2 Custom Scorers

One of the most worked over aspects of the computational development was in the design and implementation of the new custom scorers. To properly calculate equivalent dose and subsequently secondary cancer risk, both a neutron dose scorer and a neutron energy scorer was needed. These scorers required careful design, as the ICRP 92 weighting factors assume a lack of specific knowledge of the radiation interactions occurring in the tissue while with Geant4 every interaction is tracked and can be known. Therefore, in order to avoid misusing the ICRP 92 weighting factors, the scorers had to be designed to replicate the assumptions underpinning the weighting factor's intended purpose.

The weighting factors defined by the ICRP 92 are meant to be applied to a measured dose with respect to incident fields. In this definition, it does not matter what particle ultimately is responsible for a deposition of dose, but rather the probability of the incident radiation of producing secondaries of high relative biological effect. However, the ICRP 92 also acknowledges that the radiobiological effectiveness of the field can fluctuate as it passes through tissue and the quality of the incident field may not equal the characteristics of the field at an internal point within the tissue or organ of interest. Since the weighting factor corresponds to the quality of the incident radiation field, it works best for structures at or near the surface of the skin. The ICRP 92 specifically acknowledges that on the scale of the human body, "the external and internal field characteristics differ markedly" [62].

As the hybrid performance will be framed in terms of neutron impact on proton therapy for this thesis, it was important to characterize the neutron fields throughout the patient. To this end, neutron dose was defined as any and all dose deposited by a particle which could, at some point in its history, be traced back to a neutron. In terms of custom scorer development, a neutron tag was created in Geant4 which was applied to the track information of each neutron as soon as it was generated. This tag was then propagated to all descendants of that neutron, effectively collating the dose of all particles generated by neutrons. As a note, because the neutron dose was defined here to include descendants, it is possible for neutron dose to be scored in voxels where no neutrons pass through. For this study, to match the definition of weighting factor as applying to incident radiation, all dose deposited in the patient which was not delivered by a particle with the neutron dose tag was counted as dose from the primary proton field. As mentioned, the ICRP 92 does acknowledge that the quality of the proton field may technically not be the same throughout a large volume, however unlike with neutrons, the formal recommendations are to use the same radiation weighting factor of 2 regardless of field quality. In this way the total dose scored in the patient volume was split into neutron dose which will use the energy dependent neutron weighting factor, and non-neutron dose which will be referred to as "therapeutic proton dose" and use the proton weighting factor of 2.

The other custom scorers created for this project are both neutron energy scorers. The scorers were designed to reflect ICRP 92's emphasis on the importance of the neutron field quality as it is incident to the particular tissue of interest by scoring the neutron energy in each voxel throughout the body. The two scoring methods share a similar approach, but differ on how the neutron energy is weighted (by relative fluence/path length through

the voxel, or by the relative contribution to local energy transfer in that voxel to charged particles (kinetic energy released in matter, or KERMA). Each scoring method (fluence and KERMA), requires two separate scorers. For example for the fluence weighting, the first scorer is needed to sum the neutron energies multiplied by their respective fluence contribution, the second is needed to sum the fluence contributions alone. A weighted average could then be calculated for both fluence and KERMA weighting. At the end of the simulation processing, there will be a resultant voxel-wise 3D map of the average neutron energy throughout the patient's whole body, which can subsequently be converted into a 3D map of the neutron weighting factor (described in more detail in Section 4.4.1). Fig 3.2 illustrates the effect of the fluence/KERMA weighting method on the weighting factor. In this figure, the point of highest neutron weighting factor for both weighting methods is outside of the primary fields (in this case two parallel opposing fields at the prostate level) which reinforces the importance of understanding the impact out-of-field neutron dose has on the patient. Between the two methods, the KERMA-weighted neutron energy consistently returns overall higher neutron energy weighting factors, however due to the naturally lower doses in those regions it is unclear at this stage how much that ultimately impacts equivalent dose and secondary cancer risk estimates.

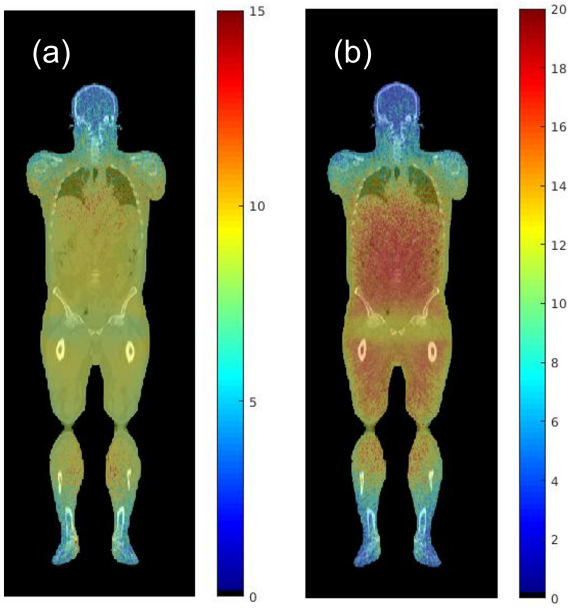

Figure 3.2: A diagram visualizing the energy dependent neutron weighting factor (unitless) from a prostate treatment plan throughout a male WBCT using the fluence-weighted neutron energy scorer (a) and the KERMA-weighted neutron energy scorer (b).

3.3 Material Assignment for Voxelized Geometry

As mentioned previously, the implementation of Geant4 used in this thesis creates the voxel geometry from the information in ".g4dcm" files which are derived from DICOM images. The HU values of each voxel are converted first to a corresponding density value based on a CT calibration curve. These conversions are machine specific, and this implementation came with a calibration curve corresponding to the X-ray CT scanner used at the LMU University Hospital. However, a new curve using the "Generic CT" curve data available in a research version of RayStation 7 was created. RayStation would use the "Generic CT" curve to calculate the RSP of the materials in the image during treatment planning. This curve was then used when making material assignments in Geant4 to match RayStation as closely as possible. The calibration information used in this project is given in Table 3.1, where any HU value between the given points is calculated via linear interpolation.

Once a density has been calculated for each voxel, that density is then assigned a corresponding material ID based on the data from another conversion file. This file is based on the Schneider material density data [131] and bins voxels with a range of density into discrete materials. The only change needed for this process was to separate it out from the main Geant4 implementation and modify it to be compatible with a material list which contains both Schneider materials (for voxelized regions) and organ-based materials (specific to mesh regions). Making the ".g4dcm" creation an independent process from the geometry construction was chosen 1) so that the fidelity of the converted ".g4dcm"

Table 3.1: CT Hounsfield Units to Density Conversion Curve from RayStation for a Generic CT

Hounsfield Unit	Density ($\frac{g}{cm^3}$)
-100,000	1.20e-03
-992	1.20e-03
-976	1.21e-03
-480	5.0e-01
-96	9.5e-01
48	1.05
128	1.1
528	1.35
967	1.6
1488	1.85
1824	2.1
2224	2.4
2640	2.7
2832	2.83
2833	7.87
100,000	7.87

file could be checked prior to simulation and since it 2) gives more direct control of the conversion process to ensure correct material assignment.

The final step for voxelized geometry material construction is the density fine-tuning of the HU-based materials. Once the ".g4dcm" files are created, they can be implemented in Geant4 as usual. However, at this stage voxels with a variety of HUs have been coarsely binned into the same material, leading to a poor representation of the tissue complexity in each CT slice. To mitigate this, when Geant4 reads in the ".g4dcm" files, it performs an additional fine-tuning, where if the voxel density (from the CT to density conversion) differs from that of its assigned base material by a margin of 0.001 $\frac{g}{cm^3}$, then a new material is created, with the same elemental composition as the original base material, but with a density that matches the voxel.

3.4 Calibration to RayStation Stopping Powers

Finally, as another step to ensure agreement between the implementation of Geant4 and the dose distribution calculated by the TPS, the mean excitation energies of the HU-based Geant4 materials have been modified such that the Geant4 and RayStation stopping powers match. It was possible to calibrate the materials like this because the stopping power of a material is described by the Bethe-Bloch equation, which includes a dependency on the mean excitation energy as $\ln(1/I)$, where I is the mean excitation energy. For a given material in Geant4, the I value can be varied and the corresponding stopping powers calculated by Geant4 can be retrieved. By creating a logarithmic fit to this data (reflecting the $\ln(1/I)$ dependence), the impact of the I value on the stopping power in that material can be modelled. In this way, if the amount by how much the stopping power should be adjusted is known, the I value can be adjusted to achieve that change.

The first step was to create a mono-material computational box phantom for each HU-based material used in Geant4. The box phantoms were large enough to fully stop a proton pencil beam of 150 MeV (selected as a representative treatment energy), to ensure that the calibration was not overly energy dependent. The only exception was the material representing extremely low density HU values (less than -950) where the box phantom size needed to stop the beam would have been computationally unreasonable. Since for this material very low density material the calibration would be unlikely to have a significant impact on dose calculation, it was left unchanged from its default value. Each box phantom was then exposed to a 150 MeV proton pencil beam in both RayStation and in Geant4. The dose calculation information was exported from RayStation, and the absorbed dose to material was scored in Geant4. Using Matlab, both sets of data were fit to the Bragg peak (specifically the region of the depth dose curve which registered at least 70% of the max dose) using a fourth order polynomial fit. Based on this fit, the depth at which the dose falloff reached 80% of the maximum dose, or the R80, which is a standard measurement of the range of a proton beam, was calculated. The percent difference was calculated between the R80s to determine the amount by which the stopping power needed adjustment. Since the stopping power is $\frac{\mathrm{d}E}{\mathrm{d}x}$, the range and the stopping power have an inversely dependent

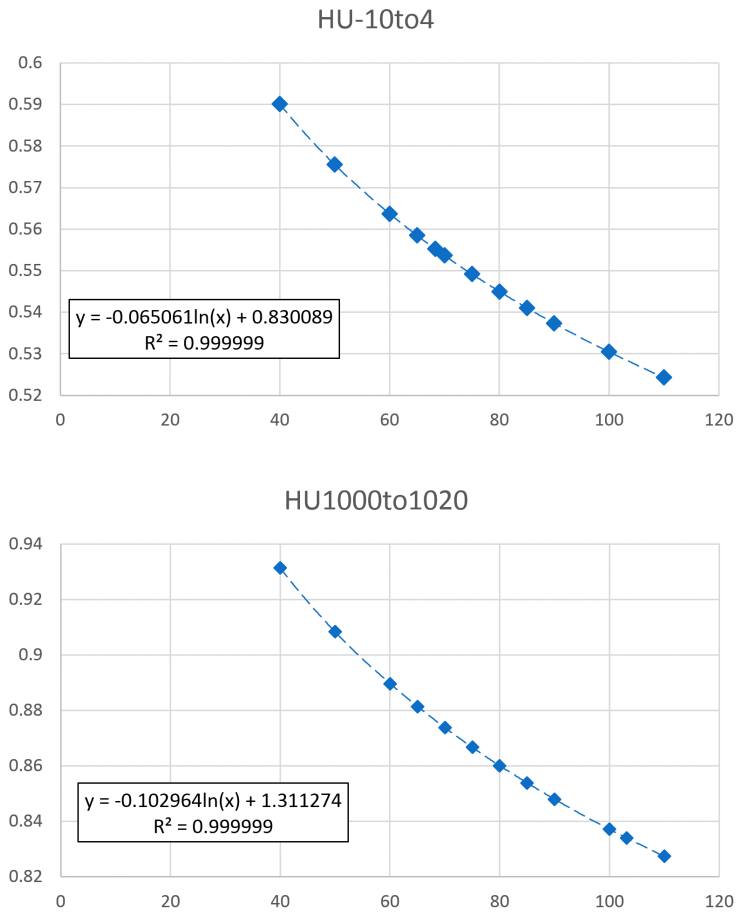

Figure 3.3: For two materials representing soft tissue (HU -10 to 4) and denser material such as bone (HU 1000 to 1020), these plots show the logarithmic relationship between stopping power and I value, as well as each of their unique fits used to calculated the I value needed to achieve the same stopping power (and thus range) as the corresponding material in RayStation.

relationship: if stopping power increases, the range experiences a linear decrease. Using this information the necessary change in stopping power to result in a matching range in RayStation can be calculated.

At this point, the required change in stopping power needed to achieve the same range has been calculated. From here, the corresponding change in the mean excitation energy needed to achieve that change in stopping power must be calculated. Shown here in Figure 3.3 is an example for two materials how changing the I value effects the stopping power and their respective logarithmic curve fits. The general form of the fit takes the form:

$$\frac{\mathrm{d}E}{\mathrm{d}x} = a \times \ln(I) + b \tag{3.1}$$

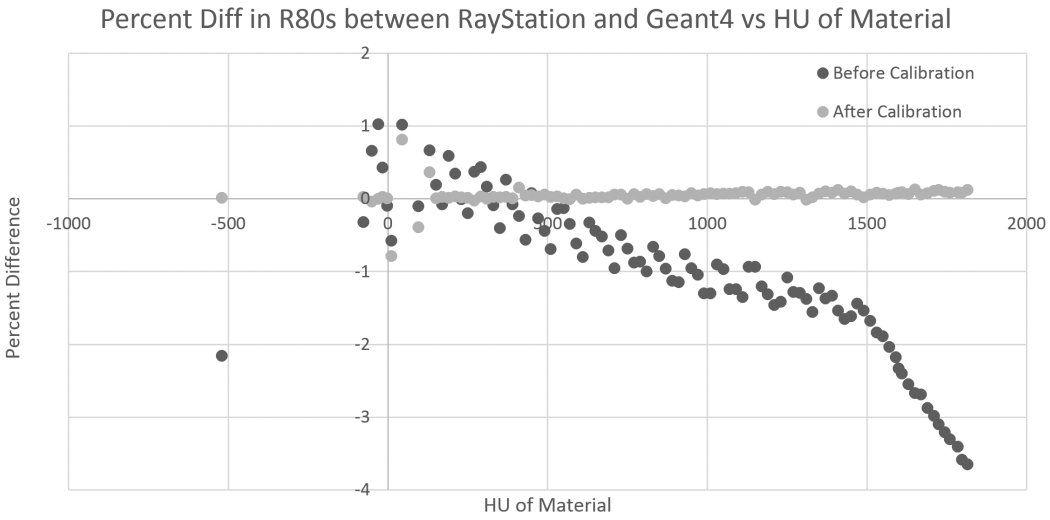

Figure 3.4: For each of the tested materials, this figure shows the percent difference in R80 range in Geant4 from the RayStation values before (dark gray) and after (light gray) the I value calibration.

where $\frac{\mathrm{d}E}{\mathrm{d}x}$ is the stopping power, I is the mean excitation energy, and a and b are fit parameters. Once the curve fit and the stopping power needed to achieve the correct proton range are known, I can be solved as:

$$I = \mathrm{e}^{\frac{\frac{\mathrm{d}E}{\mathrm{d}x} - b}{a}} \tag{3.2}$$

This calculation was repeated for all HU-based materials used in the Geant4 implementation. On average across the entire range of materials, on average the mean excitation energy was adjusted by approximately 8%. However, as HU increased, typically magnitude of the I value adjustment would also increase, so on average for all materials of less than 1400 HU the I value was adjusted by 4%. Considering that this HU range covers the vast majority of organic materials present in a CT scan, this was considered to be an acceptable level of change.

After all of the excitation energies were adjusted, the simulation with the 150 MeV proton beam was repeated, along with the subsequent depth-dose curve fit and R80 calculation. Figure 3.4 shows the results of the calibration, with the percent difference from RayStation of the proton beam range in Geant4 plotted against the HU value of the box phantoms. The average difference in range before the calibration was about 1% or 0.1 cm. After calibration, that difference dropped to 0.05% or 0.005 cm.

3.5 Converting Treatment Plans to Geant4

The final part of computational development which needed to be done to execute the validation and testing of the hybrid was a script capable of effectively exporting the treatment plan from RayStation and converting it into beam data which can be interpreted by Geant4. This in turn can be split into two main sub-categories: converting the beam weighting from monitor units to particle number, and translating the beam angles and directions. Other beam qualities, like pencil beam width and proton energy, can be taken directly from RayStation using basic Python scripting commands. For both of the major sub-categories listed, RayStation's scripting capabilities (in Python) must be used to not only retrieve information from RayStation, but also perform some modifications to ensure the beams produced in Geant4 simulations match those prescribed by RayStation. As a small note, for each spot in the RayStation treatment plan, a corresponding particle source must be defined in Geant4.

3.5.1 MU to Number of Particles

To get an accurate spot weight for Geant4, it is necessary to know: how many monitor units is assigned to each beam angle in RayStation, the relative weight of each spot in a given field, and what is the conversion from the number of MUs to the number of particles for a given beam energy. The first two of the three are simple, and can be retrieved easily from RayStation using a simple Python script. The number of MU attributed to each spot in the beam plan is now known.

Raystation natively weights each of the spots used in an active scanning proton plan in terms of monitor units, since that is what is required to actually deliver a treatment fraction. However, Geant4 weights each particle source by the relative probability of a particle originating from that source. Geant4 uses relative weighting, so theoretically as long as each beam has the same fractional weight, the same beam plan will be simulated. However, since the number of particles delivered by a single MU is dependent on the energy of the proton beam, the MU weighting cannot be used to simulate in Geant4. The relative weighting of the MUs must be converted into a weighting by number of particles. Several proton machines were already commissioned in the RayStation version at LMU, so there was the option to select one which also had logged absolute dosimetry data for ions per MU and beam energy. By fitting this data to a second order polynomial, a function, given in Equation 3.3, was created which converts a given spot MU from Raystation to its corresponding number of particles. This curve was tested by converting and then simulating the male pelvis treatment plan (described in Chapter 4.3.1) on a small scale. Once it was confirmed the the method was successfully able to convert the Geant4 dose to match the planned clinical data, Equation 3.3 was used when converting all treatment plans.

$$Np_{spot} = MU_{spot} * [-1.138 \times 10^3 * E^2 + 9.182 \times 10^5 * E + 2.381 \times 10^6] \qquad (3.3)$$

Where Np_{spot} is the number of particles delivered to a given spot in the treatment plan,

MU_{spot} is the number of monitor units delivered to a given spot, and E is the beam energy for that spot.

3.5.2 Converting Geometric Beam Qualities

Other beam properties which needed significant adaptation to replicate in Geant4 included the beam origin point, beam direction, the source shape/distribution, and angle of the source shape (to clarify, for a circular source, that circular shape could be rotated even with a consistent particle direction; the shape of the beam from an outside perspective would fluctuate between a full circle and a line as the source shape rotates about an axis).

Natively in RayStation, beam information is given via spot coordinates in beam's eye view, along with data on the isocenter, gantry angle and patient couch positioning. The first step was to convert the spot position from the beam's eye view coordinate system into a particle source origin in the patient-oriented "world" coordinate system, where positive X is the patient left side, positive Y is posterior to the patient, and positive Z is superior

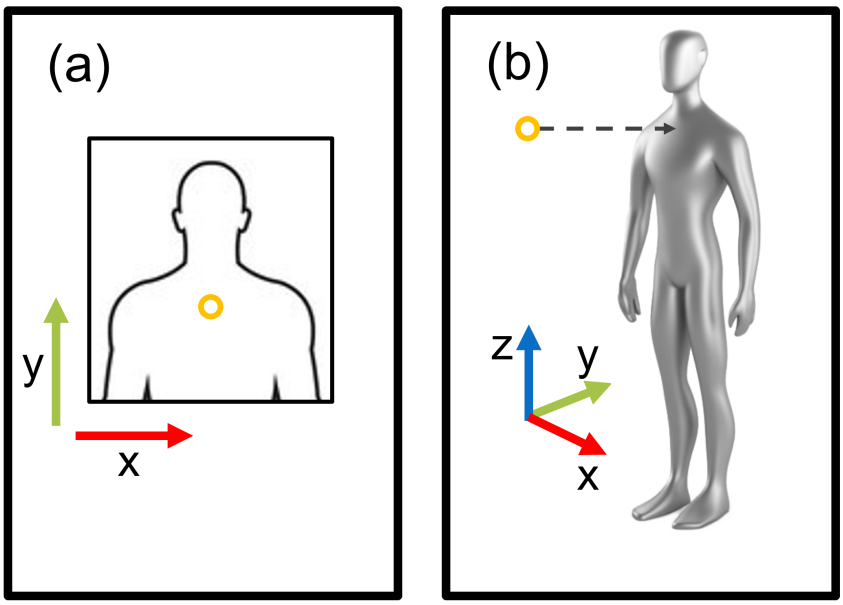

Figure 3.5: Subfigure a) shows the coordinate system given by the RayStation TPS, where the perspective is from the beam's eye view and the circle represents an individual spot in the proton treatment plan. Only X and Y coordinates are given, all other spatial data must be calculated using the gantry angle, couch angle, and isocenter coordinates. Subfigure b) shows the so-called world coordinate system used by Geant4, where the circle represents the particle source and the dotted line represents the path of the proton beam towards the target.

to the patient. A visualization of these two systems is shown in Figure 3.5. To accurately translate the spot coordinates, a matrix had to be constructed that was capable of correctly converting the beam's eye view coordinate system into the patient world coordinate system regardless of rotation of the beam angle around the patient Z axis and a couch angle around the patient Y axis. This was split into three steps: the conversion from beam's eye view to world coordinate system for a beam at 0°and a couch angle of 0°, a rotation of the converted coordinates about the beam angle, and a rotation of the converted coordinates about the couch angle.

The spot coordinates were first given an artificial "Z" coordinate of 100 cm in the beam's eye view coordinate system to represent the distance between the patient and the source (RayStation did not provide this Z coordinate so it had to be approximated). A distance of 100 cm was chosen to ensure it would always be behind the range shifters if one was present (remember the shifters had to be placed far enough from the patient to avoid conflicting Geant4 containers, which in practice is a translation of roughly 15 cm), and because 100 cm is a common source-axis distance (SAD) in clinical radiotherapy. After all of the conversions and the shifting to match the isocenter, it is likely that the actual distance from the patient did not precisely match what would be expected by that machine, however it was a close enough approximation for the purposes of this thesis. After the spot coordinate was given the Z coordinate, it was converted into the patient world coordinate system. At this stage, all particle source positions would be directly in front of the patient's anterior surface. Next, the gantry and couch angle rotation matrices were applied to move the particle source about the patient. Another approximation made in this method is with respect to an unstated angle in the beam direction. In a real proton pencil beam delivery system, there is one opening through with the protons are directed at an angle guided by magnets. However, with the system used here it is assumed that this angle is 0 and that the opening itself is somehow translated to coincide with the respective spot position. To picture the effect this would have, imagine a proton treatment which treats a circular place, instead of the beams forming a cone as in a true clinical case, with the approximation used in this thesis they would instead form a cylinder.

Similarly to the spot coordinate conversion, the beam and couch angles also are imperative when calculating the particle source direction and the rotation of the particle source shape. The beam direction is calculated by pulling information on the gantry angle from RayStation and applying the rotation matrix that was already created for the couch angle. The beam shape must be perpendicular to the beam direction, and so is calculated via the cross product in two steps: first by the cross of the beam direction with the vector [0,0,1], then by taking the cross product of the beam direction with the output from the first step.

All other beam qualities could be retrieved directly from RayStation with only minor re-calculation if needed. Beam energy and energy variance was taken directly from RayStation with no modification. Beam shape was set to a Gaussian, and beam width was converted to a Gaussian full-width half-maximum based on the spot size at isocenter given by RayStation. Unfortunately, no information on distance to the source, beam size at the source, or the beam divergence angle could be found, so the source size could not be accurately calculated from the spot size. Because of this, and because ultimately the

goal was comparing relative performance between the WBCT and the other phantoms, not absolute reproduction of the treatment plan in Geant4, the value given by RayStation was used as is.

Chapter 4

Validating the Hybrid Geometry

With the hybrid methodology developed and the computational framework in place, the next steps were to design and execute a study to quantify and assess the hybrid's ability to predict organ dose throughout the whole body. To this end, a small set of hybrids were constructed to represent the broadest range of conditions manageable with limited patient image resources. These hybrids were constructed from whole-body CT scans which would serve as the ground truth, focusing on hypothetical treatment plans in the pelvis and in the head and neck. Also included as controls are the default mesh-type computational phantoms (MRCPs) and the MRCPs which had been scaled to patient measurements. For each of the planned treatment sites, a pencil beam proton treatment plan was created on a research version of the RayStation treatment planning system. Each treatment plan was subsequently simulated on each of the patient representations (WBCT, hybrid, scaled MRCP, and default MRCP). Each simulation scored total dose, neutron dose, and then had calculated KERMA- and fluence-weighted equivalent dose using the custom scorers described in Section 3.2. Each dose quantity was then evaluated for a selection of organs spread throughout the entire body and compared across the four patient representations.

4.1 Hybrids Created for Geometry Validation

The source WBCTs were selected from a small library of patient images provided by the LMU University Hospital. These WBCTs represented patients who were undergoing whole-body radiotherapy, but who did not have any solid tumors. This allows for both the freedom to choose any convenient hypothetical treatment site, and the challenge of creating a treatment plan where there is no malignant tumor volume. The two WBCTs chosen for geometry validation were the largest male and the smallest female CT which did not have extensive metallic implants or fillings. Choosing the largest and smallest of the available WBCTs was meant to test as much as possible if the scaling factor was able to adequately adjust the MRCP to match the true patient dimensions. From each of the two WBCTs, two hypothetical treatment sites were considered: one in the pelvis, and one in the head and neck. Since both of these sites are on opposite ends of the torso, which contains the

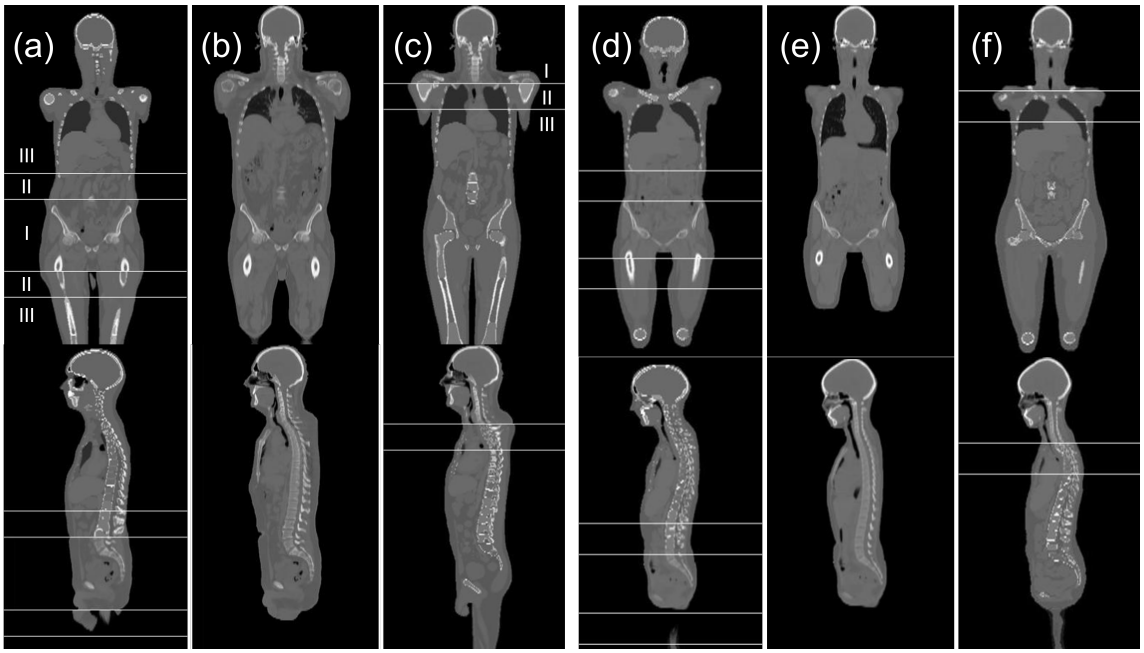

Figure 4.1: All hybrid phantoms developed for the geometry validation study side by side with their respective WBCT. Subfigures a), b), and c) show the male hybrids [pelvis in a) and head and neck in c)] flanking the male WBCT in b). Subfigures d), e), and f) show the female hybrids [pelvis in d) and head and neck in f)] flanking the female WBCT in e). The pelvic hybrids have each of the three segments demarcated by a white line and labelled in subfigure (a) from top to bottom: upper out-of-field scaled MRCP (III), upper transition (II), in-field CT (I), lower transition (II), and lower out-of-field scaled MRCP (III). The head and neck hybrids are similarly demarcated and labelled in subfigure (c) from top to bottom: in-field CT (I), transition (II), and out-of-field scaled MRCP (III).

vast majority of the organs of interest, analyzing these sites in particular would give the greatest possible distance from the treatment field to a potential secondary cancer site. Furthermore, not only is the head and neck in particular indicated for proton therapy, but the treatment plans can be subject to a great amount of variation (such as in beam angles) which could potentially impact out-of-field dose and subsequently secondary cancer risk.

The hybrid creation process itself was covered extensively in Chapter 2, suffice it to say here that 4 hybrids were created using these two WBCTs and the 4 in-fields (2 male, 2 female; 2 pelvis, 2 head and neck). The chosen in-fields for the pelvis extended from a couple centimeters from the inferior of the anal verge to the superior edge of the pelvis bony anatomy. The chosen in-fields for the head and neck extended from the most superior extent of the skull down to just beneath the superior apex of the lungs. The hybrid phantoms along with their respective WBCTs are shown here in Figure 4.1.

4.2 Organ Contouring and Masking

A set of organs for each treatment site were selected based on a mixture of patient sex, positioning throughout the body/relative to the treatment field, ease of contouring, presence of equivalent structure as an independent mesh in the MRCP, and potential interest as a secondary cancer site. These are the organs used in the post-simulation analysis to assess the hybrid's ability to perform as a predictive tool for whole-body dose distributions. In addition to these structures, further in-field organs were identified as organs at risk (OARs) for the purposes of treatment planning. It was possible for a given organ to appear on both lists (for example, the bladder in the pelvis treatments would be both a planning OAR and an important organ for post-simulation analysis), however, more frequently the planning OARs and other structures were not used outside of treatment planning.

No matter what the structure was used for, it was important to have the ability to delineate these organs both in the CT/voxel images and in the MRCP mesh phantoms. For treatment planning, this requires contours drawn within the treatment planning system (TPS). For dose analysis, since the scorers return a voxel-based 3D map of the scored quantity along defined coordinates, volumetric voxel-arrays of each relevant organ are needed to overlay and isolate the organ dose or equivalent dose in a process referred to here as masking. All structures contained in a voxelized region had to be contoured first using the treatment planning system before an organ mask could be created.

4.2.1 Organ Contouring for Voxelized Geometry

All organ contouring was done within an implementation of the research version of RayStation 7. Contours for all planning organs were made on the in-field CT segments, while contours needed for post-simulation analysis were made on the WBCTs and the voxelized regions of the hybrid (in-field + transition slice DICOM images). All contouring was done according to available anatomical atlases from the Radiation Therapy Oncology Group and NRG Oncology [25] and adjusted based on feedback by physicians and medical residents at the Trento Proton Therapy Center.

Contouring the organs in the CT images was quite challenging because of the low resolution and poor image contrast in the WBCTs used in this thesis. Planning CT slice thicknesses can range from 1.5-3 mm depending on the type of treatment, however, these WBCTs have a slice thickness of 5 mm. This was a particular issue for contouring the treatment planning volumes, especially in the head and neck sites because of the large number of fine structures which were difficult to distinguish on the CT and were frequently too small to be contoured on more than one slice of the CT. For example, the lenses of the eyes, the optic nerves, the brainstem, and the cochleas were all very difficult to accurately contour on the available images. Furthermore, the low soft tissue contrast made contouring the colon for the pelvis treatment sites very difficult, particularly as most of the contouring atlases used a "bowel bag" technique which included the whole gut, and these simulations required a stand-alone colon volume to match the style of the MRCP mesh colon structures.

Another important note is in the particular case of the heart. While there is a full

heart mesh structure in the MRCP which can be used to create an organ mask, this volume includes tissue which is excluded in the contouring guidelines.

4.2.2 Organ Masking

There were two approaches to create the organ mask depending on whether the organ (or part of the organ) was contained in either a mesh or a voxelized region. If the organ was even partially contained in the mesh, this process was relatively simple. A Matlab code capable of voxelizing the MRCP was previously created and described (Section 2.2). the only necessary modification was to adjust the script to take an organ ID as an input and only voxelize that single structure, and remove the organ re-ordering and recombination steps. If the mesh-based organ is part of a hybrid, the voxel dimensions would be re-calculated to match the dimensions of the hybrid scoring grid, to ensure as accurate an overlay as possible.

If an organ was at least partially contoured in RayStation, the contour would then need to be converted into a voxel mask to use in the dose analysis. The DICOM RT-Struct was exported from RayStation and an in-house script was developed to first connect the RT-Struct back to the original DICOM image, then use code written by Olesen and Landberg [108] which converts the coordinate point cloud representing the structure's contour into a 3D voxel array which can be used as a voxel mask. One thing to note is that in the case of contours of partial body images (such as the truncated in-field or in-field plus transition slices), the resulting voxel mask was the same dimensions as that of the partial body image source. If a partial body voxel mask had to be applied to a whole-body scoring grid, then a number of empty padding slices were added to couch the voxel mask and place it accurately over the appropriate anatomy.

For organs with segments in both mesh and voxel structures (such as the colon in the pelvis hybrids), or contained in both the in-field and the transition slices (or outside the in-field in the WBCT), it was necessary to combine multiple organ masks together to form a cohesive hybrid phantom organ mask. To keep the organ masks in the dose analysis as close to those used to plan the treatment as possible, the in-field CT contours (rather than those of the WBCT) were used to generate the in-field portion of all organ masks which were at least partially contained in the CT. For example, the lung can be partially contained in the head and neck CT in-field. To calculate the dose to this organ in the WBCT geometry, it would be necessary to combine the contour mask from the planning in-field CT contour with the contour mask from the WBCT contour. With this method, the in-field CT segment of the lung uses the same contour in the WBCT and the hybrid. After all organ masks had been created from each method (CT contour conversion and mesh voxelization), they were overlayed onto the source CT and meshes to check for misalignment.

4.3 Designing and Simulating Treatment Plans

The four treatment plans for this study were chosen to be a prostate treatment for the male pelvis, a cervical cancer treatment for the female pelvis, a meningioma plan for the female head and neck, and a nasopharyngeal plan for the male head and neck. As the WBCTs don't have any solid tumors, all treatment plans represent hypothetical treatments and ultimately serve the sole purpose of comparing the dose distributions between the phantoms against the WBCT ground truth. Despite full treatment plans not technically being necessary for a distribution comparison, a significant effort was made to create clinically reasonable treatment plans. For each of these plans, key organs at risk (OARs), beam angles, fractionation schemes, and dose objectives were taken from the literature and cross-checked by a clinical proton medical physicist at the Trento Proton Therapy Center for clinical reasonability.

4.3.1 Male Pelvis: Prostate

For the male pelvis treatment site, a treatment plan was designed for a hypothetical prostate cancer. The organs at risk guiding the dose objectives were: prostate, bladder, rectum, and femoral heads. The organs which were considered for post-simulation dose analysis were: prostate, bladder, colon, liver, heart, and brain. The prostate plan utilized lateral parallel-opposed beams to target the PTV, here defined as the prostate volume plus a margin of 8 mm in all directions except posteriorly, which used a margin of 5 mm. This margin was chosen based on a range of reasonable clinical margins available in the literature with a reduction posteriorly to spare the rectum (Teh et al 2003 [150], Meijer et al 2008 [95], Oehler et al 2014 [107]). Prescribed dose to the PTV was defined as 79.2 Gy to 95% of the CTV volume based on literature guidelines [44][90]. In the final optimized plan, the rectum met the following constraints: V75 $<$ 5%, V70 $<$ 10%, V60 $<$ 10%, and V40 $<$ 15% which fall well within the limits in the literature [148], where a constraint of V75 $<$ 5% means that less than 5% of the organ at risk volume received 75 Gy. The bladder met the following constraints in the optimized plan: V75 $<$ 7%, V70 $<$ 10%, V50 $<$ 20%, and V30 $<$ 30%, which also fall within literature dose limits [153]. Finally, the femoral heads were planned to have a D1 of 35.6 Gy, well under the maximum dose limit of 50 Gy, where D1 of 35 Gy means that the 1% of the organ volume receiving the most dose, received 35 Gy. Figure 4.2 shows the prostate treatment plan as simulated in Geant4 from axial, sagittal, and coronal views.

4.3.2 Female Pelvis: Cervical Cancer

For the female pelvis treatment site, a treatment plan was designed for a hypothetical cervical cancer with some nodal volume involvement. Two PTVs were defined for primary and nodal risk volumes based on consensus contouring guidelines from the literature [87][58]. The organs at risk guiding the dose objectives were: the bladder, the bowel bag, the rectum, and the femoral heads. The organs which were considered for post-simulation

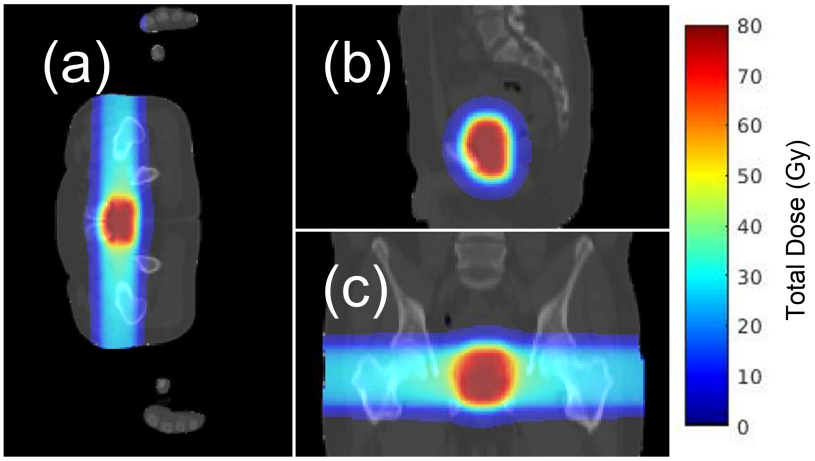

Figure 4.2: The prostate treatment plan simulated on the male pelvis hybrid, associated WBCT, and mesh phantoms. The figure shows the total dose (Gy) from the plan in axial (a), sagittal (b), and coronal (c) views on the in-field CT.

dose analysis were: bladder, colon, kidneys, liver, heart, and brain. The cervical treatment plan consisted of two sets of three fields each. The first delivered the bulk of the treatment and consisted of two posterior oblique fields mirrored across from each other, each at a 30° angle from the anteroposterior (AP) axis, and a single anterior field, angled superiorly from the patient to avoid excess dose to the bowel bag when targeting the nodal volumes. The second set of fields delivered a boost to the high risk PTV volume, and consisted of a single posterior field, and two anterior oblique fields mirrored at 45° from the AP axis [93][58][88]. The nodal volume was prescribed 50.4 Gy and the primary volume was prescribed 59.4 Gy (the 9 Gy delta was delivered by the boost fields) [93]. Due to the overlap of several volumes with the PTVs, it was not possible to meet the OAR constraints delineated in Shang et al 2020 (except the femoral heads), but the planned doses were within the range of the plans created by Marnitz et al 2015 [93]. Figure 4.3 shows the cervical treatment plan as simulated in Geant4 from axial, sagittal, and coronal views.

4.3.3 Male Head and Neck: Nasopharyngeal Cancer

For the male head and neck treatment site, a treatment plan was designed for a hypothetical nasopharyngeal cancer. The PTV was contoured using a clinical treatment plan from the Trento Proton Therapy Center as reference. The organs at risk guiding the dose objectives were: the brainstem, left and right optic nerves, the optic chiasm, left and right eyes, spinal cord, temporomandibular joint, left and right cochlea, and left and right parotid glands. The organs which were considered for post-simulation dose analysis were: brain, left and right eye, thyroid, heart, lungs, and bladder. The treatment was delivered by three fields, one posterior, two anterior oblique at a 45° from the AP axis and angled superiorly by 15°

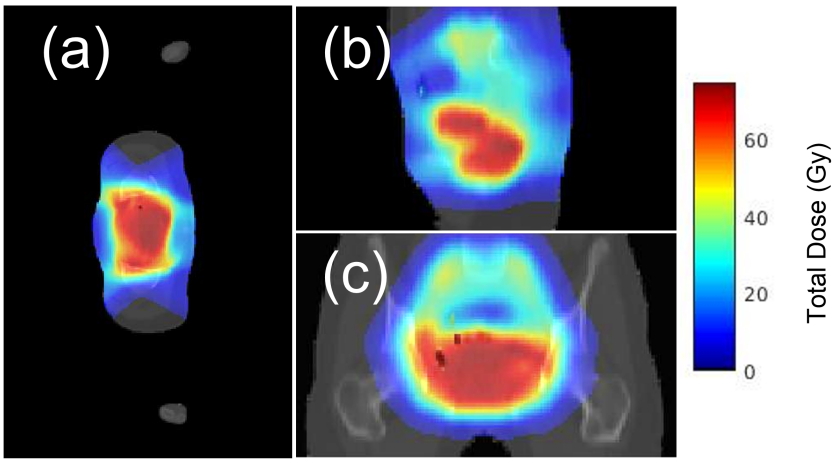

Figure 4.3: The cervical cancer treatment plan simulated on the female pelvis hybrid, associated WBCT, and mesh phantoms. The figure shows the total dose (Gy) from the plan in axial (a), sagittal (b), and coronal (c) views on the in-field CT.

to avoid excess dose to optic structures (beam number and angles based on a treatment plan from the Trento Proton Therapy Center). This plan used two PTVs representing the gross disease plus margins and immediately proximal high-risk nodal volumes. The primary PTV was prescribed 70 Gy to 95% volume and the high-risk nodal volume was prescribed 60 Gy to 95% volume [159]. All OAR dose constraints were taken directly from and fell within the international guidelines for dose constraint recommendations in nasopharyngeal carcinoma [83]. Figure 4.4 shows the nasopharyngeal treatment plan as simulated in Geant4 from axial, sagittal, and coronal views.

4.3.4 Female Head and Neck: Meningioma

For the female head and neck treatment site, a treatment plan was designed for a hypothetical meningioma. The PTV was contoured using a clinical treatment plan from the Trento Proton Therapy Center as reference. The organs at risk guiding the dose objectives were: left and right eyes, left and right optic nerves, temporomandibular joint, spinal cord, brain, brainstem, optic chiasm, and left and right cochleas. The organs which were considered for post-simulation dose analysis were: brain, left and right eye, thyroid, heart, lungs, and bladder. This treatment plan used three fields, all angled inferiorly from above the patient's skull at a 45° angle. Two of the fields were lateral left oblique at a 15° angle from the left-right axis while the third was a lateral right field (beam number and angles based on a clinical plan from the Trento Proton Therapy Center). This plan only had a single PTV, which was prescribed 54 Gy to 95% volume [123]. Dose constraints for the OARs were based on a combination of Combs et al 2020 [34] and Lee et al 2019 [83] (which included general head and neck OAR constraints). Figure 4.5 shows the meningioma treatment plan as simulated in Geant4 from axial, sagittal, and coronal views.

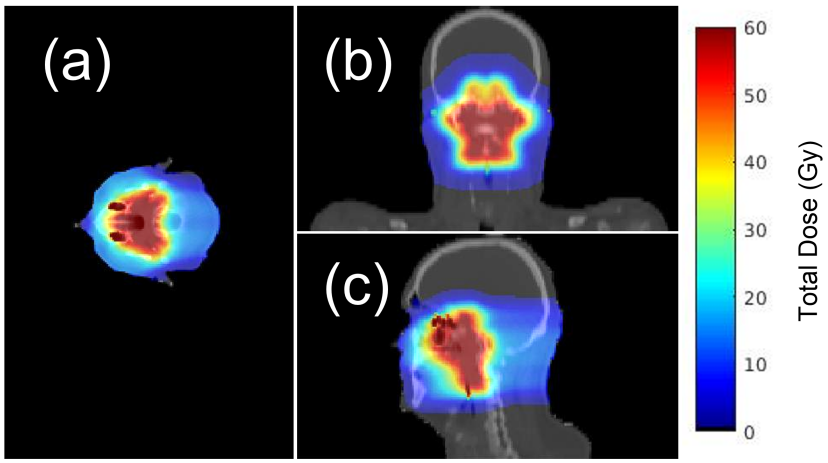

Figure 4.4: The nasopharyngeal treatment plan simulated on the male head and neck hybrid, associated WBCT, and mesh phantoms. The figure shows the total dose (Gy) from the plan in axial (a), sagittal (b), and coronal (c) views on the in-field CT.

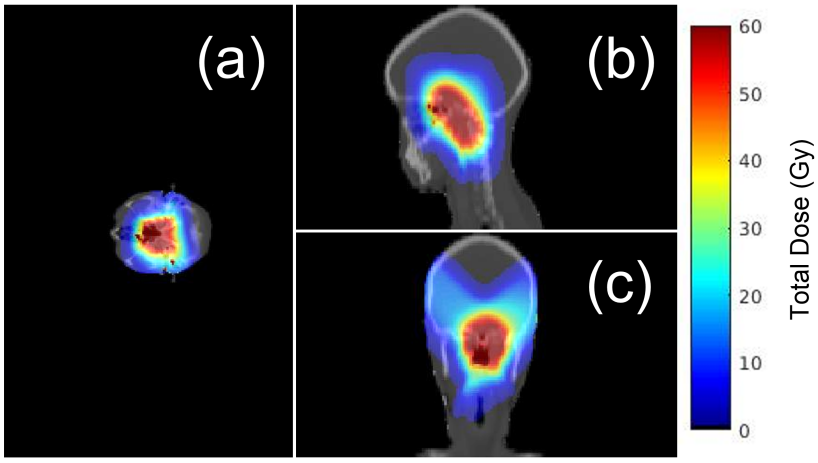

Figure 4.5: The meningioma treatment plan simulated on the female head and neck hybrid, associated WBCT, and mesh phantoms. The figure shows the total dose (Gy) from the plan in axial (a), sagittal (b), and coronal (c) views on the in-field CT.

4.3.5 Simulations

All treatment plans were exported from RayStation using an in-house code described in Section 3.5. Each treatment plan was simulated on the hybrid, the scaled MRCP, the default MRCP, and the WBCT using the Geant4 implementation described in Chapter 3, running 500 statistically independent jobs of 1 million particles each. All jobs used random seeds based on the job ID number, which were consistent across all phantoms. All six scorers previously discussed in Section 3.2 were tracked for all simulation jobs (total dose, neutron dose, total KERMA transferred, total neutron fluence, KERMA contribution multiplied by the contributing neutron's energy, and the fluence contribution multiplied by the contributing neutron's energy). The scoring grids for all voxel-based phantoms were aligned to their respective CT dimensions. For the mesh phantom only they were aligned to the same dimensions used to voxelize them for Matlab imaging and hybrid construction. In the hybrid, the scoring grid was aligned to the voxel portion of the in-field and transition, and then further extended to cover the full height of the out-of-field. This scoring grid will have the same out-of-field alignment in Z as the scaled MRCP, however due to the differing voxel resolutions and extent in X and Y, the hybrid scoring grid will be slightly misaligned compared to the scaled MRCP. However, since the mesh organs are masked along the same scoring grid as the hybrid, there is no misalignment between the mesh organ masks and the scored hybrid anatomy.

One important thing to note is that only the patient geometry was built in Geant4. There was no treatment room geometry or any representation of a delivery machine. This means that the scored quantities from these simulations are not necessarily accurate to what would actually be delivered to the patient in the clinic, as the leakage and scatter components of stray radiation are absent. This was considered acceptable for the purposes of this study as 1) the priority was to evaluate relative dose distribution prediction, not to calibrate fully to physical measurements or judge the magnitude of out-of-field dose delivered to a patient and 2) these treatment plans are all designed to be active scanning proton plans, in which internally generated neutrons are the primary contribution to stray neutron dose [55].

4.4 Data Analysis

After simulation, the next stage was processing the simulation outputs and comparing the performance of the three phantoms against the ground truth WBCT. Each scorer produced its own output file for each simulation job. All simulation outputs were converted into 3D Matlab arrays using an in-house script and then the outputs for 50-job increments were combined to effectively yield 10 batches of data for each scorer for each patient representation. At this point there are 3D voxel distributions for each scored quantity, each representing 50 million particle histories.

4.4.1 Calculating Equivalent Dose

As a reminder, the following scored quantities have been tallied: total dose, neutron dose, total KERMA transferred, total neutron fluence, KERMA contribution multiplied by the contributing neutron's energy, and the fluence contribution multiplied by the contributing neutron's energy. The four quantities used to assess hybrid predictive performance are: total dose, neutron dose, KERMA-weighted equivalent dose, and fluence-weighted equivalent dose. Therefore, before using the organ masks to evaluate the dose quantities, the equivalent dose must first be calculated using the scored quantity distributions.

First, the therapeutic proton and neutron contributions to dose were isolated. The neutron dose was already pre-calculated as an inherent scorer, and the therapeutic proton dose was calculated by simply subtracting the neutron dose from the total dose scorer. Thus isolated, the therapeutic proton dose was multiplied by the ICRP 92 proton weighting factor of 2. This weighted proton equivalent dose component was then set aside for later.

To calculate the neutron equivalent dose from the neutron dose component, first a voxel-wise representation of the energy dependent neutron weighting factor based on the two weighting methods was required. To calculate the average neutron energy per voxel, for example for the KERMA-weighted scorers, the 3D grid with the tracked KERMA contribution multiplied by the contributing neutron energy data from one custom scorer was divided by the total KERMA scoring grid from another custom scorer. This is described by Equation 4.1 shown below:

$$E_{\text{mean}} = \frac{\sum_{i=0}^{\text{num voxels}} [\text{KERMA}_{\text{event}} \times E_{\text{event}}]}{\sum_{i=0}^{\text{num voxels}} \text{KERMA}_{\text{event}}} \tag{4.1}$$

where E_{event} is the neutron energy prior to a given interaction, "event" refers to an incidence of energy transference from a neutron which occurs in a scored voxel, and $\text{KERMA}_{\text{event}}$ describes the amount of kinetic energy transferred to charged particles by the neutron in a given interaction.

In this way the weighted average neutron energy per voxel across the full scored space is calculated. In regions where the statistics were low, dividing by these paired scorers would yield a "Not a Number" result in the voxels where no energy transfer by neutrons was registered, and so after the division these NaN voxels were manually reset to equal 0. This was then repeated for the paired fluence scorers.

With the newly calculated neutron energy arrays, the analytical model for the ICRP 92 energy-depended weighting factor can be used to calculate the weighting factor for each voxel in a given batch. The ICRP 92 model for neutron weighting factor is as follows:

$$w_{\text{R}} = 2.5[2 - e^{-4E} + 6\text{e}^{\frac{-ln(E)^2}{4}} + \text{e}^{\frac{-ln(\frac{E}{30})^2}{2}}] \tag{4.2}$$

where w_{R} is the weighting factor and E is the neutron energy. Both the KERMA- and fluence-weighted neutron energy arrays were input into this formula to calculate the neutron

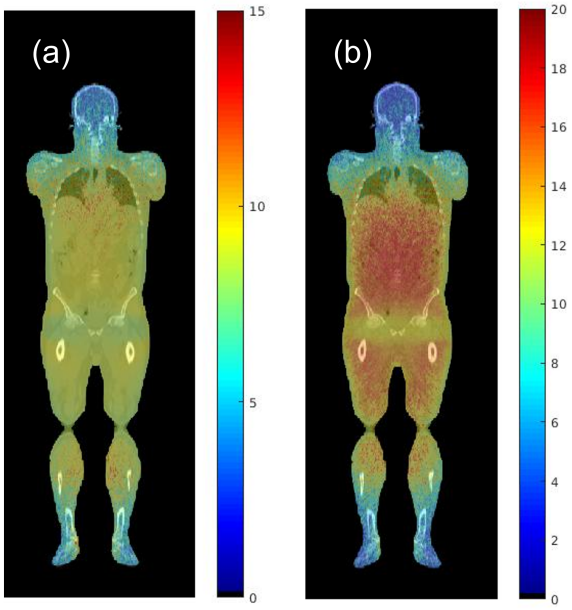

Figure 4.6: Reproduction of Figure 3.2. A diagram visualizing the energy dependent neutron weighting factor (unitless) from a prostate treatment plan throughout a male WBCT using the fluence-weighted neutron energy scorer (a) and the KERMA-weighted neutron energy scorer (b).

weighting factor for each voxel in the array. An example of what the final neutron weighting factor arrays look like was previously shown in Figure 3.2 and has been reproduced for easy reference below in Figure 4.6. As mentioned previously, a key point to take from this is that the region corresponding to the highest neutron weighting factor is outside the primary proton fields. This is because of the nature of the energy-dependent neutron weighting factor, which peaks at 20 for a neutron energy of 1 MeV. Inside the primary proton field, the generated neutrons are likely to be a higher energy than 1 MeV (weighting factor approaches 5 with increasing neutron energy), and so the weighting factor is lessened compared to the region just outside the treatment field, where the neutrons are more likely to have lost some energy. The minimum weighting factor possible is 2.5 when neutron energy approaches 0 MeV, corresponding to regions very far from the treatment field (head and feet in Figure 4.6). Then, similarly to how the proton dose was multiplied by 2, the neutron dose was multiplied element-wise by the neutron weighting factor array to yield the neutron equivalent dose. Total equivalent dose for both the KERMA- and fluence-weighting methods was then calculated by adding the proton equivalent dose with the respectively weighted neutron equivalent dose.

The final stage for each of the dose quantity arrays was to scale the magnitude of the array to match expected clinical levels. This scaling was based on the total number of simulated particles per batch and the calculated actual number of particles from the

exported treatment plan using the MU to particle number conversion described in Section 3.5.1. Monte Carlo simulations very rarely simulate the full particle count of a clinical treatment plan, as that would take a prohibitive amount of time for a negligible increase in accuracy inside the treatment field. Similarly in this case, it was not feasible to simulate the full treatment plan. Where one job of 1 million particles might take 6 hours, which represents 2% of one batch, one job of 7.2E10 particles (representing 2% of the total particles of the male pelvis treatment plan) would take 361 days. Since the full plans cannot be simulated on that scale, the dose quantities must be adjusted based on the relative number of particles simulated. The MU to particle conversion which was required for converting the treatment plan from RayStation to Geant4 was already discussed in Chapter 3. This conversion was used previously to calculate the number of particles needed for a given spot in the treatment plan, so to obtain the total number of particles per plan was a simple matter of summing the particles needed for each individual spot. Because of the MU to particle number conversion described in Section 3.5.1, not only are the converted plan's beam weights based on relative particle number but also the number of particles simulated per batch (50 million) and the number of particles which would be needed to achieve full clinical dose specifications are now known. So to scale the dose quantities, it was possible to apply a simple ratio of the number of particles per plan divided by the number of particles simulated (always 50 million for this project). Although the number of particles in a given treatment plan varied depending on each plan, all plans used a number of particles in the order of magnitude of 1E12. For example for the male head and neck plan, the total number of particles needed for the plan was 3.61E12. This means that only 0.001% of the total number of particles were simulated for a given batch of that treatment site. Despite simulating such a small percentage of the full treatment plan, the total number of particles simulated per batch in this thesis was able to achieve statistical uncertainty of <0.1% for total dose in in-field organs. For the out-of-field, the uncertainty fluctuates based on distance from the treatment fields and size of the organ. The total dose statistical uncertainty for the brain in the pelvis plans was about 2%. The same quantity for the bladder in the head and neck plans was 6% in the female plan and 12% in the male plan.

4.4.2 Organ Dose Quantity Calculation

Once the dose quantity arrays were fully prepared, the next step was to isolate from each of them the portion corresponding to the designated organs of interest. The organ masks discussed in Section 4.2.2 are 3D binary voxel arrays where if a voxel is contained inside an organ it is assigned a value of 1, otherwise it is assigned a value of 0. For this calculation, all voxels which have a 0 value were re-assigned to instead have a NaN value. Then, a voxelwise multiplication of an organ array with a given dose quantity array is performed to isolate the organ dose/equivalent dose. The average dose/equivalent dose was calculated by summing all voxels in the isolated organ array, excluding the NaN voxels. This was then divided by the number of voxels in the organ mask which had a value of 1. This way, the inclusion of all voxels which were a part of a given organ was ensured, even if that

voxel did not score any measure of the dose quantity. This process was repeated for all organs of interest for a given treatment site across all patient representations and all data batches.

With this method of data collection there is the possibility to, particularly in in-field organs, make some assessments about what fraction of the organ receives what level of dose (via dose volume histograms, for example). However for this study a single value was used for each organ representing the average dose quantity delivered to that organ. The average value was considered sufficient as most of the organs lay outside the treatment field and were unlikely to receive any steep dose gradients. Furthermore, for the in-field, it would be highly unlikely that either of the mesh phantoms would outperform the hybrid considering that the WBCT and the hybrid share identical CT images in that region, so no useful information regarding relative performance would be gained by examining the 3D dose distribution in the in-field organs. For future studies, after the addition of a treatment room and machine geometry in the simulation, it may be of interest to evaluate 3D secondary cancer risk distributions for organs which lay across the in-field and transition regions.

4.4.3 Assessing Phantom Predictive Performance

The percent difference for each of the 10 batches' various scored dose quantities was calculated for each phantom, using the corresponding value from the WBCT as the ground truth. These percent differences were averaged across the 10 batches for a given specific phantom, organ, treatment plan, and dose quantity, with error defined as the 25^{th} and 75^{th} percentile variation. Similarly to the percent difference, the dose quantities themselves for each of the 10 batches in a given patient representation, treatment plan, and organ were also averaged together where the error was defined as the 25^{th} and 75^{th} percentile variation. The term "case" is defined here as referring to a certain combination of dose quantity, treatment plan, and organ. For example, one case would be the scored total dose in the brain in the female pelvis plan. For each case, the three phantoms (hybrid, scaled MRCP, and default MRCP) were categorized as either the closest, intermediate, or farthest, depending on the absolute value of the percent difference from the WBCT. If two phantoms gave values for a case for which the 25^{th} and 75^{th} percentiles overlapped, they would be considered to have performed equivalently and would be categorized under the same rank. For example, if the hybrid phantom gave a percent difference from the WBCT of $4.0 \pm 0.5\%$ and the scaled MRCP gave $-4.5 \pm 0.5\%$ for the same case, both the hybrid and the scaled MRCP would be assigned the same performance rank. If two phantoms performed equivalently and the third performed inferiorly, then the two phantoms would be categorized as "closest", the third would be assigned "farthest", and no "intermediate" category would be assigned for that case.

4.4.4 Hybrid Performance Results

Table 4.1 shows the performance of the phantoms as a fraction of cases which gave the closest predicted dose quantity value as the WBCT. For the in- and near-field, the hybrid most frequently provides the closest estimate to the WBCT by far, with 98% of a total 56 cases yielding a "closest" rank. The only case where it achieved an "intermediate" rank over a "closest" rank was a near-field case for the neutron dose in the colon for the male pelvis case. The scaled MRCP typically provided the next best estimate in the in- and near-field, followed by the default MRCP. The out-of-field cases were a little more varied. The hybrid was by far the least likely to provide the farthest estimate of dose or equivalent dose with only 2% of a total 48 cases. There was only a single case where the hybrid was the farthest estimate: the liver in the male pelvis plan scoring neutron dose. That said, while the hybrid was outside of the 25th-75th perecentiles defined as the uncertainties in that case, in absolute terms the hybrid was very close to matching the "intermediate" phantom with a 0.467 mGy estimate/ 25% difference in the hybrid versus 0.455 mGy estimate / 22% in the default MRCP (which was the "intermediate" rank). In the out-of-field, the hybrid very frequently shared the "closest" rank with one or both of the other phantoms, reflecting the higher uncertainties and the similar/shared anatomy. For each of the phantoms, the most common ranking for cases in the out-of-field was "closest", and furthermore the hybrid had more "closest" ranks over the scaled MRCP by one case. Also for the hybrid, after "closest", the next most common rank was "intermediate". However unlike in the hybrid, for both the scaled MRCP and the default MRCP the next most common ranking after "closest" was "farthest".

In the out-of-field the scaled MRCP yielded the farthest estimate of the dose quantity in 35% of cases, and for the default MRCP it further increased to 40% of cases. In stark contrast, the hybrid had only a single case (2%) where it yielded the farthest estimate. Essentially, while all phantoms had similar effectiveness in providing the closest estimate of the ground truth scored dose quantities for the chosen organs in the out-of-field, if any phantom other than the hybrid yielded the closest estimate, the hybrid was by far the most likely to yield the next closest.

Table 4.1: Fraction of cases by dose quantity prediction performance for all phantoms across all treatment sites.

Organ Location	Rank of Prediction with respect to WBCT ground truth	Hybrid	Scaled MRCP	Default MRCP
In/Near-Field	Closest	0.98	0.09	0.04
	Intermediate	0.02	0.61	0.30
	Farthest	0.00	0.30	0.66
Out-of-field	Closest	0.56	0.54	0.44
	Intermediate	0.42	0.10	0.17
	Farthest	0.02	0.35	0.40

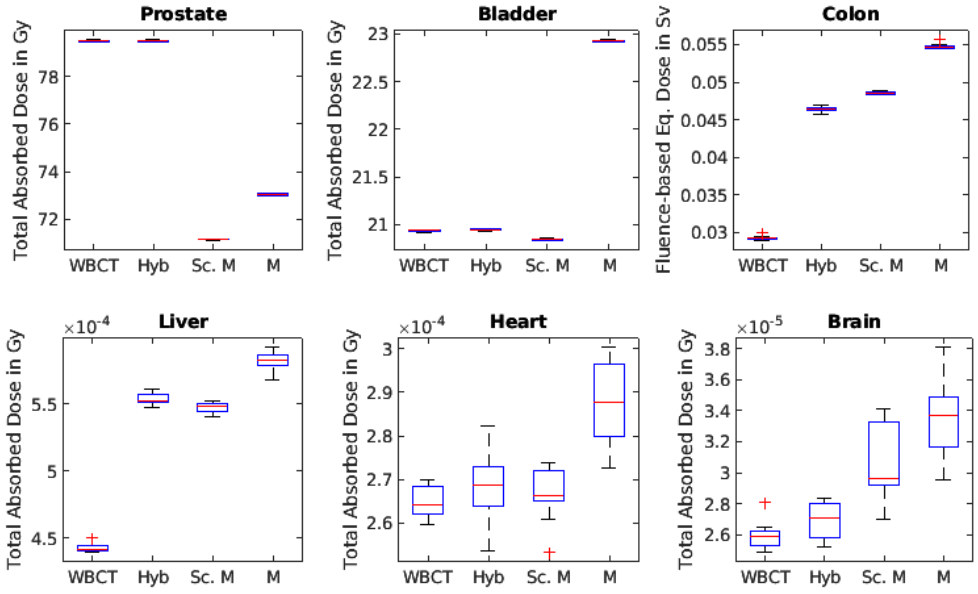

Figure 4.7: Boxplots of the total organ absorbed dose in Gy for the in- and near-field (prostate, bladder, colon) and out-of-field (liver, heart, brain) organs from the prostate treatment plan in the male pelvis for all four patient representations (WBCT, hybrid, scaled MRCP, and unscaled MRCP). The central mark is the median, the box edges are the 25th and 75th percentiles, the crosses are outliers (defined as points that are more than 1.5 times the interquartile range away from the 25th and 75th quartiles), and the whiskers extend to the extreme data points not including outliers.

For each treatment site, boxplot figures were made showing the calculated value for each dose quantity for all examined organs. The boxplots for the total dose in the male pelvis treatment plan is given in Figure 4.7. From this figure the trend described before can be clearly seen. In and near the treatment field the hybrid provides the best estimate of total dose. In the out-of-field the uncertainties grow, and in the case of the heart, both the hybrid and the scaled MRCP provide equivalent predictions and would be classified together as being the "closest" phantoms to the WBCT ground truth. In the liver it can be seen that the scaled MRCP actually provides a closer estimate to the ground truth than the hybrid. The boxplots for the other dose quantities for the male pelvis treatment plan as well as those for the other treatment sites are given in the Appendix A. In addition to the complete set of boxplots, full quantitative information for all treatment sites and all dose quantities, see Appendix B.

Figures 4.8-4.11 shows the percent difference from the WBCT for all dose quantities and organs for an individual treatment site. In these figures not only is the relative performance of the phantoms clearly visible, but also shows some information on the magnitude of difference from the WBCT and from each other. One thing which is clear through these

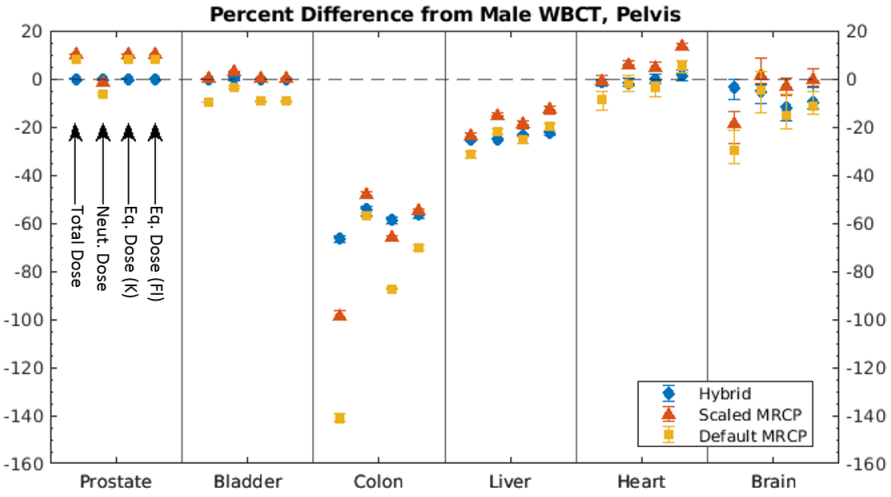

Figure 4.8: Dose quantity percent differences from the WBCT ground truth for the prostate treatment plan in all organs and phantoms: the hybrid (circle), scaled MRCP (triangle), and default MRCP (square). For each organ, the four markers from left to right correspond to the total absorbed dose, the neutron absorbed dose, the total equivalent dose using the KERMA-weighted neutron energy scorer, and the total equivalent dose using the fluence-weighted neutron energy scorer. Error bars correspond to the 25$^{\text{th}}$ and 75$^{\text{th}}$ percentiles.

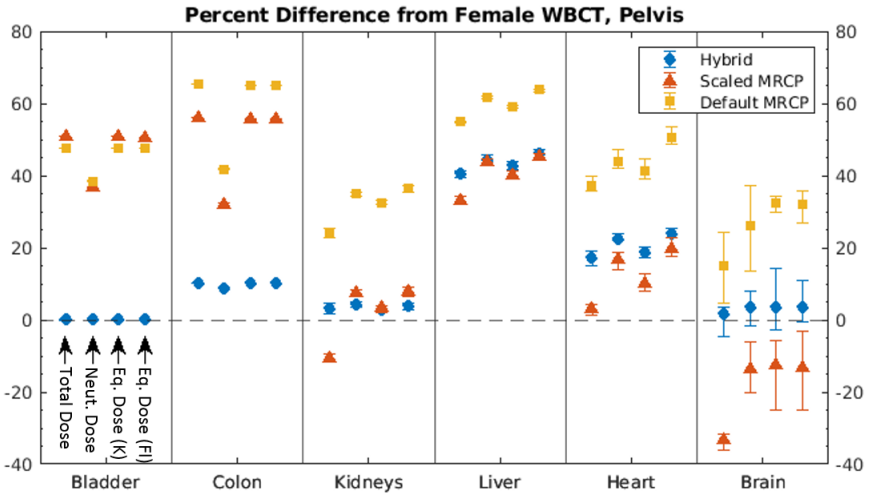

Figure 4.9: Dose quantity percent differences from the WBCT ground truth for the cervical cancer treatment plan in all organs and phantoms: the hybrid (circle), scaled MRCP (triangle), and default MRCP (square). For each organ, the four markers from left to right correspond to the total absorbed dose, the neutron absorbed dose, the total equivalent dose using the KERMA-weighted neutron energy scorer, and the total equivalent dose using the fluence-weighted neutron energy scorer. Error bars correspond to the 25$^{\text{th}}$ and 75$^{\text{th}}$ percentiles.

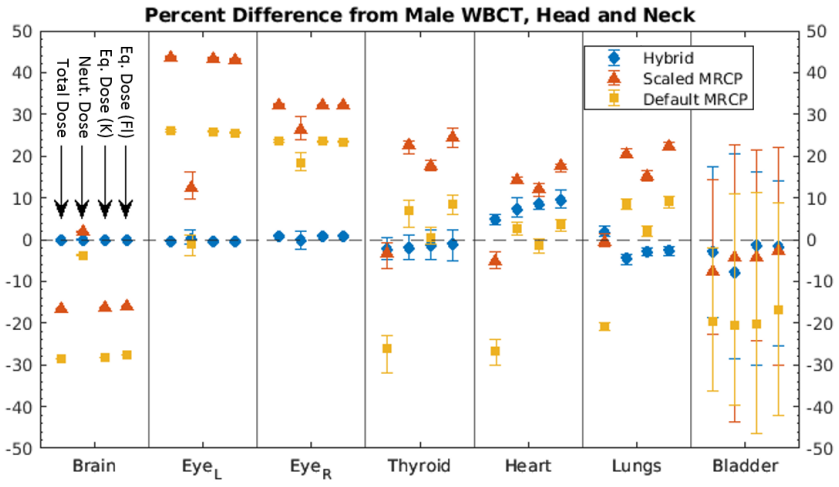

Figure 4.10: Dose quantity percent differences from the WBCT ground truth for the nasopharyngeal carcinoma treatment plan in all organs and phantoms: the hybrid (circle), scaled MRCP (triangle), and default MRCP (square). For each organ, the four markers from left to right correspond to the total absorbed dose, the neutron absorbed dose, the total equivalent dose using the KERMA-weighted neutron energy scorer, and the total equivalent dose using the fluence-weighted neutron energy scorer. Error bars correspond to the 25$^{\text{th}}$ and 75$^{\text{th}}$ percentiles.

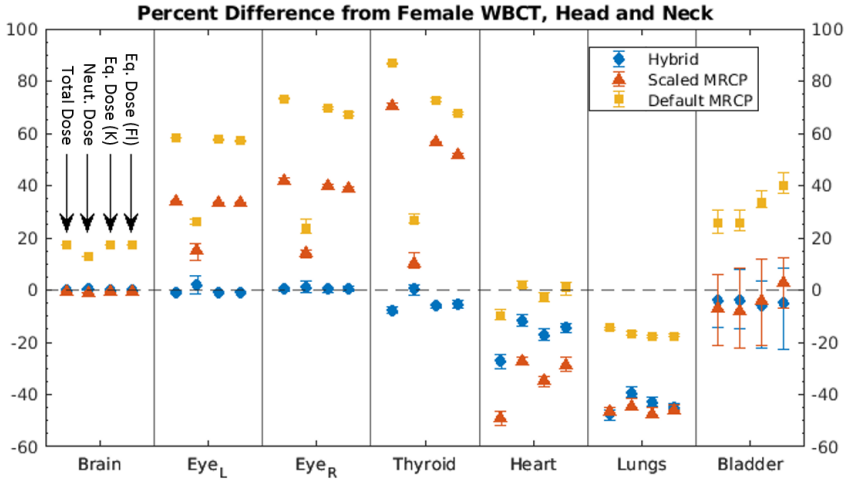

Figure 4.11: Dose quantity percent differences from the WBCT ground truth for the meningioma treatment plan in all organs and phantoms: the hybrid (circle), scaled MRCP (triangle), and default MRCP (square). For each organ, the four markers from left to right correspond to the total absorbed dose, the neutron absorbed dose, the total equivalent dose using the KERMA-weighted neutron energy scorer, and the total equivalent dose using the fluence-weighted neutron energy scorer. Error bars correspond to the 25$^{\text{th}}$ and 75$^{\text{th}}$ percentiles.

figures is that while the hybrid is most frequently the best predictor of the chosen dose quantities, there can be cases (particularly in the out-of-field) where the scaled MRCP or even the default MRCP outperforms the hybrid, similar to the liver case regarding the Figure 4.7 boxplots.

Across all the treatment sites, if an organ was in or near the treatment field, then the equivalent dose tended to match the total dose in terms of the percent difference from the WBCT (visible for example in the MRCPs performance in the brain and eyes in Figures 4.10 and 4.11). This is likely due to the dominance of the therapeutic dose in that region, with a relatively small impact of the neutron dose. Conversely, in the out-of-field, the equivalent dose varies a lot more. A little fluctuation is present between the two weighting methods, but overall the equivalent dose tends to be closer to the percent difference of the neutron dose scorer than the total dose scorer (clearly visible in the brain in Figure 4.9 and the heart and lungs in Figure 4.10).

Another important thing to note, that while the percent differences in the out-of-field can be quite high (frequently between 20-50% difference from the WBCT) the absolute difference in dose or equivalent dose is often not significant. For example, in the extreme distance case of the bladder in the male head and neck treatment plan, both the hybrid and the scaled MRCP had a prediction of less than 5% difference from the ground truth for fluence-weighted equivalent dose while the default MRCP had a 20% difference. However, in terms of absolute numbers the difference is quite small, with the hybrid, scaled MRCP, and default MRCP yielding equivalent dose estimates of 99.3 μSv, 102 μSv, and 115 μSv respectively.

4.4.5 Considerations for the Hybrid Phantoms

This section will go over some smaller aspects of this particular study which are worth detailing. The first is that for this particular study, there is a small amount of error in the hybrid in-field organs for the head and neck treatment sites which is not present in the pelvis treatment sites. This is due to some resampling of the organ masks which is only necessary in cases where the same WBCT is used to make multiple hybrids with different treatment sites. There would never be a need for two hybrid treatment sites from a single image in a clinical situation (and also it would not likely be a WBCT to begin with), and so since the error induced was less than 1%, it was considered to be an acceptable error. This error is produced because, prior to each hybrid creation, as stated in Chapter 2, the WBCT is manually rigidly translated and resampled to align over a particular treatment site anatomy. This means that the WBCT orientation for the pelvis hybrid and for the head and neck hybrid are slightly misaligned from each other. For a set of phantoms and their corresponding WBCT, there will be perfect alignment, but both treatment site plans were simulated on a single WBCT image set which happened to be the one shifted and sampled into the space to match the pelvis anatomy. The anatomy in the pelvis-shifted and the head and neck-shifted WBCTs are identical, and so it was considered unnecessary to prepare multiple copies of the same WBCT for use in Geant4 simulations. The treatment plans, although both planned on the pelvis-shifted WBCT, were appropriately translated

so there was no misalignment of the plans themselves. However, the head and neck in-field CT contours were drawn on the in-field CT which was excised from the WBCT shifted to match the head and neck anatomy. Therefore, in order to use the same contours to mask the dose in both the WBCT and in the hybrid in-field, a small shift and resampling of the contour masks was required to translate from the head and neck-shifted contours to match the pelvis-shifted WBCT. As a result of this resampling, a small error (<1%) was introduced specifically when comparing the in-field of the hybrid to the WBCT in the head and neck treatment sites.

This error is only introduced in cases where 1) the same WBCT is used as the in-field for two different treatment sites (clinically unlikely) and 2) when the treatment plan is simulated on a WBCT which is translated and resampled separately from the in-field CT.

Another observation from the results is that the hybrid sometimes provides a less accurate estimate of dose due to the simplicity of the scaling factor. The scaling factor designed for this study is a simple linear factor in each of the three dimensions. However, this is inherently designed to scale to specific anatomical features, and cannot guarantee a similar alignment in organs and other soft tissue. This means that, even though the hybrid is scaled to match the WBCT dimensions of some bony anatomy, it could result in poor organ alignment compared to the scaled MRCP or even the default MRCP. Figure 4.12 shows a simplified illustration of how scaling for one region of the anatomy cannot guarantee precise alignment of other anatomical regions. This can result in out-of-field organs being at different distances from the treatment field, which is the primary influence on whether they accurately measure the dose quantity to that organ.

To test this explanation, the total dose in the liver in the male pelvis treatment plan was examined, which was a case where the scaled MRCP performed better than the hybrid phantom which both outperformed the default MRCP. To isolate the influences of the different organ shapes and positioning, multiple tests were conducted. In the first setup, the

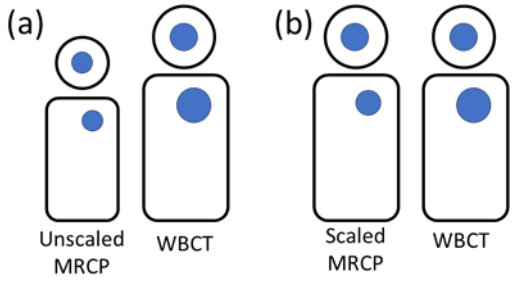

Figure 4.12: A diagram illustrating how even with scaling that matches certain dimensions of the patient CT, there is not a guarantee that the whole internal anatomy will also match. Subfigure (a) shows the starting CT and mesh phantom with organ sizes and placement exaggerated for visualization purposes. Then in (b) the MRCP is scaled and now matches the physical size of the WBCT and the internal measurements of one organ in the head, but has different size/placement of an organ in the chest.

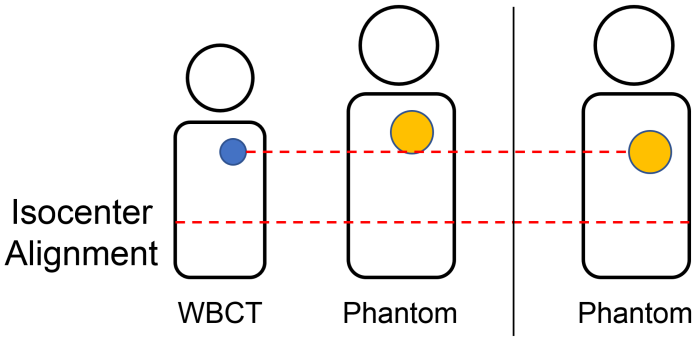

Figure 4.13: A diagram illustrating the first test to understand the influences on masked organ dose in cases where the scaled MRCP or default MRCP outperformed the hybrid. In this test, the organ mask of the phantom was translated such that the distance to the isocenter matched that of the WBCT.

liver organ masks in each of the phantoms was translated to match the same distance from the isocenter as in the WBCT. First, the distance between the treatment plan isocenter and the WBCT liver organ mask center of mass was measured by subtracting the coordinates of the liver organ mask's center of mass from the isocenter. Then this measurement was repeated for the three phantoms' respective liver organ masks' center of mass. For each phantom, the difference between the two distances was calculated in three dimensions, and then the liver organ mask was translated by that difference such that the vector from the isocenter to the liver center of mass matched that of the WBCT. The new translated liver organ mask was then applied to that phantom's respective total dose distribution and the organ dose was isolated as if the liver was positioned in the translated location. A figure visualizing this process is shown in Figure 4.13. The results of that shift are shown compared with the original values prior to the shift in Table 4.2.

From this test, not only do all phantoms show an increased level of accuracy, the relative performance of the phantoms also shifts dramatically. Where before the scaled MRCP provided the most accurate estimate of dose, closely followed by the hybrid, then further

Table 4.2: Comparison of the dose delivered to the liver and percent difference from the ground truth in the first test setup with the organ mask in its default location/geometry and in the second case after translating each phantom's organ mask to match WBCT distance from isocenter.

	Original Values		After Translation	
Patient Representation Type	Dose	% Diff	Dose	% Diff
WBCT	4.43E-04	N/A	4.43E-04	N/A
Hybrid	5.54E-04	25.0	4.26E-04	-3.9
Scaled MRCP	5.47E-04	23.5	5.07E-04	14.5
Default MRCP	5.82E-04	31.4	5.01E-04	13.1

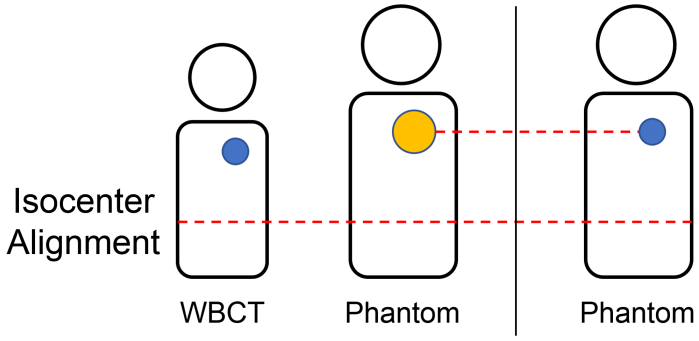

Figure 4.14: A diagram illustrating the second test to understand the influences on masked organ dose in cases where the scaled MRCP or default MRCP outperformed the hybrid. In this test, the organ mask of the WBCT was transplanted into the phantom such that the distance to the isocenter matched that of the phantom's native organ.

back the default MRCP, the results of this test place the hybrid not only significantly closer to the WBCT, but also over the two MRCPs (which are roughly equivalent, with a slight advantage to the default MRCP). This indicates that if the scaling factor had correctly positioned the liver, then the hybrid would have yielded a good estimate of total dose (<5% difference from the WBCT).

The next test was to evaluate the impact of the different organ masks between the WBCT and the phantoms. A similar setup to the first experiment was made, but rather than shifting the native phantom organ mask to match the WBCT distance, the WBCT organ mask was instead transplanted into the phantom dose distribution at the location of the original phantom organ's center of mass. For an illustrated diagram, see Figure 4.14. The results of the transplant compared with the original values are shown in Table 4.3. In this test, the relative rank of each phantom was unaffected, and even the magnitude of difference between the phantoms was unchanged, with the scaled MRCP being slightly better than the hybrid, which are both more significantly improved over the default MRCP. The only small change was that the magnitude of the percent difference from the WBCT

Table 4.3: Comparison of the dose delivered to the liver and percent difference from the ground truth in the second test setup with the organ mask in its default location/geometry and in the second case after transplanting the WBCT organ mask into the phantom organ's location.

	Original Values		After Translation	
Patient Representation Type	Dose	% Diff	Dose	% Diff
WBCT	4.43E-04	N/A	4.43E-04	N/A
Hybrid	5.54E-04	25.0	5.70E-04	28.8
Scaled MRCP	5.47E-04	23.5	5.63E-04	27.2
Default MRCP	5.82E-04	31.4	6.06E-04	36.7

was worsened by a few percent for each phantom. This reinforces the idea that the shape of the organ mask plays less of a role than its location relative to the treatment field.

The final minor point to make here is with respect to computation time. Each job might take between 2-7 hours depending on a variety of conditions. The geometry type had a small impact, but was far outweighed by the impact of the different patients themselves. A change from a CT voxel geometry to a hybrid or mesh type geometry might add 10-30 minutes whereas the difference between the male and female simulations was around 4-5 hours. However, further testing would be required to make any concrete statements on the exact impact of the influencing factors (such as number of volumes in the geometry, scoring volumes, treatment plan complexity, cluster load, etc.).

Chapter 5

Risk Modelling Using Hybrid Phantoms

Despite the hybrid phantom now having demonstrated its ability to provide whole-body dose distributions, it is not necessarily the case that the same pattern of performance would be observed when the risk models were implemented. Additionally, the initial verification study of the hybrid only included 4 hybrids total, from only 2 patient whole-body CTs. To this end, seven hybrids were created, each from their own unique patient WBCT and all regionally focused on the head and neck anatomy. Similarly to the previous chapter, individual treatment plans were designed for each patient in-field anatomy. These treatment plans were then simulated in Geant4 on the hybrid, scaled MRCP, and ground truth WBCT. The default MRCP was omitted from the simulations and analysis as the initial study found no significant pattern of improved prediction over the hybrid or scaled MRCP. Using the same scorers developed previously, equivalent dose was calculated for all simulated geometries and the predictive ability of the hybrid was compared to that of the scaled MRCP with the intent to reproduce the results of the initial validation. Furthermore, five risk models were implemented in the post-simulation data analysis (linear no-threshold, two linear-plateau, and two linear-exponential models) to cover a wide range of potential dose-response relationships. Similarly to the equivalent dose, the hybrid and scaled MRCP's risk predictive ability was compared, with particular focus on whether the different models impacted hybrid performance.

5.1 Hybrids for Risk Model Implementation

The hybrids created for this study were based once again on anonymized WBCTs provided by the LMU University Hospital. The source WBCTs were taken from the same library as those from the previous study, therefore these WBCTs once again did not have any solid tumor volumes. WBCTs which had significant metallic implants or fillings were avoided. Four male and three female WBCTs were selected, spanning as much anatomical variability as possible given the available WBCTs and the selection criteria. Included within those

seven WBCTs were the two from the initial geometry verification, representing the largest male and the smallest female WBCT. As opposed to the initial hybrid geometry verification, where both the pelvis and the head and neck treatment sites were examined, for this study, all treatment planning and all hybrids were focused on the head and neck anatomy. The head and neck was chosen because of the variety of target volume shapes and sizes, the variety of clinical treatment setups which can affect out-of-field dose and subsequently secondary cancer risk, and because the head and neck is often indicated for proton therapy due to the conformality which can spare many complex organs at risk located in that anatomical region.

The hybrids were created using the same process described in Chapter 2, and for each of them the chosen in-field extended from the most superior point of the skull down to the superior apex of the lungs. In this way, any given in-field would include the requisite anatomy for a wide range of head and neck tumor volume types (including those with significant nodal involvement in the neck). These hybrids can be viewed in Figures 5.1 and 5.2, where they have been split into the male hybrids (Pats 1-4) and the female hybrids (Pats 5-7), each shown in coronal and sagittal view alongside their respective WBCT.

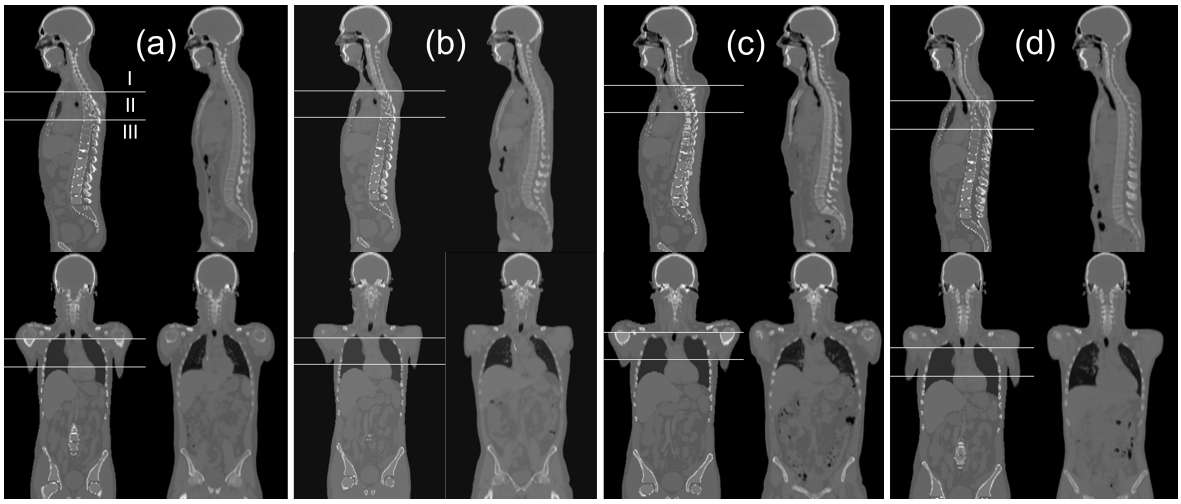

Figure 5.1: The male hybrid phantoms used for the risk modelling investigation side by side with their respective WBCTs representing patients 1-4 in both sagittal and coronal views. For each sub-figure (a), (b), (c), and (d), the hybrid is on the left and the WBCT is on the right. The hybrid has each of the three segments (from top to bottom in each torso: in-field CT (I), transition (II), and out-of-field scaled MRCP (III)) demarcated by a white line and labelled in subfigure (a), where the shared anatomy is the most superior segment of the head and neck.

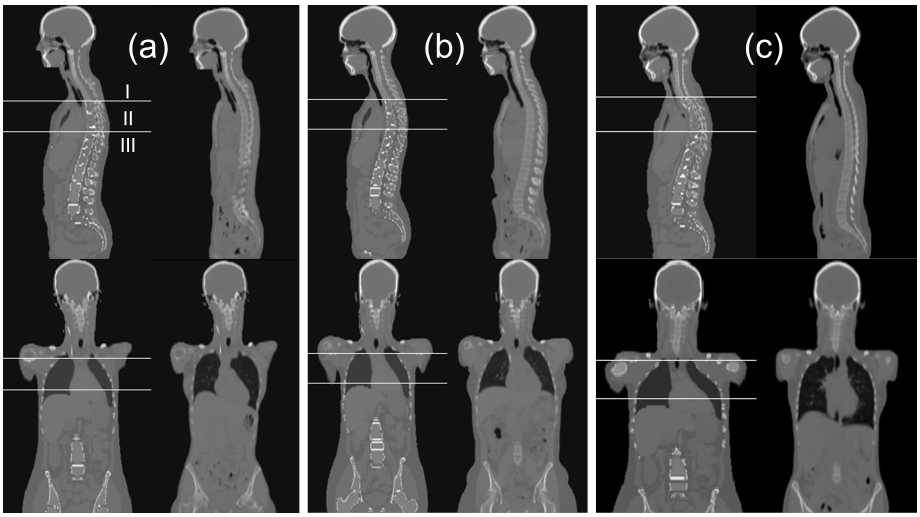

Figure 5.2: The female hybrid phantoms used in the risk modelling study side by side with their respective WBCTs representing patients 5-7. For each sub-figure a), b), c), and d), the hybrid is on the left and the WBCT is on the right. The hybrid has each of the three segments (from top to bottom in each torso: in-field CT (I), transition (II), and out-of-field scaled MRCP (III)) demarcated by a white line and labelled in subfigure (a), where the shared anatomy is the most superior segment of the head and neck.

5.2 Treatment Planning and Organ Contouring

Unlike in the initial hybrid geometry verification, all 7 of the treatment plans were delivered on the same region of anatomy. This means that these hybrids all share the same organs to assess whole-body dose distributions rather than having separate lists. For this part of the thesis, the selected organs for post-simulation analysis were: brain, left eye, right eye, thyroid, lungs, liver, kidneys, and bladder. All in-field CTs contained the brain, left and right eyes, and the thyroid, and some also contained the most superior apex of the lung. The in-field organs were classified as the brain and eyes. The thyroid was classified as near-field, because while it was always contained in the in-field CT, depending on whether a given plan targeted nodal volumes in the neck, the thyroid could be positioned a few millimeters or several centimeters from the edge of the field. The out-of-field organs consisted of all remaining organs: lungs, liver, kidneys, and bladder. These organs were contoured and masked as described in Section 4.2, such that every patient representation (hybrid, WBCT, and scaled MRCP) had a contour or a mask for each of these organs.

The treatment planning for these seven patient anatomies was separated into two categories. The first category consisted of the two head and neck treatment plans from Chapter 4, replicated again for use in risk analysis. For some technical reasons, the treatment machine used to plan in the TPS was changed for the next portion of the thesis involving risk analysis. Therefore the two original head and neck treatment plans had to be re-planned on the new machine. Other than this, the approach and all of the dose objectives for these

two plans were identical to those described in Sections 4.3.3 and 4.3.4.

For the other five patients, each treatment plan was adapted directly from anonymized clinical head and neck proton plans provided by the Trento Proton Therapy Center. These five plans were deliberately selected to have a variety of beam setups, varied target volumes both with and without inclusion of nodal volumes, and finally, unlike previous plans, the inclusion of range shifters. Organ at risk contouring was guided both by the atlases described in Section 4.2.1 [25] and by the contours belonging to the corresponding Trento clinical plan. One difficulty in replicating the Trento plans is that there are no solid tumor volumes in the patient CTs used in this thesis. In the Trento plans, the presence of these solid volumes can press against and distort the natural shape of the OARs. If the shape of the CTV or PTV contour is directly replicated within the WBCT in-fields, then a significant volume of healthy OAR tissue could be included as the WBCTs lack the physical tumor which would distort that anatomy. To avoid this, if a CTV or PTV was positioned between two OARs, the contour was altered to attempt to match the volume of OARs contained in the Trento plans target contours rather than the full volume of the targets themselves. Although this did result in a reduction of the target volumes and change in shape relative to the original plans, the volumes were still of a significant, clinically relevant size. The smallest treated volume for a single plan PTV was 59 cm^3 and the average volume of the largest PTV in each plan was 235 cm^3.

Once the OARs and targets were contoured for the five new plans, the beam setups were adapted as closely as possible for the new plans. In some cases, alterations were needed to 1) be compatible with the treatment machine available in the RayStation TPS and 2) not cause a geometrical conflict when simulating in Geant4. Since the simulation took place in a single treatment geometry, beam angles which required range shifters had to be spaced apart far enough to avoid volume overlap between the range shifters in Geant4. Not only that, but even when there was only a single range shifter, the beam angles had to be spaced out enough to avoid beam intersection with a range shifter volume placed for another beam. Finally, the range shifters and the beam sources were given an increased distance to the patient. This was done partially because it was required from the TPS machine used in treatment planning for this thesis, and partially to avoid the intersection of the range shifter volume with the terminal extents of the patient CT (described more in Section 5.3).

All initial dose objectives, both for target coverage and OAR sparing, were taken directly from the Trento treatment plans and the initial treatment plan was optimized with these objectives. After optimization with the copied dose objectives, the predicted dose distribution was calculated and compared against those from the original plans. When the dose delivered to the target and OARs differed from the Trento plans (target underdosing or OAR overdosing by at least 2 Gy), the dose objective parameters were adjusted to push the distribution to match to the clinical plan. In cases where even after adjustments there were still deviations from the Trento plans (for example due to unavoidable anatomical differences or technical reasons), then the treatment plans were adjusted to prioritize coverage to the PTV at the expense of OAR sparing. After this stage, all OARs which received at least >2 Gy higher dose in the WBCT plans than in the Trento plans were first

checked if they exceeded the dose objectives set by the optimization and then cross-checked against clinical toxicity limits available in the literature to ensure none of them exceeded those limits [29] [28] [132] [22]. Figures 5.3 and 5.4 show representative axial, sagittal, and coronal slices of each of the seven head and neck treatment plans when simulated on the WBCT.

For some plans, particularly those involving large nodal structures or multiple beam sets, the total number of spots in the plan had to be reduced by increasing the minimum allowable beam weight. This was necessary due to file size limits on jobs submitted to the LMU computing cluster which was used to run all simulations for this thesis. Each spot in the plan must be described in the job file, so the size limit on file input to the cluster effectively limited the maximum number of spots which could be allowed for each treatment plan. This resulted in a decrease in dose uniformity to the target and some deviation from the Trento plan dose distributions in the treatment plans which required the spot number reduction.

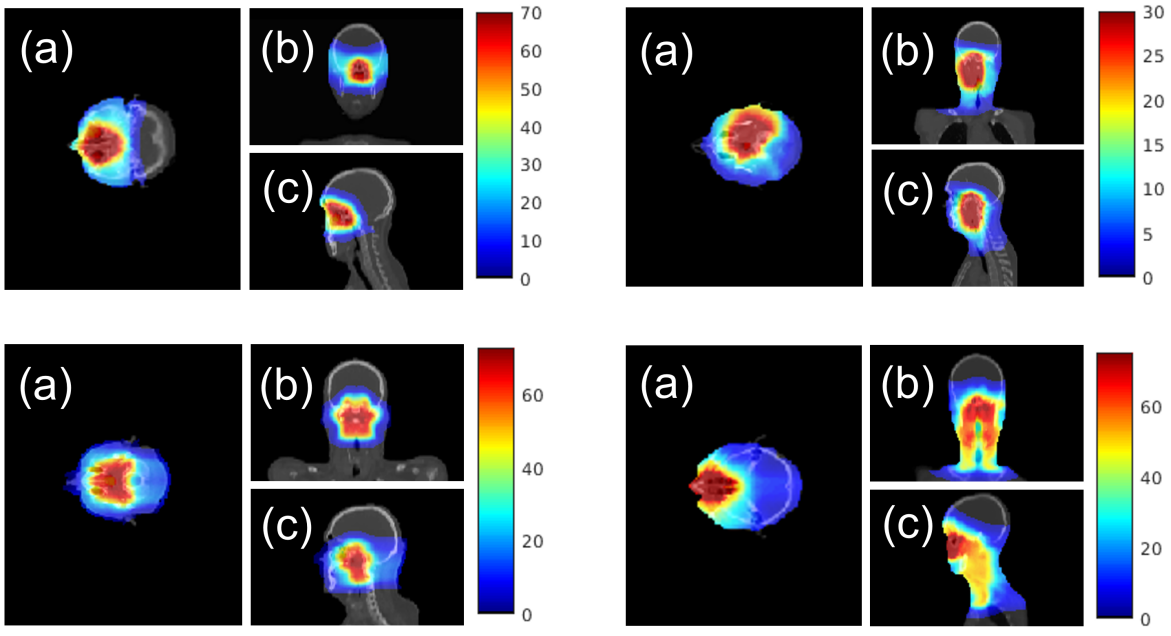

Figure 5.3: The simulated total absorbed dose from the complete treatment plans for the male patients 1 through 4 shown on the WBCTs in (a) axial, (b) coronal, and (c) sagittal views. Dose is given in units of Gy.

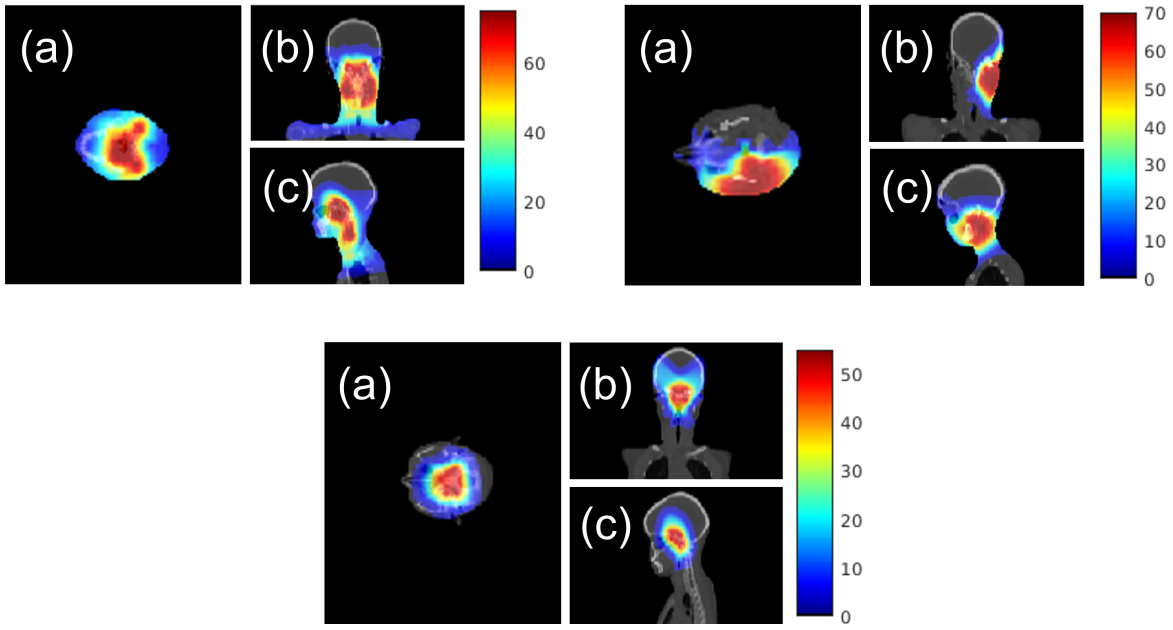

Figure 5.4: The simulated total absorbed dose from the complete treatment plans for the female patients 5 through 7 shown on the WBCTs in (a) axial, (b) coronal, and (c) sagittal views. Dose is given in units of Gy.

5.3 Simulating the Treatment Plans

The simulation was analogous in set-up to the initial hybrid geometry validation described in Chapter 4, with the omission of the default MRCP simulations and the inclusion of range shifters in the simulation geometry if called for by the treatment plan. For each plan which required the use of range shifters, the correct dimensions and positioning about the patient's head was calculated and constructed based on the information given in the treatment plan. This calculation was necessary due to the TPS giving the range shifter position in terms of gantry angle and couch angle while Geant4 requires global coordinates and rotation angles. Since the range shifters are rotated through the same angles as their respective proton beams, these angles and range shifter position can be calculated using basic trigonometry with the angle components and isocenter data which have already been converted via the treatment plan beam exportation described in Section 3.5. The constructed range shifters were composed of solid lucite as it was designated in the TPS with exactly matching elemental composition, density, and excitation energy. The thickness of the material was similarly taken directly from the TPS data on the machine used for treatment planning. In the simulation geometry, the distance of the range shifter from the isocenter needed to

be increased by approximately 15 cm, as in many cases placing the shifter at the correct distance would cause the patient geometry container to intersect with the range shifter volume. In Geant4, two volumes are not allowed to intersect and two materials cannot be assigned to the same volume. In some of the plans, the region containing the range shifter might intersect with the lateral corners of the WBCT. Although these regions contained no actual patient anatomy, from the perspective of Geant4, they are assigned to the air material, and Geant4 will not override it with the range shifter material. Other than the range shifters, no other external geometry such as treatment room or delivery machine was simulated.

All plans were exported using the in-house script described in Section 3.5. These plans were then simulated on each of their respective hybrid, scaled MRCP, and WBCT. Each plan was simulated on a given geometry with 500 jobs of 1 million particles each for a total of 500 million particles. All six scorers developed in Section 3.2 (total dose, neutron dose, total KERMA, total neutron fluence, KERMA contribution multiplied by the contributing neutron's energy, and the fluence contribution multiplied by the contributing neutron's energy) were used to score the whole body as all were necessary for the calculation of equivalent dose and subsequently secondary cancer risk. Again, similar to the simulation methods in Section 4.3.5, the scoring grids were aligned over the natural voxelization pattern of the CT image for those patient representations with voxel geometry (for the hybrid that scoring grid was then extended over the mesh geometry). For the scaled MRCP, the scoring grid was constructed to align with the voxelized version of the scaled MRCP used to create the transition region.

5.4 Risk Models

For the risk implementation, it was important to evaluate whether the hybrid phantom performance was dependent on the chosen secondary cancer risk model. Particularly because risk models for doses >2.5 Sv have a lot of inherent variability and uncertainty. The three base models used in this part of the project are the linear no-threshold (LNT), the linear-plateau, and the linear-exponential model. For the latter two models, two variations were tested for each which modified the dose point at which the model plateaued or reached the maximum risk. The selected dose points were 10 Sv and 40 Sv to model a large range of potential dose-response relationships and to match the risk models used in previous literature [49][48][121][120]. These points are referred to here for simplicity as "inflection points" even though mathematically that is not strictly true. All of the models used here aim to replicate the LNT model at low doses (less than 2.5 Sv) to keep in line with current recommendations by the BEIR VII report [36]. All of the models use the organ specific risk coefficients as defined by the BEIR VII, although for the linear-exponential and linear-plateau models those coefficients are slightly adjusted to shift the low-dose region of the curves to more closely match the LNT model. For all of the models, additional variants for the ERR or EAR can also be calculated. Using these models, ERR is given as a percent increase in risk over that of an unirradiated population while EAR is given in units of the

number of occurrences of secondary cancer per 10,000 person years (10k PY) and similarly represents the occurrences in excess of those experienced by an unirradiated population.

All of the risk models use some inherent parameters defined in Table 12-2 of the BEIR VII [36]. The form of ERR/EAR calculation used in the BEIR VII publication is

$$\text{ERR}(x,a) \text{ or } \text{EAR}(x,a) = \beta_s D e^{\gamma x^*} (\frac{a}{60})^{\eta} \tag{5.1}$$

where β_s is a sex specific parameter listed in Table 12-2 of the BEIR VII, D is the equivalent dose in Sv, γ and η are both parameters which "quantify the dependence of ERR and EAR" on x and a (also given in Table 12-2 of the BEIR VII), a is attained age, x is the age at exposure, and x^* is given by 0 if $x \geq 30$ and $\frac{x-30}{10}$ otherwise. As most of these are constant parameters given a specific organ, attained age, and age at exposure, the organ specific risk coefficient can be defined as:

$$\mu_T = \beta_s e^{\gamma x^*} (\frac{a}{60})^{\eta} \tag{5.2}$$

for a given organ and patient with an age of exposure and attained age. For the purposes of this project, as there was no age information provided with the patient WBCT data, all calculations for the organ specific risk coefficient were done assuming an age of exposure of 45 and an attained age of 65. For all other parameters of the organ specific risk coefficient (β_s, γ, and η), the value for the EAR or ERR calculations were taken directly from the corresponding sections of Table 12-2 of the BEIR VII Report.

The simplest of the three secondary cancer risk models used (five including the inflection point variants), is the linear no-threshold model, which is calculated in the following way, and which expands to the original BEIR VII model given in Eqn. 5.1 when substituting in Eqn. 5.2 for $\mu_{T,\text{ERR}}$:

$$\text{ERR}_T = H_T \times \mu_{T,\text{ERR}} \tag{5.3}$$

where ERR is the excess relative risk, H_T is the equivalent dose delivered to a given tissue/organ, $\mu_{T,\text{ERR}}$ is the organ specific risk coefficient for the ERR of a given tissue. Similarly, the EAR is calculated as:

$$\text{EAR}_T = H_T \times \mu_{T,\text{EAR}} \tag{5.4}$$

where EAR is the excess absolute risk, and the $\mu_{T,\text{EAR}}$ is the organ specific risk coefficient evaluated for EAR calculation rather than ERR calculation.

The EAR using the linear-plateau model is calculated as

$$\text{EAR}_T = \frac{\mu_{T,\text{EAR}}}{\alpha} \cdot (1 - e^{-\alpha H_T}) \tag{5.5}$$

and for the linear-exponential model EAR is calculated as

$$\text{EAR}_T = H_T \cdot \mu_{T,\text{EAR}} \cdot e^{-\alpha H_T} \tag{5.6}$$

where EAR_T is the EAR per 10k PY, $\mu_{T,\text{EAR}}$ is the model and organ specific risk coefficient, α is an additional parameter which controls the shape of the curve specific to inflection

Table 5.1: Table of the α values used in this thesis compared against the values from Fontenot et al 2010 [48]

Model	Inflection Point (Sv)	α	α, Fontenot
LNT	N/A	N/A	N/A
Linear-Plateau	10	0.230259	0.25
	40	0.057565	0.068
Linear-Exponential	10	0.1	0.09
	40	0.025	0.025

point, and H_T is equivalent dose in Sv. ERR is calculated via equivalent equations where $\mu_{T,\text{EAR}}$ is substituted for $\mu_{T,\text{ERR}}$.

For the linear-exponential and linear-plateau models (for both 10 and 40 Sv inflection points), an additional parameter α had to be calculated to shape the curve to match their respective inflection points. The α value for the linear-exponential model was defined such that the point of maximum risk occurs at the selected dose point (10 or 40 Sv). This was calculated by taking the derivative of the linear-exponential function in Eqn. 5.6 with respect to H_T, setting the derivative of risk equal to zero, and setting H_T to be either 10 or 40 Sv depending on the desired inflection point. For the linear-plateau model, there is no mathematical inflection point, and furthermore the plateau is not a true plateau, but rather an asymptote. Therefore to calculate the α value for this model, the inflection point was chosen to represent the point at which the risk reached 90% of the asymptotic limit of the model. To calculate this, the core aspect of the function guiding the shape of the curve was isolated to be

$$Y = 1 - e^{-\alpha H_T} \tag{5.7}$$

from Eqn 5.5 where Y is a non-physical quantity. As H_T approaches infinity, this function will approach a maximum value of 1. Therefore, the α value necessary to reach 90% of that maximum can be calculated by setting Y equal to 0.9 and solving for α for each respective H_T inflection point (10 or 40 Sv). Previous studies utilizing these models calculated some of the α values empirically [49] [48], and these are shown in Table 5.1 compared against the values used here.

Additionally, for each of these models, the value of the organ specific risk coefficient was slightly adjusted to more closely match the LNT model at low-doses. For each of the models and their respective α values, the organ specific risk coefficient was set such that the model yielded the same risk as the LNT model at a dose point of 1 Sv. As both the linear-exponential and linear-plateau models are inherently curves, with only linear-approximating sections, setting the point of equality at 1 Sv means that as dose either gets higher or lower than 1 Sv there will be some slight deviations. However, in the 0-2.5 Sv range the approximation is close to linear. The calculation for this adjustment to the μ_T coefficient was performed for all models for both these α values and those used by Fontenot et al 2010 [48] to ensure that the new α values resulted in changes consistent with the literature. Overall, the difference between the adjusted risk coefficients using the

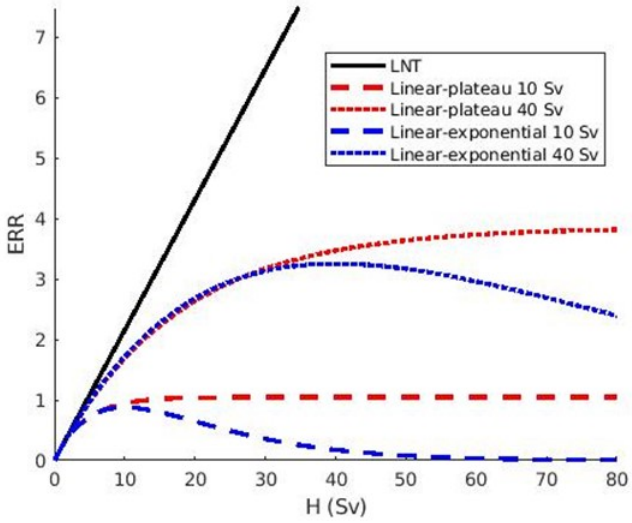

Figure 5.5: The 5 risk models used in this thesis: linear no-threshold (LNT), linear-plateau with an inflection at 10 Sv and at 40 Sv, and linear-exponential with an inflection at 10 Sv and at 40 Sv.

Fontenot α values and the new α values was less than 1% in all models. All risk models used in this thesis are shown in Figure 5.5, using the α and $\mu_{T,\mathrm{ERR}}$ values calculated for the ERR of a generic organ for a patient with an age at exposure of 45 and an attained age of 65.

5.5 Data Analysis

Similarly to the procedure described in Section 4.4, for a given patient representation, each group of 500 simulations was split into 10 batches of 50 simulations each for a total of 50 million particles simulated per batch. As this part of the thesis was focused on risk, total and neutron dose prediction was not directly compared as previously done. Instead, the focus was on the two equivalent dose calculation methods and the five risk models. Equivalent dose was calculated for each of the 10 batches for the three patient representations in the same way described in Section 4.4.1 and then isolated for each organ using the same methodology as in Section 4.4.2. To calculate risk, the average equivalent dose value per organ as well as the 25^{th} and 75^{th} percentiles were used in each of the risk formulas with the corresponding μ_T and α values (described in the previous section) to calculate EAR and ERR for all organs in all patient representations. The risk calculation was completed separately using both KERMA- and fluence- weighted equivalent dose estimates.

For clarity, a case is defined here as an equivalent dose or risk evaluation in a specific organ for a given treatment plan. For example, one case for equivalent dose would be the

KERMA-weighted equivalent dose in the left eye in Patient 3. For risk, an example of a case would be the linear-plateau model with inflection at 40 Sv to predict the EAR in the liver of Patient 4 based on the fluence-weighted equivalent dose calculation.

The better performing phantom for a given organ and patient in this comparison was defined by whichever phantom gave the smallest absolute difference in equivalent dose or risk respectively from the WBCT ground truth. The two phantoms were considered to be equal predictors of equivalent dose or risk for a given organ if the 25^{th} and 75^{th} percentiles of the respective quantity estimate overlapped. Additionally, in the case of one phantom overestimating the ground truth and the other underestimating, the two phantoms were considered equal predictors if the absolute value of the difference of the 25^{th} and 75^{th} percentiles from the ground truth overlapped. For example, if the equivalent dose in the scaled MRCP differed from the WBCT by -4.5 $\pm$ 0.5 mSv, and the hybrid by 4.0 $\pm$ 0.5 mSv, then they would be considered as having equal ability to predict the equivalent dose in that organ.

5.6 Phantom Comparison Using Equivalent Dose

Regardless of whether the KERMA- or fluence-weighted neutron energy scoring was used for equivalent dose calculation, in all considered patients the hybrid provided better than or equal predictions compared to the scaled MRCP for organs designated as in- or near-field. As a reminder, the in- or near- field organs were defined as the brain, the left and right eyes, and the thyroid, and all were entirely contained in the in-field CT segment of the hybrid phantom shared by the WBCT. The essential results are collated in Table 5.2, where in 95% of the in-and-near-field cases the hybrid was better than the scaled MRCP alone out of a total 56 cases (two equivalent dose scorers, four in-and-near-field organs, seven patients). In the remaining 3 (5%) cases, the scaled MRCP performed equivalently to the hybrid. This is consistent with what might be expected considering that by definition the hybrid and WBCT share the in-field anatomy while the scaled MRCP does not.

For the organs outside the treatment field (defined here as the lungs, liver, kidneys, and bladder for all patients) the hybrid provided superior estimates than the scaled MRCP in 48% out of a total 56 cases and equivalent estimates in 34% of cases. In the remaining 18%, the scaled MRCP outperformed the hybrid phantom (Table 5.2). Figure 5.6 shows boxplots of the equivalent doses per organ calculated using the KERMA-weighted neutron energy scorer for a single patient (Pat 1). The top row of boxplots shows that for the in- and near- field organs, the hybrid accurately represents the ground truth WBCT. Outside

Table 5.2: Fraction of organs by phantom which gave the best equivalent dose prediction. In/near-field: brain, left and right eyes, thyroid. Out-of-field: lungs, liver, kidneys, bladder.

Organ Location	Hybrid	Scaled MRCP	Equivalent Performance
In-and Near-Field	0.95	0.00	0.05
Out-of-Field	0.48	0.18	0.34

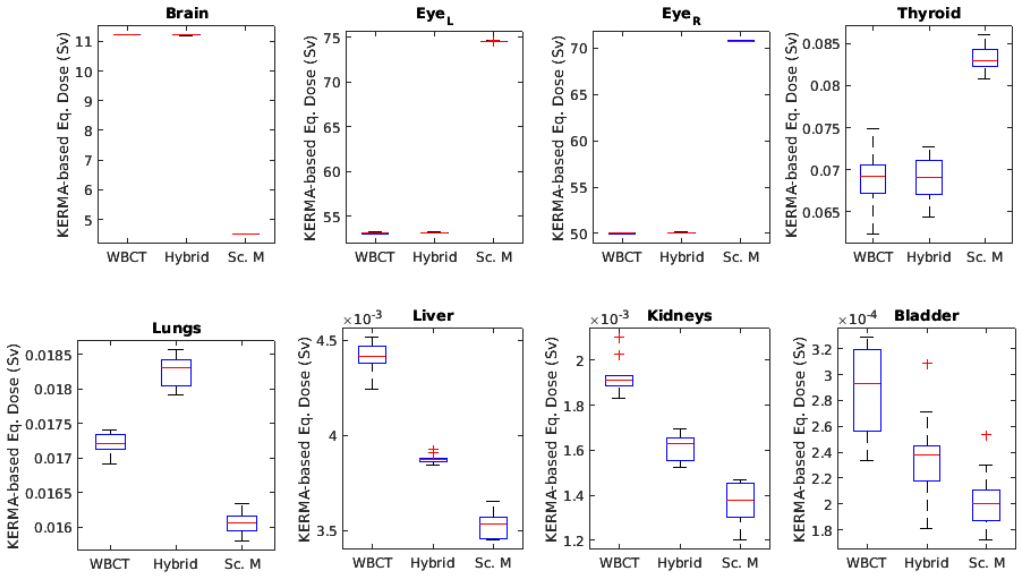

Figure 5.6: Boxplots of the KERMA-weighted equivalent dose in Sv for the in- and near-field (brain, left eye, right eye, thyroid) and out-of-field (lungs, liver, kidneys, bladder) organs from the Pat 1 treatment plan for the three patient representations (WBCT, hybrid, and scaled MRCP). The central mark is the median, the box edges are the 25th and 75th percentiles, the crosses are outliers (defined as points that are more than 1.5 times the interquartile range away from the 25th and 75th quartiles), and the whiskers extend to the extreme data points not including outliers.

of the treatment field, in the transition and mesh regions of the hybrid phantom, typically the hybrid still exhibits an improvement over the scaled MRCP, but may differ from the ground truth WBCT value. For boxplots of the equivalent dose using the fluence-weighted scorer, and for the other patients, see Appendix C Figures C.1-C.14. For the full set of quantitative equivalent dose values, see Appendix D Tables D.1-D.7.

In addition to the number of cases in each rank, it is also insightful to look at the average deviation from the WBCT for each rank category. For equivalent dose, this information is given in Table 5.3. The average absolute value of the percent difference for hybrid cases in the in-field which are superior to the scaled MRCP (where the hybrid shares the CT anatomy of the WBCT) is 0.18%. The scaled MRCP had no superior cases in the in-field and an average percent difference of 30.6%. In the out-of-field, the hybrid has similar average percent differences for cases which are both inferior and superior to the scaled MRCP (9.3-13.5% respectively). This contrasts sharply with the out-of-field scaled MRCP cases, where the average percent difference varied across superior and inferior cases from 2.4% to 25.5%. Given that range in the scaled MRCP, when the scaled MRCP is superior in the out-of-field, it has a much lower average percent difference (2.4%) than the hybrid

Table 5.3: Equivalent dose prediction average percent difference from WBCT of organs falling under the superior/inferior performance category for both phantoms. In/near-field: brain, left and right eyes, thyroid. Out-of-field: lungs, liver, kidneys, bladder.

Organ Location	Hybrid		Scaled MRCP	
	Superior	Inferior	Superior	Inferior
In-and Near-Field	0.18	N/A	N/A	30.62
Out-of-Field	13.53	9.34	2.42	25.50

does when it is the superior case (13.5%).

When the hybrid provides a superior out-of-field prediction, on average it improves on the percent difference by approximately a 12% over the scaled MRCP. Conversely, in cases where the scaled MRCP outperforms the hybrid, not only is the difference between the two phantoms reduced to an average of about 7%, but also in the overall average percent difference for both phantoms is lower.

5.7 Phantom Comparison Using Risk

For each patient, the ERR and EAR was calculated for the five selected risk models and for both the fluence- and KERMA-weighted neutron energy scorer. This resulted in 20 estimates of risk (10 each for ERR and EAR) for a given organ in a given patient representation (WBCT, hybrid, scaled MRCP) for each treatment plan. Overall, across all in-field organ risk estimates (brain, left and right eyes, and thyroid), the hybrid outperformed the scaled MRCP in 96% of cases and performed equally to scaled MRCP in 4% out of 560 total cases. Across the out-of-field organs (lungs, liver, kidneys, and bladder) the hybrid outperformed the scaled MRCP in 51.8% of cases, performed equivalently in 28.6% of cases, and performed worse than the scaled MRCP in 19.6% of cases, also out of 560 total cases (Table 5.4). For the full set of quantitative secondary cancer risk estimates, see Appendix D Tables D.8-D.42.

Figure 5.7 shows the EAR per ten thousand person years (10k PY) predicted for all organs and all patients, using the KERMA-weighted neutron energy scorer for each of the 5 risk models. As all of the models share the linear model in low dose regions, it was possible to observe the cases where choice of phantom had a higher impact than choice of risk model. It is also possible from this figure to see not only which phantom best predicted the ground truth for each EAR case, but also the magnitude of the difference with respect

Table 5.4: Fraction of organs by phantom which gave the best risk prediction. In/near-field: brain, left and right eyes, thyroid. Out-of-field: lungs, liver, kidneys, bladder.

Organ Location	Hybrid	Scaled MRCP	Equivalent Performance
In-and Near-Field	0.96	0.00	0.04
Out-of-Field	0.52	0.19	0.29

to the WBCT and to each other.

Analogously to the equivalent dose analysis, the average absolute value deviation from the WBCT for each risk prediction rank category in both the hybrid and scaled MRCP cases provides some additional insight. These values for the risk are given in Table 5.5. While the numbers are slightly different, overall a similar pattern emerged as in the equivalent dose. In the in-field organs, the cases where the hybrid was superior had an average percent difference from the ground truth of 0.25%, and there were no inferior in-field hybrid cases. Out-of-field, the average percent difference between the superior and inferior hybrid cases ranged from 9.3-12.6%, while the same quantity for the scaled MRCP cases ranged from 3.2-25.9%. For an out-of-field case where the hybrid gave the superior estimate, the difference between the hybrid and the scaled MRCP was 13.3%. Correspondingly, when the scaled MRCP gave the superior case, the average difference from the hybrid was 6.1%.

5.7.1 Impact of Model Choice on Risk Prediction

The five different risk models frequently had a significant impact on the magnitude of the risk prediction in organs receiving >1 Sv. However, the relative performance of the hybrid compared to the scaled MRCP was completely unaffected by choice of risk model. For a given organ subjected to a given treatment plan, if the hybrid outperformed the scaled MRCP using one risk model, it subsequently outperformed the scaled MRCP using every other risk model for both EAR and ERR.

Figure 5.8 shows the EAR for all patients for each of the five risk models. The organs receiving the highest dose have the greatest difference between the risk models. For organs receiving less than 2.5 Sv, where the linear-plateau and linear-exponential models are designed to match the LNT model, the difference in predicted risk between the models is minimal. Despite being matched to the LNT in the low dose-region, it is still possible to have some small deviations outside of the calibration point (1 Sv). This is because the non-LNT models are inherently non-linear, and the point of approximate linearity is matched at the 1 Sv equivalent dose point. In regions receiving close to zero dose, the models are going to deviate more than at the point of alignment. From this figure, across all risk models, the scaled MRCP most visibly deviates from the hybrid and WBCT in tissues receiving between 0.1 and 11 Sv. This dose level is more likely to correspond to tissues in or near the treatment field and may include some organs which are entirely

Table 5.5: Risk prediction average percent difference from WBCT of organs falling under the superior/inferior performance category for both phantoms. In/near-field: brain, left and right eyes, thyroid. Out-of-field: lungs, liver, kidneys, bladder.

Organ Location	Hybrid		Scaled MRCP	
	Superior	Inferior	Superior	Inferior
In-and Near-Field	0.25	N/A	N/A	28.24
Out-of-Field	12.56	9.29	3.15	25.92

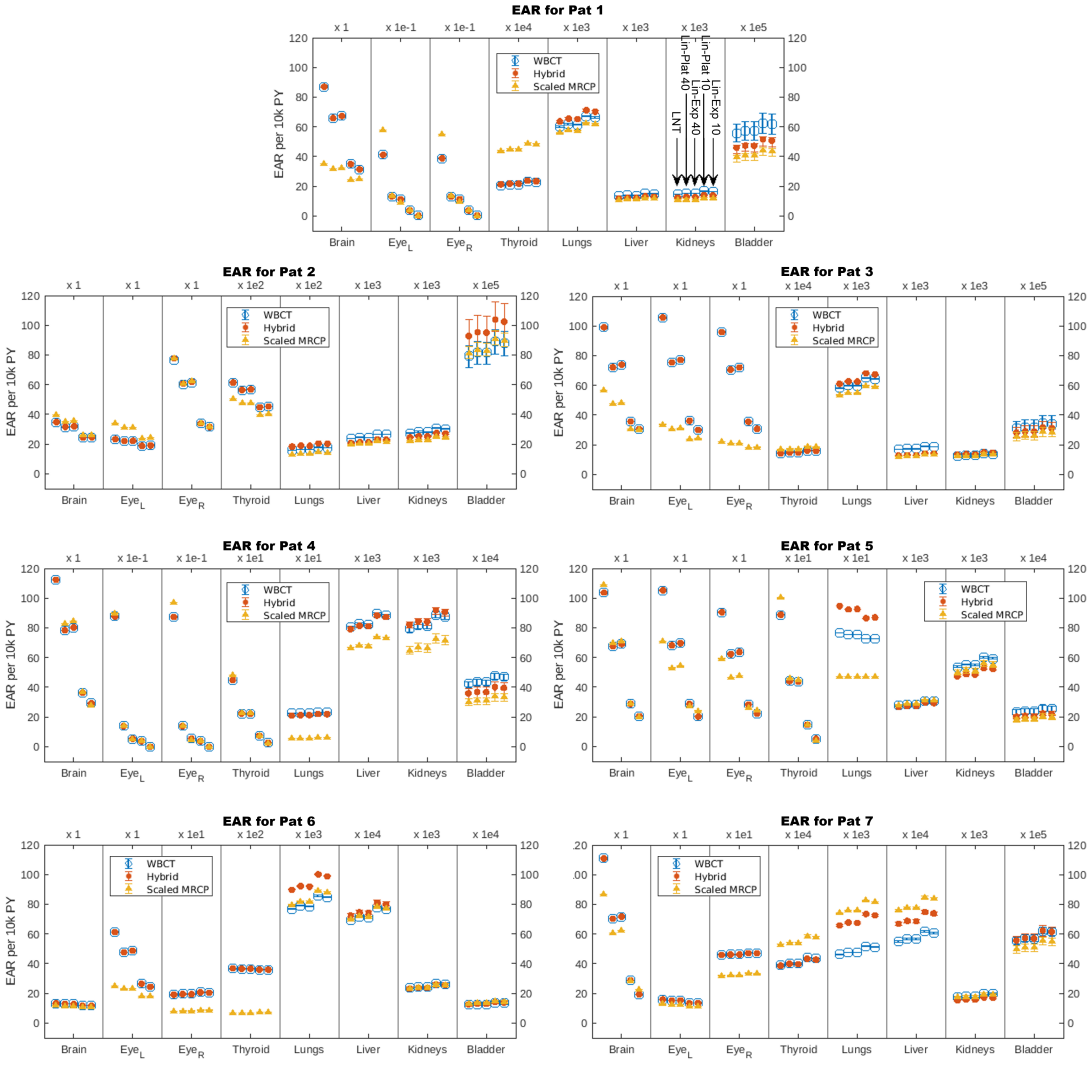

Figure 5.7: A comparison of the EAR predictions using the KERMA-weighted neutron energy scorer for equivalent dose for the 5 risk models across all 7 patients, all 8 selected organs, and all 3 patient representations. Each column corresponds to a particular organ where the WBCT, hybrid, and scaled MRCP are represented by a blue open circle, a red filled circle, and a yellow filled triangle respectively. Within a particular column, there are five points from left to right corresponding to each risk model. From left to right: linear no-threshold (LNT), linear-plateau with inflection at 40 Sv, linear-exponential with inflection at 40 Sv, linear-plateau with inflection at 10 Sv, and linear-exponential with inflection at 10 Sv. For visibility, the predicted risk and error for all models was multiplied by the specified power of 10 at the top of each of their respective columns. Error bars representing the 25th and 75th percentile are given for every measurement, but are only visible in some very far out-of-field organs.

contained in the in-field CT, such as the brain. This region also corresponds to the part of the hybrid phantom which most heavily utilizes patient-specific anatomy (both the CT and the patient-specific transition region).

5.7.2 Impact of Neutron Energy Weighting on Risk Prediction

The choice of KERMA- or fluence-weighted neutron energy scoring for equivalent dose calculation did not greatly impact the magnitude of predicted risk in any of the patient representations. Overall, using the KERMA-weighted scorer resulted in slightly higher absolute risk predictions compared to those using the fluence-weighted scorer. However, relative performance of the hybrid and scaled MRCP was not often affected. Across all the in-field organs (brain, left eye and right eyes, and thyroid), the choice of scorer did not impact relative hybrid performance at all. That is, for in-field organs, if the hybrid provided a superior prediction of risk compared to the scaled MRCP using the KERMA-weighted scorer, then it likewise provided a superior prediction when using the fluence-weighted scorer.

However, outside of the treatment field, there were a few cases where changing the scorer also changed which phantom provided the closest estimate of risk relative to the ground truth WBCT. These changes were consistent for a given organ across ERR and EAR calculations and across all implemented risk models. For the 4 out-of-field organs (lungs, liver, kidneys, and bladder) across 7 patients, when switching from the fluence-weighted scorer to the KERMA-weighted scorer, in 64% of cases the switch did not impact relative performance. In 25% of cases, changing from the fluence-weighted scorer to the KERMA-weighted scorer resulted in the hybrid improving its relative rank prediction over compared to the scaled MRCP. In the remaining 11% of cases, this change resulted in the hybrids relative rank worsening compared to the scaled MRCP.

Although in general the KERMA-weighted scorer yielded higher estimates of risk, quantitatively the difference between the two scorers is quite small in the out-of-field. For example, in the out-of-field organs the largest quantitative difference between the two scorers was observed in the lungs of the Pat 5 scaled MRCP using the LNT model, where the choice in scorer resulted in a change in the EAR of from 4.53 to 4.68 per 10k PY and a change in the ERR from 1.10 to 1.14 for the fluence and KERMA-weighted scorers respectively. In other out-of-field organs for all other patients, the difference in ERR was typically <0.01 and the difference in EAR per 10K PY was typically <0.04 between scorers.

The deviation in risk estimation caused by the different scorers was less than the inherent uncertainty in the different risk models for most cases. The precise relationship between the relative uncertainties depends on the dose to the organ (factor impacting variance based on risk model) and the distance from the field (factor impacting variance based on scorer type). For organs inside the field or receiving more than $\sim$0.1 Sv, the risk model uncertainty was greater than the uncertainty introduced from the different scorer types. Similarly, for organs very far from the treatment field (typically receiving <2 mSv), the risk model uncertainty outweighed the scorer choice uncertainty. Organs in between those two regions (for these plans typically the liver, kidneys, and sometimes lung) the scorer

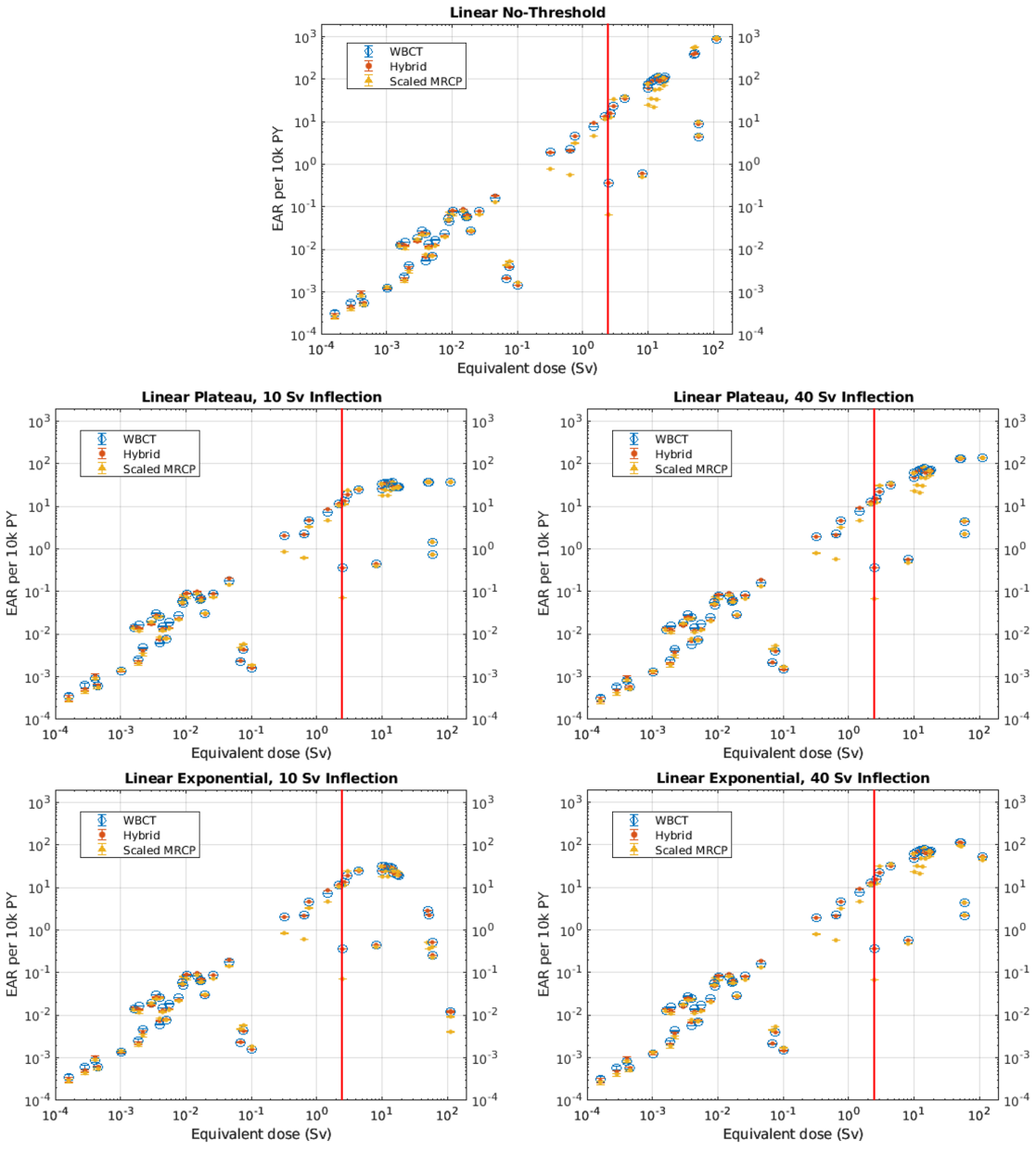

Figure 5.8: The predicted EAR for all organs across all patients. The linear portion of each model is consistent between all models in the low dose region (<2.5 Sv), that region of commonality has been marked by a vertical line in all subfigures for easy reference.

uncertainty was the same or larger than the risk model uncertainty. As an example of this, the EAR of the kidneys in the Pat 4 WBCT using the LNT model was 54.4 per 10k PY using the fluence-weighted scorer and 79.3 for the KERMA-weighted scorer. However for the same organ and patient representation using the linear-plateau model with a 10 Sv inflection point, the EAR was 60.8 per 10k PY using the fluence-weighted scorer and 88.7 for the KERMA-weighted scorer. This means that, for this specific case, changing the risk model resulted in an estimated change of $\sim$8 incidences of secondary cancer per 10k PY while changing the neutron energy scorer resulted in an estimated change of $\sim$26 incidences per 10k PY.

This relationship between the relative uncertainties of the scorer versus the risk model is likely due to a complicated interplay of the dominating factors at different dose levels, dose components, and distance from the field. At high doses (>2.5 Sv) the risk models will have the strongest influence over uncertainty due to different curve shapes after that equivalent dose point. Not only that, but at these levels the proton dose is dominant, and the change in neutron weighting factor from the different scorers is unlikely to affect the risk estimate as much. At lower doses (> 0.1 Sv), the risk model influence is lessened, but in this dose region it is also likely that the dose is similarly dominated by the proton component of dose, so the change in neutron weighting factor has less of an influence. In regions far from the field, where both neutron dose dominates and where the neutron weighting factor differs significantly between the KERMA and fluence weighting, the choice of scorer is the stronger influencing factor. In the furthest extreme ranges from the treatment field, such as the brain in the prostate plan, the neutron weighting factor does not change significantly with KERMA versus fluence weighting (reference Figure 4.6) and the risk model again becomes the strongest influence over uncertainty. Risk model choice can have a significant impact on the uncertainty, even in the 0<2.5 Sv range where the models are supposed to be approximately the LNT model, because the point of confluence was selected to be 1 Sv. Because both the linear-exponential and linear-plateau models are not truly linear in the low dose regions, if dose deviates from 1 Sv, the models' risk prediction will similarly begin to deviate.

Chapter 6

Discussion

In this chapter, the primary results of the thesis will be discussed. This will include the results of the hybrid creation as well as the equivalent dose and risk predictive abilities of the hybrid. Further, these results will be placed in the context of relevant literature with additional evaluation of the strengths, limitations, and future directions.

6.1 Hybrid Creation

A method has been established to create whole-body computational patient representations which include patient-specific images and measurements combined with segments of an adult mesh-type computational phantom. Detailed in Chapter 2 and the work of Kollitz et al 2022 [77], the methodology is flexible with respect to body size, patient sex, and treatment site. As further mesh phantoms are developed, the hybrid process can be refined even further to better fit patients of varied ages, pregnancy status, weight distributions, etc. The hybrid geometry was able to be seamlessly constructed in Geant4 Monte Carlo and did not overly extend the computation time compared to the WBCT. The code required to create a hybrid phantom and the full instructional manual is given in the Git repository hosted by the Ludwig Maximilian University of Munich.

6.1.1 Place in the Literature

The term "hybrid phantom" has been used by other research groups to refer to computational phantoms which use multiple geometry representations in a single phantom. For example, the hybrid phantoms developed at the University of Florida are a composite of NURBS and polygon mesh structures which can then be voxelized for use in MC simulations (Lee et al 2007 [84], Bolch et al 2010 [19], Hurtado et al 2012 [60]). These phantoms can be adjusted to represent varied body types and positions, with patient-specificity as a goal. However, these phantoms are fully reliant on non-patient-specific anatomical representations and they do not integrate patient CT data.

The work of Kuzmin et al 2018 [81] is much more comparable to the work of this

thesis. In this paper, Kuzmin et al describes a method to automatically extend a partial body CT using a computational phantom selected from a library based on patient height and weight. When the CT anatomy was merged into the reference phantom, a boundary registration was used to match the external contour of the phantom to that of the CT. The end result of this process is a whole-body patient-specific conceptually similar to the CT-mesh phantoms described here.

Some important differences between the work of Kuzmin and of this thesis include:

- This thesis uses a tetrahedral mesh instead of NURBS/polygon-mesh in the out-of-field, allowing the hybrids here to be simulated directly without need for voxelization.
- The CT-phantom merge points were selected manually in this thesis and algorithmically in the work of Kuzmin.
- This thesis uses a deformable image registration algorithm to match both internal and external anatomical features in the transition region while Kuzmin uses edge boundary registration.
- This thesis relies on a scaling factor to adjust the MRCP for a single gender to match a variety of patient geometries, while the work of Kuzmin used a library containing computational phantoms corresponding to a variety of patient heights, weights, and body types.

Overall, these papers demonstrate a developing interest in personalized medicine, where more and more patient specific information is used to tailor cancer treatments. This trend is not just for radiation therapy [115] [72] [12], but also in cancer care in general (for example genetic testing for targetable tumor mutations [10]).

6.1.2 Strengths and Limitations

The hybrid creation process is flexible with respect to treatment site and patient sex. Based on the results shown in this thesis and in Kollitz et al 2022 [77] (second publication on risk modelling forthcoming), the hybrid is capable of delivering whole-body dose and secondary cancer risk predictions which can provide improved accuracy compared to a reference phantom alone. Furthermore, while this thesis focused on proton therapy, the hybrid methodology itself could theoretically be used to predict whole-body dose and secondary cancer risk presented in other radiotherapy modalities. The hybrid creation is independent of treatment machine or room geometry, and can easily be placed in any relevant simulation environment given the proper scripting materials. Additionally, the process outlined in this thesis can be adapted for new MRCPs as they are released, or even NURBS/polygon-mesh phantoms given that those segments would need voxelization for use in simulation. The hybrid itself provides the known in-field and a best guess out-of-field in a single simulation geometry. This includes a transition region just outside of the in-field which provides a better approximation of OAR positioning via a blending deformation in the region most likely to receive the highest level of dose outside of the patient CT.

However, in the current version of the methodology, the deformable image registration, despite providing an acceptable level of anatomy matching and blending, can often result in anatomically infeasible geometry. This could potentially affect the dose distribution (especially in the case of bone and lung deformations) and the contouring fidelity in the transition region. Similarly, the current scaling factor is simplistic, and cannot guarantee an anatomical match for all OAR sizes and placements outside of the treatment field. Both of these limitations can lead to inaccuracies in the predicted dose for the affected OARs. Furthermore, the current process to create a hybrid is not fully automated, and relies on a few manual decisions, tasks, and calculations. This is a barrier for potential clinical use due to the time needed to create a hybrid phantom for a given patient. Additional limitations for clinical treatment planning optimization are:

- Treatment planning systems do not allow the import of tetrahedral mesh structures.
- Even if voxelized and imported as a DICOM, the TPS analytical dose calculation models have reduced ability to calculate dose outside of the treatment field as they were not designed for that purpose, necessitating comprehensive whole-body MC simulations.
- Secondary cancer risk as an optimization parameter is not directly implemented in clinical treatment planning.

Despite these limitations, the hybrid methodology will be a useful tool in assessing patient-specific whole-body dose distributions and evaluating treatment planning choices to minimize secondary cancer risk.

6.1.3 Future Directions

Future directions for improving hybrid creation include: automation, future-proofing the code, pediatric mesh phantom integration, and refining the scaling factor and deformable registration. As described in this thesis, the hybrid creation process relies on significant manual input using multiple software tools. To improve this process, some further refinement and automation should be introduced to facilitate efficient creation and reduce human error. For example, the work of Kuzmin et al 2018 developed an algorithm to select the ideal anatomical "merge points" in the reference phantom based on the bony anatomy of the CT in-field. Integrating that kind of automatic algorithm in the hybrid workflow described in this thesis would allow for faster and more consistent definition of the extents of the out-of-field segments and transition regions. Furthermore, the scaling factor calculation might also be partially automated using the calculated merge points of such an algorithm to list the dimensions of the phantom in-field as required for the scaling factor calculations. The other inputs for the scaling factor calculation (in this case, spine height and pelvis width and depth) could potentially be generated from automatic segmentation of the bony anatomy [156], Seim et al 2008 [134].

Currently, the scripts developed to create the hybrid are highly dependent on the formatting of the source files. For example, the voxelization of the mesh phantoms is dependent on the material naming convention of the MRCPs which were granted for use in this thesis. If this convention were to change, or the materials themselves to change, then this script would no longer function and the fix would be difficult to navigate for someone unfamiliar with the code. Similarly, the script to convert the polygon mesh to a tetrahedral mesh is dependent on the text file formatting of the ".obj" files exported by Blender. The script currently functions when using Blender version 7, but it is possible that using other Blender versions would alter the output and break this script. If this kind of error was encountered by a new user, the error source would not be readily apparent and would require in-depth knowledge of how 3-D mesh data is encoded in text files. Future development could include steps to future-proof these scripts. Not only by making them more flexible, but also by adding a series of detailed error catches to help direct the user to the point of the script which might trigger these errors. This is particularly relevant due to the introduction of pediatric MRCPs [30]. As pediatric cases are of the most interest specifically with proton therapy and secondary cancer, it would be beneficial to pro-actively ensure that the hybrid methodology is compatible with these MRCPs. Theoretically there is no reason that the workflow would not work for pediatric patients, however technically there may be barriers to implementing the same tools to create pediatric phantoms.

Finally, the hybrid creation process would benefit from a refinement of the scaling factor and the deformable image registration used to create the transition region. The current scaling factor uses the height dimension of the spine and the width and depth of the pelvis to scale the whole body of the MRCP. This can lead to misalignment of organs which do not necessarily have the same relative size and positioning relative to the bony anatomy between the MRCP and the ground truth patient anatomy (known in the case of the WBCT, unknown in a clinical case). However if the scaling factor could be refined to include measurements at multiple points throughout the torso, or to integrate surface scanning data in its calculation, then it might be possible to reduce misalignment of the out-of-field OARs. Similarly, if the deformable image registration used to create the transition region could be improved, then it is less likely for biologically infeasible discontinuities to be present in organs at the border of the CT in-field and the transition region. Particularly in the lung and bony anatomy, these discontinuities could potentially disturb the dose distribution and reduce the accuracy of the hybrid prediction for organs which have at least some volume contained within the transition region.

6.2 Hybrid Predictive Ability

6.2.1 Dose and Equivalent Dose

Chapter 4 investigated the hybrid's ability to predict both dose and equivalent dose while Chapter 5 dealt with equivalent dose and secondary cancer risk. As the equivalent dose results of Chapter 5 were meant to reproduce and expand on those of Chapter 4, they have

been included in this subsection as well.

Dose and Equivalent Dose: Chapter 4

This section specifically discusses the dose and equivalent dose predictive ability in the context of the work of Kollitz et al 2022 [77] and described in Chapter 4.

In both pelvis and head and neck treatment sites, for all tested in-field organs for all scorers, the hybrid outperformed the generic mesh phantoms, both scaled and unscaled. This could be anticipated since for the in-field region the WBCT and the hybrid contain identical CT images. Organs partially in the treatment field or outside the radiation field but still within the designated in-field CT region also typically showed an advantage in the hybrid over the MRCPs. The only exception was the neutron dose in the colon in the male prostate treatment plan, which gave a slight 6% / 0.17 mGy advantage to the scaled MRCP over the hybrid, and the KERMA-weighted equivalent dose in the same organ in the same treatment site which was within uncertainties of the best performing phantom. This is likely due to the colon being very large where the in-field only contained a small part of the organ. Therefore it is possible that the in-field portion of the colon is more closely matched by the hybrid, but that when considering the whole organ the dose estimate from the scaled MRCP happens to be slightly closer to the WBCT ground truth. For example, both the hybrid and the scaled MRCP overestimated dose to the colon, so it could be the case that the colon mesh shared in the out-of-field by both phantoms has less volume stretching superiorly from the in-field and so naturally the average dose is more than the WBCT as the organ is overall closer to the treatment field. However, in the in-field, there might be a larger volume of organ in the WBCT than in the scaled MRCP, so when the in-field is spliced into the hybrid, there is an increase to dose in the organ and therefore relatively higher overestimation of dose than the scaled MRCP.

Far outside of the treatment field, the largest factor in whether a given phantom predicted the same value as the WBCT was the distance of that organ from the treatment field. However, matching the organ distance of the WBCT cannot be guaranteed in the hybrid for every organ, since there are inherent relative anatomical differences between the mesh reference phantoms and an individual patient and the scaling factor is a linear adjustment in each dimension. Since the vertical scaling factor is calibrated to spine height, for both pelvic and head and neck treatment sites, the hybrid performed better than or equal to all other phantoms for the tested organs at the most extreme points of the anatomy (bladder for head and neck fields and brain for pelvic fields). The only exception was again in the male pelvis treatment site in the brain, where the scaled MRCP outperformed the hybrid by 9% / 1.2 μGy.

In individual treatment sites, there was some observed fluctuation between the relative performance of the hybrid, scaled MRCP, and unscaled MRCP outside the treatment field. However, there was only one scorer in one organ in one treatment site where the hybrid was the worst performing of the three phantoms (neutron dose scorer in the liver in the male pelvic treatment plan). Even in this case, the ground truth dose estimate was 371-373 μGy including uncertainties and the difference in dose estimates between the worst and

best performing phantom was 36-40 μGy including uncertainties.

In most cases the hybrid is an improvement over using a generic or even a scaled reference phantom, but no given organ is a guaranteed improvement due to the inherent anatomical differences. This fluctuation in hybrid performance was most frequently observed in organs which are far outside the treatment field, but still part of the central torso. For example, in the female head and neck treatment, after scaling down the MRCP, the scaled MRCP and hybrid have a heart placement which is overall closer to the treatment field than in the CT. This results in a higher dose to the heart than in the CT. However, in the unscaled MRCP, while the heart has the same shape and relative anatomical positioning as the hybrid and scaled MRCP, the heart is farther away from the treatment field than in the hybrid or scaled MRCP. This results in a lower average dose to the organ which happens to align with the expected WBCT value. This is an inherent limitation of the simplistic scaling factor and of attempting to create a facsimile of the patients out-of-field without having knowledge of the unimaged organs positioning. Without knowing this, there is no reasonable way to predict which organs the hybrid will misrepresent. That said, if this region is known, then it would be better served by being directly included as part of the known in-field, rather than being mimicked by a mesh phantom. The hybrid serves its purpose precisely because this information is absent.

Overall, in the out-of-field the scaled MRCP and the hybrid were both more likely to provide the closest approximation of the patient WBCT ground truth than the unscaled MRCP. Although some individual organs may be better predicted by one over the other, in most cases the difference between them was small, and typically in the favor of the hybrid. Even in the cases of the most extreme percentile differences between the hybrid and the WBCT in the out-of-field, the absolute difference in the simulated organ dose was quite small. For example a 47.5% difference from the ground truth in total dose in the lungs in the female head and neck was a 0.49 mGy absolute difference, and a 44.4% difference in neutron dose in the liver in the female pelvis was a 0.95 mGy absolute difference.

Equivalent Dose: Chapter 5

This section discusses the equivalent dose predictive ability in the context of the work described in Chapter 5. This short section serves primarily to reproduce and expand on the results of Kollitz et al 2022 [77] (which used two WBCTs and four total hybrids) with respect to the hybrids ability to predict equivalent dose to organs throughout the whole body. Remember for this section of the thesis the default MRCP was omitted so the only geometries were the WBCT, hybrid, and scaled MRCP. In this part of the thesis, the equivalent dose results reflected the same pattern found in Kollitz et al and described in Section 6.2.1. The hybrid yielded as good as or better predictions of equivalent dose for all in-field organs across all patients. The selected out-of-field organs were most frequently best predicted by the hybrid (48% of all out-of-field organs), closely followed by equivalently predicted by both (34%). The least probable, though still likely, result was that the out-of-field organ was best predicted by the scaled MRCP, which occurred in 18% of the studied cases.

In addition to this, in the out-of-field region the hybrid exhibited a more consistent average percent difference from the WBCT compared to the scaled MRCP. Whether a hybrid case was superior or inferior to the scaled MRCP, the average percent difference did not differ much (∼13% for superior cases and ∼9% for inferior ones). For the scaled MRCP, however, the superior cases had an average difference of ∼3% while the inferior cases had an average difference of ∼26%. This indicates that the scaled MRCP has a much higher variance in predictive ability. Furthermore, when the hybrid is superior to the scaled MRCP, the gain in percent accuracy is on average approximately twice as high as when the scaled MRCP is superior to the hybrid.

6.2.2 Secondary Cancer Risk

The results described in Chapter 5 Section 5.7 represent the first steps into exploring the applications of a patient-specific hybrid CT-mesh computational phantom in risk prediction. When expanding to the secondary cancer risk from the equivalent dose, a similar pattern emerged, but with a slightly stronger preference for the hybrid phantom in out-of-field organs. As with equivalent dose, the secondary cancer risk to the in-field organs was predicted by the hybrid as well as or better than the scaled MRCP in all cases. In the out-of-field cases, following the pattern of the equivalent dose predictions, the hybrid yielded a superior prediction of risk compared to the scaled MRCP in most out-of-field organs (51.8%) and an equivalent prediction in a little over a quarter of the cases (28.6%). The scaled MRCP was again the least likely to yield the closest prediction of risk at 19.6% of cases. Additionally, the risk prediction followed the same pattern as equivalent dose with respect to the average percent difference of the hybrid or scaled MRCP from the WBCT (detailed in Section 6.2.1 under the "Discussion of Chapter 5").

One small thing to note is that there are some cases where the scaled MRCP and hybrid appear to give equally good predictions for some organs in the in-field receiving higher levels of dose (for example the brain in Pat 6). This could potentially be caused by a few things such as: 1) a small absolute difference in equivalent dose or risk which, despite being statistically separate, is difficult to visualize on a log-log scale or even a linear scale covering a large range of values or 2) regions where organs receive close to prescription levels of dose might be at least partially contained in the PTV contours (planned to receive high and uniform dose), leading to a more even distribution and similar predictions of dose at prescription levels despite the different anatomies and perturbed dose distribution between the MRCP and hybrid.

The hybrid phantom is able to retain the integrity of the in-field while providing an improvement over a scaled MRCP alone for whole-body equivalent dose and secondary cancer risk prediction. Furthermore, the hybrids ability to predict risk compared to the scaled MRCP was not impacted by the choice of risk model or type of risk. Therefore, despite the inherent uncertainties in calculating the absolute quantity of risk, the hybrid could be a useful tool for comparative ERR/EAR prediction when using any of the 5 models investigated.

The one factor that did change how the hybrid predicted risk relative to the scaled

MRCP was the choice of neutron energy scorer. The scorer choice only changed relative rank of hybrid versus scaled MRCP in out-of-field organs, and even in that region the majority of the organ risks maintained their relative accuracy across both phantoms. However, when changing the scorer did effect the relative predictive performance (i.e. if hybrid was superior or vice versa), the most common change was the KERMA-weighted scorer favoring the hybrid phantom compared to the fluence-weighted scorer.

Both of the neutron energy scorers were designed to replicate as best as possible the conditions given by the ICRP 92 [62] such that the use of the energy-dependent neutron weighting factor model would be valid. However, due to the nature of the ICRP conditions (a mono-energetic field of neutrons impacting a target), an exact replication of these conditions for internally generated neutrons is impossible. The scorers as they stand represent a balance between the granularity of detail that is possible to access with Monte Carlo simulations and the generality of the neutron weighting factor model which accounts for probabilistic interactions while unable to know specifics.

Despite the hybrid clearly showing an advantage in risk prediction over the scaled MRCP based on percent difference from the WBCT (especially in the in-field by construction), it is still necessary to discuss the absolute advantage and whether that warrants the effort of constructing a hybrid phantom. Because the absolute risk predictions in this thesis are incomplete due to a lack of machine and room geometry in the simulation (besides range shifters when required by the treatment plan), only the difference in predicted risk in terms of the internally generated neutrons will be discussed.

Most organs designated as outside the treatment field (lungs, liver, kidneys, and bladder) received less than 1 Sv of equivalent dose. The only exception was the lungs in Pat 5, which received 1.46 or 1.48 Sv using the fluence-weighted and KERMA-weighted scorer respectively in the ground truth WBCT (1.81 and 1.83 Sv in the hybrid and <1 Sv for both in the scaled MRCP). These organs all fall under the LNT-matching portion of the investigated risk models, and therefore the absolute quantity of predicted risk for both ERR and EAR was relatively consistent across all the tested models. These are also the organs which yielded the lowest risk of secondary cancer according to those models. While the hybrid did most frequently provide a superior risk prediction over the scaled MRCP in this region, the risk predicted was quite small, on the scale of 10^{-2} EAR per 10k PY or 10^{-4} ERR for the kidneys and liver and 10^{-4} EAR per 10k PY or 10^{-5} ERR for the bladder. So while the hybrid might give a 15% improvement over the scaled MRCP (as it did for the EAR in the kidneys of Pat 4), that resulted in a difference between the hybrid and scaled MRCP of 0.0172 EAR per 10k PY. It is reasonable to ask whether unaccounted for uncertainties might overtake any observed superiority of the hybrid, or whether this level of EAR is of interest when considering treatment planning optimization.

To address the first question, the hybrid phantom and the scaled MRCP are intrinsically similar in the out-of-field since the hybrid out-of-field is made from a segment taken directly from the scaled MRCP. If the only region of interest is contained completely in the mesh part of the hybrid phantom, then the effort needed to create a hybrid will likely mean it would be easier and equivalently useful to use a scaled MRCP alone considering that part of the anatomy would be the same in both. However, the real strength of the

hybrid phantom lies in 1) the preservation of the in-field, 2) the inclusion of the deformed transition region, and 3) the ability to create whole body dose and risk distributions with a single simulation geometry. The preservation of the in-field region means that the dose distribution entering the region beyond the CT is as accurate as possible, in addition to having the deformable registration in the transition region working to match patient anatomy bordering the CT image. Furthermore, it is unlikely that there would be a clinical scenario where simultaneously the far out-of-field risk is of interest and the in and near field risk is not of interest, meaning that it is unlikely to encounter a scenario where the hybrid would not provide any benefit over the scaled MRCP.

To address the second question, the findings from Diallo et al 2009 reported that for their cohort of 115 pediatric patients who underwent radiation therapy (primarily cobalt-60 γ rays, but also including high-energy X-rays, electrons, and others) experiencing a secondary cancer, 27% of all SMNs were in regions receiving <1 Gy, and a full 6% were observed in regions receiving <0.1 Gy [42]. While this is not fully transferable to the results of this thesis due to the use of absorbed dose in Diallo and equivalent dose here, as well as the different treatment modalities and machine and room geometries, the key takeaway message is that tissues outside of the treatment field receiving very low doses are still potential host to a non-negligible number of secondary cancers. In addition to this, some of the most prevalent types of secondary cancer are sarcoma, thyroid, breast, and CNS (Jenkinson et al 2004 [68]; Diallo et al 2009 [42], Berrington de Gonzalez et al 2013 [14]). Of those origin sites, only the thyroid was included in this thesis. The intent was to elucidate the hybrids ability to predict the risk throughout the body, not make any statements on the magnitude or alleviation of risk. The inclusion of other sites in future studies could potentially show significant levels of risk in these sites even when outside of the treatment field.

In summary, the hybrid phantom has demonstrated from the results that it possesses the capability to provide patient-specific estimates of equivalent dose and secondary cancer risk when out-of-field patient anatomy is unknown. The hybrids predictive ability is unhindered by choice of risk type or model. This information can be used to predict secondary cancer risk directly from a given treatment plan or alternatively inform organ dose limits in a patient presenting for re-irradiation. The hybrid gives the most benefit for organs partially contained in the patient CT which are relatively close to the treatment field. Not only does the hybrid have the most impact from an anatomical/geometric perspective over the mesh phantoms alone, but also this is the region most likely to experience a secondary malignancy (Diallo et al 2009 [42]). Furthermore, while the hybrid has less patient specificity in the far-field, it is capable of maintaining the accuracy of the treatment planning CT while also providing a realistic whole-body dose distribution data from a single simulation geometry. This kind of hybrid could potentially be used for designing risk-optimized treatment plans, or reconstructing dose for a patient presenting for re-irradiation.

6.2.3 Place in the Literature

This sections splits the literature context into two: other hybrid computational phantoms and the calculated estimates of stray neutron radiation dose.

Other Hybrid Phantoms

The results of this thesis are most comparable with those of Kuzmin et al 2018 [81], which similarly used patient CT data and reference computational phantoms in their phantoms. Like the results of this thesis, Kuzmin et al found good agreement between the WBCT and the composite phantom within the CT region and variable, though favorable to the phantom, agreement outside the CT region. This shared pattern can be seen specifically when referencing Figure 7 of Kuzmin et al 2018 [81] and the boxplots from this thesis comparing dose quantity estimates across patient representations for multiple organs. One of the main differences between the approach of this thesis and of Kuzmin is the choice of out-of-field representation and the method of blending the in- and out-of-field together (as discussed in Section 6.1.1). It is unlikely that the use of deformable image registration in the transition would in general result in any significant dosimetric impact compared to the boundary registration used by Kuzmin. Deformable image registration could possibly show a benefit over boundary registration in cases where there is a significant dose gradient within an organ located in the transition region, where the internal deformation might serve to more accurately reflect the ground truth organ shape. However, the deformable registration can also result in infeasible transformations and this comparison with boundary registration has yet to be investigated.

Neutron Dose

The neutron equivalent dose calculated from the simulations in this thesis was within what could be expected from a proton scanning system based on the literature (Hälg and Schneider 2020 [55]), although in organs far from the treatment field (>20 cm) the simulations in this thesis typically underestimated the neutron equivalent dose when compared to the results of Hälg and Schneider. For example, in the male head and neck treatment plan, the thyroid at a distance of ∼13.5 cm from the treatment field yielded a neutron equivalent dose of ∼800 μSv/Gy which is within the expected range of about 100-1000 μSv/Gy based on scanning measurements, taken in a combination of water tank, solid water, and polymethyl methacrylate (PMMA) material phantoms, at an angle of 90° from the treatment beam (Hälg and Schneider 2020 [55]). At a much greater distance of ∼72 cm, the bladder in the same treatment plan yielded a neutron equivalent dose of ∼0.8 μSv/Gy, when according to Hälg and Schneider at this distance the neutron equivalent dose is expected to be slightly less than 10 μSv/Gy. However, there are some conditions which influence the comparison with the work of Hälg and Schneider. For example, since this thesis utilized clinically reasonable treatment plans, there were multiple beams at varied angles, which reduces the viability of a comparison with measurements taken at precise angles with respect to a single field.

For the purposes of this work, it was considered sufficient to neglect the influence of the machine and treatment room because 1) the treatment plan utilized a pencil beam scanning system so the neutron dose from leakage/scattering would not be as large as in a passive scattering system (Hälg and Schneider 2020 [55]) and 2) evaluating the relative performance between the WBCT, the hybrid, and the mesh phantoms was of greatest importance.

6.2.4 Strengths and Limitations

One of the biggest limitations with respect to getting absolute dose and equivalent dose predictions is the lack of geometry for a treatment machine and vault in the simulations. The only simulated geometry present was the patient representation itself, with pencil beam sources representing the beam exiting the delivery machine. Although this is not as significant for active proton beam scanning, it still represents missing components of the out-of-field dose. Additionally, as mentioned in Section 3.5.2, some aspects of the true beam geometry (for example intra-field angle differences due to the scanning process and the true distance from source to patient and therefore spot size) were sacrificed due to technical limitations and a lack of available information about the machine from RayStation. Furthermore, although range shifters were used in the simulations, ideally they would be placed much closer to the patient to match the TPS. Not only should the issue with translation be fixed, but also the restriction on range shifter placement to avoid intersections with other range shifters or interference with nearby proton beams. In the future, for simulations which require absolute and not comparative dose predictions, these beam properties and geometry construction issues should be addressed. However, these limitations are not so burdensome to the hybrid performance evaluation as all dose and equivalent estimates are only used relative to the WBCT ground truth. Any error in these estimates stemming from the lack of environmental geometry would be systematic and impact all patient representations more or less equally.

Another limitation is the source WBCTs. The selection provided by the LMU Hospital were all of the similar body types, and the male WBCTs were additionally similar in height. This in turn limited the conclusions which can be drawn regarding the effectiveness of the scaling factor and deformable image registration. That said, the female WBCT was quite small, and the use of a more extreme scaling factor did not appear to impact the simulation results for either of the female treatment sites. While the scaling factor did not seem to lose its efficacy in the case of the much smaller female patient used in both Chapters 4 and 5, it is still limited by its relative simplicity. This was mentioned previously in Section 6.1.3 discussing the future directions of hybrid creation. The results of Section 4.4.5 confirm that the misalignment of the OARs outside of the treatment field is likely due in a large part to the inability of the scaling factor to correctly re-position all OARs in the MRCP to match those of the WBCT.

The pelvis and head and neck treatment sites investigated during this thesis are on opposite ends of the anatomical region containing radio-sensitive organs of interest. By including both of these sites in both a male and female patient, conclusions could be drawn

about organs placed at the farthest possible distance from each site's in-field. Another strength is the use of multiple equivalent dose calculation methods. Estimating the neutron dose in a voxel is dependent on the choices made to approximate the conditions of the ICRP 92 [62]. By including multiple calculation methods (weighting by fluence and KERMA), the impact of these choices both on hybrid performance and absolute equivalent dose estimates could be examined.

One of the strengths with respect to the risk prediction was the inclusion of multiple factors which could influence the hybrid's ability to predict secondary cancer risk throughout the whole body. Not only were the two equivalent dose calculations methods used, but also 5 risk models using two equivalent dose inflection points. The consistency of the hybrid performance across these factors strengthens the conclusions of this work. Additionally, although not systematically tested by using all seven treatment plans on each of the seven patients, the use of varied head and neck treatment plans for different patient anatomies also introduced potential variance which, given the hybrid's consistent performance pattern, also helps contribute to the strength of these conclusions.

Finally, another factor to consider is the computational time necessary to use Monte Carlo simulations with the hybrid phantom. From the simulations used in this work, a single job of 1 million particles could take between 3 and 26 hours, depending on the treatment plan complexity, inter-patient geometry differences (i.e. between different patients, not between a given patient's WBCT and corresponding phantoms), availability of computing cores, and inclusion of range shifters. While this would be prohibitively lengthy in a clinical setting, it should be noted the patient representation type for a given patient (WBCT, hybrid, MRCP, etc.) did not have a large impact on the simulation time compared to the variance between patient cases. For example, in a site taking 3 hours to simulate there might be a difference of $\sim$30 minutes between geometry types, in a site taking 26 hours it might be a difference of $\sim$3 hours. So, the same temporal obstacles would be in place even if a full patient whole-body CT was available and therefore is not an inherent limitation of the hybrid phantom. Another hurdle in computation is the requirement of a large number of particles to achieve better statistics far from the treatment field. Again, this is independent of the hybrid phantom, but remains a challenge when discussing whole-body Monte Carlo simulations.

6.2.5 Future Directions

The initial results from the hybrid phantoms developed in this thesis are promising, however there are many further improvements and directions which should be investigated.

Directions in Dose/Risk Computation

There are quite a few things to consider in future studies. The first is the construction of a treatment machine and room in the simulation geometry to address the limitation mentioned in the previous section. Particularly in the case of passive scattering plans, a significant component of stray radiation is produced inside the treatment head (Newhauser

and Durante 2011 [102]). Even for active scanning, the work of Englbrecht et al 2021 [45] showed that there were some significant contributions to the neutron field from the gantry components and room structure in the 0.1-10 MeV energy range, coinciding with the peak of the ICRP 92 neutron weighting factor [62]. Without this contribution, any estimate of risk cannot be accurate for a clinical scenario. For this thesis it was considered sufficient to only have the patient geometry constructed because 1) the absolute risk was of less importance in evaluating hybrid performance than relative accuracy and 2) only active scanning plans were simulated, and internally generated neutrons are the primary contributor to stray neutron dose in active scanning systems (Hälg and Schneider 2020 [55]). If clinically relevant estimates of secondary cancer risk are needed, especially considering the potential impact from the findings of Englbrecht et al 2021 [45], this geometry must be included.

A further consideration is that this thesis used Monte Carlo simulations extensively, which increases the accuracy of the results, but at the cost of computational time. Some potential solutions include using the hybrid in combination with analytical models, such as those examined in the review article by Newhauser et al 2018 [105] (primarily photon and passive scattered proton models). These types of models could be used such that the benefit of patient-specific anatomy is maintained without the computational burden of a full Monte Carlo simulation. Furthermore, some recent software developments for GPU accelerated Monte Carlo simulations might make these kinds of whole-body simulations more feasible for treatment plan optimization and build on the MC capabilities already available in a clinical environment (Qin et al 2017 [118]; Qin et al 2018 [119]; Adam et al 2020 [6]).

For some applications it might be beneficial to consider using the voxelized scaled MRCP in the out-of-field rather than the mesh structure, as the results indicate that the small change in anatomy due to the voxelization is not significant outside the treatment field. This would enable simpler simulation environments, more efficient hybrid creation, and importation into treatment planning systems. However, the mesh should be used when high anatomical fidelity is needed, or when dosimetric data is necessary for structures too fine to voxelize (such as layers of the skin or digestive tract lining).

New Hybrid Types

While only the original male and female adult MRCPs were used for this thesis, more mesh phantoms are in development, including pediatric phantoms (Choi et al 2021 [30]) and adult phantoms with varied body types (Choi et al 2020 [31]). The hybrid phantom methodology developed in this thesis will be compatible to any of these new mesh phantoms with only a few technical adjustments, which allows the use of both MRCP selection to match patient body type and the custom scaling factor to further refine the reference phantom to match patient anatomy. As pediatric cases are a high priority for secondary cancer prevention, the hybrid phantom methodology and dose predictive ability could provide important information to better guide pediatric treatment planning decisions.

Other next steps include creating hybrids from a larger sample of source WBCTs to

further verify the advantage of the hybrid in different patient anatomies, particularly for patients of higher body mass index (BMI). Using an MRCP which is significantly different from the patient body type could impact the efficacy of the scaling factor and the deformable image registration used for the transition region. Even if the scaling factor developments mentioned in Section 6.1.3 were implemented, this wouldn't necessarily be as effective on a patient body type that was very different from an MRCP. The outer dimensions might be matched, but the internal distribution of fat and organs would not correspond to exterior physical measurements and therefore would be improperly adjusted.

Directions for Analysis and Application

Other developments to consider could be full DVH-based volumetric risk calculations, especially for organs in the transition region that are closer to the treatment field, for use in risk-optimized treatment planning. Furthermore, future studies could include not just ERR or EAR, but also lifetime attributable risk (LAR). Furthermore, some retrospective analysis could be performed where available clinical dose delivery data is compared against results obtained using hybrid phantoms. While this would be helpful to evaluate the hybrid using CTs which have real tumor volumes and the corresponding clinical plans, it would be difficult to execute without the patient dimensions needed to properly calculate the scaling factor, and its possible that even the height and weight would not be available. In addition to that, it would be difficult to establish a ground truth with which to compare the out-of-field dose. In the future, perhaps some studies could be designed where some basic patient measurements are taken prior to treatment and in-vivo dosimeters at pre-specified points outside the treatment field are used for ground truth dosimetry.

Additionally, frequent sites of secondary cancer such as sarcomas, breast, CNS, or other OARs could be added to the risk calculations on a treatment site specific basis. Similarly, treatment plans targeting primary cancer sites where secondary cancer is of particular concern could be investigated using the hybrid phantom methodology. For a given treatment site where there is some freedom in beam angle selection and other planning parameters, and where the risk of secondary cancer is not insignificant, the impact of these planning choices on risk should be investigated. Ultimately the goal is to effectively use the hybrid to create risk-optimized treatment plans to minimize secondary cancer risk while maintaining clinical objectives. Some work in this area has already been done, as in the work of Wilson and Newhauser 2021 [162], but with the use of the hybrid this concept can be extended to consider the whole-body.

Other future directions in hybrid phantom applications for dose prediction could include dose reconstruction in patients presenting for re-irradiation. Particularly in the case of the re-irradiation being delivered outside of the original treatment field. While some dosimetric data from the original treatment plan inside the treated anatomy may be preserved, it is unlikely that (especially for organ only partially in the treated CT) complete OAR dosimetric knowledge is known. A hybrid phantom could be used to reconstruct and estimate the dose to these organs and help inform re-irradiation toxicity limits.

Appendix A

This section of the Appendix catalogues the full set of dose quantity boxplots generated for all four treatment sites for the purposes of hybrid verification described in Chapter 4 and given in the publication of Kollitz et al 2021 [**?**]. For all boxplots, the central mark is the median, the box edges are the 25th and 75th percentiles, the crosses are outliers (defined as points that are more than 1.5 times the interquartile range away from the 25th and 75th quartiles), and the whiskers extend to the extreme data points not including outliers.

A.1 Male Pelvis

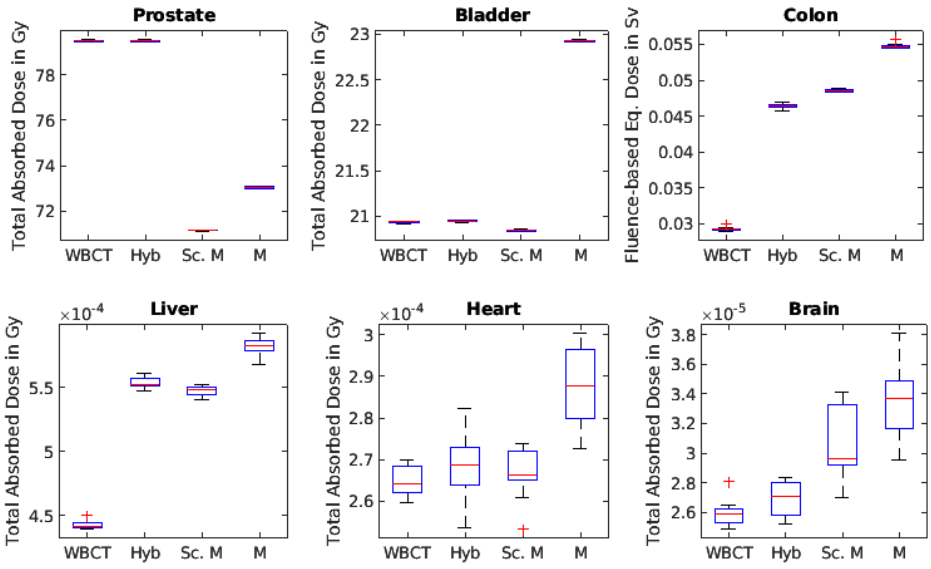

Figure A.1: Boxplots of the total organ absorbed dose in Gy for the in- and near-field (prostate, bladder, colon) and out-of-field (liver, heart, brain) organs from the prostate treatment plan in the male pelvis for all four patient representations (WBCT, hybrid, scaled MRCP, and unscaled MRCP).

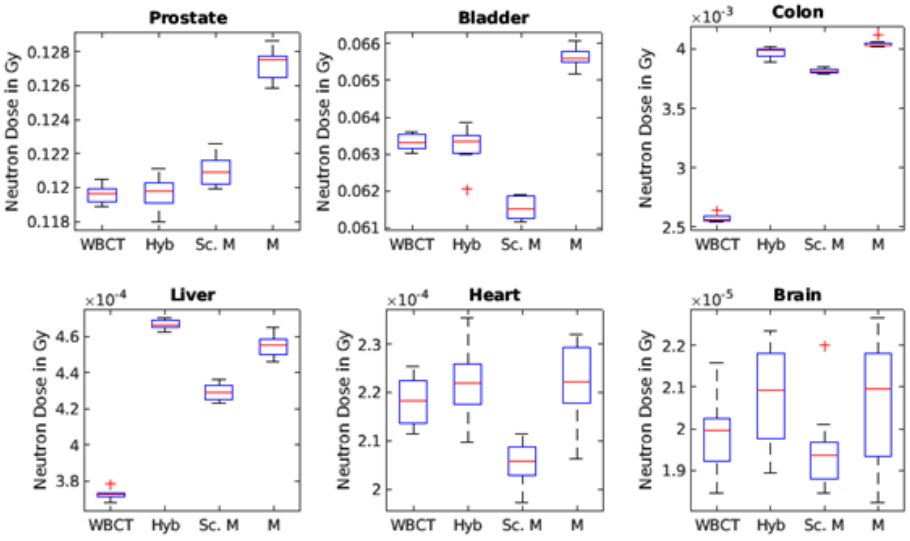

Figure A.2: Boxplots of the neutron dose in Gy for the in- and near-field (prostate, bladder, colon) and out-of-field (liver, heart, brain) organs from the prostate treatment plan in the male pelvis for all four patient representations (WBCT, hybrid, scaled MRCP, and unscaled MRCP).

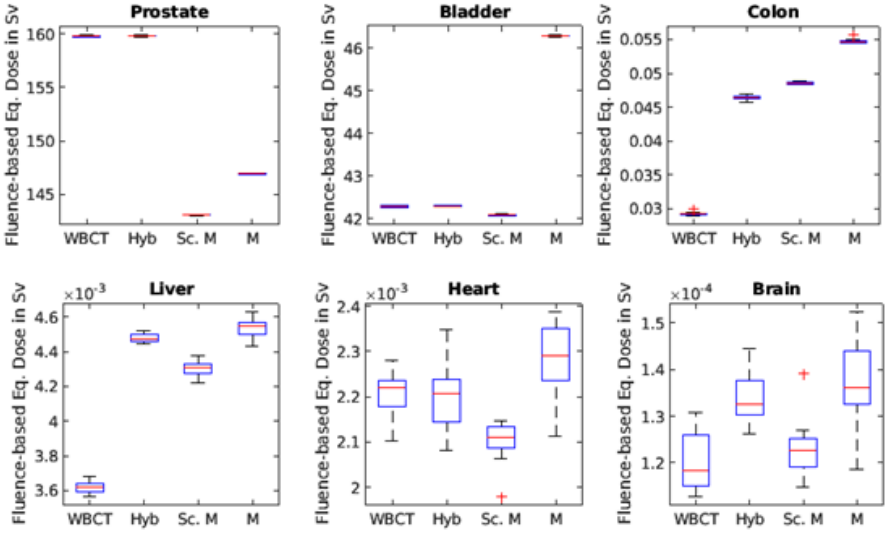

Figure A.3: Boxplots of the fluence-weighted equivalent dose in Gy for the in- and near-field (prostate, bladder, colon) and out-of-field (liver, heart, brain) organs from the prostate treatment plan in the male pelvis for all four patient representations (WBCT, hybrid, scaled MRCP, and unscaled MRCP).

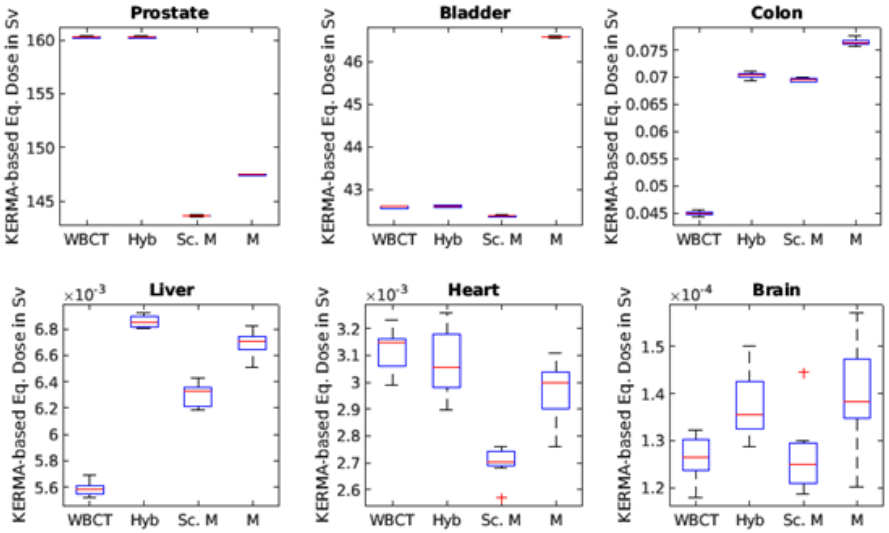

Figure A.4: Boxplots of the KERMA-weighted equivalent dose in Gy for the in- and near-field (prostate, bladder, colon) and out-of-field (liver, heart, brain) organs from the prostate treatment plan in the male pelvis for all four patient representations (WBCT, hybrid, scaled MRCP, and unscaled MRCP).

A.2 Female Pelvis

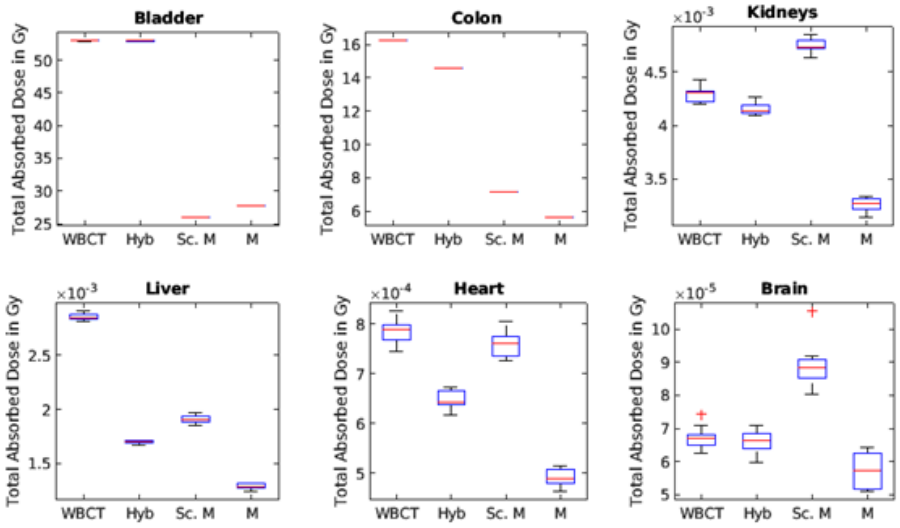

Figure A.5: Boxplots of the total organ absorbed dose in Gy for the in- and near-field (bladder, colon, kidneys) and out-of-field (liver, heart, brain) organs from the cervical cancer treatment plan in the female pelvis for all four patient representations (WBCT, hybrid, scaled MRCP, and unscaled MRCP).

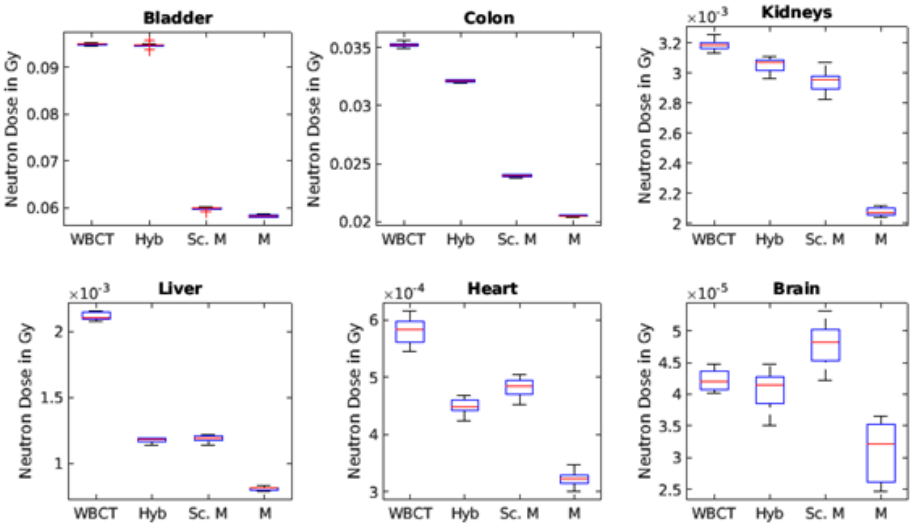

Figure A.6: Boxplots of the neutron dose in Gy for the in- and near-field (bladder, colon, kidneys) and out-of-field (liver, heart, brain) organs from the cervical cancer treatment plan in the female pelvis for all four patient representations (WBCT, hybrid, scaled MRCP, and unscaled MRCP).

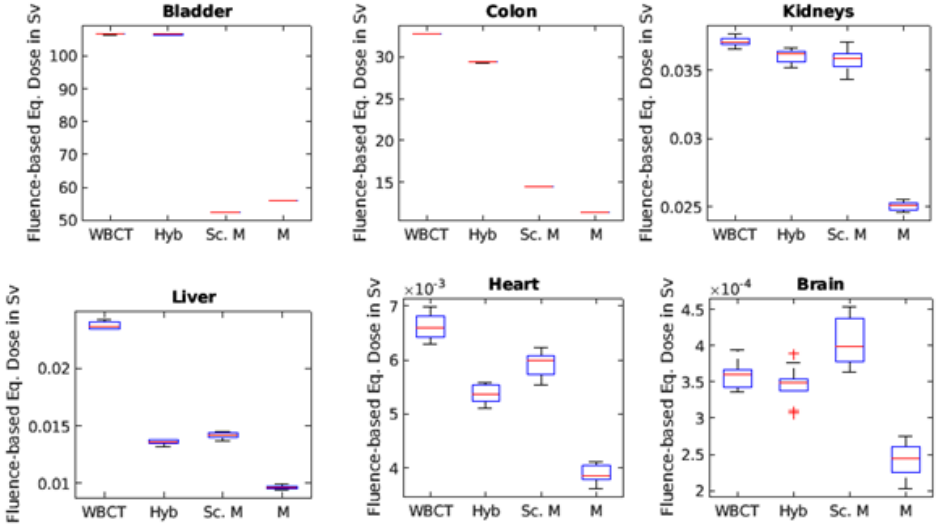

Figure A.7: Boxplots of the fluence-weighted equivalent dose in Gy for the in- and near-field (bladder, colon, kidneys) and out-of-field (liver, heart, brain) organs from the cervical cancer treatment plan in the female pelvis for all four patient representations (WBCT, hybrid, scaled MRCP, and unscaled MRCP).

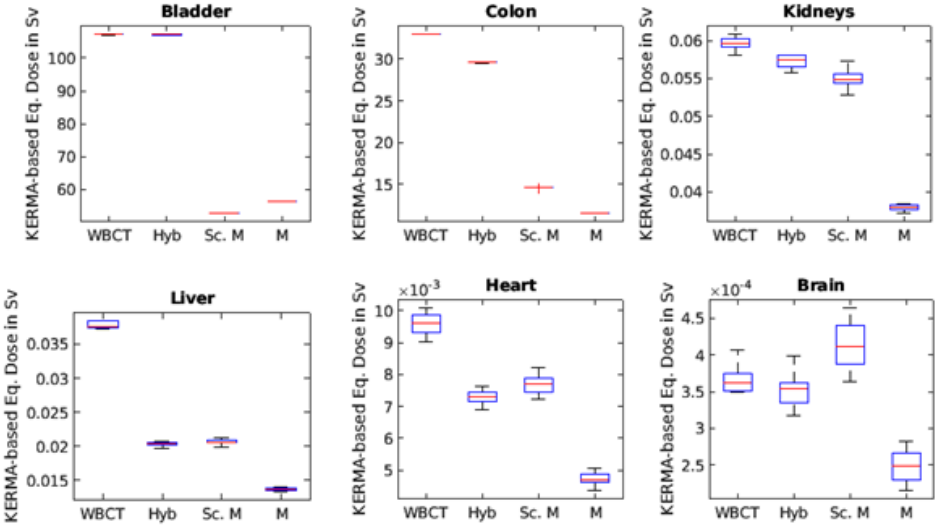

Figure A.8: Boxplots of the KERMA-weighted equivalent dose in Gy for the in- and near-field (bladder, colon, kidneys) and out-of-field (liver, heart, brain) organs from the cervical cancer treatment plan in the female pelvis for all four patient representations (WBCT, hybrid, scaled MRCP, and unscaled MRCP).

A.3 Male Head and Neck

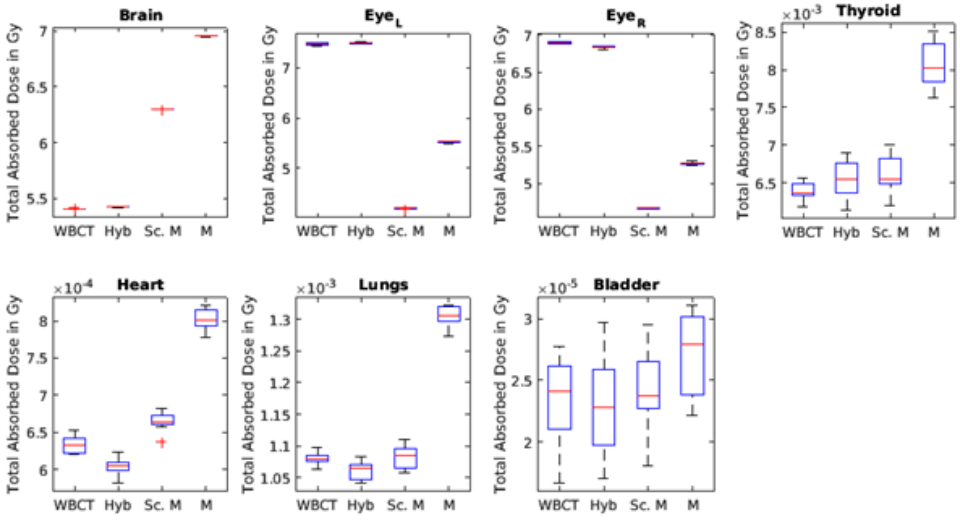

Figure A.9: Boxplots of the total organ absorbed dose in Gy for the in- and near-field (brain, left and right eyes, thyroid) and out-of-field (heart, lungs, bladder) organs from the nasopharyngeal carcinoma treatment plan in the male head and neck for all four patient representations (WBCT, hybrid, scaled MRCP, and unscaled MRCP).

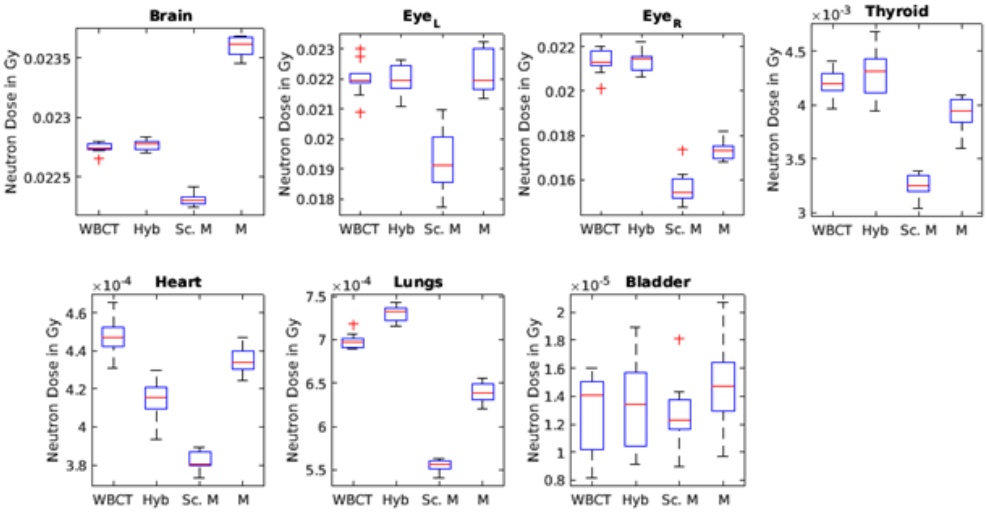

Figure A.10: Boxplots of the neutron dose in Gy for the in- and near-field (brain, left and right eyes, thyroid) and out-of-field (heart, lungs, bladder) organs from the nasopharyngeal carcinoma treatment plan in the male head and neck for all four patient representations (WBCT, hybrid, scaled MRCP, and unscaled MRCP).

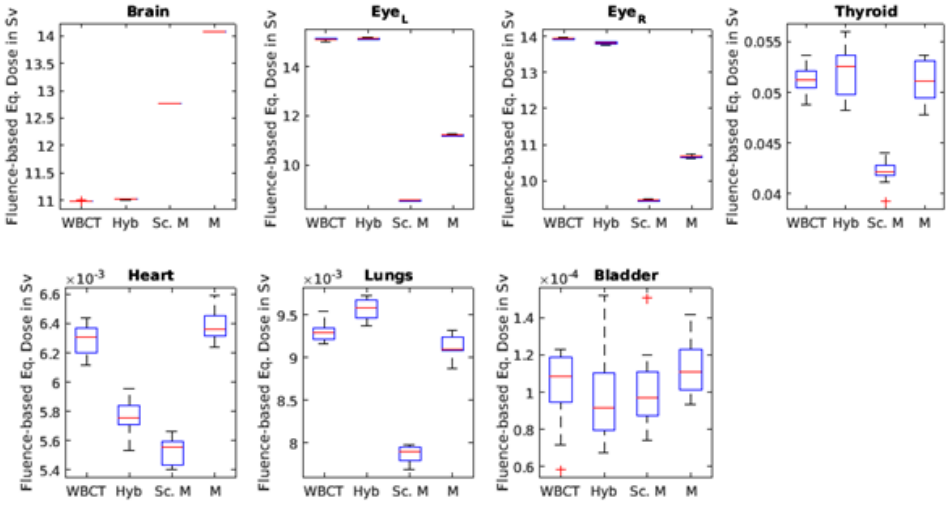

Figure A.11: Boxplots of the fluence-weighted equivalent dose in Gy for the in- and near-field (brain, left and right eyes, thyroid) and out-of-field (heart, lungs, bladder) organs from the nasopharyngeal carcinoma treatment plan in the male head and neck for all four patient representations (WBCT, hybrid, scaled MRCP, and unscaled MRCP).

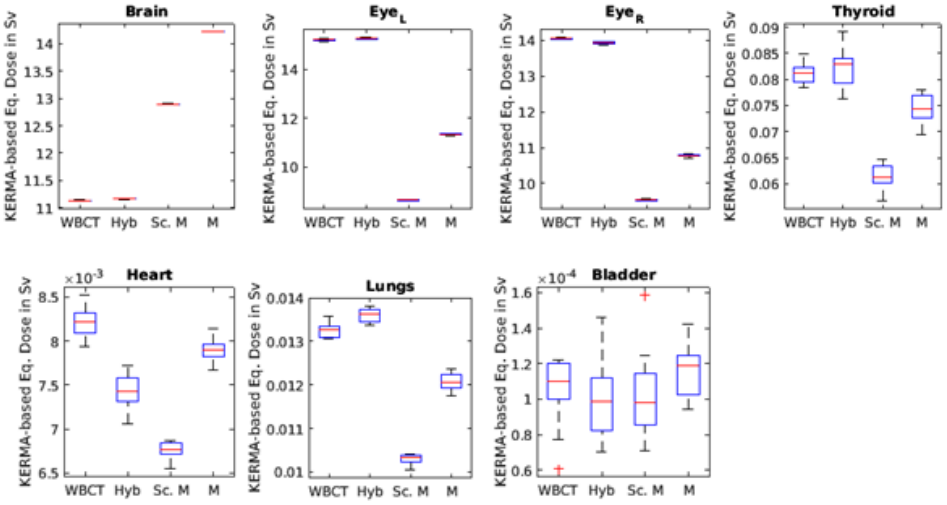

Figure A.12: Boxplots of the KERMA-weighted equivalent dose in Gy for the in- and near-field (brain, left and right eyes, thyroid) and out-of-field (heart, lungs, bladder) organs from the nasopharyngeal carcinoma treatment plan in the male head and neck for all four patient representations (WBCT, hybrid, scaled MRCP, and unscaled MRCP).

A.4 Female Head and Neck

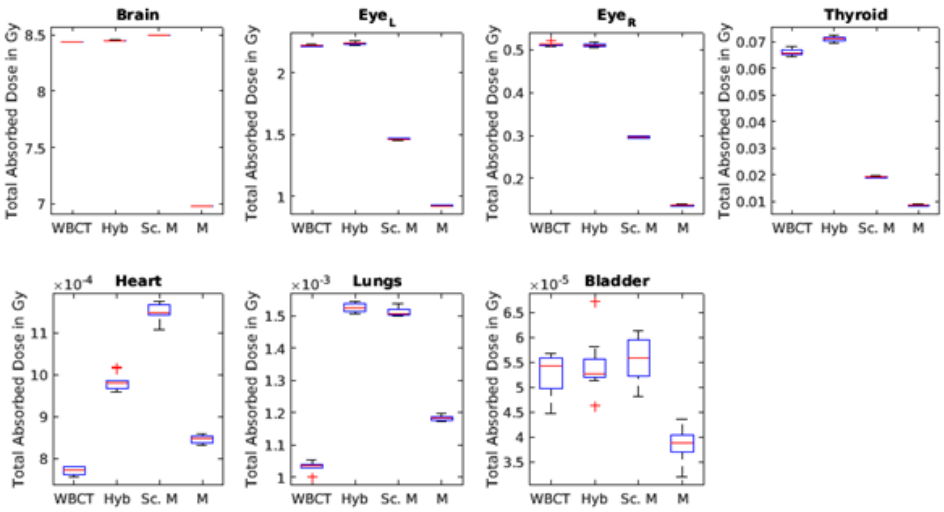

Figure A.13: Boxplots of the total organ absorbed dose in Gy for the in- and near-field (brain, left and right eyes, thyroid) and out-of-field (heart, lungs, bladder) organs from the meningioma treatment plan in the female head and neck for all four patient representations (WBCT, hybrid, scaled MRCP, and unscaled MRCP).

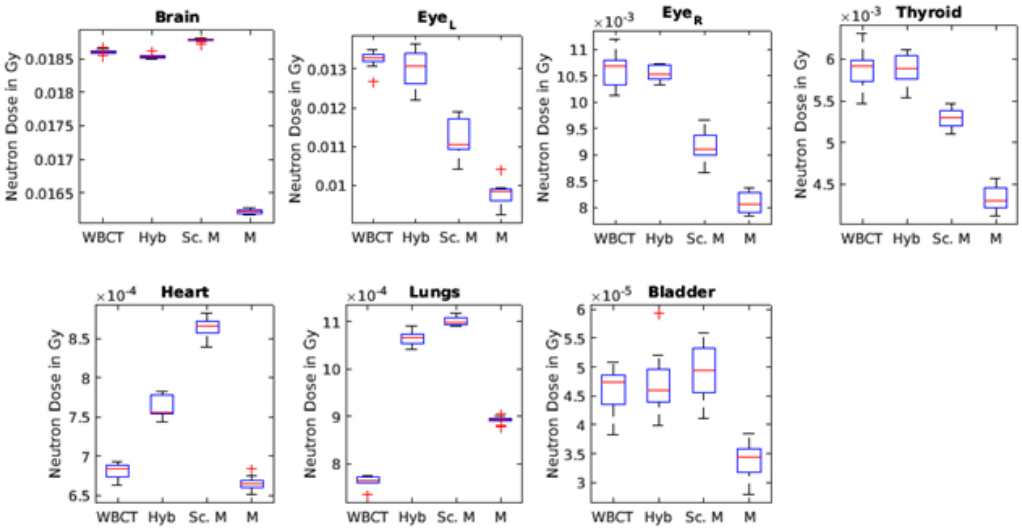

Figure A.14: Boxplots of the neutron dose in Gy for the in- and near-field (brain, left and right eyes, thyroid) and out-of-field (heart, lungs, bladder) organs from the meningioma treatment plan in the female head and neck for all four patient representations (WBCT, hybrid, scaled MRCP, and unscaled MRCP).

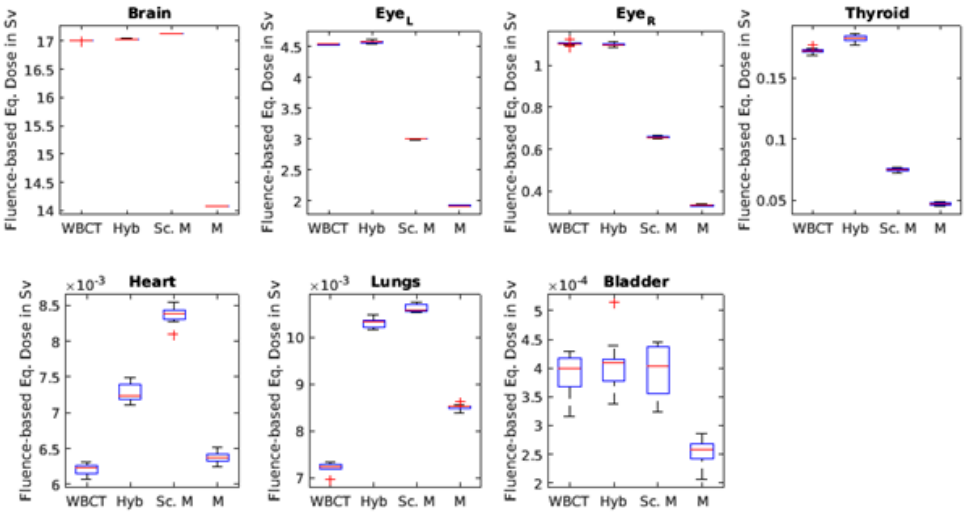

Figure A.15: Boxplots of the fluence-weighted equivalent dose in Gy for the in- and near-field (brain, left and right eyes, thyroid) and out-of-field (heart, lungs, bladder) organs from the meningioma treatment plan in the female head and neck for all four patient representations (WBCT, hybrid, scaled MRCP, and unscaled MRCP).

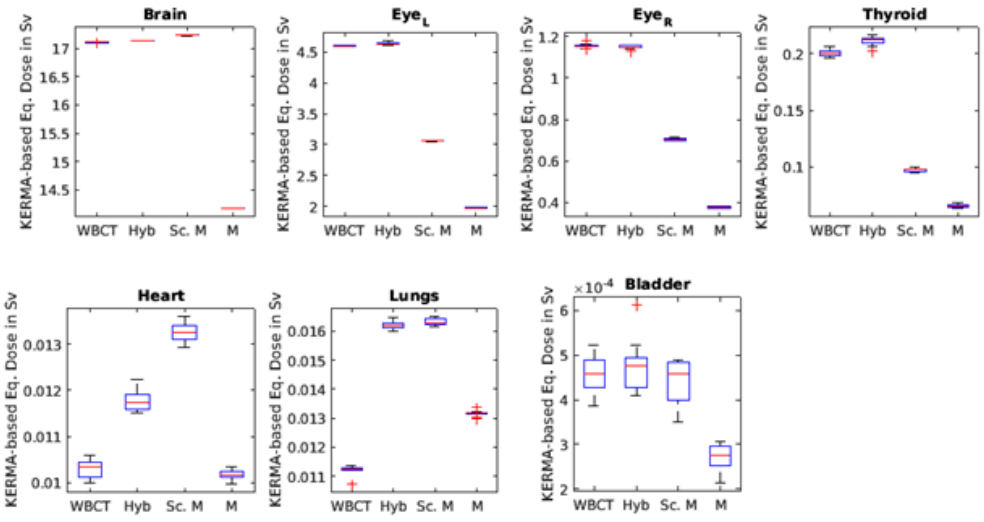

Figure A.16: Boxplots of the KERMA-weighted equivalent dose in Gy for the in- and near-field (brain, left and right eyes, thyroid) and out-of-field (heart, lungs, bladder) organs from the meningioma treatment plan in the female head and neck for all four patient representations (WBCT, hybrid, scaled MRCP, and unscaled MRCP).

Appendix B

This section of the Appendix catalogues the final quantitative data produced during the hybrid verification process described in Chapter 4 and given in the publication of Kollitz et al 2021 [**?**].

Table B.1: Quantitative Data for the Male Pelvis

Total Absorbed Dose

	Organ	WBCT Dose (Gy)		Hybrid Dose (Gy)		Scaled MRCP Dose (Gy)		MRCP Dose (Gy)	
In Field	Prostate	79.49	(79.46, 79.51)	79.49	(79.47, 79.52)	0.00 (-0.07, 0.04)	71.14 (71.13, 71.16)	10.50 (10.48, 10.53)	73.04 (73.00, 73.07)	8.12 (8.05, 8.17)
	Bladder	20.94	(20.92, 20.94)	20.94	(20.94, 20.95)	-0.04 (-0.08, 0.03)	20.84 (20.84, 20.85)	0.44 (0.40, 0.49)	22.93 (22.92, 22.93)	-9.51 (-9.58, -9.45)
Near Field	Colon	5.55E-03	(5.52E-03, 5.58E-03)	9.24E-03	(9.21E-03, 9.27E-03)	-66.45 (-68.01, -65.52)	1.10E-02 (1.10E-02, 1.10E-02)	-98.49 (-99.84, -96.53)	1.34E-02 (1.33E-02, 1.35E-02)	-141.42 (-142.46, -139.19)
Far Field	Liver	4.43E-04	(4.40E-04, 4.44E-04)	5.54E-04	(5.51E-04, 5.57E-04)	-25.00 (-25.58, -24.44)	5.47E-04 (5.44E-04, 5.50E-04)	-23.55 (-24.43, -22.65)	5.82E-04 (5.79E-04, 5.87E-04)	-31.39 (-32.80, -30.13)
	Heart	2.65E-04	(2.62E-04, 2.68E-04)	2.68E-04	(2.64E-04, 2.73E-04)	-1.34 (-3.15, -0.17)	2.66E-04 (2.65E-04, 2.72E-04)	-0.64 (-2.10, 1.21)	2.87E-04 (2.80E-04, 2.96E-04)	-8.40 (-13.06, -5.27)
	Brain	2.60E-05	(2.53E-05, 2.63E-05)	2.69E-05	(2.58E-05, 2.80E-05)	-3.73 (-8.50, -0.52)	3.07E-05 (2.92E-05, 3.32E-05)	-18.37 (-26.99, -13.62)	3.37E-05 (3.16E-05, 3.49E-05)	-29.89 (-35.32, -21.20)

Absorbed Neutron Dose

	Organ	WBCT Dose (Gy)		Hybrid Dose (Gy)		Scaled MRCP Dose (Gy)		MRCP Dose (Gy)	
In Field	Prostate	1.20E-01	(1.19E-01, 1.20E-01)	1.20E-01	(1.19E-01, 1.20E-01)	-0.07 (-0.83, 0.54)	1.21E-01 (1.20E-01, 1.22E-01)	-1.22 (-1.87, -0.30)	1.27E-01 (1.26E-01, 1.28E-01)	-6.32 (-6.74, -5.56)
	Bladder	6.33E-02	(6.32E-02, 6.35E-02)	6.33E-02	(6.30E-02, 6.35E-02)	0.07 (-0.58, 0.88)	6.15E-02 (6.13E-02, 6.19E-02)	2.83 (2.33, 3.21)	6.56E-02 (6.55E-02, 6.58E-02)	-3.67 (-4.22, -3.17)
Near Field	Colon	2.58E-03	(2.56E-03, 2.59E-03)	3.98E-03	(3.94E-03, 4.00E-03)	-54.34 (-56.69, -53.21)	3.81E-03 (3.80E-03, 3.83E-03)	-48.08 (-49.56, -46.78)	4.04E-03 (4.03E-03, 4.05E-03)	-56.90 (-57.58, -55.66)
Far Field	Liver	3.72E-04	(3.71E-04, 3.73E-04)	4.67E-04	(4.65E-04, 4.69E-04)	-25.26 (-25.51, -24.84)	4.29E-04 (4.25E-04, 4.33E-04)	-15.22 (-15.22, -13.92)	4.55E-04 (4.50E-04, 4.58E-04)	-22.17 (-23.05, -21.03)
	Heart	2.19E-04	(2.14E-04, 2.23E-04)	2.22E-04	(2.18E-04, 2.26E-04)	-1.83 (-2.89, 0.46)	2.05E-04 (2.03E-04, 2.09E-04)	5.94 (5.62, 7.28)	2.23E-04 (2.18E-04, 2.29E-04)	-1.90 (-5.30, 1.20)
	Brain	1.98E-05	(1.92E-05, 2.03E-05)	2.08E-05	(1.98E-05, 2.18E-05)	-5.01 (-10.43, -2.56)	1.95E-05 (1.88E-05, 1.97E-05)	1.49 (-1.95, 8.46)	2.07E-05 (1.93E-05, 2.18E-05)	-4.45 (-13.90, 3.22)

Equivalent Dose using Fluence-Weighted Neutron Energy

	Organ	WBCT Eq. Dose (Sv)		Hybrid Eq. Dose (Sv)		Scaled MRCP Eq. Dose (Sv)		MRCP Eq. Dose (Sv)	
In Field	Prostate	159.77	(159.71, 159.82)	159.78	(159.75, 159.83)	0.00 (-0.06, 0.04)	143.08 (143.05, 143.12)	10.45 (10.43, 10.47)	146.90 (146.82, 146.96)	8.06 (8.00, 8.10)
	Bladder	42.29	(42.27, 42.31)	42.31	(42.30, 42.33)	-0.03 (-0.07, 0.03)	42.09 (42.08, 42.10)	0.47 (0.43, 0.52)	46.28 (46.27, 46.30)	-9.44 (-9.51, -9.38)
Near Field	Colon	2.92E-02	(2.90E-02, 2.93E-02)	4.64E-02	(4.62E-02, 4.66E-02)	-58.79 (-60.33, -57.69)	4.85E-02 (4.84E-02, 4.87E-02)	-66.09 (-66.99, -65.05)	5.48E-02 (5.45E-02, 5.49E-02)	-87.46 (-87.46, -86.81)
Far Field	Liver	3.62E-03	(3.59E-03, 3.64E-03)	4.48E-03	(4.46E-03, 4.50E-03)	-23.69 (-23.64, -22.81)	4.30E-03 (4.27E-03, 4.33E-03)	-18.88 (-20.71, -17.51)	4.54E-03 (4.50E-03, 4.57E-03)	-25.39 (-27.03, -23.89)
	Heart	2.21E-03	(2.18E-03, 2.24E-03)	2.21E-03	(2.14E-03, 2.24E-03)	-0.01 (-2.17, 1.74)	2.10E-03 (2.09E-03, 2.14E-03)	4.93 (4.04, 6.84)	2.29E-03 (2.24E-03, 2.35E-03)	-3.61 (-7.34, -1.63)
	Brain	1.20E-04	(1.15E-04, 1.26E-04)	1.34E-04	(1.30E-04, 1.38E-04)	-11.74 (-17.59, -3.53)	1.23E-04 (1.19E-04, 1.25E-04)	-2.78 (-7.04, 0.10)	1.38E-04 (1.33E-04, 1.44E-04)	-15.04 (-20.82, -6.16)

Equivalent Dose using KERMA-Weighted Neutron Energy

	Organ	WBCT Eq. Dose (Sv)		Hybrid Eq. Dose (Sv)		Scaled MRCP Eq. Dose (Sv)		MRCP Eq. Dose (Sv)	
In Field	Prostate	160.27	(160.20, 160.33)	160.28	(160.24, 160.33)	0.00 (-0.07, 0.05)	143.61 (143.57, 143.64)	10.40 (10.38, 10.42)	147.44 (147.35, 147.49)	8.01 (7.96, 8.05)
	Bladder	42.59	(42.57, 42.61)	42.61	(42.59, 42.63)	-0.04 (-0.06, 0.01)	42.38 (42.37, 42.39)	0.50 (0.44, 0.54)	46.58 (46.57, 46.59)	-9.37 (-9.45, -9.30)
Near Field	Colon	4.49E-02	(4.47E-02, 4.52E-02)	7.03E-02	(7.00E-02, 7.07E-02)	-56.56 (-57.94, -55.03)	6.95E-02 (6.92E-02, 6.97E-02)	-54.72 (-55.92, -54.37)	7.64E-02 (7.60E-02, 7.67E-02)	-70.15 (-71.44, -68.94)
Far Field	Liver	5.59E-03	(5.55E-03, 5.61E-03)	6.86E-03	(6.81E-03, 6.89E-03)	-22.67 (-23.54, -21.38)	6.30E-03 (6.22E-03, 6.35E-03)	-12.68 (-14.88, -11.35)	6.69E-03 (6.65E-03, 6.74E-03)	-19.77 (-21.56, -18.48)
	Heart	3.13E-03	(3.06E-03, 3.16E-03)	3.08E-03	(2.98E-03, 3.18E-03)	1.62 (-0.81, 3.86)	2.70E-03 (2.69E-03, 2.74E-03)	13.49 (11.94, 14.89)	2.96E-03 (2.90E-03, 3.04E-03)	5.08 (2.39, 7.39)
	Brain	1.26E-04	(1.24E-04, 1.30E-04)	1.38E-04	(1.32E-04, 1.42E-04)	-9.58 (-12.45, -3.45)	1.26E-04 (1.21E-04, 1.30E-04)	-0.23 (-2.78, 3.97)	1.40E-04 (1.35E-04, 1.47E-04)	-11.40 (-14.80, -5.11)

Table B.2: Quantitative Data for the Female Pelvis

Total Absorbed Dose

	Organ	WBCT Dose (Gy)	Hybrid Dose (Gy)	% Difference	Scaled MRCP Dose (Gy)	% Difference	MRCP Dose (Gy)	% Difference
In Field	Bladder	52.95 (52.94 , 52.98)	52.95 (52.93 , 52.96)	0.02 (-0.03 , 0.05)	26.02 (26.01 , 26.03)	50.87 (50.85 , 50.89)	27.73 (27.73 , 27.74)	47.63 (47.61 , 47.64)
	Colon	16.24 (16.23 , 16.24)	14.57 (14.56 , 14.57)	10.30 (10.27 , 10.33)	7.15 (7.15 , 7.15)	56.00 (55.98 , 56.01)	5.63 (5.63 , 5.64)	65.30 (65.28 , 65.31)
Near Field	Kidneys	4.28E-03 (4.23E-03 , 4.32E-03)	4.15E-03 (4.11E-03 , 4.19E-03)	3.32 (1.84 , 4.66)	4.75E-03 (4.72E-03 , 4.79E-03)	-10.42 (-11.41 , -9.57)	3.27E-03 (3.22E-03 , 3.32E-03)	24.13 (22.88 , 25.49)
Far Field	Liver	2.86E-03 (2.84E-03 , 2.88E-03)	1.70E-03 (1.69E-03 , 1.71E-03)	40.46 (39.55 , 41.42)	1.91E-03 (1.88E-03 , 1.94E-03)	33.16 (32.16 , 34.22)	1.30E-03 (1.28E-03 , 1.31E-03)	54.93 (54.46 , 55.17)
	Heart	7.76E-04 (7.68E-04 , 7.98E-04)	6.50E-04 (6.38E-04 , 6.67E-04)	17.37 (14.95 , 19.21)	7.63E-04 (7.36E-04 , 7.75E-04)	3.22 (1.39 , 4.17)	4.87E-04 (4.79E-04 , 5.07E-04)	37.30 (35.66 , 39.99)
	Brain	6.65E-05 (6.49E-05 , 6.81E-05)	6.56E-05 (6.39E-05 , 6.83E-05)	1.77 (-4.60 , 3.58)	8.72E-05 (8.53E-05 , 9.08E-05)	-33.07 (-36.11 , -31.76)	5.51E-05 (5.18E-05 , 6.24E-05)	14.91 (4.48 , 24.15)

Absorbed Neutron Dose

	Organ	WBCT Dose (Gy)	Hybrid Dose (Gy)	% Difference	Scaled MRCP Dose (Gy)	% Difference	MRCP Dose (Gy)	% Difference
In Field	Bladder	9.49E-02 (9.47E-02 , 9.49E-02)	9.46E-02 (9.44E-02 , 9.47E-02)	0.18 (-0.12 , 0.39)	5.99E-02 (5.98E-02 , 6.01E-02)	36.78 (36.50 , 36.93)	5.83E-02 (5.81E-02 , 5.84E-02)	38.49 (38.27 , 38.68)
	Colon	3.53E-02 (1.19E-01 - 1.20E-01)	3.21E-02 (3.20E-02 , 3.22E-02)	8.85 (8.57 , 9.03)	2.39E-02 (2.39E-02 , 2.40E-02)	32.00 (31.61 , 32.45)	2.05E-02 (2.05E-02 , 2.06E-02)	41.75 (41.51 , 42.05)
Near Field	Kidneys	3.19E-03 (3.17E-03 , 3.21E-03)	3.04E-03 (3.02E-03 , 3.08E-03)	4.30 (3.70 , 4.92)	2.96E-03 (2.89E-03 , 2.98E-03)	7.56 (6.72 , 8.38)	2.07E-03 (2.06E-03 , 2.10E-03)	34.88 (34.34 , 35.55)
Far Field	Liver	2.12E-03 (2.09E-03 , 2.15E-03)	1.17E-03 (1.16E-03 , 1.19E-03)	44.38 (43.23 , 45.74)	1.19E-03 (1.18E-03 , 1.21E-03)	43.72 (42.67 , 44.81)	8.18E-04 (7.99E-04 , 8.18E-04)	61.60 (61.19 , 61.89)
	Heart	5.73E-04 (5.61E-04 , 5.98E-04)	4.48E-04 (4.42E-04 , 4.61E-04)	22.49 (21.87 , 23.79)	4.85E-04 (4.71E-04 , 4.95E-04)	16.82 (13.77 , 18.69)	3.15E-04 (3.15E-04 , 3.30E-04)	43.97 (42.04 , 47.24)
	Brain	4.21E-05 (4.06E-05 , 4.36E-05)	4.00E-05 (3.85E-05 , 4.28E-05)	3.58 (-1.71 , 8.04)	4.80E-05 (4.53E-05 , 5.02E-05)	-13.52 (-20.06 , -6.09)	2.97E-05 (2.61E-05 , 3.52E-05)	26.19 (13.38 , 37.15)

Equivalent Dose using Fluence-Weighted Neutron Energy

	Organ	WBCT Eq. Dose (Sv)	Hybrid Eq. Dose (Sv)	% Difference	Scaled MRCP Eq. Dose (Sv)	% Difference	MRCP Eq. Dose (Sv)	% Difference
In Field	Bladder	106.60 (106.56 , 106.63)	106.58 (106.54 , 106.60)	0.02 (-0.02 , 0.05)	52.47 (52.45 , 52.49)	50.77 (50.75 , 50.80)	55.90 (55.89 , 55.90)	47.56 (47.54 , 47.58)
	Colon	32.74 (32.73 , 32.75)	29.37 (29.37 , 29.38)	10.29 (10.24 , 10.32)	14.47 (14.47 , 14.47)	55.80 (55.79 , 55.82)	11.43 (11.42 , 11.43)	65.10 (65.09 , 65.12)
Near Field	Kidneys	3.71E-02 (3.69E-02 , 3.73E-02)	3.60E-02 (3.56E-02 , 3.64E-02)	2.91 (2.25 , 3.03)	3.58E-02 (3.53E-02 , 3.62E-02)	3.37 (2.19 , 3.81)	2.51E-02 (2.47E-02 , 2.53E-02)	32.44 (31.87 , 33.31)
Far Field	Liver	2.37E-02 (2.34E-02 , 2.40E-02)	1.36E-02 (1.35E-02 , 1.37E-02)	42.64 (41.54 , 43.99)	1.42E-02 (1.40E-02 , 1.43E-02)	40.06 (38.97 , 41.35)	9.68E-03 (9.58E-03 , 9.77E-03)	59.11 (58.58 , 59.33)
	Heart	6.62E-03 (6.43E-03 , 6.82E-03)	5.37E-03 (5.23E-03 , 5.53E-03)	18.79 (17.32 , 20.17)	5.93E-03 (5.74E-03 , 6.09E-03)	10.24 (7.91 , 12.60)	3.89E-03 (3.79E-03 , 4.04E-03)	41.13 (39.08 , 44.72)
	Brain	3.61E-04 (3.42E-04 , 3.67E-04)	3.47E-04 (3.37E-04 , 3.54E-04)	3.46 (-2.91 , 14.10)	4.04E-04 (3.78E-04 , 4.38E-04)	-12.40 (-24.83 , -5.87)	2.43E-04 (2.25E-04 , 2.60E-04)	32.52 (29.91 , 34.27)

Equivalent Dose using KERMA-Weighted Neutron Energy

	Organ	WBCT Eq. Dose (Sv)	Hybrid Eq. Dose (Sv)	% Difference	Scaled MRCP Eq. Dose (Sv)	% Difference	MRCP Eq. Dose (Sv)	% Difference
In Field	Bladder	107.16 (107.13 , 107.20)	107.14 (107.11 , 107.17)	0.02 (-0.03 , 0.05)	52.85 (52.83 , 52.87)	50.68 (50.66 , 50.70)	56.27 (56.25 , 56.28)	47.49 (47.48 , 47.51)
	Colon	32.96 (32.96 , 32.97)	29.58 (29.57 , 29.58)	10.28 (10.24 , 10.31)	14.63 (14.63 , 14.63)	55.61 (55.60 , 55.62)	11.56 (11.56 , 11.57)	64.92 (64.91 , 64.94)
Near Field	Kidneys	5.96E-02 (5.91E-02 , 6.02E-02)	5.72E-02 (5.65E-02 , 5.80E-02)	3.93 (2.89 , 4.59)	5.49E-02 (5.44E-02 , 5.57E-02)	7.86 (6.49 , 8.95)	3.79E-02 (3.76E-02 , 3.83E-02)	36.39 (35.52 , 37.29)
Far Field	Liver	3.78E-02 (3.74E-02 , 3.84E-02)	2.04E-02 (2.02E-02 , 2.06E-02)	46.00 (44.94 , 47.38)	2.07E-02 (2.05E-02 , 2.10E-02)	45.21 (44.14 , 46.18)	1.37E-02 (1.35E-02 , 1.39E-02)	63.79 (63.27 , 63.99)
	Heart	9.58E-03 (9.33E-03 , 9.86E-03)	7.30E-03 (7.17E-03 , 7.46E-03)	23.78 (22.69 , 25.34)	7.69E-03 (7.45E-03 , 7.90E-03)	19.73 (17.52 , 22.84)	4.74E-03 (4.62E-03 , 4.88E-03)	50.45 (48.64 , 53.58)
	Brain	3.66E-04 (3.52E-04 , 3.75E-04)	3.53E-04 (3.35E-04 , 3.62E-04)	3.51 (-0.41 , 11.11)	4.13E-04 (3.87E-04 , 4.40E-04)	-13.14 (-25.06 , -3.13)	2.48E-04 (2.29E-04 , 2.66E-04)	32.12 (26.71 , 35.80)

Table B.3: Quantitative Data for the Male Head and Neck

Total Absorbed Dose

	Organ	WBCT Dose (Gy)	Hybrid Dose (Gy)	Hybrid % Difference	Scaled MRCP Dose (Gy)	Scaled MRCP % Difference	MRCP Dose (Gy)	MRCP % Difference
In Field	Brain	5.41 (5.41, 5.41)	5.42 (5.42, 5.43)	-0.28 (-0.31, -0.24)	6.30 (6.30, 6.30)	-16.45 (-16.49, -16.41)	6.95 (6.95, 6.95)	-28.53 (-28.54, -28.50)
	Eye_L	7.48 (7.47, 7.49)	7.50 (7.49, 7.51)	-0.33 (-0.59, -0.14)	4.20 (4.20, 4.21)	43.81 (43.71, 43.85)	5.53 (5.52, 5.54)	26.07 (25.87, 26.25)
	Eye_R	6.90 (6.89, 6.91)	6.83 (6.83, 6.84)	0.92 (0.62, 1.13)	4.67 (4.66, 4.67)	32.35 (32.23, 32.44)	5.27 (5.26, 5.28)	23.56 (23.32, 23.80)
Near Field	Thyroid	6.39E-03 (6.33E-03, 6.49E-03)	6.53E-03 (6.36E-03, 6.77E-03)	-2.30 (-4.84, 0.54)	6.59E-03 (6.48E-03, 6.82E-03)	-3.20 (-6.84, -0.88)	8.06E-03 (7.85E-03, 8.34E-03)	-26.18 (-31.91, -22.94)
Far Field	Heart	6.33E-04 (6.22E-04, 6.41E-04)	6.03E-04 (5.98E-04, 6.10E-04)	4.74 (3.46, 5.95)	6.65E-04 (6.61E-04, 6.73E-04)	-5.02 (-6.98, -2.92)	8.02E-04 (7.93E-04, 8.15E-04)	-26.72 (-30.00, -24.03)
	Lungs	1.08E-03 (1.08E-03, 1.09E-03)	1.06E-03 (1.05E-03, 1.07E-03)	1.59 (0.87, 3.21)	1.08E-03 (1.07E-03, 1.10E-03)	-0.37 (-1.84, 1.41)	1.30E-03 (1.30E-03, 1.32E-03)	-20.90 (-21.71, -19.76)
	Bladder	2.33E-05 (2.10E-05, 2.62E-05)	2.33E-05 (1.98E-05, 2.59E-05)	-2.81 (-18.52, 17.42)	2.43E-05 (2.27E-05, 2.65E-05)	-7.62 (-22.80, 14.26)	2.73E-05 (2.39E-05, 3.01E-05)	-19.47 (-36.37, -1.86)

Absorbed Neutron Dose

	Organ	WBCT Dose (Gy)	Hybrid Dose (Gy)	Hybrid % Difference	Scaled MRCP Dose (Gy)	Scaled MRCP % Difference	MRCP Dose (Gy)	MRCP % Difference
In Field	Brain	2.27E-02 (2.27E-02, 2.28E-02)	2.28E-02 (2.27E-02, 2.28E-02)	-0.12 (-0.29, 0.11)	2.23E-02 (2.23E-02, 2.23E-02)	1.91 (1.78, 2.10)	2.36E-02 (2.35E-02, 2.37E-02)	-3.75 (-3.92, -3.56)
	Eye_L	2.20E-02 (2.19E-02, 2.22E-02)	2.20E-02 (2.17E-02, 2.24E-02)	0.12 (-0.95, 2.37)	1.92E-02 (1.86E-02, 2.01E-02)	12.48 (9.60, 16.17)	2.22E-02 (2.17E-02, 2.30E-02)	-1.09 (-3.93, 1.19)
	Eye_R	2.13E-02 (2.11E-02, 2.18E-02)	2.13E-02 (2.10E-02, 2.16E-02)	-0.22 (-2.40, 2.02)	1.57E-02 (1.52E-02, 1.60E-02)	26.45 (24.04, 29.39)	1.74E-02 (1.70E-02, 1.75E-02)	18.32 (16.39, 20.86)
Near Field	Thyroid	4.20E-03 (4.13E-03, 4.29E-03)	4.28E-03 (4.12E-03, 4.43E-03)	-1.92 (-4.77, 0.97)	3.26E-03 (3.20E-03, 3.35E-03)	22.54 (20.67, 23.72)	3.91E-03 (3.84E-03, 4.06E-03)	6.94 (3.01, 9.35)
Far Field	Heart	4.47E-04 (4.42E-04, 4.52E-04)	4.14E-04 (4.09E-04, 4.21E-04)	7.37 (5.29, 10.08)	3.82E-04 (3.79E-04, 3.87E-04)	14.45 (13.36, 15.03)	4.35E-04 (4.30E-04, 4.40E-04)	2.69 (1.11, 4.12)
	Lungs	6.98E-04 (6.91E-04, 7.02E-04)	7.30E-04 (7.23E-04, 7.37E-04)	-4.60 (-6.09, -3.41)	5.55E-04 (5.52E-04, 5.61E-04)	20.47 (19.58, 21.73)	6.39E-04 (6.31E-04, 6.49E-04)	8.54 (7.20, 9.81)
	Bladder	1.29E-05 (1.02E-05, 1.50E-05)	1.33E-05 (1.04E-05, 1.57E-05)	-7.78 (-28.60, 20.43)	1.28E-05 (1.16E-05, 1.37E-05)	-4.13 (-43.78, 22.76)	1.47E-05 (1.30E-05, 1.64E-05)	-20.39 (-39.66, 10.97)

Equivalent Dose using Fluence-Weighted Neutron Energy

	Organ	WBCT Eq. Dose (Sv)	Hybrid Eq. Dose (Sv)	Hybrid % Difference	Scaled MRCP Eq. Dose (Sv)	Scaled MRCP % Difference	MRCP Eq. Dose (Sv)	MRCP % Difference
In Field	Brain	10.99 (10.98, 10.99)	11.02 (11.01, 11.02)	-0.27 (-0.29, -0.24)	12.77 (12.76, 12.76)	-16.15 (-16.18, -16.12)	14.08 (14.07, 14.08)	-28.12 (-28.14, -28.10)
	Eye_L	15.11 (15.10, 15.15)	15.16 (15.14, 15.18)	-0.32 (-0.66, -0.15)	8.54 (8.53, 8.55)	43.49 (43.30, 43.58)	11.21 (11.19, 11.24)	25.80 (25.62, 26.06)
	Eye_R	13.95 (13.93, 13.96)	13.82 (13.80, 13.84)	0.91 (0.63, 1.11)	9.45 (9.43, 9.45)	32.27 (32.13, 32.39)	10.67 (10.65, 10.69)	23.50 (23.29, 23.76)
Near Field	Thyroid	5.13E-02 (5.04E-02, 5.21E-02)	5.20E-02 (4.97E-02, 5.36E-02)	-1.33 (-4.73, 2.45)	4.22E-02 (4.18E-02, 4.28E-02)	17.80 (16.53, 18.98)	5.11E-02 (4.95E-02, 5.32E-02)	######## (-1.22, 2.93)
Far Field	Heart	6.29E-03 (6.20E-03, 6.37E-03)	5.75E-03 (5.71E-03, 5.84E-03)	8.57 (7.26, 10.32)	5.53E-03 (5.44E-03, 5.60E-03)	12.13 (10.42, 13.48)	6.38E-03 (6.32E-03, 6.45E-03)	-1.50 (-3.29, 0.04)
	Lungs	9.30E-03 (9.21E-03, 9.35E-03)	9.56E-03 (9.46E-03, 9.67E-03)	-2.81 (-3.71, -1.91)	7.87E-03 (7.79E-03, 7.96E-03)	15.35 (14.12, 16.66)	9.12E-03 (9.09E-03, 9.24E-03)	1.90 (0.92, 3.10)
	Bladder	1.01E-04 (9.48E-05, 1.19E-04)	9.93E-05 (7.94E-05, 1.10E-04)	-1.53 (-30.22, 16.31)	1.02E-04 (8.73E-05, 1.11E-04)	-4.2848 (-24.11, 21.30)	1.15E-04 (1.01E-04, 1.23E-04)	-20.24 (-46.49, 11.15)

Equivalent Dose using KERMA-Weighted Neutron Energy

	Organ	WBCT Eq. Dose (Sv)	Hybrid Eq. Dose (Sv)	Hybrid % Difference	Scaled MRCP Eq. Dose (Sv)	Scaled MRCP % Difference	MRCP Eq. Dose (Sv)	MRCP % Difference
In Field	Brain	11.13 (11.13, 11.13)	11.16 (11.16, 11.16)	-0.27 (-0.29, -0.23)	12.90 (12.90, 12.90)	-15.88 (-15.91, -15.84)	14.22 (14.22, 14.22)	-27.75 (-27.77, -27.73)
	Eye_L	15.22 (15.21, 15.25)	15.27 (15.25, 15.29)	-0.34 (-0.73, -0.12)	8.64 (8.63, 8.66)	43.21 (42.99, 43.35)	11.33 (11.31, 11.36)	25.56 (25.42, 25.83)
	Eye_R	14.06 (14.04, 14.07)	13.93 (13.91, 13.95)	0.89 (0.66, 1.05)	9.54 (9.52, 9.54)	32.16 (32.02, 32.30)	10.77 (10.76, 10.79)	23.37 (23.18, 23.64)
Near Field	Thyroid	8.12E-02 (7.94E-02, 8.22E-02)	8.20E-02 (7.93E-02, 8.39E-02)	-1.04 (-4.95, 2.33)	6.12E-02 (6.03E-02, 6.33E-02)	24.63 (22.22, 26.57)	7.43E-02 (7.25E-02, 7.69E-02)	8.43 (6.06, 10.63)
Far Field	Heart	8.20E-03 (8.09E-03, 8.32E-03)	7.42E-03 (7.32E-03, 7.58E-03)	9.49 (7.63, 11.75)	6.75E-03 (6.72E-03, 6.85E-03)	17.64 (16.13, 18.17)	7.90E-03 (7.82E-03, 7.97E-03)	3.66 (2.14, 4.85)
	Lungs	1.33E-02 (1.31E-02, 1.33E-02)	1.36E-02 (1.35E-02, 1.37E-02)	-2.58 (-3.88, -1.70)	1.03E-02 (1.02E-02, 1.04E-02)	22.32 (21.35, 23.25)	1.20E-02 (1.19E-02, 1.22E-02)	9.09 (7.64, 10.27)
	Bladder	1.04E-04 (1.00E-04, 1.20E-04)	1.03E-04 (8.22E-05, 1.12E-04)	-1.84 (-25.34, 14.14)	1.04E-04 (8.55E-05, 1.15E-04)	-2.48 (-30.19, 22.13)	1.16E-04 (1.02E-04, 1.25E-04)	-16.73 (-42.16, 8.81)

Table B.4: Quantitative Data for the Female Head and Neck

Total Absorbed Dose

	Organ	WBCT Dose (Gy)	Hybrid Dose (Gy)	Hybrid % Difference	Scaled MRCP Dose (Gy)	Scaled MRCP % Difference	MRCP Dose (Gy)	MRCP % Difference
In Field	Brain	8.43 (8.43, 8.43)	8.45 (8.45, 8.45)	-0.19 (-0.21, -0.17)	8.49 (8.49, 8.50)	-0.71 (-0.74, -0.71)	6.98 (6.98, 6.98)	17.23 (17.22, 17.24)
	Eye_L	2.22 (2.22, 2.22)	2.24 (2.23, 2.24)	-0.88 (-1.33, -0.52)	1.46 (1.46, 1.47)	34.19 (34.07, 34.22)	9.26E-01 (9.22E-01, 9.30E-01)	58.29 (58.04, 58.47)
	Eye_R	5.13E-01 (5.11E-01, 5.14E-01)	5.10E-01 (5.08E-01, 5.12E-01)	0.43 (-0.45, 1.23)	2.96E-01 (2.94E-01, 2.99E-01)	42.22 (41.60, 42.76)	1.37E-01 (1.36E-01, 1.38E-01)	73.24 (72.95, 73.58)
Near Field	Thyroid	6.60E-02 (6.52E-02, 6.68E-02)	7.11E-02 (7.04E-02, 7.16E-02)	-7.79 (-9.12, -6.61)	1.92E-02 (1.88E-02, 1.95E-02)	70.84 (70.13, 71.36)	8.66E-03 (8.41E-03, 8.81E-03)	86.86 (86.52, 87.10)
Far Field	Heart	7.71E-04 (7.62E-04, 7.79E-04)	9.81E-04 (9.65E-04, 9.84E-04)	-27.36 (-30.17, -24.89)	1.15E-03 (1.14E-03, 1.17E-03)	-49.10 (-51.89, -46.59)	8.46E-04 (8.37E-04, 8.54E-04)	-9.83 (-11.26, -7.17)
	Lungs	1.03E-03 (1.03E-03, 1.04E-03)	1.52E-03 (1.51E-03, 1.54E-03)	-47.56 (-49.98, -45.72)	1.51E-03 (1.50E-03, 1.52E-03)	-46.32 (-47.80, -44.83)	1.18E-03 (1.17E-03, 1.19E-03)	-14.44 (-15.28, -14.31)
	Bladder	5.25E-05 (4.97E-05, 5.57E-05)	5.43E-05 (5.19E-05, 5.55E-05)	-3.88 (-14.31, 5.75)	5.55E-05 (5.23E-05, 5.95E-05)	-6.69 (-21.12, 6.17)	3.88E-05 (3.70E-05, 4.05E-05)	25.64 (21.69, 30.71)

Absorbed Neutron Dose

	Organ	WBCT Dose (Gy)	Hybrid Dose (Gy)	Hybrid % Difference	Scaled MRCP Dose (Gy)	Scaled MRCP % Difference	MRCP Dose (Gy)	MRCP % Difference
In Field	Brain	1.86E-02 (1.86E-02, 1.86E-02)	1.85E-02 (1.85E-02, 1.85E-02)	0.37 (0.17, 0.54)	1.88E-02 (1.88E-02, 1.88E-02)	-0.93 (-1.04, -0.76)	1.62E-02 (1.62E-02, 1.62E-02)	12.82 (12.67, 13.02)
	Eye_L	1.32E-02 (1.32E-02, 1.34E-02)	1.30E-02 (1.26E-02, 1.34E-02)	1.77 (-1.27, 5.65)	1.12E-02 (1.09E-02, 1.17E-02)	15.49 (11.34, 17.74)	9.79E-03 (9.60E-03, 9.89E-03)	26.05 (25.02, 27.30)
	Eye_R	1.06E-02 (1.03E-02, 1.08E-02)	1.05E-02 (1.04E-02, 1.07E-02)	0.85 (-1.11, 3.56)	9.13E-03 (9.00E-03, 9.37E-03)	14.15 (12.45, 15.42)	8.09E-03 (7.90E-03, 8.29E-03)	23.82 (21.89, 27.35)
Near Field	Thyroid	5.90E-03 (5.74E-03, 5.98E-03)	5.87E-03 (5.75E-03, 6.03E-03)	0.25 (-2.08, 1.77)	5.28E-03 (5.20E-03, 5.39E-03)	10.26 (8.41, 14.29)	4.32E-03 (4.22E-03, 4.45E-03)	26.53 (25.50, 29.27)
Far Field	Heart	6.81E-04 (6.74E-04, 6.88E-04)	7.61E-04 (7.54E-04, 7.79E-04)	-11.82 (-13.82, -9.17)	8.65E-04 (8.57E-04, 8.72E-04)	-27.03 (-28.84, -25.44)	6.66E-04 (6.60E-04, 6.69E-04)	2.15 (1.06, 3.63)
	Lungs	7.63E-04 (7.60E-04, 7.71E-04)	1.06E-03 (1.05E-03, 1.07E-03)	-39.48 (-41.12, -36.98)	1.10E-03 (1.09E-03, 1.11E-03)	-44.40 (-45.47, -41.63)	8.92E-04 (8.90E-04, 8.94E-04)	-16.89 (-17.47, -16.02)
	Bladder	4.59E-05 (4.35E-05, 4.85E-05)	4.74E-05 (4.40E-05, 4.95E-05)	-3.94 (-14.65, 7.82)	4.89E-05 (4.55E-05, 5.32E-05)	-7.69 (-22.31, 8.18)	3.39E-05 (3.18E-05, 3.59E-05)	25.53 (22.53, 30.49)

Equivalent Dose using Fluence-Weighted Neutron Energy

	Organ	WBCT Eq. Dose (Sv)	Hybrid Eq. Dose (Sv)	Hybrid % Difference	Scaled MRCP Eq. Dose (Sv)	Scaled MRCP % Difference	MRCP Eq. Dose (Sv)	MRCP % Difference
In Field	Brain	17.00 (17.00, 17.00)	17.03 (17.03, 17.04)	-0.18 (-0.20, -0.17)	17.12 (17.12, 17.13)	-0.71 (-0.73, -0.71)	14.08 (14.08, 14.08)	17.19 (17.18, 17.20)
	Eye_L	4.54 (4.53, 4.54)	4.57 (4.56, 4.58)	-0.82 (-1.16, -0.50)	3.00 (3.00, 3.01)	33.79 (33.67, 33.75)	1.92 (1.92, 1.93)	57.58 (57.34, 57.85)
	Eye_R	1.10 (1.10, 1.10)	1.10 (1.09, 1.10)	0.47 (-0.80, 1.15)	6.59E-01 (6.56E-01, 6.63E-01)	40.24 (39.53, 40.60)	3.34E-01 (3.31E-01, 3.37E-01)	69.72 (69.28, 70.03)
Near Field	Thyroid	1.72E-01 (1.71E-01, 1.73E-01)	1.82E-01 (1.81E-01, 1.84E-01)	-5.87 (-7.07, -5.43)	7.46E-02 (7.37E-02, 7.56E-02)	56.67 (55.92, 56.96)	4.69E-02 (4.57E-02, 4.74E-02)	72.77 (71.91, 73.35)
Far Field	Heart	6.21E-03 (6.15E-03, 6.27E-03)	7.27E-03 (7.19E-03, 7.40E-03)	-17.08 (-19.15, -14.62)	8.36E-03 (8.31E-03, 8.44E-03)	-34.77 (-36.94, -32.99)	6.38E-03 (6.33E-03, 6.42E-03)	-2.77 (-4.50, -0.92)
	Lungs	7.22E-03 (7.19E-03, 7.27E-03)	1.03E-02 (1.02E-02, 1.04E-02)	-43.03 (-44.32, -41.09)	1.06E-02 (1.06E-02, 1.07E-02)	-47.17 (-48.11, -45.03)	8.51E-03 (8.48E-03, 8.54E-03)	-17.99 (-18.39, -17.26)
	Bladder	3.87E-04 (3.67E-04, 4.18E-04)	4.06E-04 (3.77E-04, 4.15E-04)	-6.09 (-22.23, 3.54)	3.97E-04 (3.56E-04, 4.37E-04)	-4.04 (-21.01, 11.95)	2.54E-04 (2.42E-04, 2.68E-04)	33.78 (31.43, 38.16)

Equivalent Dose using KERMA-Weighted Neutron Energy

	Organ	WBCT Eq. Dose (Sv)	Hybrid Eq. Dose (Sv)	Hybrid % Difference	Scaled MRCP Eq. Dose (Sv)	Scaled MRCP % Difference	MRCP Eq. Dose (Sv)	MRCP % Difference
In Field	Brain	17.11 (17.10, 17.11)	17.14 (17.13, 17.14)	-0.18 (-0.20, -0.17)	17.23 (17.23, 17.23)	-0.73 (-0.75, -0.73)	14.18 (14.17, 14.18)	17.13 (17.12, 17.13)
	Eye_L	4.60 (4.60, 4.61)	4.64 (4.62, 4.65)	-0.78 (-1.13, -0.43)	3.06 (3.06, 3.07)	33.48 (33.39, 33.52)	1.98 (1.97, 1.98)	57.07 (56.78, 57.41)
	Eye_R	1.15 (1.15, 1.16)	1.15 (1.15, 1.15)	0.52 (-0.47, 1.28)	7.05E-01 (7.01E-01, 7.08E-01)	38.99 (38.27, 39.51)	3.77E-01 (3.71E-01, 3.81E-01)	67.38 (66.79, 67.92)
Near Field	Thyroid	2.01E-01 (1.99E-01, 2.02E-01)	2.12E-01 (2.10E-01, 2.14E-01)	-5.31 (-6.72, -3.83)	9.70E-02 (9.58E-02, 9.76E-02)	51.73 (51.04, 52.43)	6.52E-02 (6.39E-02, 6.59E-02)	67.51 (67.10, 68.32)
Far Field	Heart	1.03E-02 (1.01E-02, 1.04E-02)	1.18E-02 (1.16E-02, 1.19E-02)	-14.27 (-16.15, -12.80)	1.33E-02 (1.31E-02, 1.34E-02)	-28.74 (-30.91, -25.52)	1.02E-02 (1.01E-02, 1.02E-02)	1.14 (-2.13, 2.98)
	Lungs	1.12E-02 (1.12E-02, 1.13E-02)	1.62E-02 (1.61E-02, 1.63E-02)	-44.79 (-45.62, -43.21)	1.63E-02 (1.62E-02, 1.64E-02)	-45.72 (-45.83, -43.99)	1.32E-02 (1.32E-02, 1.32E-02)	-17.61 (-17.79, -16.96)
	Bladder	4.58E-04 (4.27E-04, 4.90E-04)	4.76E-04 (4.26E-04, 4.93E-04)	-4.94 (-22.88, 8.30)	4.40E-04 (3.99E-04, 4.83E-04)	2.78 (-7.10, 12.46)	2.72E-04 (2.53E-04, 2.96E-04)	40.03 (37.14, 44.88)

Appendix C

This section of the Appendix catalogues the full set of equivalent dose boxplots described in Chapter 5 generated for all the purposes of extending the hybrid verification in preparation for risk modelling analysis. For all boxplots, the central mark is the median, the box edges are the 25th and 75th percentiles, the crosses are outliers (defined as points that are more than 1.5 times the interquartile range away from the 25th and 75th quartiles), and the whiskers extend to the extreme data points not including outliers. Additionally, the ERR counterparts to Figures 5.7 and 5.8 depicting the EAR are also included.

C.1 Equivalent Dose Boxplots

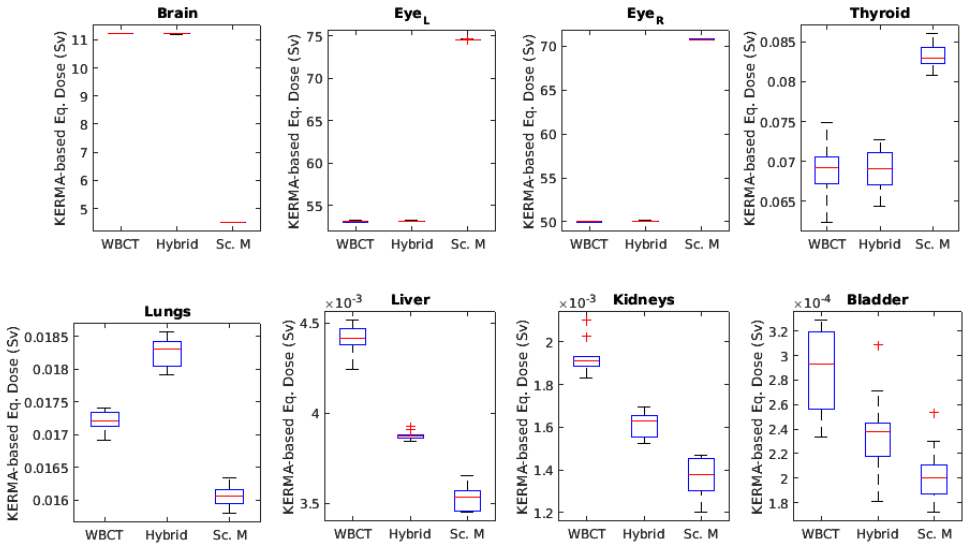

Figure C.1: Boxplots of the KERMA-weighted equivalent dose in Sv for the in- and near-field (brain, left eye, right eye, thyroid) and out-of-field (lungs, liver, kidneys, bladder) organs from the Pat 1 treatment plan for the three patient representations (WBCT, hybrid, and scaled MRCP).

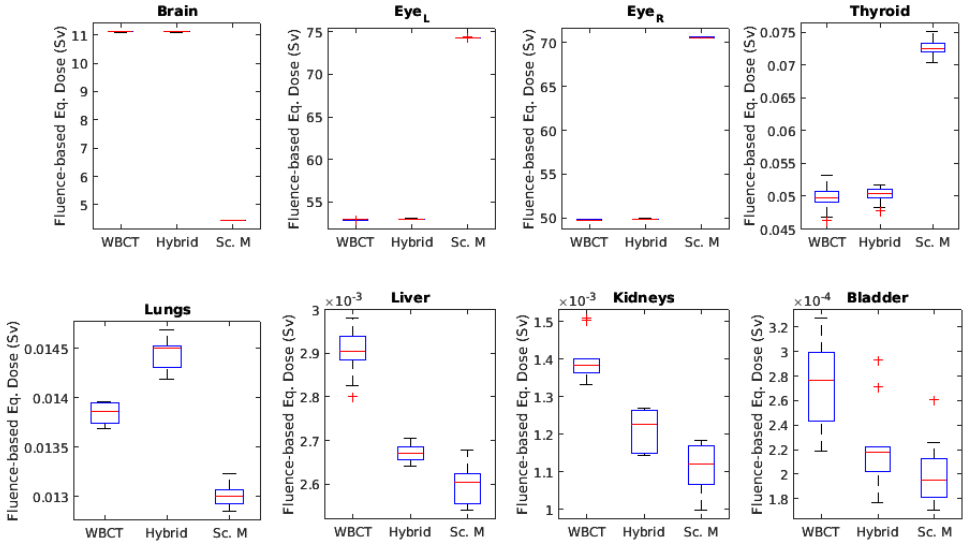

Figure C.2: Boxplots of the fluence-weighted equivalent dose in Sv for the in- and near-field (brain, left eye, right eye, thyroid) and out-of-field (lungs, liver, kidneys, bladder) organs from the Pat 1 treatment plan for the three patient representations (WBCT, hybrid, and scaled MRCP).

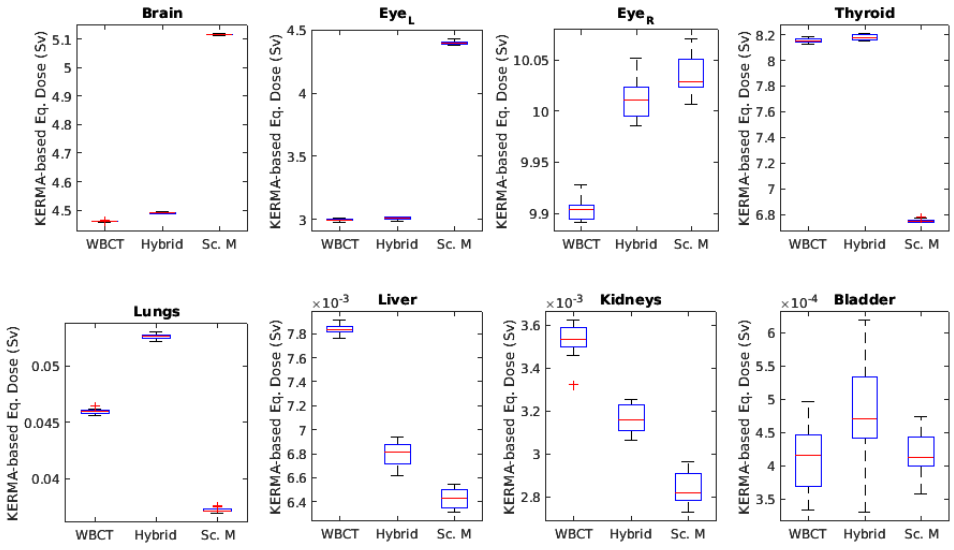

Figure C.3: Boxplots of the KERMA-weighted equivalent dose in Sv for the in- and near-field (brain, left eye, right eye, thyroid) and out-of-field (lungs, liver, kidneys, bladder) organs from the Pat 2 treatment plan for the three patient representations (WBCT, hybrid, and scaled MRCP).

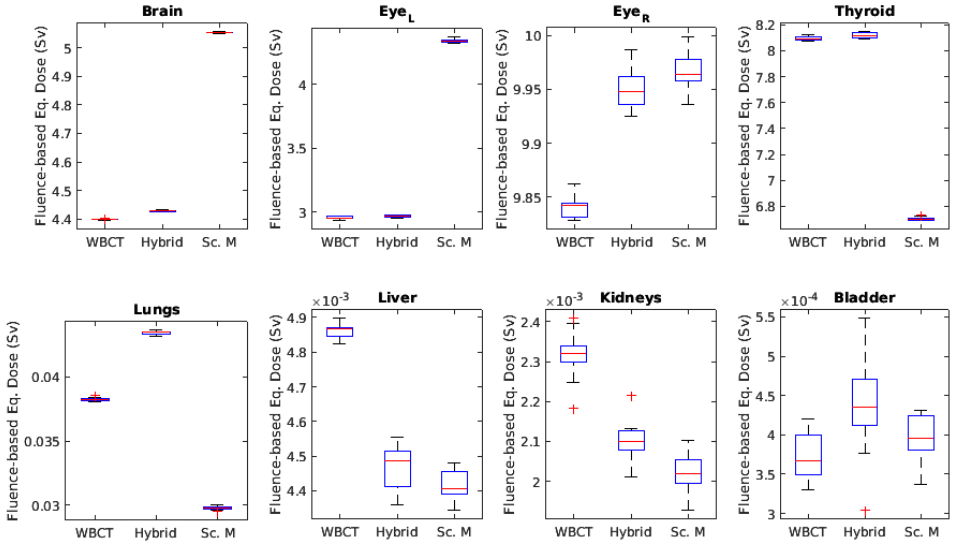

Figure C.4: Boxplots of the fluence-weighted equivalent dose in Sv for the in- and near-field (brain, left eye, right eye, thyroid) and out-of-field (lungs, liver, kidneys, bladder) organs from the Pat 2 treatment plan for the three patient representations (WBCT, hybrid, and scaled MRCP).

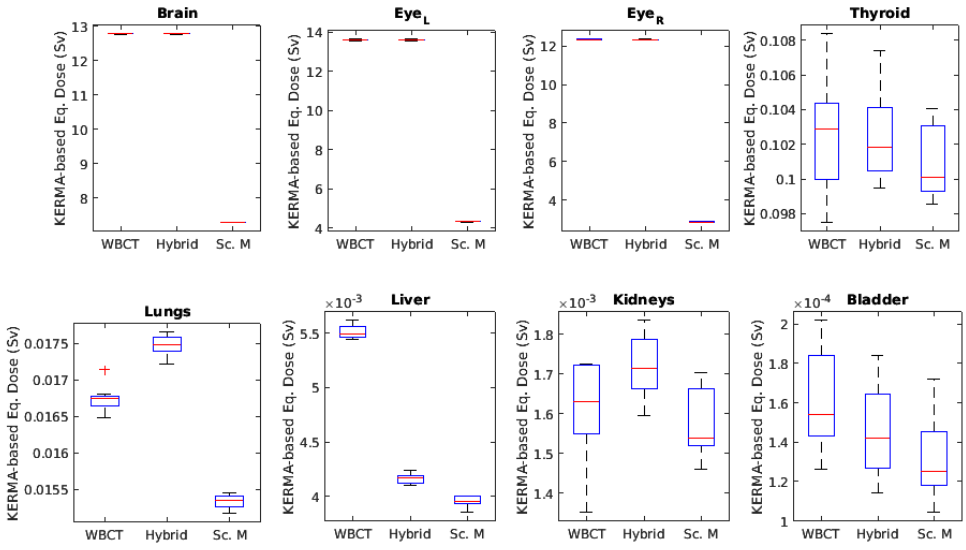

Figure C.5: Boxplots of the KERMA-weighted equivalent dose in Sv for the in- and near-field (brain, left eye, right eye, thyroid) and out-of-field (lungs, liver, kidneys, bladder) organs from the Pat 3 treatment plan for the three patient representations (WBCT, hybrid, and scaled MRCP).

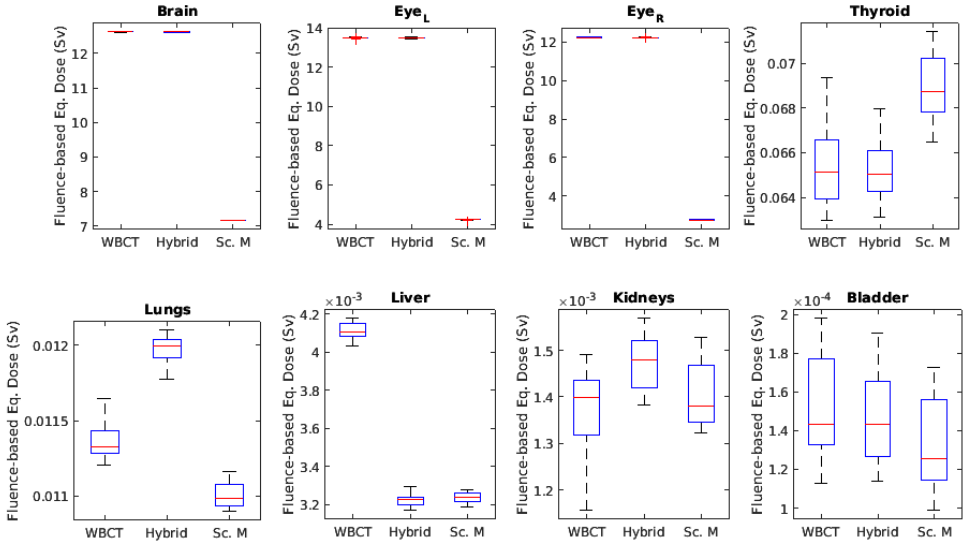

Figure C.6: Boxplots of the fluence-weighted equivalent dose in Sv for the in- and near-field (brain, left eye, right eye, thyroid) and out-of-field (lungs, liver, kidneys, bladder) organs from the Pat 3 treatment plan for the three patient representations (WBCT, hybrid, and scaled MRCP).

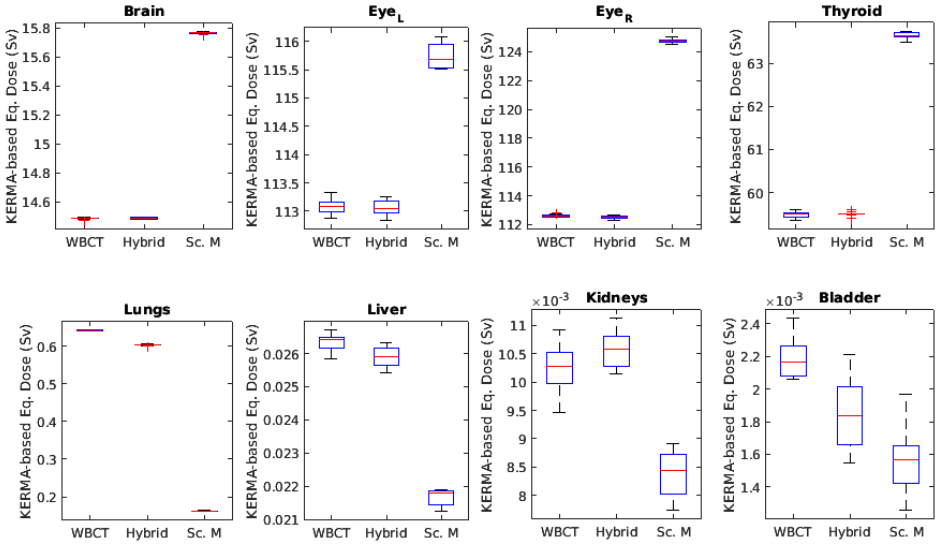

Figure C.7: Boxplots of the KERMA-weighted equivalent dose in Sv for the in- and near-field (brain, left eye, right eye, thyroid) and out-of-field (lungs, liver, kidneys, bladder) organs from the Pat 4 treatment plan for the three patient representations (WBCT, hybrid, and scaled MRCP).

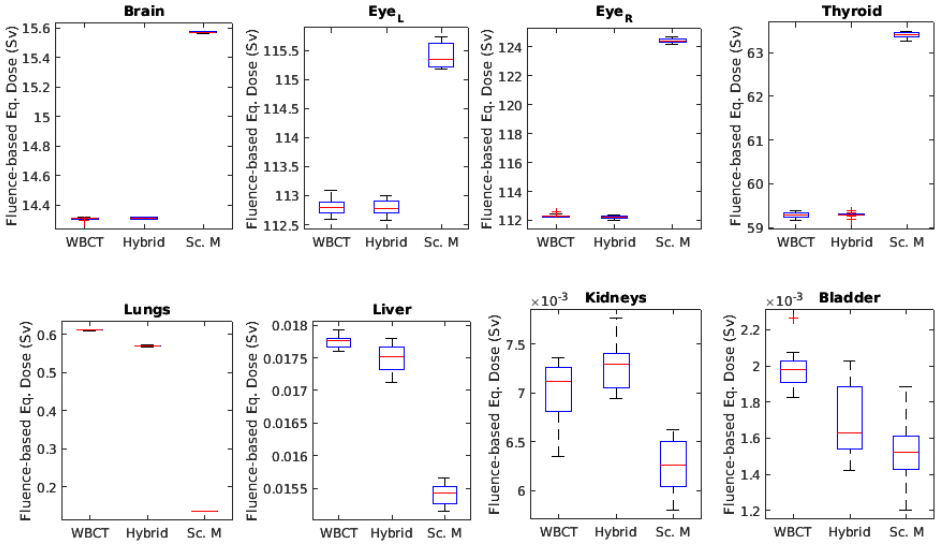

Figure C.8: Boxplots of the fluence-weighted equivalent dose in Sv for the in- and near-field (brain, left eye, right eye, thyroid) and out-of-field (lungs, liver, kidneys, bladder) organs from the Pat 4 treatment plan for the three patient representations (WBCT, hybrid, and scaled MRCP).

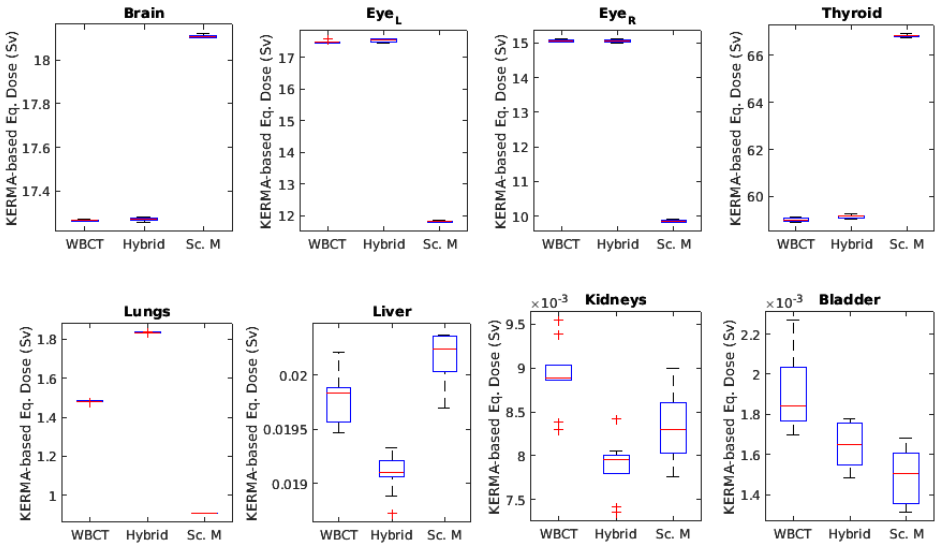

Figure C.9: Boxplots of the KERMA-weighted equivalent dose in Sv for the in- and near-field (brain, left eye, right eye, thyroid) and out-of-field (lungs, liver, kidneys, bladder) organs from the Pat 5 treatment plan for the three patient representations (WBCT, hybrid, and scaled MRCP).

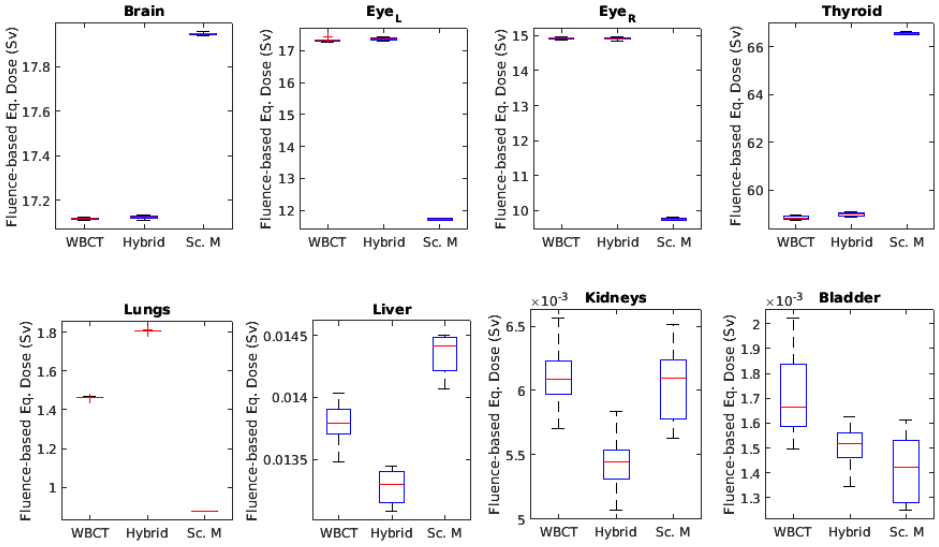

Figure C.10: Boxplots of the fluence-weighted equivalent dose in Sv for the in- and near-field (brain, left eye, right eye, thyroid) and out-of-field (lungs, liver, kidneys, bladder) organs from the Pat 5 treatment plan for the three patient representations (WBCT, hybrid, and scaled MRCP).

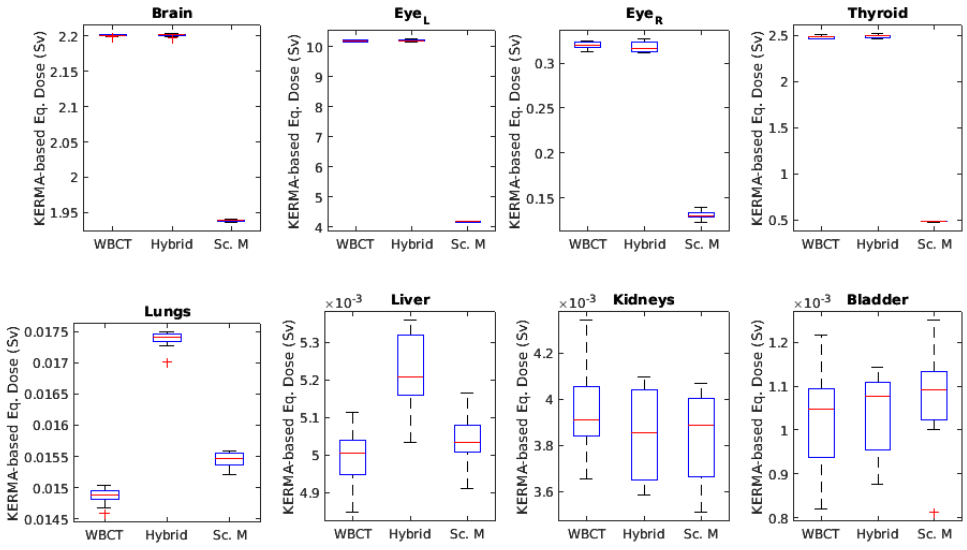

Figure C.11: Boxplots of the KERMA-weighted equivalent dose in Sv for the in- and near-field (brain, left eye, right eye, thyroid) and out-of-field (lungs, liver, kidneys, bladder) organs from the Pat 6 treatment plan for the three patient representations (WBCT, hybrid, and scaled MRCP).

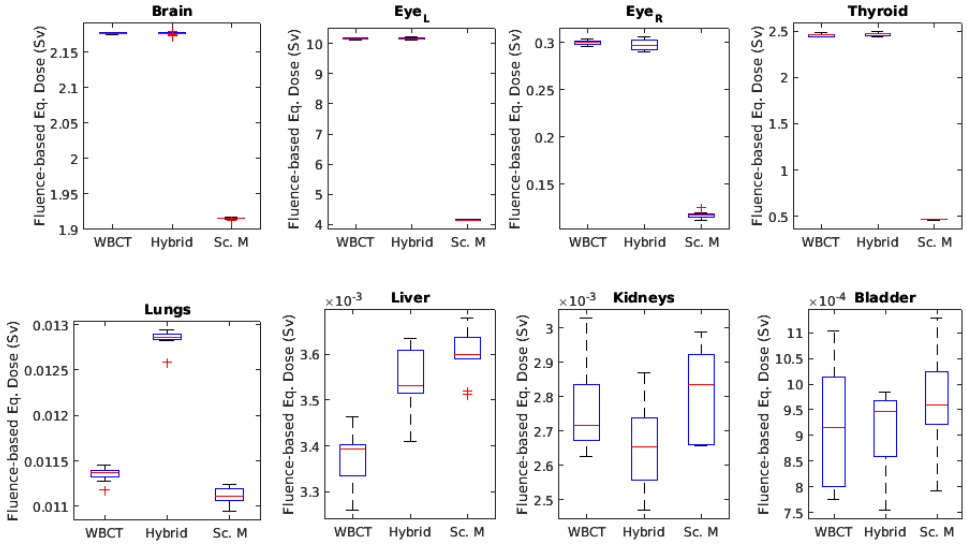

Figure C.12: Boxplots of the fluence-weighted equivalent dose in Sv for the in- and near-field (brain, left eye, right eye, thyroid) and out-of-field (lungs, liver, kidneys, bladder) organs from the Pat 6 treatment plan for the three patient representations (WBCT, hybrid, and scaled MRCP).

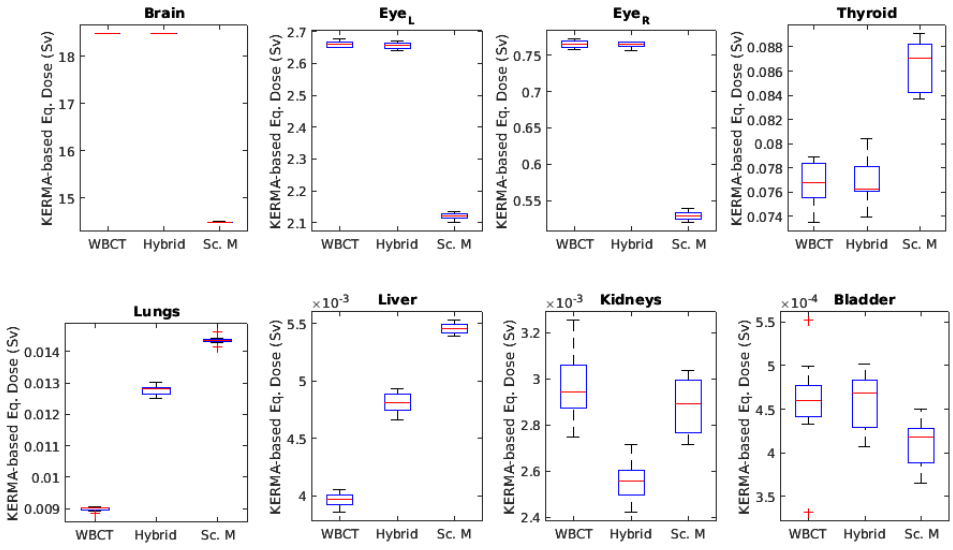

Figure C.13: Boxplots of the KERMA-weighted equivalent dose in Sv for the in- and near-field (brain, left eye, right eye, thyroid) and out-of-field (lungs, liver, kidneys, bladder) organs from the Pat 7 treatment plan for the three patient representations (WBCT, hybrid, and scaled MRCP).

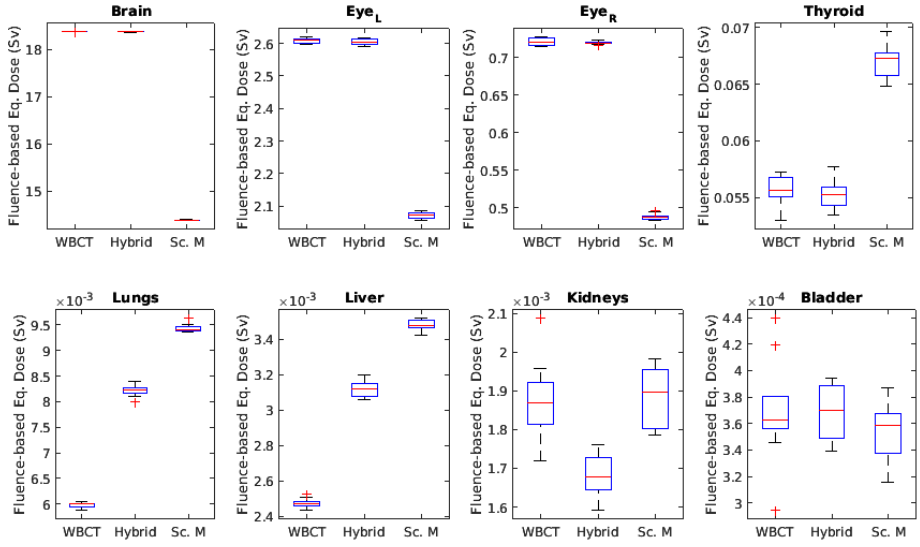

Figure C.14: Boxplots of the fluence-weighted equivalent dose in Sv for the in- and near-field (brain, left eye, right eye, thyroid) and out-of-field (lungs, liver, kidneys, bladder) organs from the Pat 7 treatment plan for the three patient representations (WBCT, hybrid, and scaled MRCP).

C.2 ERR Risk Figures

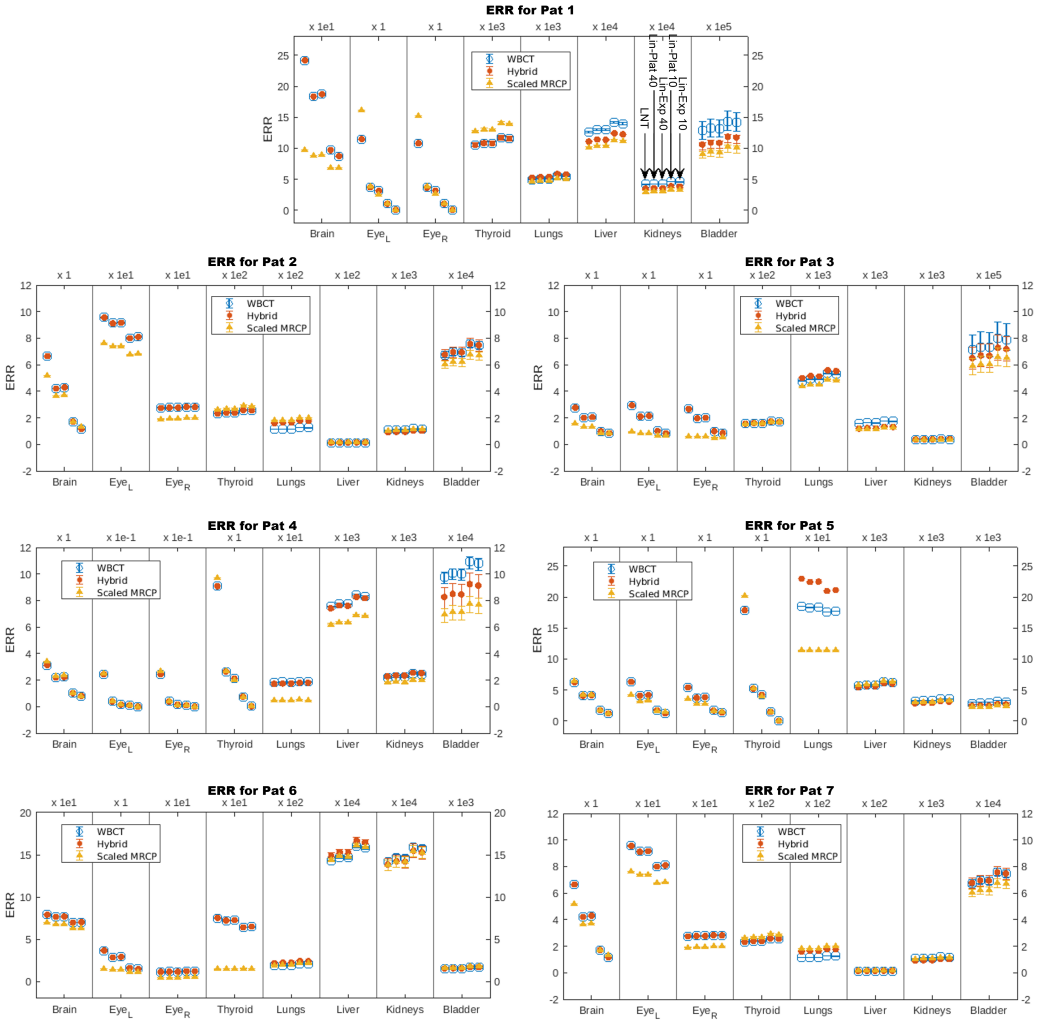

Figure C.15: A comparison of the ERR predictions using the KERMA-weighted neutron energy scorer for equivalent dose for the 5 risk models across all 7 patients, all 8 selected organs, and all 3 patient representations. Each column corresponds to a particular organ where the WBCT, hybrid, and scaled MRCP are represented by an open circle, a filled circle, and a filled triangle respectively. Within a particular column, there are five points from left to right corresponding to each risk model. From left to right: linear no-threshold (LNT), linear-plateau with inflection at 40 Sv, linear-exponential with inflection at 40 Sv, linear-plateau with inflection at 10 Sv, and linear-exponential with inflection at 10 Sv. For visibility, the predicted risk for all models was multiplied by the power of 10 at the top of each of their respective columns. Error bars representing the 25th and 75th percentile are given for every measurement, but are only visible in some very far out-of-field organs.

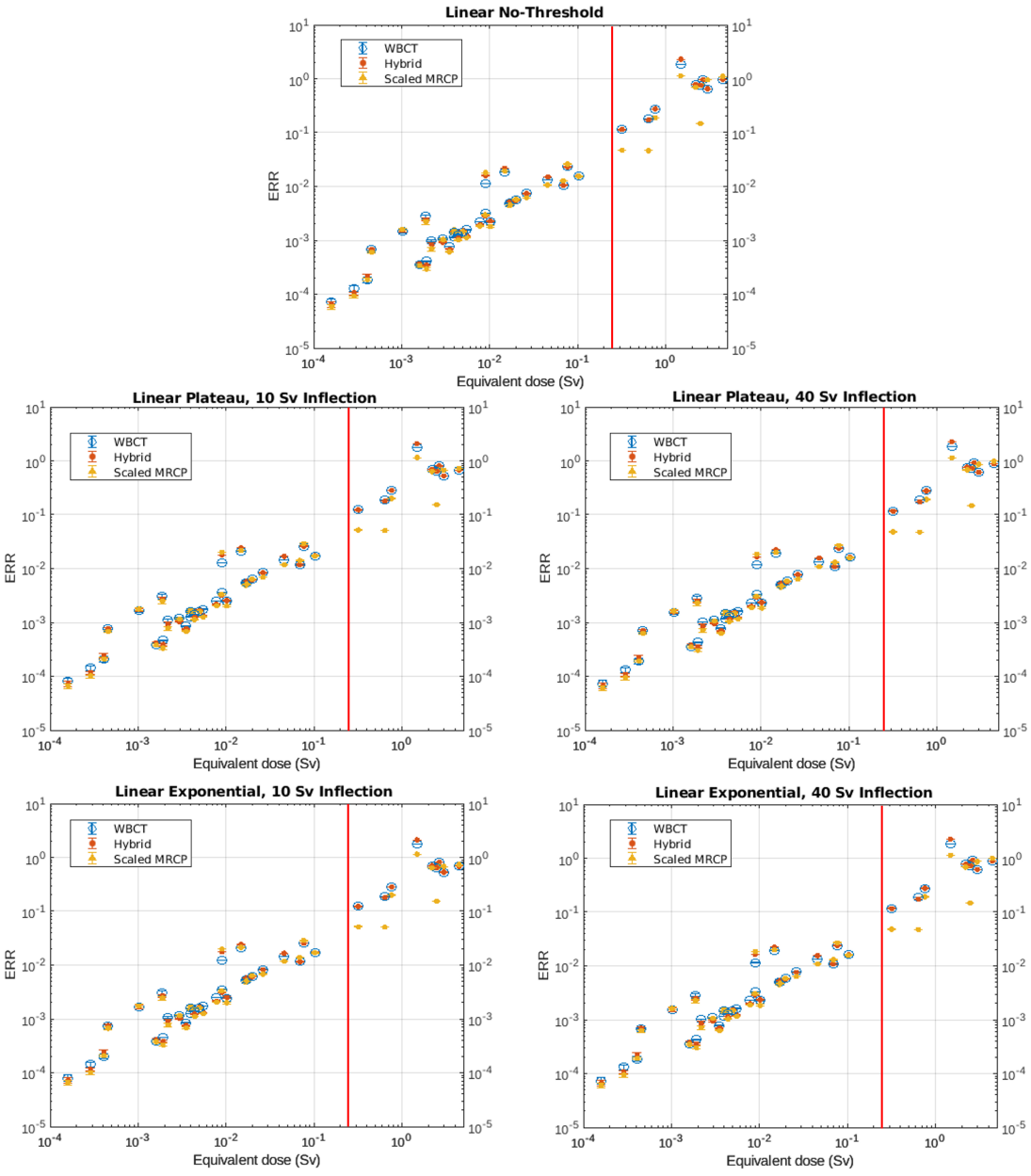

Figure C.16: The predicted ERR for all organs across all patients. The linear portion of each model is consistent between all models in the low dose region (<2.5 Sv), that region of commonality has been marked by a vertical line in all subfigures for easy reference.

Appendix D

The full quantitative data for equivalent dose and risk prediction for the work described in Chapter 5.

D.1 Equivalent Dose Tables

Table D.1: Equivalent dose in Pat 1 using both fluence- and KERMA-weighted neutron energy scorers

Patient 1

Equivalent Dose using Fluence-Weighted Neutron Energy

	Organ	WBCT Eq. Dose (Sv)		Hybrid Eq. Dose (Sv)		% Difference	Scaled MRCP Eq. Dose (Sv)		% Difference
In Field	Brain	11.11	(11.11 , 11.11)	11.11	(11.11 , 11.11)	0.00 (-0.02 , 0.04)	4.46	(4.46 , 4.46)	59.88 (59.86 , 59.90)
	Eye_L	52.89	(52.86 , 52.91)	52.95	(52.92 , 52.97)	-0.12 (-0.18 , -0.08)	74.34	(74.32 , 74.35)	-40.54 (-40.66 , -40.46)
	Eye_R	49.79	(49.76 , 49.83)	49.87	(49.85 , 49.90)	-0.16 (-0.27 , -0.06)	70.56	(70.53 , 70.60)	-41.70 (-41.85 , -41.58)
Near Field	Thyroid	4.98E-02	(4.91E-02 , 5.07E-02)	5.01E-02	(4.98E-02 , 5.11E-02)	-0.73 (-3.67 , 3.84)	7.26E-02	(7.21E-02 , 7.33E-02)	-46.03 (-49.67 , -39.12)
Far Field	Lungs	1.38E-02	(1.37E-02 , 1.39E-02)	1.44E-02	(1.43E-02 , 1.45E-02)	-4.32 (-6.11 , -3.23)	1.30E-02	(1.29E-02 , 1.31E-02)	6.08 (5.10 , 6.84)
	Liver	2.90E-03	(2.89E-03 , 2.94E-03)	2.67E-03	(2.66E-03 , 2.69E-03)	8.00 (7.19 , 8.89)	2.60E-03	(2.55E-03 , 2.62E-03)	10.42 (8.10 , 12.65)
	Kidneys	1.40E-03	(1.36E-03 , 1.40E-03)	1.21E-03	(1.15E-03 , 1.26E-03)	13.39 (8.30 , 16.91)	1.11E-03	(1.07E-03 , 1.17E-03)	20.44 (16.57 , 21.91)
	Bladder	2.73E-04	(2.43E-04 , 2.99E-04)	2.23E-04	(2.02E-04 , 2.22E-04)	16.70 (7.71 , 25.32)	2.01E-04	(1.81E-04 , 2.13E-04)	24.94 (13.40 , 34.99)

Equivalent Dose using KERMA-Weighted Neutron Energy

	Organ	WBCT Eq. Dose (Sv)		Hybrid Eq. Dose (Sv)		% Difference	Scaled MRCP Eq. Dose (Sv)		% Difference
In Field	Brain	11.21	(11.20 , 11.21)	11.21	(11.20 , 11.21)	0.00 (-0.02 , 0.04)	4.52	(4.52 , 4.52)	59.65 (59.63 , 59.67)
	Eye_L	53.08	(53.04 , 53.11)	53.15	(53.12 , 53.16)	-0.13 (-0.19 , -0.10)	74.54	(74.53 , 74.55)	-40.42 (-40.53 , -40.35)
	Eye_R	50.00	(49.96 , 50.03)	50.07	(50.05 , 50.10)	-0.15 (-0.27 , -0.07)	70.77	(70.73 , 70.81)	-41.55 (-41.68 , -41.45)
Near Field	Thyroid	6.89E-02	(6.72E-02 , 7.06E-02)	6.90E-02	(6.70E-02 , 7.11E-02)	-0.39 (-2.50 , 2.87)	8.32E-02	(8.23E-02 , 8.43E-02)	-21.23 (-26.18 , -14.54)
Far Field	Lungs	1.72E-02	(1.71E-02 , 1.73E-02)	1.83E-02	(1.81E-02 , 1.84E-02)	-6.10 (-7.15 , -5.01)	1.61E-02	(1.60E-02 , 1.62E-02)	6.61 (6.09 , 7.05)
	Liver	4.41E-03	(4.38E-03 , 4.47E-03)	3.88E-03	(3.86E-03 , 3.88E-03)	12.08 (10.69 , 13.97)	3.53E-03	(3.46E-03 , 3.57E-03)	19.97 (18.15 , 21.75)
	Kidneys	1.93E-03	(1.88E-03 , 1.93E-03)	1.61E-03	(1.55E-03 , 1.66E-03)	16.39 (12.13 , 20.81)	1.37E-03	(1.30E-03 , 1.45E-03)	28.74 (24.67 , 30.88)
	Bladder	2.87E-04	(2.57E-04 , 3.19E-04)	2.37E-04	(2.17E-04 , 2.45E-04)	16.05 (5.79 , 24.36)	2.04E-04	(1.87E-04 , 2.10E-04)	27.48 (17.62 , 36.78)

Table D.2: Equivalent dose in Pat 2 using both fluence- and KERMA-weighted neutron energy scorers

Patient 2

Equivalent Dose using Fluence-Weighted Neutron Energy

	Organ	WBCT Eq. Dose (Sv)	Hybrid Eq. Dose (Sv)	Hybrid % Difference		Scaled MRCP Eq. Dose (Sv)	Scaled MRCP % Difference
In Field	Brain	4.40 (4.40 , 4.40)	4.43 (4.43 , 4.43)	-0.66 (-0.70 , -0.64)	5.05	(5.05 , 5.05)	-14.88 (-14.91 , -14.81)
	Eye_L	2.95 (2.95 , 2.96)	2.96 (2.96 , 2.97)	-0.30 (-0.76 , 0.21)	4.34	(4.33 , 4.35)	-46.93 (-47.64 , -46.15)
	Eye_R	9.84 (9.83 , 9.84)	9.95 (9.94 , 9.96)	-1.12 (-1.19 , -1.01)	9.97	(9.96 , 9.98)	-1.29 (-1.50 , -1.14)
Near Field	Thyroid	8.09 (8.08 , 8.11)	8.12 (8.10 , 8.14)	-0.30 (-0.54 , 0.00)	6.70	(6.69 , 6.70)	17.17 (17.02 , 17.27)
Far Field	Lungs	3.83E-02 (3.82E-02 , 3.83E-02)	4.35E-02 (4.33E-02 , 4.35E-02)	-13.57 (-14.00 , -13.34)	2.98E-02	(2.97E-02 , 2.98E-02)	22.18 (22.06 , 22.39)
	Liver	4.86E-03 (4.85E-03 , 4.87E-03)	4.47E-03 (4.41E-03 , 4.52E-03)	8.12 (6.91 , 9.42)	4.41E-03	(4.39E-03 , 4.46E-03)	9.18 (8.46 , 9.62)
	Kidneys	2.32E-03 (2.30E-03 , 2.34E-03)	2.10E-03 (2.08E-03 , 2.13E-03)	9.16 (8.33 , 12.33)	2.02E-03	(1.99E-03 , 2.06E-03)	12.61 (11.43 , 13.56)
	Bladder	3.72E-04 (3.50E-04 , 4.00E-04)	4.35E-04 (4.11E-04 , 4.71E-04)	-18.24 (-33.59 , -10.49)	3.97E-04	(3.80E-04 , 4.25E-04)	-7.02 (-13.46 , -1.82)

Equivalent Dose using KERMA-Weighted Neutron Energy

	Organ	WBCT Eq. Dose (Sv)	Hybrid Eq. Dose (Sv)	Hybrid % Difference		Scaled MRCP Eq. Dose (Sv)	Scaled MRCP % Difference
In Field	Brain	4.46 (4.46 , 4.46)	4.49 (4.49 , 4.49)	-0.64 (-0.68 , -0.61)	5.12	(5.11 , 5.12)	-14.66 (-14.69 , -14.60)
	Eye_L	3.00 (2.99 , 3.01)	3.01 (3.00 , 3.02)	-0.35 (-0.86 , 0.14)	4.40	(4.38 , 4.41)	-46.67 (-47.48 , -45.81)
	Eye_R	9.90 (9.89 , 9.91)	10.01 (9.99 , 10.02)	-1.10 (-1.21 , -0.97)	10.04	(10.02 , 10.05)	-1.33 (-1.59 , -1.11)
Near Field	Thyroid	8.15 (8.14 , 8.17)	8.18 (8.16 , 8.20)	-0.32 (-0.56 , 0.01)	6.75	(6.74 , 6.75)	17.16 (16.94 , 17.27)
Far Field	Lungs	4.60E-02 (4.58E-02 , 4.61E-02)	5.26E-02 (5.25E-02 , 5.28E-02)	-14.51 (-15.29 , -13.96)	3.72E-02	(3.71E-02 , 3.73E-02)	19.06 (18.95 , 19.39)
	Liver	7.83E-03 (7.81E-03 , 7.86E-03)	6.78E-03 (6.71E-03 , 6.87E-03)	13.40 (11.96 , 14.38)	6.43E-03	(6.35E-03 , 6.50E-03)	17.94 (17.08 , 18.45)
	Kidneys	3.53E-03 (3.50E-03 , 3.59E-03)	3.16E-03 (3.11E-03 , 3.23E-03)	10.24 (9.16 , 11.91)	2.84E-03	(2.78E-03 , 2.91E-03)	19.48 (18.88 , 21.14)
	Bladder	4.10E-04 (3.70E-04 , 4.46E-04)	4.78E-04 (4.42E-04 , 5.34E-04)	-18.62 (-38.70 , -6.59)	4.17E-04	(3.99E-04 , 4.43E-04)	-2.66 (-11.23 , 4.49)

Table D.3: Equivalent dose in Pat 3 using both fluence- and KERMA-weighted neutron energy scorers

Patient 3

Equivalent Dose using Fluence-Weighted Neutron Energy

	Organ	WBCT Eq. Dose (Sv)	Hybrid Eq. Dose (Sv)	Hybrid % Difference	Scaled MRCP Eq. Dose (Sv)	Scaled MRCP % Difference
In Field	Brain	12.62 (12.62 , 12.62)	12.62 (12.61 , 12.62)	0.01 (-0.01 , 0.03)	7.18 (7.18 , 7.18)	43.10 (43.09 , 43.11)
	Eye_L	13.50 (13.49 , 13.50)	13.50 (13.47 , 13.52)	0.00 (-0.14 , 0.24)	4.23 (4.23 , 4.24)	68.64 (68.53 , 68.76)
	Eye_R	12.22 (12.21 , 12.24)	12.22 (12.21 , 12.22)	0.04 (-0.06 , 0.11)	2.76 (2.75 , 2.77)	77.42 (77.35 , 77.47)
Near Field	Thyroid	6.55E-02 (6.40E-02 , 6.66E-02)	6.52E-02 (6.43E-02 , 6.61E-02)	0.38 (-2.57 , 3.46)	6.89E-02 (6.78E-02 , 7.02E-02)	-5.16 (-7.51 , -3.68)
Far Field	Lungs	1.14E-02 (1.13E-02 , 1.14E-02)	1.20E-02 (1.19E-02 , 1.20E-02)	-5.41 (-6.63 , -4.68)	1.10E-02 (1.09E-02 , 1.11E-02)	3.14 (2.60 , 3.86)
	Liver	4.11E-03 (4.08E-03 , 4.15E-03)	3.22E-03 (3.20E-03 , 3.24E-03)	21.54 (20.45 , 22.63)	3.24E-03 (3.22E-03 , 3.26E-03)	21.23 (20.68 , 21.90)
	Kidneys	1.37E-03 (1.32E-03 , 1.44E-03)	1.47E-03 (1.42E-03 , 1.52E-03)	-7.86 (-9.64 , -1.63)	1.41E-03 (1.35E-03 , 1.47E-03)	-2.88 (-3.46 , -0.40)
	Bladder	1.51E-04 (1.33E-04 , 1.77E-04)	1.46E-04 (1.26E-04 , 1.65E-04)	1.21 (-12.18 , 15.91)	1.31E-04 (1.14E-04 , 1.56E-04)	11.35 (0.55 , 25.12)

Equivalent Dose using KERMA-Weighted Neutron Energy

	Organ	WBCT Eq. Dose (Sv)	Hybrid Eq. Dose (Sv)	Hybrid % Difference	Scaled MRCP Eq. Dose (Sv)	Scaled MRCP % Difference
In Field	Brain	12.78 (12.78 , 12.78)	12.78 (12.78 , 12.78)	0.01 (-0.01 , 0.03)	7.30 (7.30 , 7.30)	42.90 (42.89 , 42.91)
	Eye_L	13.62 (13.61 , 13.64)	13.62 (13.59 , 13.64)	0.02 (-0.15 , 0.24)	4.33 (4.32 , 4.35)	68.19 (68.05 , 68.34)
	Eye_R	12.35 (12.34 , 12.36)	12.35 (12.33 , 12.35)	0.03 (-0.08 , 0.12)	2.85 (2.84 , 2.86)	76.91 (76.83 , 76.95)
Near Field	Thyroid	1.03E-01 (1.00E-01 , 1.04E-01)	1.02E-01 (1.00E-01 , 1.04E-01)	0.11 (-3.60 , 3.72)	1.01E-01 (9.93E-02 , 1.03E-01)	1.48 (0.19 , 3.96)
Far Field	Lungs	1.67E-02 (1.66E-02 , 1.68E-02)	1.75E-02 (1.74E-02 , 1.76E-02)	-4.54 (-5.48 , -3.88)	1.53E-02 (1.53E-02 , 1.54E-02)	8.35 (7.72 , 9.06)
	Liver	5.52E-03 (5.47E-03 , 5.57E-03)	4.17E-03 (4.12E-03 , 4.19E-03)	24.46 (23.87 , 25.06)	3.95E-03 (3.94E-03 , 4.00E-03)	28.30 (28.00 , 29.01)
	Kidneys	1.61E-03 (1.55E-03 , 1.72E-03)	1.72E-03 (1.66E-03 , 1.79E-03)	-7.23 (-9.42 , -0.90)	1.57E-03 (1.52E-03 , 1.66E-03)	1.85 (-2.88 , 6.46)
	Bladder	1.60E-04 (1.43E-04 , 1.84E-04)	1.46E-04 (1.27E-04 , 1.65E-04)	7.36 (-5.18 , 17.61)	1.32E-04 (1.18E-04 , 1.45E-04)	15.94 (10.64 , 30.93)

Table D.4: Equivalent dose in Pat 4 using both fluence- and KERMA-weighted neutron energy scorers

Patient 4

Equivalent Dose using Fluence-Weighted Neutron Energy

	Organ	WBCT Eq. Dose (Sv)	Hybrid Eq. Dose (Sv)	Hybrid % Difference	Scaled MRCP Eq. Dose (Sv)	Scaled MRCP % Difference
In Field	Brain	14.31 (14.31 , 14.31)	14.31 (14.31 , 14.32)	-0.02 (-0.06 , 0.02)	15.57 (15.57 , 15.57)	-8.81 (-8.83 , -8.78)
	Eye_L	112.82 (112.71 , 112.88)	112.80 (112.70 , 112.91)	0.02 (-0.13 , 0.18)	115.42 (115.22 , 115.62)	-2.31 (-2.56 , -2.15)
	Eye_R	112.31 (112.21 , 112.32)	112.23 (112.12 , 112.32)	0.07 (-0.01 , 0.17)	124.41 (124.32 , 124.51)	-10.78 (-10.86 , -10.73)
Near Field	Thyroid	59.28 (59.23 , 59.32)	59.29 (59.29 , 59.30)	-0.02 (-0.11 , 0.05)	63.40 (63.36 , 63.46)	-6.94 (-7.07 , -6.83)
Far Field	Lungs	6.11E-01 (6.11E-01 , 6.12E-01)	5.69E-01 (5.69E-01 , 5.70E-01)	6.86 (6.67 , 7.07)	1.37E-01 (1.37E-01 , 1.37E-01)	77.61 (77.55 , 77.68)
	Liver	1.77E-02 (1.77E-02 , 1.78E-02)	1.75E-02 (1.73E-02 , 1.77E-02)	1.39 (0.39 , 2.62)	1.54E-02 (1.53E-02 , 1.55E-02)	13.24 (12.51 , 13.99)
	Kidneys	7.01E-03 (6.80E-03 , 7.26E-03)	7.29E-03 (7.05E-03 , 7.40E-03)	-4.25 (-8.79 , -0.90)	6.27E-03 (6.05E-03 , 6.50E-03)	10.31 (3.37 , 16.52)
	Bladder	1.99E-03 (1.91E-03 , 2.02E-03)	1.67E-03 (1.54E-03 , 1.88E-03)	15.74 (5.30 , 24.86)	1.52E-03 (1.42E-03 , 1.61E-03)	23.51 (17.21 , 30.83)

Equivalent Dose using KERMA-Weighted Neutron Energy

	Organ	WBCT Eq. Dose (Sv)	Hybrid Eq. Dose (Sv)	Hybrid % Difference	Scaled MRCP Eq. Dose (Sv)	Scaled MRCP % Difference
In Field	Brain	14.49 (14.48 , 14.49)	14.49 (14.48 , 14.49)	-0.02 (-0.05 , 0.00)	15.77 (15.76 , 15.77)	-8.84 (-8.87 , -8.81)
	Eye_L	113.10 (113.00 , 113.16)	113.07 (112.98 , 113.19)	0.02 (-0.11 , 0.18)	115.75 (115.52 , 115.94)	-2.34 (-2.60 , -2.19)
	Eye_R	112.60 (112.51 , 112.64)	112.52 (112.43 , 112.60)	0.07 (0.00 , 0.14)	124.75 (124.69 , 124.84)	-10.80 (-10.86 , -10.72)
Near Field	Thyroid	59.48 (59.42 , 59.53)	59.50 (59.50 , 59.51)	-0.03 (-0.16 , 0.06)	63.64 (63.61 , 63.71)	-6.99 (-7.08 , -6.88)
Far Field	Lungs	6.41E-01 (6.40E-01 , 6.42E-01)	6.03E-01 (6.02E-01 , 6.04E-01)	5.95 (5.68 , 6.24)	1.62E-01 (1.62E-01 , 1.63E-01)	74.68 (74.55 , 74.80)
	Liver	2.64E-02 (2.62E-02 , 2.65E-02)	2.59E-02 (2.57E-02 , 2.61E-02)	1.69 (0.89 , 2.70)	2.16E-02 (2.14E-02 , 2.19E-02)	17.88 (17.30 , 18.76)
	Kidneys	1.02E-02 (9.98E-03 , 1.05E-02)	1.06E-02 (1.03E-02 , 1.08E-02)	-3.80 (-8.54 , 2.35)	8.37E-03 (8.02E-03 , 8.73E-03)	17.89 (11.40 , 24.10)
	Bladder	2.19E-03 (2.08E-03 , 2.26E-03)	1.85E-03 (1.66E-03 , 2.01E-03)	15.66 (8.67 , 24.19)	1.55E-03 (1.42E-03 , 1.65E-03)	28.96 (23.44 , 36.16)

Table D.5: Equivalent dose in Pat 5 using both fluence- and KERMA-weighted neutron energy scorers

Patient 5

Equivalent Dose using Fluence-Weighted Neutron Energy

	Organ	WBCT Eq. Dose (Sv)	Hybrid Eq. Dose (Sv)	Hybrid % Difference	Scaled MRCP Eq. Dose (Sv)	Scaled MRCP % Difference
In Field	Brain	17.12 (17.11 , 17.12)	17.12 (17.12 , 17.13)	-0.04 (-0.08 , -0.02)	17.95 (17.94 , 17.95)	-4.84 (-4.87 , -4.81)
	Eye_L	17.34 (17.31 , 17.34)	17.37 (17.34 , 17.41)	-0.223359 (-0.62 , 0.14)	11.72 (11.70 , 11.74)	32.40 (32.23 , 32.54)
	Eye_R	14.92 (14.89 , 14.94)	14.92 (14.89 , 14.95)	0.01 (-0.21 , 0.20)	9.75 (9.73 , 9.77)	34.62 (34.36 , 34.83)
Near Field	Thyroid	58.82 (58.76 , 58.89)	58.97 (58.90 , 59.02)	-0.25 (-0.46 , -0.07)	66.56 (66.52 , 66.59)	-13.16 (-13.24 , -13.12)
Far Field	Lungs	1.46 (1.46 , 1.47)	1.81 (1.81 , 1.81)	-23.47 (-23.56 , -23.37)	0.87872896 (8.78E-01 , 8.79E-01)	40.01 (39.96 , 40.05)
	Liver	1.38E-02 (1.37E-02 , 1.39E-02)	0.0132828 (1.31E-02 , 1.34E-02)	3.54 (2.64 , 4.82)	0.01434345 (1.42E-02 , 1.45E-02)	-4.16 (-4.71 , -3.02)
	Kidneys	6.11E-03 (5.97E-03 , 6.23E-03)	0.0054181 (5.31E-03 , 5.54E-03)	11.19 (8.78 , 17.20)	0.00604031 (5.78E-03 , 6.24E-03)	0.93 (-6.20 , 7.69)
	Bladder	1.72E-03 (1.59E-03 , 1.84E-03)	0.001503 (1.46E-03 , 1.56E-03)	11.75 (6.37 , 20.38)	0.00142989 (1.28E-03 , 1.53E-03)	16.11 (9.17 , 24.24)

Equivalent Dose using KERMA-Weighted Neutron Energy

	Organ	WBCT Eq. Dose (Sv)	Hybrid Eq. Dose (Sv)	Hybrid % Difference	Scaled MRCP Eq. Dose (Sv)	Scaled MRCP % Difference
In Field	Brain	17.27 (17.26 , 17.27)	17.27 (17.27 , 17.28)	-0.04 (-0.08 , -0.02)	18.11 (18.10 , 18.11)	-4.89 (-4.93 , -4.86)
	Eye_L	17.49 (17.45 , 17.49)	17.53 (17.49 , 17.57)	-0.223733 (-0.62 , 0.20)	11.82 (11.80 , 11.84)	32.40 (32.22 , 32.54)
	Eye_R	15.06 (15.04 , 15.09)	15.06 (15.03 , 15.09)	0.02 (-0.23 , 0.23)	9.86 (9.83 , 9.88)	34.56 (34.29 , 34.78)
Near Field	Thyroid	59.00 (58.95 , 59.07)	59.15 (59.08 , 59.19)	-0.25 (-0.46 , -0.06)	66.82 (66.78 , 66.84)	-13.25 (-13.34 , -13.21)
Far Field	Lungs	1.48 (1.48 , 1.48)	1.83 (1.83 , 1.84)	-23.79 (-23.85 , -23.67)	0.90824795 (9.08E-01 , 9.09E-01)	38.73 (38.66 , 38.78)
	Liver	1.98E-02 (1.96E-02 , 1.99E-02)	0.0190962 (1.91E-02 , 1.92E-02)	3.50 (2.14 , 4.34)	0.02016769 (2.00E-02 , 2.04E-02)	-1.92 (-2.47 , -0.96)
	Kidneys	8.91E-03 (8.86E-03 , 9.03E-03)	0.0078729 (7.79E-03 , 8.00E-03)	11.47 (10.49 , 15.08)	0.00831665 (8.03E-03 , 8.60E-03)	6.39 (-0.61 , 12.75)
	Bladder	1.89E-03 (1.77E-03 , 2.03E-03)	0.0016461 (1.55E-03 , 1.76E-03)	12.28 (3.56 , 20.73)	0.00149447 (1.36E-03 , 1.61E-03)	20.61 (12.17 , 27.13)

Table D.6: Equivalent dose in Pat 6 using both fluence- and KERMA-weighted neutron energy scorers

Patient 6

Equivalent Dose using Fluence-Weighted Neutron Energy

	Organ	WBCT Eq. Dose (Sv)	Hybrid Eq. Dose (Sv)	Hybrid % Difference	Scaled MRCP Eq. Dose (Sv)	Scaled MRCP % Difference
In Field	Brain	2.18 (2.18 , 2.18)	2.18 (2.18 , 2.18)	-0.01 (-0.35 , 0.14)	1.92 (1.91 , 1.92)	12.01 (11.93 , 12.05)
	Eye_L	10.16 (10.13 , 10.19)	10.16 (10.15 , 10.18)	-0.05 (-0.37 , 0.15)	4.16 (4.15 , 4.16)	59.08 (58.93 , 59.28)
	Eye_R	3.00E-01 (2.98E-01 , 3.02E-01)	2.98E-01 (2.92E-01 , 3.03E-01)	0.70 (-1.68 , 2.77)	1.17E-01 (1.15E-01 , 1.18E-01)	60.98 (60.15 , 62.20)
Near Field	Thyroid	2.46 (2.44 , 2.47)	2.46 (2.45 , 2.47)	-0.35 (-1.10 , 0.11)	4.64E-01 (4.63E-01 , 4.67E-01)	81.09 (80.97 , 81.21)
Far Field	Lungs	1.13E-02 (1.13E-02 , 1.14E-02)	1.28E-02 (1.28E-02 , 1.29E-02)	-13.21 (-13.70 , -12.53)	1.11E-02 (1.11E-02 , 1.12E-02)	2.06 (1.06 , 2.65)
	Liver	3.38E-03 (3.33E-03 , 3.40E-03)	3.54E-03 (3.52E-03 , 3.61E-03)	-4.93 (-7.26 , -2.82)	3.60E-03 (3.59E-03 , 3.64E-03)	-6.62 (-7.91 , -4.10)
	Kidneys	2.77E-03 (2.67E-03 , 2.84E-03)	2.65E-03 (2.56E-03 , 2.74E-03)	3.84 (-0.86 , 10.64)	2.82E-03 (2.66E-03 , 2.92E-03)	-2.08 (-9.25 , 2.06)
	Bladder	9.12E-04 (8.00E-04 , 1.01E-03)	9.13E-04 (8.60E-04 , 9.69E-04)	-1.63 (-19.99 , 8.08)	9.73E-04 (9.22E-04 , 1.02E-03)	-8.98 (-23.36 , 3.34)

Equivalent Dose using KERMA-Weighted Neutron Energy

	Organ	WBCT Eq. Dose (Sv)	Hybrid Eq. Dose (Sv)	Hybrid % Difference	Scaled MRCP Eq. Dose (Sv)	Scaled MRCP % Difference
In Field	Brain	2.20 (2.20 , 2.20)	2.20 (2.20 , 2.20)	-0.02 (-0.09 , 0.01)	1.94 (1.94 , 1.94)	11.90 (11.83 , 11.95)
	Eye_L	10.19 (10.16 , 10.21)	10.19 (10.17 , 10.21)	-0.05 (-0.37 , 0.15)	4.18 (4.17 , 4.18)	59.01 (58.87 , 59.20)
	Eye_R	3.20E-01 (3.17E-01 , 3.23E-01)	3.18E-01 (3.12E-01 , 3.23E-01)	0.60 (-1.34 , 3.06)	1.30E-01 (1.29E-01 , 1.33E-01)	59.20 (58.24 , 60.23)
Near Field	Thyroid	2.48 (2.47 , 2.49)	2.49 (2.48 , 2.50)	-0.33 (-1.09 , 0.19)	4.83E-01 (4.81E-01 , 4.86E-01)	80.53 (80.41 , 80.62)
Far Field	Lungs	1.49E-02 (1.48E-02 , 1.50E-02)	1.74E-02 (1.73E-02 , 1.75E-02)	-16.88 (-17.51 , -15.83)	1.54E-02 (1.54E-02 , 1.56E-02)	-3.93 (-4.83 , -3.32)
	Liver	4.99E-03 (4.95E-03 , 5.04E-03)	5.21E-03 (5.16E-03 , 5.32E-03)	-4.40 (-6.17 , -2.30)	5.03E-03 (5.01E-03 , 5.08E-03)	-0.86 (-2.78 , 1.51)
	Kidneys	3.95E-03 (3.84E-03 , 4.06E-03)	3.85E-03 (3.65E-03 , 4.04E-03)	2.27 (-5.08 , 10.77)	3.84E-03 (3.66E-03 , 4.00E-03)	2.47 (-4.60 , 7.84)
	Bladder	1.02E-03 (9.39E-04 , 1.09E-03)	1.04E-03 (9.54E-04 , 1.11E-03)	-3.61 (-18.18 , 11.84)	1.07E-03 (1.02E-03 , 1.13E-03)	-7.49 (-21.98 , 6.46)

Table D.7: Equivalent dose in Pat 7 using both fluence- and KERMA-weighted neutron energy scorers

Patient 7

Equivalent Dose using Fluence-Weighted Neutron Energy

	Organ	WBCT Eq. Dose (Sv)	Hybrid Eq. Dose (Sv)	Hybrid % Difference	Scaled MRCP Eq. Dose (Sv)	Scaled MRCP % Difference
In Field	Brain	18.37 (18.37 , 18.38)	18.38 (18.37 , 18.38)	0.00 (-0.01 , 0.01)	14.39 (14.39 , 14.39)	21.67 (21.67 , 21.68)
	Eye_L	2.61 (2.60 , 2.61)	2.60 (2.60 , 2.61)	0.13 (-0.10 , 0.33)	2.07 (2.06 , 2.08)	20.58 (20.27 , 20.93)
	Eye_R	7.21E-01 (7.17E-01 , 7.26E-01)	7.20E-01 (7.19E-01 , 7.21E-01)	0.14 (-0.39 , 0.80)	4.88E-01 (4.85E-01 , 4.89E-01)	32.30 (31.81 , 32.77)
Near Field	Thyroid	5.57E-02 (5.51E-02 , 5.68E-02)	5.52E-02 (5.44E-02 , 5.59E-02)	0.83 (-1.14 , 4.04)	6.70E-02 (6.57E-02 , 6.77E-02)	-20.30 (-21.86 , -19.13)
	Lungs	5.99E-03 (5.95E-03 , 6.01E-03)	8.21E-03 (8.17E-03 , 8.26E-03)	-37.17 (-38.77 , -36.41)	9.43E-03 (9.37E-03 , 9.47E-03)	-57.49 (-59.27 , -55.89)
Far Field	Liver	2.47E-03 (2.46E-03 , 2.48E-03)	3.12E-03 (3.08E-03 , 3.15E-03)	-26.07 (-27.28 , -25.08)	3.48E-03 (3.47E-03 , 3.51E-03)	-40.71 (-41.94 , -39.60)
	Kidneys	1.88E-03 (1.81E-03 , 1.92E-03)	1.68E-03 (1.65E-03 , 1.73E-03)	10.26 (6.04 , 13.75)	1.88E-03 (1.80E-03 , 1.95E-03)	-0.58 (-6.82 , 5.80)
	Bladder	3.69E-04 (3.56E-04 , 3.80E-04)	3.69E-04 (3.49E-04 , 3.89E-04)	-0.94 (-7.34 , 5.03)	3.53E-04 (3.37E-04 , 3.68E-04)	3.23 (-5.06 , 11.78)

Equivalent Dose using KERMA-Weighted Neutron Energy

	Organ	WBCT Eq. Dose (Sv)	Hybrid Eq. Dose (Sv)	Hybrid % Difference	Scaled MRCP Eq. Dose (Sv)	Scaled MRCP % Difference
In Field	Brain	18.48 (18.48 , 18.48)	18.48 (18.48 , 18.48)	0.00 (0.00 , 0.00)	14.49 (14.49 , 14.49)	21.60 (21.59 , 21.61)
	Eye_L	2.66 (2.65 , 2.67)	2.66 (2.65 , 2.66)	0.14 (-0.16 , 0.22)	2.12 (2.11 , 2.13)	20.30 (19.95 , 20.79)
	Eye_R	7.66E-01 (7.62E-01 , 7.70E-01)	7.64E-01 (7.62E-01 , 7.68E-01)	0.17 (-0.43 , 1.22)	5.29E-01 (5.24E-01 , 5.33E-01)	30.94 (30.51 , 31.49)
Near Field	Thyroid	7.67E-02 (7.56E-02 , 7.84E-02)	7.67E-02 (7.61E-02 , 7.81E-02)	-0.07 (-2.39 , 2.66)	8.66E-02 (8.42E-02 , 8.82E-02)	-12.90 (-15.25 , -11.50)
	Lungs	8.99E-03 (8.96E-03 , 9.02E-03)	1.28E-02 (1.26E-02 , 1.28E-02)	-42.09 (-42.82 , -41.07)	1.44E-02 (1.43E-02 , 1.44E-02)	-59.85 (-61.26 , -58.80)
Far Field	Liver	3.97E-03 (3.92E-03 , 4.01E-03)	4.82E-03 (4.74E-03 , 4.89E-03)	-21.35 (-22.78 , -19.70)	5.46E-03 (5.42E-03 , 5.50E-03)	-37.56 (-39.90 , -36.39)
	Kidneys	2.96E-03 (2.87E-03 , 3.06E-03)	2.56E-03 (2.50E-03 , 2.61E-03)	13.23 (9.34 , 16.39)	2.88E-03 (2.77E-03 , 2.99E-03)	2.34 (-4.75 , 9.59)
	Bladder	4.57E-04 (4.42E-04 , 4.77E-04)	4.59E-04 (4.29E-04 , 4.83E-04)	-1.61 (-7.93 , 6.49)	4.10E-04 (3.88E-04 , 4.28E-04)	8.72 (3.14 , 18.58)

D.2 Secondary Cancer Risk Tables

D.2.1 Pat 1

Table D.8: EAR and ERR in Pat 1 using the LNT model and both neutron energy scorers

LNT

Excess Absolute Risk using Fluence-Weighted Neutron Energy

		WBCT	Hybrid		Scaled MRCP	
	Organ	EAR per 10k PY	EAR per 10k PY	% Difference	EAR per 10k PY	% Difference
In Field	Brain	86.18 (86.17, 86.19)	86.18 (86.17, 86.19)	0.00 (-0.02, 0.03)	34.58 (34.56, 34.59)	-59.88 (-59.89, -59.86)
	Eye_L	410.32 (410.10, 410.48)	410.80 (410.51, 410.95)	0.12 (0.03, 0.26)	576.68 (576.55, 576.79)	40.54 (40.46, 40.60)
	Eye_R	386.28 (386.03, 386.56)	386.88 (386.70, 387.12)	0.15 (0.08, 0.33)	547.37 (547.10, 547.70)	41.70 (41.59, 41.84)
Near Field	Thyroid	2.06E-03 (2.01E-03, 2.09E-03)	2.12E-03 (2.10E-03, 2.14E-03)	3.16 (0.71, 7.58)	4.35E-03 (4.28E-03, 4.41E-03)	111.30 (105.56, 115.99)
Far Field	Lungs	4.83E-02 (4.79E-02, 4.86E-02)	5.04E-02 (4.99E-02, 5.06E-02)	4.31 (3.09, 6.50)	4.53E-02 (4.51E-02, 4.56E-02)	-6.08 (-7.01, -5.24)
	Liver	8.87E-03 (8.81E-03, 8.97E-03)	8.16E-03 (8.11E-03, 8.20E-03)	-8.03 (-8.76, -6.08)	7.94E-03 (7.80E-03, 8.01E-03)	-10.47 (-12.12, -9.24)
	Kidneys	1.08E-02 (1.06E-02, 1.09E-02)	9.37E-03 (8.90E-03, 9.81E-03)	-13.56 (-18.39, -4.73)	8.61E-03 (8.27E-03, 9.07E-03)	-20.61 (-24.30, -16.48)
	Bladder	5.30E-04 (4.72E-04, 5.80E-04)	4.33E-04 (3.92E-04, 4.30E-04)	-18.32 (-30.13, 2.40)	3.90E-04 (3.52E-04, 4.12E-04)	-26.34 (-37.25, -15.86)

Excess Absolute Risk using KERMA-Weighted Neutron Energy

		WBCT	Hybrid		Scaled MRCP	
	Organ	EAR per 10k PY	EAR per 10k PY	% Difference	EAR per 10k PY	% Difference
In Field	Brain	86.93 (86.92, 86.94)	86.93 (86.92, 86.94)	0.00 (-0.02, 0.03)	35.08 (35.07, 35.09)	-59.65 (-59.66, -59.63)
	Eye_L	411.80 (411.49, 412.00)	412.32 (412.08, 412.42)	0.13 (0.03, 0.28)	578.25 (578.18, 578.31)	40.42 (40.32, 40.49)
	Eye_R	387.84 (387.56, 388.09)	388.43 (388.29, 388.65)	0.15 (0.07, 0.32)	549.00 (548.68, 549.33)	41.55 (41.42, 41.68)
Near Field	Thyroid	2.06E-03 (2.01E-03, 2.09E-03)	2.12E-03 (2.10E-03, 2.14E-03)	3.16 (0.71, 7.58)	4.35E-03 (4.28E-03, 4.41E-03)	111.30 (105.56, 115.99)
Far Field	Lungs	6.00E-02 (5.97E-02, 6.05E-02)	6.36E-02 (6.29E-02, 6.43E-02)	6.10 (4.83, 8.66)	5.60E-02 (5.56E-02, 5.63E-02)	-6.62 (-7.38, -5.73)
	Liver	1.35E-02 (1.34E-02, 1.37E-02)	1.18E-02 (1.18E-02, 1.19E-02)	-12.10 (-12.85, -10.18)	1.08E-02 (1.06E-02, 1.09E-02)	-20.02 (-21.73, -18.61)
	Kidneys	1.49E-02 (1.46E-02, 1.50E-02)	1.25E-02 (1.21E-02, 1.28E-02)	-16.51 (-19.90, -10.73)	1.06E-02 (1.01E-02, 1.13E-02)	-28.91 (-32.77, -24.54)
	Bladder	5.57E-04 (4.98E-04, 6.19E-04)	4.60E-04 (4.22E-04, 4.75E-04)	-17.36 (-28.52, 5.86)	3.96E-04 (3.64E-04, 4.08E-04)	-28.82 (-38.38, -18.53)

Excess Relative Risk using Fluence-Weighted Neutron Energy

		WBCT	Hybrid		Scaled MRCP	
	Organ	ERR	ERR	% Difference	ERR	% Difference
In Field	Brain	2.40 (2.40, 2.40)	2.40 (2.40, 2.40)	0.00 (-0.02, 0.03)	9.62E-01 (0.96, 0.96)	-59.88 (-59.89, -59.86)
	Eye_L	11.41 (11.41, 11.42)	11.43 (11.42, 11.43)	0.12 (0.03, 0.26)	16.04 (16.04, 16.04)	40.54 (40.46, 40.60)
	Eye_R	10.75 (10.74, 10.75)	10.76 (10.76, 10.77)	0.15 (0.08, 0.33)	15.23 (15.22, 15.24)	41.70 (41.59, 41.84)
Near Field	Thyroid	7.61E-03 (7.49E-03, 7.74E-03)	7.65E-03 (7.60E-03, 7.79E-03)	0.56 (-1.15, 4.89)	1.11E-02 (1.10E-02, 1.12E-02)	45.70 (43.14, 48.84)
Far Field	Lungs	3.96E-03 (3.93E-03, 3.99E-03)	4.13E-03 (4.09E-03, 4.15E-03)	4.31 (3.09, 6.50)	3.72E-03 (3.70E-03, 3.74E-03)	-6.08 (-7.01, -5.24)
	Liver	8.31E-04 (8.26E-04, 8.40E-04)	7.64E-04 (7.60E-04, 7.68E-04)	-8.03 (-8.76, -6.08)	7.44E-04 (7.31E-04, 7.50E-04)	-10.47 (-12.12, -9.24)
	Kidneys	3.02E-04 (2.94E-04, 3.02E-04)	2.61E-04 (2.48E-04, 2.73E-04)	-13.56 (-18.39, -4.73)	2.40E-04 (2.30E-04, 2.52E-04)	-20.61 (-24.30, -16.48)
	Bladder	1.22E-04 (1.09E-04, 1.34E-04)	9.97E-05 (9.04E-05, 9.92E-05)	-18.32 (-30.13, 2.40)	9.00E-05 (8.10E-05, 9.50E-05)	-26.34 (-37.25, -15.86)

Excess Relative Risk using KERMA-Weighted Neutron Energy

		WBCT	Hybrid		Scaled MRCP	
	Organ	ERR	ERR	% Difference	ERR	% Difference
In Field	Brain	2.42 (2.42, 2.42)	2.42 (2.42, 2.42)	0.00 (-0.02, 0.03)	9.76E-01 (0.98, 0.98)	-59.65 (-59.66, -59.63)
	Eye_L	11.45 (11.45, 11.46)	11.47 (11.46, 11.47)	0.13 (0.03, 0.28)	16.09 (16.08, 16.09)	40.42 (40.32, 40.49)
	Eye_R	10.79 (10.78, 10.80)	10.80 (10.80, 10.81)	0.15 (0.07, 0.32)	15.27 (15.26, 15.28)	41.55 (41.42, 41.68)
Near Field	Thyroid	1.05E-02 (1.03E-02, 1.08E-02)	1.05E-02 (1.02E-02, 1.08E-02)	0.15 (-3.63, 8.00)	1.27E-02 (1.26E-02, 1.29E-02)	20.82 (17.55, 24.36)
Far Field	Lungs	4.92E-03 (4.90E-03, 4.96E-03)	5.22E-03 (5.16E-03, 5.27E-03)	6.10 (4.83, 8.66)	4.60E-03 (4.56E-03, 4.62E-03)	-6.62 (-7.38, -5.73)
	Liver	1.26E-03 (1.25E-03, 1.28E-03)	1.11E-03 (1.11E-03, 1.11E-03)	-12.10 (-12.85, -10.18)	1.01E-03 (9.89E-04, 1.02E-03)	-20.02 (-21.73, -18.61)
	Kidneys	4.16E-04 (4.07E-04, 4.16E-04)	3.47E-04 (3.35E-04, 3.57E-04)	-16.51 (-19.90, -10.73)	2.96E-04 (2.81E-04, 3.14E-04)	-28.91 (-32.77, -24.54)
	Bladder	1.28E-04 (1.15E-04, 1.43E-04)	1.06E-04 (9.71E-05, 1.09E-04)	-17.36 (-28.52, 5.86)	9.13E-05 (8.38E-05, 9.40E-05)	-28.82 (-38.38, -18.53)

Table D.9: EAR and ERR in Pat 1 using the linear plateau model with a 10 Sv inflection point and both neutron energy scorers

Linear-Plateau 10 Sv

Excess Absolute Risk using Fluence-Weighted Neutron Energy

	Organ	WBCT EAR per 10k PY	Hybrid EAR per 10k PY	Hybrid % Difference	Scaled MRCP EAR per 10k PY	Scaled MRCP % Difference
In Field	Brain	34.80 (34.80, 34.80)	34.80 (34.80, 34.80)	0.00 (0.00, 0.01)	24.20 (24.20, 24.21)	-30.44 (-30.46, -30.43)
	Eye_L	37.72 (37.72, 37.72)	37.72 (37.72, 37.72)	0.00 (0.00, 0.00)	37.72 (37.72, 37.72)	0.00 (0.00, 0.00)
	Eye_R	37.72 (37.72, 37.72)	37.72 (37.72, 37.72)	0.00 (0.00, 0.00)	37.72 (37.72, 37.72)	0.00 (0.00, 0.00)
Near Field	Thyroid	2.30E-03 (2.25E-03, 2.34E-03)	2.37E-03 (2.35E-03, 2.40E-03)	3.15 (0.71, 7.57)	4.85E-03 (4.78E-03, 4.92E-03)	110.93 (105.21, 115.60)
Far Field	Lungs	5.40E-02 (5.36E-02, 5.44E-02)	5.63E-02 (5.58E-02, 5.66E-02)	4.30 (3.08, 6.49)	5.07E-02 (5.04E-02, 5.09E-02)	-6.07 (-7.00, -5.23)
	Liver	9.92E-03 (9.87E-03, 1.00E-02)	9.13E-03 (9.08E-03, 9.18E-03)	-8.03 (-8.76, -6.08)	8.89E-03 (8.73E-03, 8.97E-03)	-10.47 (-12.11, -9.24)
	Kidneys	1.21E-02 (1.18E-02, 1.22E-02)	1.05E-02 (9.97E-03, 1.10E-02)	-13.56 (-18.39, -4.73)	9.64E-03 (9.26E-03, 1.01E-02)	-20.61 (-24.30, -16.48)
	Bladder	5.93E-04 (5.28E-04, 6.49E-04)	4.85E-04 (4.39E-04, 4.82E-04)	-18.32 (-30.13, 2.40)	4.37E-04 (3.94E-04, 4.62E-04)	-26.34 (-37.25, -15.86)

Excess Absolute Risk using KERMA-Weighted Neutron Energy

	Organ	WBCT EAR per 10k PY	Hybrid EAR per 10k PY	Hybrid % Difference	Scaled MRCP EAR per 10k PY	Scaled MRCP % Difference
In Field	Brain	34.86 (34.86, 34.86)	34.86 (34.86, 34.86)	0.00 (0.00, 0.01)	24.40 (24.40, 24.41)	-30.00 (-30.01, -29.99)
	Eye_L	37.72 (37.72, 37.72)	37.72 (37.72, 37.72)	0.00 (0.00, 0.00)	37.72 (37.72, 37.72)	0.00 (0.00, 0.00)
	Eye_R	37.72 (37.72, 37.72)	37.72 (37.72, 37.72)	0.00 (0.00, 0.00)	37.72 (37.72, 37.72)	0.00 (0.00, 0.00)
Near Field	Thyroid	2.30E-03 (2.25E-03, 2.34E-03)	2.37E-03 (2.35E-03, 2.40E-03)	3.15 (0.71, 7.57)	4.85E-03 (4.78E-03, 4.92E-03)	110.93 (105.21, 115.60)
Far Field	Lungs	6.70E-02 (6.67E-02, 6.76E-02)	7.11E-02 (7.03E-02, 7.18E-02)	6.08 (4.82, 8.64)	6.26E-02 (6.22E-02, 6.30E-02)	-6.60 (-7.37, -5.72)
	Liver	1.51E-02 (1.50E-02, 1.53E-02)	1.33E-02 (1.32E-02, 1.33E-02)	-12.10 (-12.84, -10.17)	1.21E-02 (1.18E-02, 1.22E-02)	-20.01 (-21.72, -18.60)
	Kidneys	1.67E-02 (1.64E-02, 1.68E-02)	1.40E-02 (1.35E-02, 1.44E-02)	-16.50 (-19.90, -10.73)	1.19E-02 (1.13E-02, 1.26E-02)	-28.91 (-32.76, -24.54)
	Bladder	6.23E-04 (5.57E-04, 6.93E-04)	5.15E-04 (4.72E-04, 5.32E-04)	-17.36 (-28.52, 5.86)	4.44E-04 (4.07E-04, 4.57E-04)	-28.82 (-38.38, -18.53)

Excess Relative Risk using Fluence-Weighted Neutron Energy

	Organ	WBCT ERR	Hybrid ERR	Hybrid % Difference	Scaled MRCP ERR	Scaled MRCP % Difference
In Field	Brain	9.68E-01 (9.68E-01, 9.68E-01)	9.68E-01 (9.68E-01, 9.68E-01)	0.00 (0.00, 0.01)	6.73E-01 (6.73E-01, 6.73E-01)	-30.44 (-30.46, -30.43)
	Eye_L	1.05 (1.05, 1.05)	1.05 (1.05, 1.05)	0.00 (0.00, 0.00)	1.05 (1.05, 1.05)	0.00 (0.00, 0.00)
	Eye_R	1.05 (1.05, 1.05)	1.05 (1.05, 1.05)	0.00 (0.00, 0.00)	1.05 (1.05, 1.05)	0.00 (0.00, 0.00)
Near Field	Thyroid	8.47E-03 (8.33E-03, 8.62E-03)	8.51E-03 (8.46E-03, 8.67E-03)	0.56 (-1.15, 4.86)	1.23E-02 (1.22E-02, 1.24E-02)	45.32 (42.78, 48.43)
Far Field	Lungs	4.43E-03 (4.39E-03, 4.46E-03)	4.62E-03 (4.58E-03, 4.64E-03)	4.30 (3.08, 6.49)	4.16E-03 (4.13E-03, 4.18E-03)	-6.07 (-7.00, -5.23)
	Liver	9.30E-04 (9.24E-04, 9.41E-04)	8.55E-04 (8.50E-04, 8.60E-04)	-8.03 (-8.76, -6.08)	8.32E-04 (8.18E-04, 8.40E-04)	-10.47 (-12.11, -9.24)
	Kidneys	3.38E-04 (3.30E-04, 3.38E-04)	2.92E-04 (2.77E-04, 3.05E-04)	-13.56 (-18.39, -4.73)	2.68E-04 (2.57E-04, 2.82E-04)	-20.61 (-24.30, -16.48)
	Bladder	1.37E-04 (1.22E-04, 1.50E-04)	1.12E-04 (1.01E-04, 1.11E-04)	-18.32 (-30.13, 2.40)	1.01E-04 (9.07E-05, 1.06E-04)	-26.34 (-37.25, -15.86)

Excess Relative Risk using KERMA-Weighted Neutron Energy

	Organ	WBCT ERR	Hybrid ERR	Hybrid % Difference	Scaled MRCP ERR	Scaled MRCP % Difference
In Field	Brain	9.70E-01 (9.70E-01, 9.70E-01)	9.70E-01 (9.70E-01, 9.70E-01)	0.00 (0.00, 0.01)	6.79E-01 (6.79E-01, 6.79E-01)	-30.00 (-30.01, -29.99)
	Eye_L	1.05 (1.05, 1.05)	1.05 (1.05, 1.05)	0.00 (0.00, 0.00)	1.05 (1.05, 1.05)	0.00 (0.00, 0.00)
	Eye_R	1.05 (1.05, 1.05)	1.05 (1.05, 1.05)	0.00 (0.00, 0.00)	1.05 (1.05, 1.05)	0.00 (0.00, 0.00)
Near Field	Thyroid	1.17E-02 (1.14E-02, 1.20E-02)	1.17E-02 (1.14E-02, 1.20E-02)	0.15 (-3.61, 7.93)	1.41E-02 (1.39E-02, 1.43E-02)	20.62 (17.39, 24.12)
Far Field	Lungs	5.50E-03 (5.47E-03, 5.54E-03)	5.83E-03 (5.77E-03, 5.89E-03)	6.08 (4.82, 8.64)	5.14E-03 (5.10E-03, 5.16E-03)	-6.60 (-7.37, -5.72)
	Liver	1.41E-03 (1.40E-03, 1.43E-03)	1.24E-03 (1.24E-03, 1.24E-03)	-12.10 (-12.84, -10.17)	1.13E-03 (1.11E-03, 1.14E-03)	-20.01 (-21.72, -18.60)
	Kidneys	4.65E-04 (4.55E-04, 4.66E-04)	3.89E-04 (3.75E-04, 4.00E-04)	-16.50 (-19.90, -10.73)	3.31E-04 (3.15E-04, 3.51E-04)	-28.91 (-32.76, -24.54)
	Bladder	1.44E-04 (1.28E-04, 1.60E-04)	1.19E-04 (1.09E-04, 1.23E-04)	-17.36 (-28.52, 5.86)	1.02E-04 (9.38E-05, 1.05E-04)	-28.82 (-38.38, -18.53)

Table D.10: EAR and ERR in Pat 1 using the linear plateau model with a 40 Sv inflection point and both neutron energy scorers

Linear-Plateau 40 Sv

Excess Absolute Risk using Fluence-Weighted Neutron Energy

		WBCT	Hybrid		Scaled MRCP	
	Organ	EAR per 10k PY	EAR per 10k PY	% Difference	EAR per 10k PY	% Difference
In Field	Brain	65.52 (65.51 , 65.53)	65.52 (65.51 , 65.52)	0.00 (-0.02 , 0.02)	31.38 (31.37 , 31.39)	-52.10 (-52.12 , -52.08)
	Eye_L	132.08 (132.07 , 132.08)	132.10 (132.09 , 132.11)	0.02 (0.00 , 0.04)	136.76 (136.75 , 136.76)	3.54 (3.54 , 3.55)
	Eye_R	130.79 (130.77 , 130.80)	130.82 (130.81 , 130.84)	0.03 (0.01 , 0.06)	136.29 (136.29 , 136.30)	4.21 (4.20 , 4.22)
Near Field	Thyroid	2.12E-03 (2.07E-03 , 2.15E-03)	2.18E-03 (2.16E-03 , 2.21E-03)	3.16 (0.71 , 7.58)	4.47E-03 (4.40E-03 , 4.54E-03)	111.21 (105.47 , 115.89)
Far Field	Lungs	4.97E-02 (4.93E-02 , 5.00E-02)	5.18E-02 (5.13E-02 , 5.21E-02)	4.31 (3.08 , 6.50)	4.66E-02 (4.63E-02 , 4.69E-02)	-6.08 (-7.01 , -5.24)
	Liver	9.12E-03 (9.07E-03 , 9.23E-03)	8.39E-03 (8.35E-03 , 8.44E-03)	-8.03 (-8.76 , -6.08)	8.17E-03 (8.03E-03 , 8.24E-03)	-10.47 (-12.12 , -9.24)
	Kidneys	1.12E-02 (1.09E-02 , 1.12E-02)	9.65E-03 (9.16E-03 , 1.01E-02)	-13.56 (-18.39 , -4.73)	8.86E-03 (8.51E-03 , 9.33E-03)	-20.61 (-24.30 , -16.48)
	Bladder	5.45E-04 (4.85E-04 , 5.97E-04)	4.45E-04 (4.04E-04 , 4.43E-04)	-18.32 (-30.13 , 2.40)	4.02E-04 (3.62E-04 , 4.24E-04)	-26.34 (-37.25 , -15.86)

Excess Absolute Risk using KERMA-Weighted Neutron Energy

		WBCT	Hybrid		Scaled MRCP	
	Organ	EAR per 10k PY	EAR per 10k PY	% Difference	EAR per 10k PY	% Difference
In Field	Brain	65.92 (65.92 , 65.93)	65.92 (65.92 , 65.93)	0.00 (-0.01 , 0.02)	31.78 (31.78 , 31.79)	-51.79 (-51.80 , -51.77)
	Eye_L	132.15 (132.13 , 132.16)	132.17 (132.16 , 132.18)	0.02 (0.00 , 0.04)	136.78 (136.78 , 136.78)	3.50 (3.49 , 3.51)
	Eye_R	130.88 (130.86 , 130.89)	130.91 (130.90 , 130.92)	0.03 (0.01 , 0.05)	136.32 (136.31 , 136.32)	4.16 (4.14 , 4.17)
Near Field	Thyroid	2.12E-03 (2.07E-03 , 2.15E-03)	2.18E-03 (2.16E-03 , 2.21E-03)	3.16 (0.71 , 7.58)	4.47E-03 (4.40E-03 , 4.54E-03)	111.21 (105.47 , 115.89)
Far Field	Lungs	6.17E-02 (6.14E-02 , 6.22E-02)	6.55E-02 (6.47E-02 , 6.61E-02)	6.09 (4.83 , 8.66)	5.76E-02 (5.72E-02 , 5.79E-02)	-6.61 (-7.38 , -5.73)
	Liver	1.39E-02 (1.38E-02 , 1.40E-02)	1.22E-02 (1.21E-02 , 1.22E-02)	-12.10 (-12.85 , -10.18)	1.11E-02 (1.09E-02 , 1.12E-02)	-20.01 (-21.73 , -18.61)
	Kidneys	1.54E-02 (1.50E-02 , 1.54E-02)	1.28E-02 (1.24E-02 , 1.32E-02)	-16.51 (-19.90 , -10.73)	1.09E-02 (1.04E-02 , 1.16E-02)	-28.91 (-32.77 , -24.54)
	Bladder	5.73E-04 (5.12E-04 , 6.37E-04)	4.73E-04 (4.34E-04 , 4.89E-04)	-17.36 (-28.52 , 5.86)	4.08E-04 (3.74E-04 , 4.20E-04)	-28.82 (-38.38 , -18.53)

Excess Relative Risk using Fluence-Weighted Neutron Energy

		WBCT	Hybrid		Scaled MRCP	
	Organ	ERR	ERR	% Difference	ERR	% Difference
In Field	Brain	1.82 (1.82 , 1.82)	1.82 (1.82 , 1.82)	0.00 (-0.02 , 0.02)	8.73E-01 (8.73E-01 , 8.73E-01)	-52.10 (-52.12 , -52.08)
	Eye_L	3.67 (3.67 , 3.67)	3.67 (3.67 , 3.67)	0.02 (0.00 , 0.04)	3.80 (3.80 , 3.80)	3.54 (3.54 , 3.55)
	Eye_R	3.64 (3.64 , 3.64)	3.64 (3.64 , 3.64)	0.03 (0.01 , 0.06)	3.79 (3.79 , 3.79)	4.21 (4.20 , 4.22)
Near Field	Thyroid	7.82E-03 (7.69E-03 , 7.96E-03)	7.86E-03 (7.81E-03 , 8.01E-03)	0.56 (-1.15 , 4.89)	1.14E-02 (1.13E-02 , 1.15E-02)	45.61 (43.05 , 48.74)
Far Field	Lungs	4.07E-03 (4.04E-03 , 4.10E-03)	4.25E-03 (4.21E-03 , 4.27E-03)	4.31 (3.08 , 6.50)	3.83E-03 (3.80E-03 , 3.85E-03)	-6.08 (-7.01 , -5.24)
	Liver	8.55E-04 (8.49E-04 , 8.65E-04)	7.86E-04 (7.82E-04 , 7.91E-04)	-8.03 (-8.76 , -6.08)	7.65E-04 (7.52E-04 , 7.72E-04)	-10.47 (-12.12 , -9.24)
	Kidneys	3.10E-04 (3.03E-04 , 3.11E-04)	2.68E-04 (2.55E-04 , 2.81E-04)	-13.56 (-18.39 , -4.73)	2.46E-04 (2.37E-04 , 2.60E-04)	-20.61 (-24.30 , -16.48)
	Bladder	1.26E-04 (1.12E-04 , 1.38E-04)	1.03E-04 (9.30E-05 , 1.02E-04)	-18.32 (-30.13 , 2.40)	9.26E-05 (8.34E-05 , 9.78E-05)	-26.34 (-37.25 , -15.86)

Excess Relative Risk using KERMA-Weighted Neutron Energy

		WBCT	Hybrid		Scaled MRCP	
	Organ	ERR	ERR	% Difference	ERR	% Difference
In Field	Brain	1.83 (1.83 , 1.83)	1.83 (1.83 , 1.83)	0.00 (-0.01 , 0.02)	8.84E-01 (8.84E-01 , 8.84E-01)	-51.79 (-51.80 , -51.77)
	Eye_L	3.68 (3.68 , 3.68)	3.68 (3.68 , 3.68)	0.02 (0.00 , 0.04)	3.80 (3.80 , 3.80)	3.50 (3.49 , 3.51)
	Eye_R	3.64 (3.64 , 3.64)	3.64 (3.64 , 3.64)	0.03 (0.01 , 0.05)	3.79 (3.79 , 3.79)	4.16 (4.14 , 4.17)
Near Field	Thyroid	1.08E-02 (1.05E-02 , 1.11E-02)	1.08E-02 (1.05E-02 , 1.11E-02)	0.15 (-3.63 , 7.98)	1.30E-02 (1.29E-02 , 1.32E-02)	20.77 (17.51 , 24.30)
Far Field	Lungs	5.06E-03 (5.04E-03 , 5.10E-03)	5.37E-03 (5.31E-03 , 5.42E-03)	6.09 (4.83 , 8.66)	4.73E-03 (4.70E-03 , 4.75E-03)	-6.61 (-7.38 , -5.73)
	Liver	1.30E-03 (1.29E-03 , 1.32E-03)	1.14E-03 (1.14E-03 , 1.14E-03)	-12.10 (-12.85 , -10.18)	1.04E-03 (1.02E-03 , 1.05E-03)	-20.01 (-21.73 , -18.61)
	Kidneys	4.28E-04 (4.18E-04 , 4.29E-04)	3.57E-04 (3.45E-04 , 3.68E-04)	-16.51 (-19.90 , -10.73)	3.04E-04 (2.89E-04 , 3.23E-04)	-28.91 (-32.77 , -24.54)
	Bladder	1.32E-04 (1.18E-04 , 1.47E-04)	1.09E-04 (1.00E-04 , 1.13E-04)	-17.36 (-28.52 , 5.86)	9.40E-05 (8.62E-05 , 9.67E-05)	-28.82 (-38.38 , -18.53)

Table D.11: EAR and ERR in Pat 1 using the linear exponential model with a 10 Sv inflection point and both neutron energy scorers

Linear-Exponential 10 Sv

Excess Absolute Risk using Fluence-Weighted Neutron Energy

		WBCT	Hybrid		Scaled MRCP	
	Organ	EAR per 10k PY	EAR per 10k PY	% Difference	EAR per 10k PY	% Difference
In Field	Brain	31.36 (31.36, 31.36)	31.36 (31.36, 31.36)	0.00 (0.00, 0.00)	24.47 (24.47, 24.48)	-21.97 (-21.98, -21.95)
	Eye_L	2.29 (2.29, 2.28)	2.28 (2.28, 2.27)	-0.50 (-0.88, 0.10)	3.77E-01 (3.77E-01, 3.76E-01)	-83.54 (-83.58, -83.50)
	Eye_R	2.94 (2.94, 2.93)	2.92 (2.92, 2.91)	-0.61 (-0.93, 0.08)	5.22E-01 (5.23E-01, 5.20E-01)	-82.24 (-82.31, -82.15)
Near Field	Thyroid	2.27E-03 (2.22E-03, 2.31E-03)	2.34E-03 (2.32E-03, 2.37E-03)	3.15 (0.71, 7.57)	4.79E-03 (4.72E-03, 4.86E-03)	110.98 (105.26, 115.65)
Far Field	Lungs	5.33E-02 (5.29E-02, 5.37E-02)	5.56E-02 (5.51E-02, 5.59E-02)	4.30 (3.08, 6.49)	5.01E-02 (4.97E-02, 5.03E-02)	-6.07 (-7.00, -5.23)
	Liver	9.80E-03 (9.74E-03, 9.91E-03)	9.01E-03 (8.96E-03, 9.06E-03)	-8.03 (-8.76, -6.08)	8.77E-03 (8.62E-03, 8.85E-03)	-10.47 (-12.11, -9.24)
	Kidneys	1.20E-02 (1.17E-02, 1.20E-02)	1.04E-02 (9.84E-03, 1.08E-02)	-13.56 (-18.39, -4.73)	9.52E-03 (9.14E-03, 1.00E-02)	-20.61 (-24.30, -16.48)
	Bladder	5.86E-04 (5.21E-04, 6.41E-04)	4.78E-04 (4.33E-04, 4.76E-04)	-18.32 (-30.13, 2.40)	4.31E-04 (3.89E-04, 4.56E-04)	-26.34 (-37.25, -15.86)

Excess Absolute Risk using KERMA-Weighted Neutron Energy

		WBCT	Hybrid		Scaled MRCP	
	Organ	EAR per 10k PY	EAR per 10k PY	% Difference	EAR per 10k PY	% Difference
In Field	Brain	31.33 (31.33, 31.33)	31.33 (31.33, 31.33)	0.00 (0.00, 0.00)	24.67 (24.66, 24.67)	-21.27 (-21.28, -21.25)
	Eye_L	2.25 (2.26, 2.25)	2.24 (2.25, 2.24)	-0.55 (-0.95, 0.09)	3.70E-01 (3.70E-01, 3.70E-01)	-83.57 (-83.63, -83.54)
	Eye_R	2.89 (2.90, 2.88)	2.87 (2.88, 2.87)	-0.61 (-0.93, 0.04)	5.12E-01 (5.14E-01, 5.10E-01)	-82.27 (-82.35, -82.19)
Near Field	Thyroid	2.27E-03 (2.22E-03, 2.31E-03)	2.34E-03 (2.32E-03, 2.37E-03)	3.15 (0.71, 7.57)	4.79E-03 (4.72E-03, 4.86E-03)	110.98 (105.26, 115.65)
Far Field	Lungs	6.62E-02 (6.59E-02, 6.67E-02)	7.02E-02 (6.94E-02, 7.09E-02)	6.08 (4.82, 8.64)	6.18E-02 (6.14E-02, 6.22E-02)	-6.60 (-7.37, -5.72)
	Liver	1.49E-02 (1.48E-02, 1.51E-02)	1.31E-02 (1.30E-02, 1.31E-02)	-12.10 (-12.84, -10.17)	1.19E-02 (1.17E-02, 1.21E-02)	-20.01 (-21.72, -18.60)
	Kidneys	1.65E-02 (1.61E-02, 1.65E-02)	1.38E-02 (1.33E-02, 1.42E-02)	-16.50 (-19.90, -10.73)	1.17E-02 (1.12E-02, 1.25E-02)	-28.91 (-32.76, -24.54)
	Bladder	6.15E-04 (5.50E-04, 6.84E-04)	5.08E-04 (4.66E-04, 5.25E-04)	-17.36 (-28.52, 5.86)	4.38E-04 (4.02E-04, 4.51E-04)	-28.82 (-38.38, -18.53)

Excess Relative Risk using Fluence-Weighted Neutron Energy

		WBCT	Hybrid		Scaled MRCP	
	Organ	ERR	ERR	% Difference	ERR	% Difference
In Field	Brain	8.72E-01 (8.72E-01, 8.72E-01)	8.72E-01 (8.72E-01, 8.72E-01)	0.00 (0.00, 0.00)	6.81E-01 (6.81E-01, 6.81E-01)	-21.97 (-21.98, -21.95)
	Eye_L	6.36E-02 (6.38E-02, 6.35E-02)	6.33E-02 (6.35E-02, 6.32E-02)	-0.50 (-0.88, 0.10)	1.05E-02 (1.05E-02, 1.05E-02)	-83.54 (-83.58, -83.50)
	Eye_R	8.17E-02 (8.19E-02, 8.14E-02)	8.12E-02 (8.13E-02, 8.10E-02)	-0.61 (-0.93, 0.08)	1.45E-02 (1.46E-02, 1.45E-02)	-82.24 (-82.31, -82.15)
Near Field	Thyroid	8.36E-03 (8.23E-03, 8.52E-03)	8.41E-03 (8.36E-03, 8.57E-03)	0.56 (-1.15, 4.87)	1.22E-02 (1.21E-02, 1.23E-02)	45.37 (42.83, 48.49)
Far Field	Lungs	4.37E-03 (4.34E-03, 4.40E-03)	4.56E-03 (4.52E-03, 4.58E-03)	4.30 (3.08, 6.49)	4.11E-03 (4.08E-03, 4.13E-03)	-6.07 (-7.00, -5.23)
	Liver	9.18E-04 (9.12E-04, 9.29E-04)	8.44E-04 (8.40E-04, 8.49E-04)	-8.03 (-8.76, -6.08)	8.22E-04 (8.07E-04, 8.29E-04)	-10.47 (-12.11, -9.24)
	Kidneys	3.33E-04 (3.25E-04, 3.34E-04)	2.88E-04 (2.74E-04, 3.01E-04)	-13.56 (-18.39, -4.73)	2.65E-04 (2.54E-04, 2.79E-04)	-20.61 (-24.30, -16.48)
	Bladder	1.35E-04 (1.20E-04, 1.48E-04)	1.10E-04 (9.99E-05, 1.10E-04)	-18.32 (-30.13, 2.40)	9.94E-05 (8.95E-05, 1.05E-04)	-26.34 (-37.25, -15.86)

Excess Relative Risk using KERMA-Weighted Neutron Energy

		WBCT	Hybrid		Scaled MRCP	
	Organ	ERR	ERR	% Difference	ERR	% Difference
In Field	Brain	8.71E-01 (0.87, 0.87)	8.71E-01 (0.87, 0.87)	0.00 (0.00, 0.00)	6.86E-01 (0.69, 0.69)	-21.27 (-21.28, -21.25)
	Eye_L	6.27E-02 (0.06, 0.06)	6.23E-02 (0.06, 0.06)	-0.55 (-0.95, 0.09)	1.03E-02 (0.01, 0.01)	-83.57 (-83.63, -83.54)
	Eye_R	8.04E-02 (0.08, 0.08)	7.99E-02 (0.08, 0.08)	-0.61 (-0.93, 0.04)	1.43E-02 (0.01, 0.01)	-82.27 (-82.35, -82.19)
Near Field	Thyroid	1.15E-02 (1.13E-02, 1.18E-02)	1.16E-02 (1.12E-02, 1.19E-02)	0.15 (-3.61, 7.94)	1.39E-02 (1.38E-02, 1.41E-02)	20.65 (17.41, 24.15)
Far Field	Lungs	5.43E-03 (5.40E-03, 5.47E-03)	5.76E-03 (5.70E-03, 5.81E-03)	6.08 (4.82, 8.64)	5.07E-03 (5.04E-03, 5.10E-03)	-6.60 (-7.37, -5.72)
	Liver	1.39E-03 (1.38E-03, 1.41E-03)	1.23E-03 (1.22E-03, 1.23E-03)	-12.10 (-12.84, -10.17)	1.12E-03 (1.09E-03, 1.13E-03)	-20.01 (-21.72, -18.60)
	Kidneys	4.59E-04 (4.49E-04, 4.60E-04)	3.84E-04 (3.71E-04, 3.95E-04)	-16.50 (-19.90, -10.73)	3.27E-04 (3.11E-04, 3.47E-04)	-28.91 (-32.76, -24.54)
	Bladder	1.42E-04 (1.27E-04, 1.58E-04)	1.17E-04 (1.07E-04, 1.21E-04)	-17.36 (-28.52, 5.86)	1.01E-04 (9.26E-05, 1.04E-04)	-28.82 (-38.38, -18.53)

Table D.12: EAR and ERR in Pat 1 using the linear exponential model with a 40 Sv inflection point and both neutron energy scorers

Linear-Exponential 40 Sv

Excess Absolute Risk using Fluence-Weighted Neutron Energy

		WBCT	Hybrid		Scaled MRCP	
	Organ	EAR per 10k PY	EAR per 10k PY	% Difference	EAR per 10k PY	% Difference
In Field	Brain	66.93 (66.93, 66.94)	66.93 (66.93, 66.94)	0.00 (-0.02, 0.02)	31.71 (31.70, 31.72)	-52.62 (-52.64, -52.60)
	Eye_L	112.13 (112.14, 112.11)	112.08 (112.11, 112.07)	-0.04 (-0.07, 0.01)	92.19 (92.21, 92.17)	-17.78 (-17.80, -17.76)
	Eye_R	114.06 (114.08, 114.04)	114.02 (114.03, 114.00)	-0.04 (-0.06, 0.01)	96.17 (96.21, 96.13)	-15.68 (-15.72, -15.64)
Near Field	Thyroid	2.11E-03 (2.06E-03, 2.14E-03)	2.18E-03 (2.16E-03, 2.20E-03)	3.16 (0.71, 7.58)	4.46E-03 (4.38E-03, 4.52E-03)	111.22 (105.48, 115.90)
Far Field	Lungs	4.95E-02 (4.91E-02, 4.99E-02)	5.16E-02 (5.12E-02, 5.19E-02)	4.31 (3.08, 6.50)	4.65E-02 (4.62E-02, 4.67E-02)	-6.08 (-7.01, -5.24)
	Liver	9.09E-03 (9.04E-03, 9.20E-03)	8.36E-03 (8.32E-03, 8.41E-03)	-8.03 (-8.76, -6.08)	8.14E-03 (8.00E-03, 8.21E-03)	-10.47 (-12.12, -9.24)
	Kidneys	1.11E-02 (1.09E-02, 1.11E-02)	9.61E-03 (9.13E-03, 1.01E-02)	-13.56 (-18.39, -4.73)	8.83E-03 (8.48E-03, 9.30E-03)	-20.61 (-24.30, -16.48)
	Bladder	5.43E-04 (4.84E-04, 5.95E-04)	4.44E-04 (4.02E-04, 4.41E-04)	-18.32 (-30.13, 2.40)	4.00E-04 (3.60E-04, 4.23E-04)	-26.34 (-37.25, -15.86)

Excess Absolute Risk using KERMA-Weighted Neutron Energy

		WBCT	Hybrid		Scaled MRCP	
	Organ	EAR per 10k PY	EAR per 10k PY	% Difference	EAR per 10k PY	% Difference
In Field	Brain	67.35 (67.35, 67.36)	67.35 (67.35, 67.36)	0.00 (-0.01, 0.02)	32.12 (32.12, 32.13)	-52.31 (-52.32, -52.29)
	Eye_L	111.99 (112.02, 111.98)	111.95 (111.97, 111.94)	-0.04 (-0.07, 0.01)	91.97 (91.98, 91.96)	-17.88 (-17.90, -17.86)
	Eye_R	113.95 (113.97, 113.93)	113.90 (113.91, 113.89)	-0.04 (-0.06, 0.00)	95.95 (96.00, 95.91)	-15.79 (-15.83, -15.75)
Near Field	Thyroid	2.11E-03 (2.06E-03, 2.14E-03)	2.18E-03 (2.16E-03, 2.20E-03)	3.16 (0.71, 7.58)	4.46E-03 (4.38E-03, 4.52E-03)	111.22 (105.48, 115.90)
Far Field	Lungs	6.15E-02 (6.12E-02, 6.20E-02)	6.52E-02 (6.45E-02, 6.59E-02)	6.09 (4.83, 8.66)	5.74E-02 (5.70E-02, 5.77E-02)	-6.61 (-7.38, -5.73)
	Liver	1.38E-02 (1.37E-02, 1.40E-02)	1.21E-02 (1.21E-02, 1.22E-02)	-12.10 (-12.85, -10.18)	1.10E-02 (1.08E-02, 1.12E-02)	-20.01 (-21.73, -18.61)
	Kidneys	1.53E-02 (1.50E-02, 1.54E-02)	1.28E-02 (1.24E-02, 1.32E-02)	-16.51 (-19.90, -10.73)	1.09E-02 (1.04E-02, 1.16E-02)	-28.91 (-32.77, -24.54)
	Bladder	5.71E-04 (5.10E-04, 6.34E-04)	4.72E-04 (4.32E-04, 4.87E-04)	-17.36 (-28.52, 5.86)	4.06E-04 (3.73E-04, 4.18E-04)	-28.82 (-38.38, -18.53)

Excess Relative Risk using Fluence-Weighted Neutron Energy

		WBCT	Hybrid		Scaled MRCP	
	Organ	ERR	ERR	% Difference	ERR	% Difference
In Field	Brain	1.86 (1.86, 1.86)	1.86 (1.86, 1.86)	0.00 (-0.02, 0.02)	8.82E-01 (8.82E-01, 8.82E-01)	-52.62 (-52.64, -52.60)
	Eye_L	3.12 (3.12, 3.12)	3.12 (3.12, 3.12)	-0.04 (-0.07, 0.01)	2.56 (2.56, 2.56)	-17.78 (-17.80, -17.76)
	Eye_R	3.17 (3.17, 3.17)	3.17 (3.17, 3.17)	-0.04 (-0.06, 0.01)	2.68 (2.68, 2.67)	-15.68 (-15.72, -15.64)
Near Field	Thyroid	7.79E-03 (7.67E-03, 7.93E-03)	7.83E-03 (7.78E-03, 7.98E-03)	0.56 (-1.15, 4.89)	1.13E-02 (1.13E-02, 1.15E-02)	45.62 (43.06, 48.75)
Far Field	Lungs	4.06E-03 (4.03E-03, 4.09E-03)	4.23E-03 (4.20E-03, 4.26E-03)	4.31 (3.08, 6.50)	3.81E-03 (3.79E-03, 3.83E-03)	-6.08 (-7.01, -5.24)
	Liver	8.51E-04 (8.46E-04, 8.62E-04)	7.83E-04 (7.79E-04, 7.88E-04)	-8.03 (-8.76, -6.08)	7.62E-04 (7.49E-04, 7.69E-04)	-10.47 (-12.12, -9.24)
	Kidneys	3.09E-04 (3.02E-04, 3.10E-04)	2.67E-04 (2.54E-04, 2.80E-04)	-13.56 (-18.39, -4.73)	2.46E-04 (2.36E-04, 2.59E-04)	-20.61 (-24.30, -16.48)
	Bladder	1.25E-04 (1.11E-04, 1.37E-04)	1.02E-04 (9.27E-05, 1.02E-04)	-18.32 (-30.13, 2.40)	9.22E-05 (8.31E-05, 9.74E-05)	-26.34 (-37.25, -15.86)

Excess Relative Risk using KERMA-Weighted Neutron Energy

		WBCT	Hybrid		Scaled MRCP	
	Organ	ERR	ERR	% Difference	ERR	% Difference
In Field	Brain	1.87 (1.87, 1.87)	1.87 (1.87, 1.87)	0.00 (-0.01, 0.02)	8.94E-01 (8.93E-01, 8.94E-01)	-52.31 (-52.32, -52.29)
	Eye_L	3.12 (3.12, 3.11)	3.11 (3.11, 3.11)	-0.04 (-0.07, 0.01)	2.56 (2.56, 2.56)	-17.88 (-17.90, -17.86)
	Eye_R	3.17 (3.17, 3.17)	3.17 (3.17, 3.17)	-0.04 (-0.06, 0.00)	2.67 (2.67, 2.67)	-15.79 (-15.83, -15.75)
Near Field	Thyroid	1.08E-02 (1.05E-02, 1.10E-02)	1.08E-02 (1.05E-02, 1.11E-02)	0.15 (-3.63, 7.98)	1.30E-02 (1.28E-02, 1.32E-02)	20.78 (17.52, 24.31)
Far Field	Lungs	5.04E-03 (5.02E-03, 5.08E-03)	5.35E-03 (5.29E-03, 5.40E-03)	6.09 (4.83, 8.66)	4.71E-03 (4.68E-03, 4.74E-03)	-6.61 (-7.38, -5.73)
	Liver	1.29E-03 (1.28E-03, 1.31E-03)	1.14E-03 (1.13E-03, 1.14E-03)	-12.10 (-12.85, -10.18)	1.03E-03 (1.01E-03, 1.05E-03)	-20.01 (-21.73, -18.61)
	Kidneys	4.26E-04 (4.17E-04, 4.27E-04)	3.56E-04 (3.44E-04, 3.66E-04)	-16.51 (-19.90, -10.73)	3.03E-04 (2.88E-04, 3.22E-04)	-28.91 (-32.77, -24.54)
	Bladder	1.32E-04 (1.18E-04, 1.46E-04)	1.09E-04 (9.96E-05, 1.12E-04)	-17.36 (-28.52, 5.86)	9.36E-05 (8.59E-05, 9.64E-05)	-28.82 (-38.38, -18.53)

D.2.2 Pat 2

Table D.13: EAR and ERR in Pat 2 using the LNT model and both neutron energy scorers

LNT

Excess Absolute Risk using Fluence-Weighted Neutron Energy

		WBCT	Hybrid		Scaled MRCP	
	Organ	EAR per 10k PY	EAR per 10k PY	% Difference	EAR per 10k PY	% Difference
In Field	Brain	34.13 (34.12 , 34.13)	34.35 (34.34 , 34.36)	0.66 (0.62 , 0.74)	39.20 (39.20 , 39.21)	14.87 (14.84 , 14.91)
	Eye_L	22.91 (22.87 , 22.99)	22.98 (22.93 , 23.07)	0.30 (0.02 , 1.09)	33.67 (33.58 , 33.73)	46.92 (46.45 , 47.46)
	Eye_R	76.34 (76.27 , 76.37)	77.20 (77.08 , 77.28)	1.12 (0.94 , 1.42)	77.32 (77.25 , 77.40)	1.29 (1.16 , 1.39)
Near Field	Thyroid	6.12E-01 (6.11E-01 , 6.13E-01)	6.14E-01 (6.12E-01 , 6.16E-01)	0.29 (-0.03 , 0.93)	5.07E-01 (5.06E-01 , 5.07E-01)	-17.22 (-17.40 , -17.10)
Far Field	Lungs	1.33E-01 (1.33E-01 , 1.34E-01)	1.52E-01 (1.51E-01 , 1.52E-01)	13.56 (13.12 , 14.26)	1.04E-01 (1.04E-01 , 1.04E-01)	-22.18 (-22.38 , -22.00)
	Liver	1.48E-02 (1.48E-02 , 1.49E-02)	1.36E-02 (1.35E-02 , 1.38E-02)	-8.12 (-9.27 , -5.94)	1.35E-02 (1.34E-02 , 1.36E-02)	-9.19 (-9.78 , -8.32)
	Kidneys	1.80E-02 (1.78E-02 , 1.81E-02)	1.63E-02 (1.61E-02 , 1.65E-02)	-9.23 (-10.48 , -6.58)	1.57E-02 (1.55E-02 , 1.59E-02)	-12.66 (-14.07 , -11.02)
	Bladder	7.21E-04 (6.78E-04 , 7.77E-04)	8.44E-04 (7.98E-04 , 9.14E-04)	16.94 (7.57 , 41.04)	7.69E-04 (7.37E-04 , 8.24E-04)	6.65 (-1.10 , 19.17)

Excess Absolute Risk using KERMA-Weighted Neutron Energy

		WBCT	Hybrid		Scaled MRCP	
	Organ	EAR per 10k PY	EAR per 10k PY	% Difference	EAR per 10k PY	% Difference
In Field	Brain	34.61 (34.60 , 34.62)	34.83 (34.82 , 34.84)	0.64 (0.60 , 0.70)	39.68 (39.67 , 39.70)	14.66 (14.62 , 14.70)
	Eye_L	23.26 (23.22 , 23.32)	23.34 (23.29 , 23.43)	0.35 (0.08 , 1.10)	34.11 (34.00 , 34.19)	46.67 (46.16 , 47.18)
	Eye_R	76.83 (76.75 , 76.86)	77.67 (77.54 , 77.76)	1.10 (0.89 , 1.42)	77.85 (77.76 , 77.97)	1.33 (1.17 , 1.48)
Near Field	Thyroid	6.12E-01 (6.11E-01 , 6.13E-01)	6.14E-01 (6.12E-01 , 6.16E-01)	0.29 (-0.03 , 0.93)	5.07E-01 (5.06E-01 , 5.07E-01)	-17.22 (-17.40 , -17.10)
Far Field	Lungs	1.60E-01 (1.60E-01 , 1.61E-01)	1.84E-01 (1.83E-01 , 1.84E-01)	14.51 (14.00 , 15.43)	1.30E-01 (1.29E-01 , 1.30E-01)	-19.06 (-19.42 , -18.83)
	Liver	2.39E-02 (2.39E-02 , 2.40E-02)	2.07E-02 (2.05E-02 , 2.10E-02)	-13.40 (-14.32 , -11.33)	1.96E-02 (1.94E-02 , 1.99E-02)	-17.94 (-19.00 , -16.96)
	Kidneys	2.74E-02 (2.72E-02 , 2.79E-02)	2.45E-02 (2.41E-02 , 2.50E-02)	-10.29 (-12.00 , -6.20)	2.20E-02 (2.16E-02 , 2.26E-02)	-19.51 (-21.17 , -17.10)
	Bladder	7.96E-04 (7.17E-04 , 8.65E-04)	9.27E-04 (8.58E-04 , 1.04E-03)	16.40 (1.98 , 51.41)	8.10E-04 (7.74E-04 , 8.59E-04)	1.70 (-9.32 , 15.92)

Excess Relative Risk using Fluence-Weighted Neutron Energy

		WBCT	Hybrid		Scaled MRCP	
	Organ	ERR	ERR	% Difference	ERR	% Difference
In Field	Brain	9.49E-01 (9.49E-01 , 9.49E-01)	9.56E-01 (9.55E-01 , 9.56E-01)	0.66 (0.62 , 0.74)	1.09 (1.09 , 1.09)	14.87 (14.84 , 14.91)
	Eye_L	6.37E-01 (6.36E-01 , 6.39E-01)	6.39E-01 (6.38E-01 , 6.42E-01)	0.30 (0.02 , 1.09)	9.36E-01 (9.34E-01 , 9.38E-01)	46.92 (46.45 , 47.46)
	Eye_R	2.12 (2.12 , 2.12)	2.15 (2.14 , 2.15)	1.12 (0.94 , 1.42)	2.15 (2.15 , 2.15)	1.29 (1.16 , 1.39)
Near Field	Thyroid	1.24 (1.23 , 1.24)	1.24 (1.24 , 1.24)	0.30 (0.00 , 0.91)	1.02 (1.02 , 1.02)	-17.17 (-17.36 , -17.05)
Far Field	Lungs	1.09E-02 (1.09E-02 , 1.10E-02)	1.24E-02 (1.24E-02 , 1.25E-02)	13.56 (13.12 , 14.26)	8.52E-03 (8.50E-03 , 8.54E-03)	-22.18 (-22.38 , -22.00)
	Liver	1.39E-03 (1.39E-03 , 1.39E-03)	1.28E-03 (1.26E-03 , 1.29E-03)	-8.12 (-9.27 , -5.94)	1.26E-03 (1.26E-03 , 1.27E-03)	-9.19 (-9.78 , -8.32)
	Kidneys	5.00E-04 (4.96E-04 , 5.05E-04)	4.54E-04 (4.48E-04 , 4.59E-04)	-9.23 (-10.48 , -6.58)	4.37E-04 (4.30E-04 , 4.43E-04)	-12.66 (-14.07 , -11.02)
	Bladder	1.66E-04 (1.56E-04 , 1.79E-04)	1.94E-04 (1.84E-04 , 2.11E-04)	16.94 (7.57 , 41.04)	1.77E-04 (1.70E-04 , 1.90E-04)	6.65 (-1.10 , 19.17)

Excess Relative Risk using KERMA-Weighted Neutron Energy

		WBCT	Hybrid		Scaled MRCP	
	Organ	ERR	ERR	% Difference	ERR	% Difference
In Field	Brain	9.63E-01 (9.63E-01 , 9.63E-01)	9.69E-01 (9.69E-01 , 9.69E-01)	0.64 (0.60 , 0.70)	1.10 (1.10 , 1.10)	14.66 (14.62 , 14.70)
	Eye_L	6.47E-01 (6.46E-01 , 6.49E-01)	6.49E-01 (6.48E-01 , 6.52E-01)	0.35 (0.08 , 1.10)	9.49E-01 (9.46E-01 , 9.51E-01)	46.67 (14.62 , 14.70)
	Eye_R	2.14 (2.14 , 2.14)	2.16 (2.16 , 2.16)	1.10 (0.89 , 1.42)	2.17 (2.16 , 2.17)	1.33 (14.62 , 14.70)
Near Field	Thyroid	1.24 (1.24 , 1.25)	1.25 (1.25 , 1.25)	0.32 (0.04 , 0.93)	1.03 (1.03 , 1.03)	-17.16 (14.62 , 14.70)
Far Field	Lungs	1.31E-02 (1.31E-02 , 1.32E-02)	1.51E-02 (1.50E-02 , 1.51E-02)	14.51 (14.00 , 15.43)	1.06E-02 (1.06E-02 , 1.07E-02)	-19.06 (14.62 , 14.70)
	Liver	2.24E-03 (2.24E-03 , 2.25E-03)	1.94E-03 (1.92E-03 , 1.97E-03)	-13.40 (-14.32 , -11.33)	1.84E-03 (1.82E-03 , 1.86E-03)	-17.94 (14.62 , 14.70)
	Kidneys	7.61E-04 (7.55E-04 , 7.75E-04)	6.83E-04 (6.71E-04 , 6.96E-04)	-10.29 (-12.00 , -6.20)	6.13E-04 (6.01E-04 , 6.27E-04)	-19.51 (14.62 , 14.70)
	Bladder	1.83E-04 (1.65E-04 , 1.99E-04)	2.14E-04 (1.98E-04 , 2.39E-04)	16.40 (1.98 , 51.41)	1.87E-04 (1.78E-04 , 1.98E-04)	1.70 (14.62 , 14.70)

Table D.14: EAR and ERR in Pat 2 using the linear plateau model with a 10 Sv inflection point and both neutron energy scorers

Linear-Plateau 10 Sv

Excess Absolute Risk using Fluence-Weighted Neutron Energy

		WBCT	Hybrid		Scaled MRCP	
	Organ	EAR per 10k PY	EAR per 10k PY	% Difference	EAR per 10k PY	% Difference
In Field	Brain	24.02 (24.02 , 24.02)	24.11 (24.11 , 24.12)	0.38 (0.35 , 0.42)	25.94 (25.93 , 25.94)	7.98 (7.96 , 7.99)
	Eye_L	18.61 (18.59 , 18.65)	18.65 (18.62 , 18.70)	0.21 (0.01 , 0.76)	23.83 (23.80 , 23.86)	28.05 (27.79 , 28.36)
	Eye_R	33.81 (33.80 , 33.81)	33.90 (33.89 , 33.91)	0.29 (0.24 , 0.37)	33.92 (33.91 , 33.93)	0.33 (0.30 , 0.36)
Near Field	Thyroid	4.47E-01 (4.47E-01 , 4.48E-01)	4.48E-01 (4.47E-01 , 4.49E-01)	0.18 (-0.02 , 0.56)	3.97E-01 (3.96E-01 , 3.97E-01)	-11.35 (-11.47 , -11.28)
Far Field	Lungs	1.49E-01 (1.48E-01 , 1.49E-01)	1.69E-01 (1.68E-01 , 1.69E-01)	13.50 (13.05 , 14.19)	1.16E-01 (1.16E-01 , 1.16E-01)	-22.10 (-22.31 , -21.92)
	Liver	1.66E-02 (1.66E-02 , 1.66E-02)	1.53E-02 (1.51E-02 , 1.54E-02)	-8.12 (-9.26 , -5.94)	1.51E-02 (1.50E-02 , 1.52E-02)	-9.18 (-9.78 , -8.32)
	Kidneys	2.01E-02 (2.00E-02 , 2.03E-02)	1.83E-02 (1.80E-02 , 1.85E-02)	-9.22 (-10.48 , -6.58)	1.76E-02 (1.73E-02 , 1.78E-02)	-12.66 (-14.07 , -11.02)
	Bladder	8.07E-04 (7.59E-04 , 8.69E-04)	9.44E-04 (8.94E-04 , 1.02E-03)	16.94 (7.57 , 41.03)	8.61E-04 (8.25E-04 , 9.22E-04)	6.65 (-1.10 , 19.17)

Excess Absolute Risk using KERMA-Weighted Neutron Energy

		WBCT	Hybrid		Scaled MRCP	
	Organ	EAR per 10k PY	EAR per 10k PY	% Difference	EAR per 10k PY	% Difference
In Field	Brain	24.22 (24.21 , 24.22)	24.30 (24.30 , 24.31)	0.36 (0.34 , 0.40)	26.10 (26.10 , 26.11)	7.80 (7.78 , 7.82)
	Eye_L	18.80 (18.78 , 18.84)	18.85 (18.82 , 18.90)	0.24 (0.05 , 0.76)	24.01 (23.97 , 24.04)	27.70 (27.43 , 27.99)
	Eye_R	33.86 (33.85 , 33.87)	33.96 (33.94 , 33.97)	0.28 (0.23 , 0.36)	33.98 (33.97 , 33.99)	0.34 (0.30 , 0.38)
Near Field	Thyroid	4.47E-01 (4.47E-01 , 4.48E-01)	4.48E-01 (4.47E-01 , 4.49E-01)	0.18 (-0.02 , 0.56)	3.97E-01 (3.96E-01 , 3.97E-01)	-11.35 (-11.47 , -11.28)
Far Field	Lungs	1.78E-01 (1.78E-01 , 1.79E-01)	2.04E-01 (2.04E-01 , 2.05E-01)	14.42 (13.91 , 15.34)	1.45E-01 (1.44E-01 , 1.45E-01)	-18.98 (-19.34 , -18.75)
	Liver	2.68E-02 (2.67E-02 , 2.68E-02)	2.32E-02 (2.29E-02 , 2.35E-02)	-13.39 (-14.31 , -11.32)	2.20E-02 (2.17E-02 , 2.22E-02)	-17.93 (-18.99 , -16.94)
	Kidneys	3.06E-02 (3.04E-02 , 3.12E-02)	2.75E-02 (2.70E-02 , 2.80E-02)	-10.28 (-11.99 , -6.19)	2.46E-02 (2.42E-02 , 2.52E-02)	-19.51 (-21.17 , -17.09)
	Bladder	8.91E-04 (8.03E-04 , 9.68E-04)	1.04E-03 (9.60E-04 , 1.16E-03)	16.40 (1.98 , 51.41)	9.06E-04 (8.67E-04 , 9.62E-04)	1.70 (-9.32 , 15.92)

Excess Relative Risk using Fluence-Weighted Neutron Energy

		WBCT	Hybrid		Scaled MRCP	
	Organ	ERR	ERR	% Difference	ERR	% Difference
In Field	Brain	6.68E-01 (6.68E-01 , 6.68E-01)	6.71E-01 (6.71E-01 , 6.71E-01)	0.38 (0.35 , 0.42)	7.21E-01 (7.21E-01 , 7.22E-01)	7.98 (7.96 , 7.99)
	Eye_L	5.18E-01 (5.17E-01 , 5.19E-01)	5.19E-01 (5.18E-01 , 5.20E-01)	0.21 (0.01 , 0.76)	6.63E-01 (6.62E-01 , 6.64E-01)	28.05 (27.79 , 28.36)
	Eye_R	9.40E-01 (9.40E-01 , 9.40E-01)	9.43E-01 (9.43E-01 , 9.43E-01)	0.29 (0.24 , 0.37)	9.43E-01 (9.43E-01 , 9.44E-01)	0.33 (0.30 , 0.36)
Near Field	Thyroid	6.27E-01 (6.27E-01 , 6.27E-01)	6.28E-01 (6.27E-01 , 6.28E-01)	0.10 (0.00 , 0.31)	5.84E-01 (5.83E-01 , 5.84E-01)	-6.92 (-7.00 , -6.88)
Far Field	Lungs	1.22E-02 (1.22E-02 , 1.22E-02)	1.38E-02 (1.38E-02 , 1.39E-02)	13.50 (13.05 , 14.19)	9.50E-03 (9.49E-03 , 9.53E-03)	-22.10 (-22.31 , -21.92)
	Liver	1.56E-03 (1.55E-03 , 1.56E-03)	1.43E-03 (1.41E-03 , 1.45E-03)	-8.12 (-9.26 , -5.94)	1.41E-03 (1.41E-03 , 1.43E-03)	-9.18 (-9.78 , -8.32)
	Kidneys	5.59E-04 (5.55E-04 , 5.65E-04)	5.08E-04 (5.02E-04 , 5.14E-04)	-9.22 (-10.48 , -6.58)	4.89E-04 (4.82E-04 , 4.96E-04)	-12.66 (-14.07 , -11.02)
	Bladder	1.86E-04 (1.75E-04 , 2.00E-04)	2.18E-04 (2.06E-04 , 2.36E-04)	16.94 (7.57 , 41.03)	1.98E-04 (1.90E-04 , 2.13E-04)	6.65 (-1.10 , 19.17)

Excess Relative Risk using KERMA-Weighted Neutron Energy

		WBCT	Hybrid		Scaled MRCP	
	Organ	ERR	ERR	% Difference	ERR	% Difference
In Field	Brain	6.74E-01 (6.74E-01 , 6.74E-01)	6.76E-01 (6.76E-01 , 6.76E-01)	0.36 (0.34 , 0.40)	7.26E-01 (7.26E-01 , 7.26E-01)	7.80 (7.78 , 7.82)
	Eye_L	5.23E-01 (5.22E-01 , 5.24E-01)	5.24E-01 (5.24E-01 , 5.26E-01)	0.24 (0.05 , 0.76)	6.68E-01 (6.67E-01 , 6.69E-01)	27.70 (27.43 , 27.99)
	Eye_R	9.42E-01 (9.42E-01 , 9.42E-01)	9.45E-01 (9.44E-01 , 9.45E-01)	0.28 (0.23 , 0.36)	9.45E-01 (9.45E-01 , 9.45E-01)	0.34 (0.30 , 0.38)
Near Field	Thyroid	6.28E-01 (6.28E-01 , 6.29E-01)	6.29E-01 (6.29E-01 , 6.30E-01)	0.11 (0.01 , 0.31)	5.85E-01 (5.85E-01 , 5.85E-01)	-6.86 (-6.94 , -6.83)
Far Field	Lungs	1.46E-02 (1.46E-02 , 1.47E-02)	1.68E-02 (1.67E-02 , 1.68E-02)	14.42 (13.91 , 15.34)	1.19E-02 (1.18E-02 , 1.19E-02)	-18.98 (-19.34 , -18.75)
	Liver	2.51E-03 (2.50E-03 , 2.51E-03)	2.17E-03 (2.15E-03 , 2.20E-03)	-13.39 (-14.31 , -11.32)	2.06E-03 (2.03E-03 , 2.08E-03)	-17.93 (-18.99 , -16.94)
	Kidneys	8.52E-04 (8.45E-04 , 8.67E-04)	7.64E-04 (7.51E-04 , 7.79E-04)	-10.28 (-11.99 , -6.19)	6.86E-04 (6.72E-04 , 7.02E-04)	-19.51 (-21.17 , -17.09)
	Bladder	2.05E-04 (1.85E-04 , 2.23E-04)	2.39E-04 (2.21E-04 , 2.67E-04)	16.40 (1.98 , 51.41)	2.09E-04 (2.00E-04 , 2.22E-04)	1.70 (-9.32 , 15.92)

Table D.15: EAR and ERR in Pat 2 using the linear plateau model with a 40 Sv inflection point and both neutron energy scorers

Linear-Plateau 40 Sv

Excess Absolute Risk using Fluence-Weighted Neutron Energy

		WBCT	Hybrid		Scaled MRCP	
	Organ	EAR per 10k PY	EAR per 10k PY	% Difference	EAR per 10k PY	% Difference
In Field	Brain	31.02 (31.02 , 31.03)	31.20 (31.19 , 31.21)	0.58 (0.54 , 0.65)	35.00 (35.00 , 35.01)	12.83 (12.80 , 12.85)
	Eye_L	21.68 (21.65 , 21.75)	21.74 (21.70 , 21.82)	0.28 (0.02 , 1.00)	30.66 (30.58 , 30.71)	41.38 (40.97 , 41.84)
	Eye_R	59.98 (59.93 , 59.99)	60.47 (60.40 , 60.52)	0.83 (0.70 , 1.05)	60.55 (60.51 , 60.59)	0.95 (0.86 , 1.03)
Near Field	Thyroid	5.62E-01 (5.62E-01 , 5.63E-01)	5.64E-01 (5.63E-01 , 5.65E-01)	0.26 (-0.03 , 0.82)	4.75E-01 (4.74E-01 , 4.75E-01)	-15.61 (-15.78 , -15.51)
Far Field	Lungs	1.37E-01 (1.37E-01 , 1.37E-01)	1.56E-01 (1.55E-01 , 1.56E-01)	13.55 (13.10 , 14.25)	1.07E-01 (1.07E-01 , 1.07E-01)	-22.16 (-22.37 , -21.98)
	Liver	1.53E-02 (1.52E-02 , 1.53E-02)	1.40E-02 (1.39E-02 , 1.42E-02)	-8.12 (-9.26 , -5.94)	1.39E-02 (1.38E-02 , 1.40E-02)	-9.19 (-9.78 , -8.32)
	Kidneys	1.85E-02 (1.84E-02 , 1.87E-02)	1.68E-02 (1.66E-02 , 1.70E-02)	-9.22 (-10.48 , -6.58)	1.61E-02 (1.59E-02 , 1.64E-02)	-12.66 (-14.07 , -11.02)
	Bladder	7.42E-04 (6.98E-04 , 7.99E-04)	8.68E-04 (8.21E-04 , 9.40E-04)	16.94 (7.57 , 41.03)	7.92E-04 (7.59E-04 , 8.48E-04)	6.65 (-1.10 , 19.17)

Excess Absolute Risk using KERMA-Weighted Neutron Energy

		WBCT	Hybrid		Scaled MRCP	
	Organ	EAR per 10k PY	EAR per 10k PY	% Difference	EAR per 10k PY	% Difference
In Field	Brain	31.41 (31.40 , 31.41)	31.59 (31.58 , 31.59)	0.56 (0.53 , 0.61)	35.37 (35.37 , 35.38)	12.62 (12.59 , 12.65)
	Eye_L	21.98 (21.95 , 22.04)	22.05 (22.01 , 22.13)	0.32 (0.07 , 1.01)	31.01 (30.93 , 31.07)	41.08 (40.64 , 41.52)
	Eye_R	60.26 (60.22 , 60.28)	60.75 (60.67 , 60.80)	0.81 (0.66 , 1.05)	60.85 (60.80 , 60.92)	0.98 (0.87 , 1.10)
Near Field	Thyroid	5.62E-01 (5.62E-01 , 5.63E-01)	5.64E-01 (5.63E-01 , 5.65E-01)	0.26 (-0.03 , 0.82)	4.75E-01 (4.74E-01 , 4.75E-01)	-15.61 (-15.78 , -15.51)
Far Field	Lungs	1.65E-01 (1.64E-01 , 1.65E-01)	1.89E-01 (1.88E-01 , 1.89E-01)	14.48 (13.98 , 15.41)	1.33E-01 (1.33E-01 , 1.34E-01)	-19.04 (-19.40 , -18.81)
	Liver	2.46E-02 (2.46E-02 , 2.47E-02)	2.13E-02 (2.11E-02 , 2.16E-02)	-13.40 (-14.32 , -11.33)	2.02E-02 (1.99E-02 , 2.04E-02)	-17.94 (-19.00 , -16.95)
	Kidneys	2.82E-02 (2.79E-02 , 2.87E-02)	2.53E-02 (2.48E-02 , 2.58E-02)	-10.29 (-12.00 , -6.20)	2.27E-02 (2.22E-02 , 2.32E-02)	-19.51 (-21.17 , -17.10)
	Bladder	8.19E-04 (7.38E-04 , 8.90E-04)	9.53E-04 (8.83E-04 , 1.07E-03)	16.40 (1.98 , 51.41)	8.33E-04 (7.97E-04 , 8.84E-04)	1.70 (-9.32 , 15.92)

Excess Relative Risk using Fluence-Weighted Neutron Energy

		WBCT	Hybrid		Scaled MRCP	
	Organ	ERR	ERR	% Difference	ERR	% Difference
In Field	Brain	8.63E-01 (8.63E-01 , 8.63E-01)	8.68E-01 (8.68E-01 , 8.68E-01)	0.58 (0.54 , 0.65)	9.74E-01 (9.74E-01 , 9.74E-01)	12.83 (12.80 , 12.85)
	Eye_L	6.03E-01 (6.02E-01 , 6.05E-01)	6.05E-01 (6.04E-01 , 6.07E-01)	0.28 (0.02 , 1.00)	8.53E-01 (8.51E-01 , 8.54E-01)	41.38 (40.97 , 41.84)
	Eye_R	1.67 (1.67 , 1.67)	1.68 (1.68 , 1.68)	0.83 (0.70 , 1.05)	1.68 (1.68 , 1.69)	0.95 (0.86 , 1.03)
Near Field	Thyroid	1.02 (1.01 , 1.02)	1.02 (1.02 , 1.02)	0.24 (0.00 , 0.71)	8.74E-01 (8.72E-01 , 8.74E-01)	-14.03 (-14.19 , -13.93)
Far Field	Lungs	1.13E-02 (1.12E-02 , 1.13E-02)	1.28E-02 (1.27E-02 , 1.28E-02)	13.55 (13.10 , 14.25)	8.76E-03 (8.74E-03 , 8.78E-03)	-22.16 (-22.37 , -21.98)
	Liver	1.43E-03 (1.43E-03 , 1.43E-03)	1.31E-03 (1.30E-03 , 1.33E-03)	-8.12 (-9.26 , -5.94)	1.30E-03 (1.29E-03 , 1.31E-03)	-9.19 (-9.78 , -8.32)
	Kidneys	5.14E-04 (5.11E-04 , 5.19E-04)	4.67E-04 (4.61E-04 , 4.72E-04)	-9.22 (-10.48 , -6.58)	4.49E-04 (4.43E-04 , 4.56E-04)	-12.66 (-14.07 , -11.02)
	Bladder	1.71E-04 (1.61E-04 , 1.84E-04)	2.00E-04 (1.89E-04 , 2.17E-04)	16.94 (7.57 , 41.03)	1.82E-04 (1.75E-04 , 1.95E-04)	6.65 (-1.10 , 19.17)

Excess Relative Risk using KERMA-Weighted Neutron Energy

		WBCT	Hybrid		Scaled MRCP	
	Organ	ERR	ERR	% Difference	ERR	% Difference
In Field	Brain	8.74E-01 (8.74E-01 , 8.74E-01)	8.79E-01 (8.78E-01 , 8.79E-01)	0.56 (0.53 , 0.61)	9.84E-01 (9.84E-01 , 9.84E-01)	12.62 (12.59 , 12.65)
	Eye_L	6.11E-01 (6.10E-01 , 6.13E-01)	6.13E-01 (6.12E-01 , 6.16E-01)	0.32 (0.07 , 1.01)	8.63E-01 (8.60E-01 , 8.64E-01)	41.08 (40.64 , 41.52)
	Eye_R	1.68 (1.68 , 1.68)	1.69 (1.69 , 1.69)	0.81 (0.66 , 1.05)	1.69 (1.69 , 1.69)	0.98 (0.87 , 1.10)
Near Field	Thyroid	1.02 (1.02 , 1.02)	1.02 (1.02 , 1.03)	0.25 (0.03 , 0.72)	8.79E-01 (8.78E-01 , 8.79E-01)	-14.00 (-14.15 , -13.91)
Far Field	Lungs	1.35E-02 (1.35E-02 , 1.35E-02)	1.55E-02 (1.54E-02 , 1.55E-02)	14.48 (13.98 , 15.41)	1.09E-02 (1.09E-02 , 1.10E-02)	-19.04 (-19.40 , -18.81)
	Liver	2.31E-03 (2.30E-03 , 2.31E-03)	2.00E-03 (1.98E-03 , 2.02E-03)	-13.40 (-14.32 , -11.33)	1.89E-03 (1.87E-03 , 1.91E-03)	-17.94 (-19.00 , -16.95)
	Kidneys	7.83E-04 (7.77E-04 , 7.97E-04)	7.03E-04 (6.90E-04 , 7.17E-04)	-10.29 (-12.00 , -6.20)	6.30E-04 (6.18E-04 , 6.46E-04)	-19.51 (-21.17 , -17.10)
	Bladder	1.89E-04 (1.70E-04 , 2.05E-04)	2.20E-04 (2.03E-04 , 2.46E-04)	16.40 (1.98 , 51.41)	1.92E-04 (1.84E-04 , 2.04E-04)	1.70 (-9.32 , 15.92)

Table D.16: EAR and ERR in Pat 2 using the linear exponential model with a 10 Sv inflection point and both neutron energy scorers

Linear-Exponential 10 Sv

Excess Absolute Risk using Fluence-Weighted Neutron Energy

		WBCT	Hybrid		Scaled MRCP	
	Organ	EAR per 10k PY	EAR per 10k PY	% Difference	EAR per 10k PY	% Difference
In Field	Brain	24.29 (24.29, 24.29)	24.38 (24.38, 24.39)	0.37 (0.34, 0.41)	26.14 (26.14, 26.14)	7.60 (7.58, 7.61)
	Eye_L	18.85 (18.82, 18.89)	18.89 (18.86, 18.94)	0.21 (0.01, 0.77)	24.11 (24.07, 24.13)	27.91 (27.65, 28.22)
	Eye_R	31.54 (31.54, 31.54)	31.54 (31.54, 31.54)	0.01 (0.01, 0.01)	31.54 (31.54, 31.54)	0.01 (0.01, 0.01)
Near Field	Thyroid	4.53E-01 (4.52E-01, 4.53E-01)	4.54E-01 (4.53E-01, 4.54E-01)	0.17 (-0.02, 0.55)	4.02E-01 (4.01E-01, 4.02E-01)	-11.30 (-11.42, -11.22)
Far Field	Lungs	1.47E-01 (1.47E-01, 1.47E-01)	1.67E-01 (1.66E-01, 1.67E-01)	13.50 (13.06, 14.20)	1.14E-01 (1.14E-01, 1.15E-01)	-22.11 (-22.32, -21.93)
	Liver	1.64E-02 (1.64E-02, 1.64E-02)	1.51E-02 (1.49E-02, 1.52E-02)	-8.12 (-9.26, -5.94)	1.49E-02 (1.48E-02, 1.50E-02)	-9.18 (-9.78, -8.32)
	Kidneys	1.99E-02 (1.97E-02, 2.01E-02)	1.80E-02 (1.78E-02, 1.82E-02)	-9.22 (-10.48, -6.58)	1.73E-02 (1.71E-02, 1.76E-02)	-12.66 (-14.07, -11.02)
	Bladder	7.97E-04 (7.50E-04, 8.58E-04)	9.32E-04 (8.82E-04, 1.01E-03)	16.94 (7.57, 41.03)	8.50E-04 (8.15E-04, 9.11E-04)	6.65 (-1.10, 19.17)

Excess Absolute Risk using KERMA-Weighted Neutron Energy

		WBCT	Hybrid		Scaled MRCP	
	Organ	EAR per 10k PY	EAR per 10k PY	% Difference	EAR per 10k PY	% Difference
In Field	Brain	24.48 (24.48, 24.49)	24.57 (24.57, 24.57)	0.35 (0.33, 0.39)	26.30 (26.29, 26.30)	7.40 (7.38, 7.42)
	Eye_L	19.04 (19.02, 19.08)	19.09 (19.06, 19.14)	0.24 (0.06, 0.77)	24.29 (24.24, 24.32)	27.52 (27.25, 27.81)
	Eye_R	31.54 (31.54, 31.54)	31.54 (31.54, 31.54)	0.00 (0.00, 0.01)	31.54 (31.54, 31.54)	0.00 (0.00, 0.00)
Near Field	Thyroid	4.53E-01 (4.52E-01, 4.53E-01)	4.54E-01 (4.53E-01, 4.54E-01)	0.17 (-0.02, 0.55)	4.02E-01 (4.01E-01, 4.02E-01)	-11.30 (-11.42, -11.22)
Far Field	Lungs	1.76E-01 (1.76E-01, 1.77E-01)	2.02E-01 (2.01E-01, 2.02E-01)	14.43 (13.92, 15.35)	1.43E-01 (1.42E-01, 1.43E-01)	-18.99 (-19.35, -18.76)
	Liver	2.64E-02 (2.64E-02, 2.65E-02)	2.29E-02 (2.27E-02, 2.32E-02)	-13.40 (-14.31, -11.32)	2.17E-02 (2.14E-02, 2.19E-02)	-17.93 (-18.99, -16.95)
	Kidneys	3.02E-02 (3.00E-02, 3.08E-02)	2.71E-02 (2.66E-02, 2.77E-02)	-10.28 (-11.99, -6.19)	2.43E-02 (2.39E-02, 2.49E-02)	-19.51 (-21.17, -17.09)
	Bladder	8.80E-04 (7.92E-04, 9.56E-04)	1.02E-03 (9.48E-04, 1.14E-03)	16.40 (1.98, 51.41)	8.95E-04 (8.56E-04, 9.49E-04)	1.70 (-9.32, 15.92)

Excess Relative Risk using Fluence-Weighted Neutron Energy

		WBCT	Hybrid		Scaled MRCP	
	Organ	ERR	ERR	% Difference	ERR	% Difference
In Field	Brain	6.76E-01 (6.76E-01, 6.76E-01)	6.78E-01 (6.78E-01, 6.78E-01)	0.37 (0.34, 0.41)	7.27E-01 (7.27E-01, 7.27E-01)	7.60 (7.58, 7.61)
	Eye_L	5.24E-01 (5.24E-01, 5.25E-01)	5.25E-01 (5.25E-01, 5.27E-01)	0.21 (0.01, 0.77)	6.71E-01 (6.70E-01, 6.71E-01)	27.91 (27.65, 28.22)
	Eye_R	8.77E-01 (8.77E-01, 8.77E-01)	8.77E-01 (8.77E-01, 8.77E-01)	0.01 (0.01, 0.01)	8.77E-01 (8.77E-01, 8.77E-01)	0.01 (0.01, 0.01)
Near Field	Thyroid	6.08E-01 (6.07E-01, 6.08E-01)	6.08E-01 (6.08E-01, 6.08E-01)	0.06 (0.00, 0.17)	5.78E-01 (5.78E-01, 5.78E-01)	-4.82 (-4.88, -4.80)
Far Field	Lungs	1.21E-02 (1.20E-02, 1.21E-02)	1.37E-02 (1.36E-02, 1.37E-02)	13.50 (13.06, 14.20)	9.39E-03 (9.37E-03, 9.41E-03)	-22.11 (-22.32, -21.93)
	Liver	1.54E-03 (1.53E-03, 1.54E-03)	1.41E-03 (1.39E-03, 1.43E-03)	-8.12 (-9.26, -5.94)	1.40E-03 (1.39E-03, 1.41E-03)	-9.18 (-9.78, -8.32)
	Kidneys	5.52E-04 (5.48E-04, 5.58E-04)	5.01E-04 (4.95E-04, 5.07E-04)	-9.22 (-10.48, -6.58)	4.82E-04 (4.75E-04, 4.90E-04)	-12.66 (-14.07, -11.02)
	Bladder	1.84E-04 (1.73E-04, 1.98E-04)	2.15E-04 (2.03E-04, 2.33E-04)	16.94 (7.57, 41.03)	1.96E-04 (1.88E-04, 2.10E-04)	6.65 (-1.10, 19.17)

Excess Relative Risk using KERMA-Weighted Neutron Energy

		WBCT	Hybrid		Scaled MRCP	
	Organ	ERR	ERR	% Difference	ERR	% Difference
In Field	Brain	6.81E-01 (6.81E-01, 6.81E-01)	6.83E-01 (6.83E-01, 6.84E-01)	0.35 (0.33, 0.39)	7.31E-01 (7.31E-01, 7.32E-01)	7.40 (7.38, 7.42)
	Eye_L	5.30E-01 (5.29E-01, 5.31E-01)	5.31E-01 (5.30E-01, 5.32E-01)	0.24 (0.06, 0.77)	6.76E-01 (6.74E-01, 6.76E-01)	27.52 (27.25, 27.81)
	Eye_R	8.77E-01 (8.77E-01, 8.77E-01)	8.77E-01 (8.77E-01, 8.77E-01)	0.00 (0.00, 0.01)	8.77E-01 (8.77E-01, 8.77E-01)	0.00 (0.00, 0.00)
Near Field	Thyroid	6.08E-01 (6.08E-01, 6.09E-01)	6.09E-01 (6.09E-01, 6.09E-01)	0.06 (0.01, 0.17)	5.80E-01 (5.79E-01, 5.80E-01)	-4.72 (-4.77, -4.70)
Far Field	Lungs	1.45E-02 (1.44E-02, 1.45E-02)	1.66E-02 (1.65E-02, 1.66E-02)	14.43 (13.92, 15.35)	1.17E-02 (1.17E-02, 1.17E-02)	-18.99 (-19.35, -18.76)
	Liver	2.47E-03 (2.47E-03, 2.48E-03)	2.14E-03 (2.12E-03, 2.17E-03)	-13.40 (-14.31, -11.32)	2.03E-03 (2.01E-03, 2.05E-03)	-17.93 (-18.99, -16.95)
	Kidneys	8.41E-04 (8.34E-04, 8.56E-04)	7.54E-04 (7.41E-04, 7.69E-04)	-10.28 (-11.99, -6.19)	6.77E-04 (6.64E-04, 6.93E-04)	-19.51 (-21.17, -17.09)
	Bladder	2.03E-04 (1.83E-04, 2.20E-04)	2.36E-04 (2.18E-04, 2.64E-04)	16.40 (1.98, 51.41)	2.06E-04 (1.97E-04, 2.19E-04)	1.70 (-9.32, 15.92)

Table D.17: EAR and ERR in Pat 2 using the linear exponential model with a 40 Sv inflection point and both neutron energy scorers

Linear-Exponential 40 Sv

Excess Absolute Risk using Fluence-Weighted Neutron Energy

		WBCT	Hybrid		Scaled MRCP	
	Organ	EAR per 10k PY	EAR per 10k PY	% Difference	EAR per 10k PY	% Difference
In Field	Brain	31.35 (31.34 , 31.35)	31.53 (31.52 , 31.54)	0.59 (0.55 , 0.66)	35.42 (35.42 , 35.43)	13.01 (12.98 , 13.04)
	Eye_L	21.82 (21.78 , 21.89)	21.88 (21.84 , 21.96)	0.28 (0.02 , 1.01)	30.97 (30.90 , 31.02)	41.92 (41.50 , 42.39)
	Eye_R	61.20 (61.16 , 61.22)	61.72 (61.65 , 61.77)	0.84 (0.71 , 1.06)	61.79 (61.75 , 61.84)	0.97 (0.87 , 1.05)
Near Field	Thyroid	5.68E-01 (5.67E-01 , 5.69E-01)	5.69E-01 (5.68E-01 , 5.71E-01)	0.26 (-0.03 , 0.83)	4.78E-01 (4.78E-01 , 4.78E-01)	-15.78 (-15.94 , -15.67)
Far Field	Lungs	1.37E-01 (1.36E-01 , 1.37E-01)	1.55E-01 (1.55E-01 , 1.56E-01)	13.55 (13.11 , 14.25)	1.06E-01 (1.06E-01 , 1.07E-01)	-22.16 (-22.37 , -21.98)
	Liver	1.52E-02 (1.52E-02 , 1.53E-02)	1.40E-02 (1.38E-02 , 1.41E-02)	-8.12 (-9.26 , -5.94)	1.38E-02 (1.37E-02 , 1.40E-02)	-9.19 (-9.78 , -8.32)
	Kidneys	1.84E-02 (1.83E-02 , 1.86E-02)	1.67E-02 (1.65E-02 , 1.69E-02)	-9.23 (-10.48 , -6.58)	1.61E-02 (1.59E-02 , 1.63E-02)	-12.66 (-14.07 , -11.02)
	Bladder	7.40E-04 (6.96E-04 , 7.96E-04)	8.65E-04 (8.18E-04 , 9.37E-04)	16.94 (7.57 , 41.03)	7.89E-04 (7.56E-04 , 8.45E-04)	6.65 (-1.10 , 19.17)

Excess Absolute Risk using KERMA-Weighted Neutron Energy

		WBCT	Hybrid		Scaled MRCP	
	Organ	EAR per 10k PY	EAR per 10k PY	% Difference	EAR per 10k PY	% Difference
In Field	Brain	31.74 (31.74 , 31.75)	31.92 (31.91 , 31.93)	0.57 (0.53 , 0.62)	35.80 (35.80 , 35.81)	12.80 (12.77 , 12.84)
	Eye_L	22.12 (22.09 , 22.18)	22.19 (22.15 , 22.27)	0.32 (0.07 , 1.02)	31.33 (31.25 , 31.39)	41.63 (41.18 , 42.08)
	Eye_R	61.50 (61.45 , 61.51)	62.00 (61.92 , 62.06)	0.82 (0.67 , 1.06)	62.11 (62.05 , 62.18)	1.00 (0.88 , 1.11)
Near Field	Thyroid	5.68E-01 (5.67E-01 , 5.69E-01)	5.69E-01 (5.68E-01 , 5.71E-01)	0.26 (-0.03 , 0.83)	4.78E-01 (4.78E-01 , 4.78E-01)	-15.78 (-15.94 , -15.67)
Far Field	Lungs	1.64E-01 (1.64E-01 , 1.64E-01)	1.88E-01 (1.87E-01 , 1.89E-01)	14.49 (13.98 , 15.41)	1.33E-01 (1.33E-01 , 1.33E-01)	-19.04 (-19.40 , -18.81)
	Liver	2.45E-02 (2.45E-02 , 2.46E-02)	2.12E-02 (2.10E-02 , 2.15E-02)	-13.40 (-14.32 , -11.33)	2.01E-02 (1.99E-02 , 2.04E-02)	-17.94 (-19.00 , -16.95)
	Kidneys	2.80E-02 (2.78E-02 , 2.86E-02)	2.52E-02 (2.47E-02 , 2.57E-02)	-10.29 (-12.00 , -6.20)	2.26E-02 (2.21E-02 , 2.31E-02)	-19.51 (-21.17 , -17.10)
	Bladder	8.16E-04 (7.35E-04 , 8.87E-04)	9.50E-04 (8.80E-04 , 1.06E-03)	16.40 (1.98 , 51.41)	8.30E-04 (7.94E-04 , 8.81E-04)	1.70 (-9.32 , 15.92)

Excess Relative Risk using Fluence-Weighted Neutron Energy

		WBCT	Hybrid		Scaled MRCP	
	Organ	ERR	ERR	% Difference	ERR	% Difference
In Field	Brain	8.72E-01 (8.72E-01 , 8.72E-01)	8.77E-01 (8.77E-01 , 8.77E-01)	0.59 (0.55 , 0.66)	9.85E-01 (9.85E-01 , 9.86E-01)	13.01 (12.98 , 13.04)
	Eye_L	6.07E-01 (6.06E-01 , 6.09E-01)	6.09E-01 (6.08E-01 , 6.11E-01)	0.28 (0.02 , 1.01)	8.61E-01 (8.59E-01 , 8.63E-01)	41.92 (41.50 , 42.39)
	Eye_R	1.70 (1.70 , 1.70)	1.72 (1.71 , 1.72)	0.84 (0.71 , 1.06)	1.72 (1.72 , 1.72)	0.97 (0.87 , 1.05)
Near Field	Thyroid	1.03 (1.03 , 1.04)	1.04 (1.04 , 1.04)	0.24 (0.00 , 0.72)	8.87E-01 (8.86E-01 , 8.87E-01)	-14.24 (-14.40 , -14.14)
Far Field	Lungs	1.12E-02 (1.12E-02 , 1.12E-02)	1.27E-02 (1.27E-02 , 1.28E-02)	13.55 (13.11 , 14.25)	8.73E-03 (8.71E-03 , 8.75E-03)	-22.16 (-22.37 , -21.98)
	Liver	1.43E-03 (1.42E-03 , 1.43E-03)	1.31E-03 (1.29E-03 , 1.32E-03)	-8.12 (-9.26 , -5.94)	1.29E-03 (1.29E-03 , 1.31E-03)	-9.19 (-9.78 , -8.32)
	Kidneys	5.12E-04 (5.09E-04 , 5.18E-04)	4.65E-04 (4.60E-04 , 4.71E-04)	-9.23 (-10.48 , -6.58)	4.48E-04 (4.41E-04 , 4.55E-04)	-12.66 (-14.07 , -11.02)
	Bladder	1.70E-04 (1.60E-04 , 1.83E-04)	1.99E-04 (1.89E-04 , 2.16E-04)	16.94 (7.57 , 41.03)	1.82E-04 (1.74E-04 , 1.95E-04)	6.65 (-1.10 , 19.17)

Excess Relative Risk using KERMA-Weighted Neutron Energy

		WBCT	Hybrid		Scaled MRCP	
	Organ	ERR	ERR	% Difference	ERR	% Difference
In Field	Brain	8.83E-01 (8.83E-01 , 8.83E-01)	8.88E-01 (8.88E-01 , 8.88E-01)	0.57 (0.53 , 0.62)	9.96E-01 (9.96E-01 , 9.96E-01)	12.80 (12.77 , 12.84)
	Eye_L	6.15E-01 (6.14E-01 , 6.17E-01)	6.17E-01 (6.16E-01 , 6.20E-01)	0.32 (0.07 , 1.02)	8.72E-01 (8.69E-01 , 8.73E-01)	41.63 (41.18 , 42.08)
	Eye_R	1.71 (1.71 , 1.71)	1.72 (1.72 , 1.73)	0.82 (0.67 , 1.06)	1.73 (1.73 , 1.73)	1.00 (0.88 , 1.11)
Near Field	Thyroid	1.04 (1.04 , 1.04)	1.04 (1.04 , 1.05)	0.26 (0.03 , 0.74)	8.93E-01 (8.91E-01 , 8.93E-01)	-14.21 (-15.94 , -15.67)
Far Field	Lungs	1.35E-02 (1.34E-02 , 1.35E-02)	1.54E-02 (1.54E-02 , 1.55E-02)	14.49 (13.98 , 15.41)	1.09E-02 (1.09E-02 , 1.09E-02)	-19.04 (-19.40 , -18.81)
	Liver	2.30E-03 (2.29E-03 , 2.30E-03)	1.99E-03 (1.97E-03 , 2.02E-03)	-13.40 (-14.32 , -11.33)	1.89E-03 (1.86E-03 , 1.91E-03)	-17.94 (-19.00 , -16.95)
	Kidneys	7.80E-04 (7.74E-04 , 7.94E-04)	7.00E-04 (6.88E-04 , 7.14E-04)	-10.29 (-12.00 , -6.20)	6.28E-04 (6.16E-04 , 6.43E-04)	-19.51 (-21.17 , -17.10)
	Bladder	1.88E-04 (1.69E-04 , 2.04E-04)	2.19E-04 (2.03E-04 , 2.45E-04)	16.40 (1.98 , 51.41)	1.91E-04 (1.83E-04 , 2.03E-04)	1.70 (-9.32 , 15.92)

D.2.3 Pat 3

Table D.18: EAR and ERR in Pat 3 using the LNT model and both neutron energy scorers

LNT

Excess Absolute Risk using Fluence-Weighted Neutron Energy

		WBCT	Hybrid		Scaled MRCP	
	Organ	EAR per 10k PY	EAR per 10k PY	% Difference	EAR per 10k PY	% Difference
In Field	Brain	97.88 (97.87 , 97.89)	97.88 (97.86 , 97.90)	-0.01 (-0.03 , 0.04)	55.69 (55.68 , 55.70)	-43.10 (-43.11 , -43.09)
	Eye_L	104.70 (104.62 , 104.76)	104.70 (104.52 , 104.89)	0.00 (-0.18 , 0.38)	32.83 (32.79 , 32.90)	-68.64 (-68.69 , -68.58)
	Eye_R	94.83 (94.73 , 94.95)	94.79 (94.69 , 94.82)	-0.04 (-0.20 , 0.22)	21.41 (21.36 , 21.49)	-77.42 (-77.48 , -77.34)
Near Field	Thyroid	1.44E-03 (1.43E-03 , 1.44E-03)	1.44E-03 (1.41E-03 , 1.47E-03)	-0.34 (-2.24 , 4.00)	1.67E-03 (1.65E-03 , 1.70E-03)	16.27 (14.11 , 18.29)
Far Field	Lungs	3.96E-02 (3.93E-02 , 3.99E-02)	4.18E-02 (4.16E-02 , 4.20E-02)	5.40 (4.48 , 7.13)	3.84E-02 (3.81E-02 , 3.86E-02)	-3.15 (-4.10 , -2.27)
	Liver	1.26E-02 (1.25E-02 , 1.27E-02)	9.85E-03 (9.78E-03 , 9.90E-03)	-21.55 (-22.35 , -19.86)	9.89E-03 (9.82E-03 , 9.97E-03)	-21.23 (-22.00 , -20.21)
	Kidneys	1.06E-02 (1.02E-02 , 1.11E-02)	1.14E-02 (1.10E-02 , 1.18E-02)	7.24 (1.65 , 19.66)	1.09E-02 (1.04E-02 , 1.14E-02)	2.53 (-3.44 , 9.60)
	Bladder	2.94E-04 (2.58E-04 , 3.43E-04)	2.83E-04 (2.45E-04 , 3.21E-04)	-3.59 (-21.07 , 39.64)	2.54E-04 (2.22E-04 , 3.02E-04)	-13.50 (-28.74 , 13.67)

Excess Absolute Risk using KERMA-Weighted Neutron Energy

		WBCT	Hybrid		Scaled MRCP	
	Organ	EAR per 10k PY	EAR per 10k PY	% Difference	EAR per 10k PY	% Difference
In Field	Brain	99.17 (99.15 , 99.17)	99.16 (99.15 , 99.18)	-0.01 (-0.03 , 0.03)	56.62 (56.61 , 56.63)	-42.90 (-42.92 , -42.89)
	Eye_L	105.68 (105.56 , 105.80)	105.66 (105.45 , 105.81)	-0.02 (-0.25 , 0.39)	33.61 (33.52 , 33.72)	-68.19 (-68.29 , -68.09)
	Eye_R	95.80 (95.70 , 95.88)	95.77 (95.63 , 95.82)	-0.03 (-0.21 , 0.24)	22.12 (22.06 , 22.21)	-76.91 (-76.98 , -76.81)
Near Field	Thyroid	1.44E-03 (1.43E-03 , 1.44E-03)	1.44E-03 (1.41E-03 , 1.47E-03)	-0.34 (-2.24 , 4.00)	1.67E-03 (1.65E-03 , 1.70E-03)	16.27 (14.11 , 18.29)
Far Field	Lungs	5.83E-02 (5.80E-02 , 5.85E-02)	6.10E-02 (6.07E-02 , 6.13E-02)	4.53 (3.77 , 5.94)	5.35E-02 (5.32E-02 , 5.37E-02)	-8.36 (-8.98 , -7.85)
	Liver	1.68E-02 (1.67E-02 , 1.70E-02)	1.27E-02 (1.26E-02 , 1.28E-02)	-24.48 (-25.56 , -22.60)	1.21E-02 (1.20E-02 , 1.22E-02)	-28.31 (-29.05 , -27.22)
	Kidneys	1.25E-02 (1.20E-02 , 1.34E-02)	1.33E-02 (1.29E-02 , 1.39E-02)	6.58 (1.50 , 20.86)	1.22E-02 (1.18E-02 , 1.29E-02)	-2.21 (-7.14 , 7.04)
	Bladder	3.10E-04 (2.78E-04 , 3.57E-04)	2.82E-04 (2.46E-04 , 3.19E-04)	-8.98 (-23.88 , 27.21)	2.56E-04 (2.29E-04 , 2.81E-04)	-17.60 (-29.70 , 0.25)

Excess Relative Risk using Fluence-Weighted Neutron Energy

		WBCT	Hybrid		Scaled MRCP	
	Organ	ERR	ERR	% Difference	ERR	% Difference
In Field	Brain	2.72 (2.72 , 2.72)	2.72 (2.72 , 2.72)	-0.01 (-0.03 , 0.04)	1.55 (1.55 , 1.55)	-43.10 (-43.11 , -43.09)
	Eye_L	2.91 (2.91 , 2.91)	2.91 (2.91 , 2.92)	0.00 (-0.18 , 0.38)	9.13E-01 (0.91 , 0.92)	-68.64 (-68.69 , -68.58)
	Eye_R	2.64 (2.64 , 2.64)	2.64 (2.63 , 2.64)	-0.04 (-0.20 , 0.22)	5.96E-01 (0.59 , 0.60)	-77.42 (-77.48 , -77.34)
Near Field	Thyroid	1.00E-02 (9.76E-03 , 1.02E-02)	9.96E-03 (9.81E-03 , 1.01E-02)	-0.46 (-3.29 , 4.55)	1.05E-02 (1.04E-02 , 1.07E-02)	5.09 (2.08 , 7.83)
Far Field	Lungs	3.25E-03 (3.23E-03 , 3.27E-03)	3.43E-03 (3.41E-03 , 3.44E-03)	5.40 (4.48 , 7.13)	3.15E-03 (3.13E-03 , 3.17E-03)	-3.15 (-4.10 , -2.27)
	Liver	1.18E-03 (1.17E-03 , 1.19E-03)	9.22E-04 (9.16E-04 , 9.27E-04)	-21.55 (-22.35 , -19.86)	9.26E-04 (9.20E-04 , 9.33E-04)	-21.23 (-22.00 , -20.21)
	Kidneys	2.96E-04 (2.84E-04 , 3.10E-04)	3.17E-04 (3.06E-04 , 3.28E-04)	7.24 (1.65 , 19.66)	3.03E-04 (2.90E-04 , 3.17E-04)	2.53 (-3.44 , 9.60)
	Bladder	6.76E-05 (5.93E-05 , 7.92E-05)	6.52E-05 (5.65E-05 , 7.39E-05)	-3.59 (-21.07 , 39.64)	5.85E-05 (5.11E-05 , 6.96E-05)	-13.50 (-28.74 , 13.67)

Excess Relative Risk using KERMA-Weighted Neutron Energy

		WBCT	Hybrid		Scaled MRCP	
	Organ	ERR	ERR	% Difference	ERR	% Difference
In Field	Brain	2.76 (2.76 , 2.76)	2.76 (2.76 , 2.76)	-0.01 (-0.03 , 0.03)	1.58 (1.57 , 1.58)	-42.90 (-42.92 , -42.89)
	Eye_L	2.94 (2.94 , 2.94)	2.94 (2.93 , 2.94)	-0.02 (-0.25 , 0.39)	9.35E-01 (0.93 , 0.94)	-68.19 (-68.29 , -68.09)
	Eye_R	2.66 (2.66 , 2.67)	2.66 (2.66 , 2.67)	-0.03 (-0.21 , 0.24)	6.15E-01 (0.61 , 0.62)	-76.91 (-76.98 , -76.81)
Near Field	Thyroid	1.57E-02 (1.53E-02 , 1.59E-02)	1.56E-02 (1.53E-02 , 1.59E-02)	-0.20 (-3.37 , 5.54)	1.54E-02 (1.52E-02 , 1.57E-02)	-1.57 (-4.57 , 1.21)
Far Field	Lungs	4.79E-03 (4.76E-03 , 4.80E-03)	5.00E-03 (4.98E-03 , 5.03E-03)	4.53 (3.77 , 5.94)	4.39E-03 (4.37E-03 , 4.41E-03)	-8.36 (-8.98 , -7.85)
	Liver	1.58E-03 (1.56E-03 , 1.59E-03)	1.19E-03 (1.18E-03 , 1.20E-03)	-24.48 (-25.56 , -22.60)	1.13E-03 (1.13E-03 , 1.15E-03)	-28.31 (-29.05 , -27.22)
	Kidneys	3.47E-04 (3.35E-04 , 3.71E-04)	3.70E-04 (3.59E-04 , 3.86E-04)	6.58 (1.50 , 20.86)	3.40E-04 (3.28E-04 , 3.59E-04)	-2.21 (-7.14 , 7.04)
	Bladder	7.15E-05 (6.41E-05 , 8.22E-05)	6.50E-05 (5.68E-05 , 7.35E-05)	-8.98 (-23.88 , 27.21)	5.89E-05 (5.27E-05 , 6.48E-05)	-17.60 (-29.70 , 0.25)

Table D.19: EAR and ERR in Pat 3 using the linear plateau model with a 10 Sv inflection point and both neutron energy scorers

Linear-Plateau 10 Sv

Excess Absolute Risk using Fluence-Weighted Neutron Energy

		WBCT	Hybrid		Scaled MRCP	
	Organ	EAR per 10k PY	EAR per 10k PY	% Difference	EAR per 10k PY	% Difference
In Field	Brain	35.65 (35.65, 35.65)	35.65 (35.65, 35.65)	0.00 (-0.01, 0.01)	30.50 (30.49, 30.50)	-14.46 (-14.47, -14.46)
	Eye_L	36.03 (36.03, 36.04)	36.03 (36.02, 36.04)	0.00 (-0.03, 0.06)	23.48 (23.46, 23.51)	-34.83 (-34.88, -34.75)
	Eye_R	35.46 (35.45, 35.47)	35.46 (35.45, 35.46)	-0.01 (-0.04, 0.04)	17.74 (17.71, 17.79)	-49.97 (-50.06, -49.84)
Near Field	Thyroid	1.61E-03 (1.60E-03, 1.61E-03)	1.61E-03 (1.58E-03, 1.64E-03)	-0.34 (-2.23, 4.00)	1.87E-03 (1.84E-03, 1.91E-03)	16.25 (14.09, 18.27)
Far Field	Lungs	4.43E-02 (4.40E-02, 4.46E-02)	4.67E-02 (4.65E-02, 4.69E-02)	5.39 (4.48, 7.12)	4.29E-02 (4.26E-02, 4.32E-02)	-3.15 (-4.09, -2.27)
	Liver	1.40E-02 (1.40E-02, 1.42E-02)	1.10E-02 (1.09E-02, 1.11E-02)	-21.54 (-22.35, -19.85)	1.11E-02 (1.10E-02, 1.12E-02)	-21.22 (-22.00, -20.20)
	Kidneys	1.19E-02 (1.14E-02, 1.25E-02)	1.28E-02 (1.23E-02, 1.32E-02)	7.23 (1.65, 19.65)	1.22E-02 (1.17E-02, 1.27E-02)	2.53 (-3.44, 9.59)
	Bladder	3.29E-04 (2.88E-04, 3.85E-04)	3.17E-04 (2.75E-04, 3.59E-04)	-3.59 (-21.07, 39.63)	2.84E-04 (2.48E-04, 3.38E-04)	-13.50 (-28.74, 13.66)

Excess Absolute Risk using KERMA-Weighted Neutron Energy

		WBCT	Hybrid		Scaled MRCP	
	Organ	EAR per 10k PY	EAR per 10k PY	% Difference	EAR per 10k PY	% Difference
In Field	Brain	35.73 (35.73, 35.73)	35.73 (35.73, 35.73)	0.00 (0.00, 0.01)	30.69 (30.69, 30.69)	-14.10 (-14.11, -14.09)
	Eye_L	36.08 (36.07, 36.09)	36.08 (36.07, 36.09)	0.00 (-0.04, 0.06)	23.81 (23.77, 23.85)	-34.01 (-34.12, -33.89)
	Eye_R	35.52 (35.52, 35.53)	35.52 (35.51, 35.52)	-0.01 (-0.04, 0.04)	18.16 (18.12, 18.21)	-48.89 (-48.99, -48.74)
Near Field	Thyroid	1.61E-03 (1.60E-03, 1.61E-03)	1.61E-03 (1.58E-03, 1.64E-03)	-0.34 (-2.23, 4.00)	1.87E-03 (1.84E-03, 1.91E-03)	16.25 (14.09, 18.27)
Far Field	Lungs	6.52E-02 (6.49E-02, 6.54E-02)	6.81E-02 (6.78E-02, 6.85E-02)	4.52 (3.76, 5.93)	5.97E-02 (5.95E-02, 6.00E-02)	-8.35 (-8.97, -7.84)
	Liver	1.89E-02 (1.87E-02, 1.90E-02)	1.42E-02 (1.41E-02, 1.43E-02)	-24.46 (-25.55, -22.59)	1.35E-02 (1.35E-02, 1.37E-02)	-28.29 (-29.04, -27.21)
	Kidneys	1.40E-02 (1.35E-02, 1.49E-02)	1.49E-02 (1.44E-02, 1.55E-02)	6.58 (1.50, 20.85)	1.37E-02 (1.32E-02, 1.44E-02)	-2.21 (-7.14, 7.04)
	Bladder	3.47E-04 (3.11E-04, 3.99E-04)	3.16E-04 (2.76E-04, 3.57E-04)	-8.98 (-23.88, 27.21)	2.86E-04 (2.56E-04, 3.15E-04)	-17.60 (-29.70, 0.25)

Excess Relative Risk using Fluence-Weighted Neutron Energy

		WBCT	Hybrid		Scaled MRCP	
	Organ	ERR	ERR	% Difference	ERR	% Difference
In Field	Brain	9.92E-01 (9.92E-01, 9.92E-01)	9.92E-01 (9.92E-01, 9.92E-01)	0.00 (-0.01, 0.01)	8.48E-01 (8.48E-01, 8.48E-01)	-14.46 (-14.47, -14.46)
	Eye_L	1.00 (1.00, 1.00)	1.00 (1.00, 1.00)	0.00 (-0.03, 0.06)	6.53E-01 (6.53E-01, 6.54E-01)	-34.83 (-34.88, -34.75)
	Eye_R	9.86E-01 (9.86E-01, 9.87E-01)	9.86E-01 (9.86E-01, 9.86E-01)	-0.01 (-0.04, 0.04)	4.93E-01 (4.93E-01, 4.95E-01)	-49.97 (-50.06, -49.84)
Near Field	Thyroid	1.11E-02 (1.08E-02, 1.13E-02)	1.11E-02 (1.09E-02, 1.12E-02)	-0.46 (-3.26, 4.51)	1.17E-02 (1.15E-02, 1.19E-02)	5.05 (2.07, 7.77)
Far Field	Lungs	3.63E-03 (3.61E-03, 3.66E-03)	3.83E-03 (3.81E-03, 3.85E-03)	5.39 (4.48, 7.12)	3.52E-03 (3.50E-03, 3.54E-03)	-3.15 (-4.09, -2.27)
	Liver	1.32E-03 (1.31E-03, 1.33E-03)	1.03E-03 (1.02E-03, 1.04E-03)	-21.54 (-22.35, -19.85)	1.04E-03 (1.03E-03, 1.04E-03)	-21.22 (-22.00, -20.20)
	Kidneys	3.31E-04 (3.18E-04, 3.47E-04)	3.55E-04 (3.43E-04, 3.68E-04)	7.23 (1.65, 19.65)	3.40E-04 (3.25E-04, 3.54E-04)	2.53 (-3.44, 9.59)
	Bladder	7.57E-05 (6.64E-05, 8.86E-05)	7.30E-05 (6.33E-05, 8.27E-05)	-3.59 (-21.07, 39.63)	6.55E-05 (5.72E-05, 7.79E-05)	-13.50 (-28.74, 13.66)

Excess Relative Risk using KERMA-Weighted Neutron Energy

		WBCT	Hybrid		Scaled MRCP	
	Organ	ERR	ERR	% Difference	ERR	% Difference
In Field	Brain	9.94E-01 (9.94E-01, 9.94E-01)	9.94E-01 (9.94E-01, 9.94E-01)	0.00 (0.00, 0.01)	8.54E-01 (8.54E-01, 8.54E-01)	-14.10 (-14.11, -14.09)
	Eye_L	1.00 (1.00, 1.00)	1.00 (1.00, 1.00)	0.00 (-0.04, 0.06)	6.62E-01 (6.61E-01, 6.64E-01)	-34.01 (-34.12, -33.89)
	Eye_R	9.88E-01 (9.88E-01, 9.88E-01)	9.88E-01 (9.88E-01, 9.88E-01)	-0.01 (-0.04, 0.04)	5.05E-01 (5.04E-01, 5.07E-01)	-48.89 (-48.99, -48.74)
Near Field	Thyroid	1.73E-02 (1.69E-02, 1.76E-02)	1.73E-02 (1.70E-02, 1.76E-02)	-0.20 (-3.33, 5.47)	1.71E-02 (1.68E-02, 1.74E-02)	-1.55 (-4.52, 1.19)
Far Field	Lungs	5.35E-03 (5.32E-03, 5.36E-03)	5.59E-03 (5.56E-03, 5.62E-03)	4.52 (3.76, 5.93)	4.90E-03 (4.88E-03, 4.93E-03)	-8.35 (-8.97, -7.84)
	Liver	1.77E-03 (1.75E-03, 1.78E-03)	1.33E-03 (1.32E-03, 1.34E-03)	-24.46 (-25.55, -22.59)	1.27E-03 (1.26E-03, 1.28E-03)	-28.29 (-29.04, -27.21)
	Kidneys	3.89E-04 (3.74E-04, 4.16E-04)	4.14E-04 (4.02E-04, 4.32E-04)	6.58 (1.50, 20.85)	3.80E-04 (3.67E-04, 4.01E-04)	-2.21 (-7.14, 7.04)
	Bladder	8.00E-05 (7.17E-05, 9.20E-05)	7.28E-05 (6.36E-05, 8.23E-05)	-8.98 (-23.88, 27.21)	6.59E-05 (5.90E-05, 7.26E-05)	-17.60 (-29.70, 0.25)

Table D.20: EAR and ERR in Pat 3 using the linear plateau model with a 40 Sv inflection point and both neutron energy scorers

Linear-Plateau 40 Sv

Excess Absolute Risk using Fluence-Weighted Neutron Energy

		WBCT	Hybrid		Scaled MRCP	
	Organ	EAR per 10k PY	EAR per 10k PY	% Difference	EAR per 10k PY	% Difference
In Field	Brain	71.60 (71.60 , 71.61)	71.60 (71.59 , 71.61)	-0.01 (-0.02 , 0.02)	46.95 (46.94 , 46.95)	-34.44 (-34.45 , -34.43)
	Eye_L	74.91 (74.88 , 74.94)	74.91 (74.83 , 75.00)	0.00 (-0.12 , 0.25)	29.98 (29.95 , 30.04)	-59.97 (-60.02 , -59.90)
	Eye_R	70.07 (70.02 , 70.12)	70.05 (69.99 , 70.06)	-0.03 (-0.14 , 0.15)	20.37 (20.33 , 20.44)	-70.93 (-70.99 , -70.82)
Near Field	Thyroid	1.48E-03 (1.47E-03 , 1.48E-03)	1.48E-03 (1.45E-03 , 1.51E-03)	-0.34 (-2.24 , 4.00)	1.72E-03 (1.69E-03 , 1.75E-03)	16.26 (14.11 , 18.28)
Far Field	Lungs	4.08E-02 (4.05E-02 , 4.10E-02)	4.30E-02 (4.28E-02 , 4.32E-02)	5.40 (4.48 , 7.13)	3.95E-02 (3.92E-02 , 3.98E-02)	-3.15 (-4.10 , -2.27)
	Liver	1.29E-02 (1.28E-02 , 1.31E-02)	1.01E-02 (1.01E-02 , 1.02E-02)	-21.55 (-22.35 , -19.86)	1.02E-02 (1.01E-02 , 1.03E-02)	-21.23 (-22.00 , -20.21)
	Kidneys	1.09E-02 (1.05E-02 , 1.15E-02)	1.17E-02 (1.13E-02 , 1.22E-02)	7.24 (1.65 , 19.66)	1.12E-02 (1.07E-02 , 1.17E-02)	2.53 (-3.44 , 9.60)
	Bladder	3.02E-04 (2.65E-04 , 3.53E-04)	2.91E-04 (2.52E-04 , 3.30E-04)	-3.59 (-21.07 , 39.64)	2.61E-04 (2.28E-04 , 3.11E-04)	-13.50 (-28.74 , 13.67)

Excess Absolute Risk using KERMA-Weighted Neutron Energy

		WBCT	Hybrid		Scaled MRCP	
	Organ	EAR per 10k PY	EAR per 10k PY	% Difference	EAR per 10k PY	% Difference
In Field	Brain	72.24 (72.23 , 72.24)	72.24 (72.23 , 72.24)	0.00 (-0.02 , 0.02)	47.58 (47.57 , 47.58)	-34.14 (-34.16 , -34.13)
	Eye_L	75.37 (75.32 , 75.43)	75.36 (75.27 , 75.44)	-0.01 (-0.16 , 0.26)	30.61 (30.54 , 30.70)	-59.39 (-59.49 , -59.27)
	Eye_R	70.56 (70.51 , 70.60)	70.54 (70.47 , 70.57)	-0.02 (-0.15 , 0.16)	20.99 (20.94 , 21.07)	-70.25 (-70.33 , -70.13)
Near Field	Thyroid	1.48E-03 (1.47E-03 , 1.48E-03)	1.48E-03 (1.45E-03 , 1.51E-03)	-0.34 (-2.24 , 4.00)	1.72E-03 (1.69E-03 , 1.75E-03)	16.26 (14.11 , 18.28)
Far Field	Lungs	6.00E-02 (5.97E-02 , 6.02E-02)	6.27E-02 (6.24E-02 , 6.31E-02)	4.53 (3.77 , 5.94)	5.50E-02 (5.47E-02 , 5.53E-02)	-8.36 (-8.98 , -7.85)
	Liver	1.73E-02 (1.72E-02 , 1.75E-02)	1.31E-02 (1.29E-02 , 1.32E-02)	-24.47 (-25.56 , -22.60)	1.24E-02 (1.24E-02 , 1.26E-02)	-28.30 (-29.05 , -27.22)
	Kidneys	1.28E-02 (1.24E-02 , 1.37E-02)	1.37E-02 (1.33E-02 , 1.43E-02)	6.58 (1.50 , 20.86)	1.26E-02 (1.21E-02 , 1.33E-02)	-2.21 (-7.14 , 7.04)
	Bladder	3.19E-04 (2.86E-04 , 3.67E-04)	2.90E-04 (2.54E-04 , 3.28E-04)	-8.98 (-23.88 , 27.21)	2.63E-04 (2.36E-04 , 2.90E-04)	-17.60 (-29.70 , 0.25)

Excess Relative Risk using Fluence-Weighted Neutron Energy

		WBCT	Hybrid		Scaled MRCP	
	Organ	ERR	ERR	% Difference	ERR	% Difference
In Field	Brain	1.99 (1.99 , 1.99)	1.99 (1.99 , 1.99)	-0.01 (-0.02 , 0.02)	1.31 (1.31 , 1.31)	-34.44 (-34.45 , -34.43)
	Eye_L	2.08 (2.08 , 2.08)	2.08 (2.08 , 2.09)	0.00 (-0.12 , 0.25)	8.34E-01 (8.33E-01 , 8.36E-01)	-59.97 (-60.02 , -59.90)
	Eye_R	1.95 (1.95 , 1.95)	1.95 (1.95 , 1.95)	-0.03 (-0.14 , 0.15)	5.67E-01 (5.65E-01 , 5.69E-01)	-70.93 (-70.99 , -70.82)
Near Field	Thyroid	1.03E-02 (1.00E-02 , 1.04E-02)	1.02E-02 (1.01E-02 , 1.04E-02)	-0.46 (-3.28 , 4.54)	1.08E-02 (1.06E-02 , 1.10E-02)	5.08 (2.08 , 7.82)
Far Field	Lungs	3.34E-03 (3.32E-03 , 3.36E-03)	3.52E-03 (3.51E-03 , 3.54E-03)	5.40 (4.48 , 7.13)	3.24E-03 (3.22E-03 , 3.26E-03)	-3.15 (-4.10 , -2.27)
	Liver	1.21E-03 (1.20E-03 , 1.22E-03)	9.49E-04 (9.42E-04 , 9.54E-04)	-21.55 (-22.35 , -19.86)	9.53E-04 (9.46E-04 , 9.60E-04)	-21.23 (-22.00 , -20.21)
	Kidneys	3.05E-04 (2.93E-04 , 3.19E-04)	3.27E-04 (3.15E-04 , 3.38E-04)	7.24 (1.65 , 19.66)	3.12E-04 (2.99E-04 , 3.26E-04)	2.53 (-3.44 , 9.60)
	Bladder	6.96E-05 (6.11E-05 , 8.15E-05)	6.71E-05 (5.82E-05 , 7.60E-05)	-3.59 (-21.07 , 39.64)	6.02E-05 (5.26E-05 , 7.16E-05)	-13.50 (-28.74 , 13.67)

Excess Relative Risk using KERMA-Weighted Neutron Energy

		WBCT	Hybrid		Scaled MRCP	
	Organ	ERR	ERR	% Difference	ERR	% Difference
In Field	Brain	2.01 (2.01 , 2.01)	2.01 (2.01 , 2.01)	0.00 (-0.02 , 0.02)	1.32 (1.32 , 1.32)	-34.14 (-34.16 , -34.13)
	Eye_L	2.10 (2.10 , 2.10)	2.10 (2.09 , 2.10)	-0.01 (-0.16 , 0.26)	8.52E-01 (8.49E-01 , 8.54E-01)	-59.39 (-59.49 , -59.27)
	Eye_R	1.96 (1.96 , 1.96)	1.96 (1.96 , 1.96)	-0.02 (-0.15 , 0.16)	5.84E-01 (5.82E-01 , 5.86E-01)	-70.25 (-70.33 , -70.13)
Near Field	Thyroid	1.61E-02 (1.57E-02 , 1.63E-02)	1.60E-02 (1.57E-02 , 1.63E-02)	-0.20 (-3.36 , 5.52)	1.58E-02 (1.56E-02 , 1.61E-02)	-1.57 (-4.56 , 1.20)
Far Field	Lungs	4.92E-03 (4.90E-03 , 4.94E-03)	5.15E-03 (5.12E-03 , 5.17E-03)	4.53 (3.77 , 5.94)	4.51E-03 (4.49E-03 , 4.53E-03)	-8.36 (-8.98 , -7.85)
	Liver	1.62E-03 (1.61E-03 , 1.64E-03)	1.23E-03 (1.21E-03 , 1.23E-03)	-24.47 (-25.56 , -22.60)	1.16E-03 (1.16E-03 , 1.18E-03)	-28.30 (-29.05 , -27.22)
	Kidneys	3.57E-04 (3.44E-04 , 3.82E-04)	3.81E-04 (3.69E-04 , 3.97E-04)	6.58 (1.50 , 20.86)	3.49E-04 (3.37E-04 , 3.69E-04)	-2.21 (-7.14 , 7.04)
	Bladder	7.35E-05 (6.59E-05 , 8.46E-05)	6.69E-05 (5.84E-05 , 7.57E-05)	-8.98 (-23.88 , 27.21)	6.06E-05 (5.43E-05 , 6.67E-05)	-17.60 (-29.70 , 0.25)

Table D.21: EAR and ERR in Pat 3 using the linear exponential model with a 10 Sv inflection point and both neutron energy scorers

Linear-Exponential 10 Sv

Excess Absolute Risk using Fluence-Weighted Neutron Energy

		WBCT	Hybrid		Scaled MRCP	
	Organ	EAR per 10k PY	EAR per 10k PY	% Difference	EAR per 10k PY	% Difference
In Field	Brain	30.63 (30.63 , 30.63)	30.63 (30.63 , 30.63)	0.00 (0.00 , 0.01)	30.02 (30.02 , 30.02)	-1.99 (-1.99 , -1.98)
	Eye_L	30.01 (30.02 , 30.00)	30.01 (30.03 , 29.99)	0.00 (-0.06 , 0.13)	23.76 (23.74 , 23.79)	-20.81 (-20.87 , -20.72)
	Eye_R	30.87 (30.87 , 30.86)	30.87 (30.88 , 30.87)	0.01 (-0.02 , 0.07)	17.96 (17.92 , 18.00)	-41.83 (-41.93 , -41.67)
Near Field	Thyroid	1.59E-03 (1.58E-03 , 1.59E-03)	1.58E-03 (1.56E-03 , 1.62E-03)	-0.34 (-2.23 , 4.00)	1.85E-03 (1.82E-03 , 1.88E-03)	16.25 (14.10 , 18.27)
Far Field	Lungs	4.37E-02 (4.34E-02 , 4.40E-02)	4.61E-02 (4.59E-02 , 4.63E-02)	5.39 (4.48 , 7.12)	4.24E-02 (4.21E-02 , 4.27E-02)	-3.15 (-4.09 , -2.27)
	Liver	1.39E-02 (1.38E-02 , 1.40E-02)	1.09E-02 (1.08E-02 , 1.09E-02)	-21.54 (-22.35 , -19.85)	1.09E-02 (1.09E-02 , 1.10E-02)	-21.22 (-22.00 , -20.20)
	Kidneys	1.18E-02 (1.13E-02 , 1.23E-02)	1.26E-02 (1.22E-02 , 1.30E-02)	7.24 (1.65 , 19.65)	1.21E-02 (1.15E-02 , 1.26E-02)	2.53 (-3.44 , 9.59)
	Bladder	3.24E-04 (2.85E-04 , 3.80E-04)	3.13E-04 (2.71E-04 , 3.54E-04)	-3.59 (-21.07 , 39.63)	2.81E-04 (2.45E-04 , 3.34E-04)	-13.50 (-28.74 , 13.66)

Excess Absolute Risk using KERMA-Weighted Neutron Energy

		WBCT	Hybrid		Scaled MRCP	
	Organ	EAR per 10k PY	EAR per 10k PY	% Difference	EAR per 10k PY	% Difference
In Field	Brain	30.52 (30.52 , 30.52)	30.52 (30.52 , 30.52)	0.00 (0.00 , 0.01)	30.16 (30.16 , 30.16)	-1.19 (-1.20 , -1.19)
	Eye_L	29.91 (29.92 , 29.90)	29.91 (29.93 , 29.89)	0.01 (-0.07 , 0.16)	24.09 (24.05 , 24.13)	-19.47 (-19.60 , -19.32)
	Eye_R	30.79 (30.80 , 30.79)	30.80 (30.81 , 30.79)	0.01 (-0.04 , 0.07)	18.38 (18.35 , 18.44)	-40.31 (-40.43 , -40.13)
Near Field	Thyroid	1.59E-03 (1.58E-03 , 1.59E-03)	1.58E-03 (1.56E-03 , 1.62E-03)	-0.34 (-2.23 , 4.00)	1.85E-03 (1.82E-03 , 1.88E-03)	16.25 (14.10 , 18.27)
Far Field	Lungs	6.44E-02 (6.40E-02 , 6.45E-02)	6.73E-02 (6.69E-02 , 6.77E-02)	4.52 (3.77 , 5.93)	5.90E-02 (5.87E-02 , 5.93E-02)	-8.35 (-8.97 , -7.84)
	Liver	1.86E-02 (1.84E-02 , 1.88E-02)	1.41E-02 (1.39E-02 , 1.41E-02)	-24.47 (-25.55 , -22.59)	1.33E-02 (1.33E-02 , 1.35E-02)	-28.29 (-29.04 , -27.21)
	Kidneys	1.38E-02 (1.33E-02 , 1.48E-02)	1.47E-02 (1.43E-02 , 1.53E-02)	6.58 (1.50 , 20.85)	1.35E-02 (1.30E-02 , 1.42E-02)	-2.21 (-7.14 , 7.04)
	Bladder	3.43E-04 (3.07E-04 , 3.94E-04)	3.12E-04 (2.72E-04 , 3.53E-04)	-8.98 (-23.88 , 27.21)	2.82E-04 (2.53E-04 , 3.11E-04)	-17.60 (-29.70 , 0.25)

Excess Relative Risk using Fluence-Weighted Neutron Energy

		WBCT	Hybrid		Scaled MRCP	
	Organ	ERR	ERR	% Difference	ERR	% Difference
In Field	Brain	8.52E-01 (8.52E-01 , 8.52E-01)	8.52E-01 (8.52E-01 , 8.52E-01)	0.00 (0.00 , 0.01)	8.35E-01 (8.35E-01 , 8.35E-01)	-1.99 (-1.99 , -1.98)
	Eye_L	8.35E-01 (8.35E-01 , 8.35E-01)	8.35E-01 (8.35E-01 , 8.34E-01)	0.00 (-0.06 , 0.13)	6.61E-01 (6.61E-01 , 6.62E-01)	-20.81 (-20.87 , -20.72)
	Eye_R	8.59E-01 (8.59E-01 , 8.58E-01)	8.59E-01 (8.59E-01 , 8.59E-01)	0.01 (-0.02 , 0.07)	4.99E-01 (4.99E-01 , 5.01E-01)	-41.83 (-41.93 , -41.67)
Near Field	Thyroid	1.10E-02 (1.07E-02 , 1.12E-02)	1.09E-02 (1.08E-02 , 1.11E-02)	-0.46 (-3.26 , 4.52)	1.15E-02 (1.14E-02 , 1.18E-02)	5.05 (2.07 , 7.78)
Far Field	Lungs	3.59E-03 (3.56E-03 , 3.61E-03)	3.78E-03 (3.76E-03 , 3.80E-03)	5.39 (4.48 , 7.12)	3.48E-03 (3.45E-03 , 3.50E-03)	-3.15 (-4.09 , -2.27)
	Liver	1.30E-03 (1.29E-03 , 1.31E-03)	1.02E-03 (1.01E-03 , 1.02E-03)	-21.54 (-22.35 , -19.85)	1.02E-03 (1.02E-03 , 1.03E-03)	-21.22 (-22.00 , -20.20)
	Kidneys	3.27E-04 (3.14E-04 , 3.43E-04)	3.51E-04 (3.39E-04 , 3.63E-04)	7.24 (1.65 , 19.65)	3.35E-04 (3.21E-04 , 3.50E-04)	2.53 (-3.44 , 9.59)
	Bladder	7.48E-05 (6.56E-05 , 8.75E-05)	7.21E-05 (6.25E-05 , 8.17E-05)	-3.59 (-21.07 , 39.63)	6.47E-05 (5.65E-05 , 7.69E-05)	-13.50 (-28.74 , 13.66)

Excess Relative Risk using KERMA-Weighted Neutron Energy

		WBCT	Hybrid		Scaled MRCP	
	Organ	ERR	ERR	% Difference	ERR	% Difference
In Field	Brain	8.49E-01 (8.49E-01 , 8.49E-01)	8.49E-01 (8.49E-01 , 8.49E-01)	0.00 (0.00 , 0.01)	8.39E-01 (8.39E-01 , 8.39E-01)	-1.19 (-1.20 , -1.19)
	Eye_L	8.32E-01 (8.32E-01 , 8.32E-01)	8.32E-01 (8.33E-01 , 8.32E-01)	0.01 (-0.07 , 0.16)	6.70E-01 (6.69E-01 , 6.71E-01)	-19.47 (-19.60 , -19.32)
	Eye_R	8.57E-01 (8.57E-01 , 8.56E-01)	8.57E-01 (8.57E-01 , 8.57E-01)	0.01 (-0.04 , 0.07)	5.11E-01 (5.10E-01 , 5.13E-01)	-40.31 (-40.43 , -40.13)
Near Field	Thyroid	1.71E-02 (1.67E-02 , 1.74E-02)	1.71E-02 (1.68E-02 , 1.74E-02)	-0.20 (-3.33 , 5.48)	1.69E-02 (1.66E-02 , 1.72E-02)	-1.56 (-4.53 , 1.19)
Far Field	Lungs	5.28E-03 (5.25E-03 , 5.29E-03)	5.52E-03 (5.49E-03 , 5.55E-03)	4.52 (3.77 , 5.93)	4.84E-03 (4.82E-03 , 4.86E-03)	-8.35 (-8.97 , -7.84)
	Liver	1.74E-03 (1.73E-03 , 1.76E-03)	1.32E-03 (1.30E-03 , 1.32E-03)	-24.47 (-25.55 , -22.59)	1.25E-03 (1.24E-03 , 1.27E-03)	-28.29 (-29.04 , -27.21)
	Kidneys	3.84E-04 (3.70E-04 , 4.10E-04)	4.09E-04 (3.97E-04 , 4.26E-04)	6.58 (1.50 , 20.85)	3.75E-04 (3.62E-04 , 3.96E-04)	-2.21 (-7.14 , 7.04)
	Bladder	7.90E-05 (7.08E-05 , 9.08E-05)	7.19E-05 (6.28E-05 , 8.13E-05)	-8.98 (-23.88 , 27.21)	6.51E-05 (5.83E-05 , 7.17E-05)	-17.60 (-29.70 , 0.25)

Table D.22: EAR and ERR in Pat 3 using the linear exponential model with a 40 Sv inflection point and both neutron energy scorers

Linear-Exponential 40 Sv

Excess Absolute Risk using Fluence-Weighted Neutron Energy

		WBCT	Hybrid		Scaled MRCP	
	Organ	EAR per 10k PY	EAR per 10k PY	% Difference	EAR per 10k PY	% Difference
In Field	Brain	73.21 (73.20 , 73.21)	73.21 (73.20 , 73.22)	-0.01 (-0.02 , 0.03)	47.72 (47.72 , 47.73)	-34.82 (-34.83 , -34.81)
	Eye_L	76.61 (76.57 , 76.64)	76.61 (76.52 , 76.70)	0.00 (-0.12 , 0.25)	30.28 (30.25 , 30.34)	-60.47 (-60.52 , -60.40)
	Eye_R	71.63 (71.58 , 71.69)	71.61 (71.55 , 71.62)	-0.03 (-0.14 , 0.15)	20.49 (20.44 , 20.56)	-71.40 (-71.46 , -71.29)
Near Field	Thyroid	1.48E-03 (1.47E-03 , 1.48E-03)	1.47E-03 (1.45E-03 , 1.51E-03)	-0.34 (-2.24 , 4.00)	1.72E-03 (1.69E-03 , 1.75E-03)	16.26 (14.11 , 18.28)
Far Field	Lungs	4.06E-02 (4.03E-02 , 4.09E-02)	4.28E-02 (4.26E-02 , 4.30E-02)	5.40 (4.48 , 7.13)	3.93E-02 (3.91E-02 , 3.96E-02)	-3.15 (-4.10 , -2.27)
	Liver	1.29E-02 (1.28E-02 , 1.30E-02)	1.01E-02 (1.00E-02 , 1.01E-02)	-21.55 (-22.35 , -19.86)	1.01E-02 (1.01E-02 , 1.02E-02)	-21.23 (-22.00 , -20.21)
	Kidneys	1.09E-02 (1.05E-02 , 1.14E-02)	1.17E-02 (1.13E-02 , 1.21E-02)	7.24 (1.65 , 19.66)	1.12E-02 (1.07E-02 , 1.17E-02)	2.53 (-3.44 , 9.60)
	Bladder	3.01E-04 (2.64E-04 , 3.52E-04)	2.90E-04 (2.51E-04 , 3.29E-04)	-3.59 (-21.07 , 39.64)	2.60E-04 (2.27E-04 , 3.10E-04)	-13.50 (-28.74 , 13.67)

Excess Absolute Risk using KERMA-Weighted Neutron Energy

		WBCT	Hybrid		Scaled MRCP	
	Organ	EAR per 10k PY	EAR per 10k PY	% Difference	EAR per 10k PY	% Difference
In Field	Brain	73.86 (73.85 , 73.87)	73.86 (73.85 , 73.87)	0.00 (-0.02 , 0.02)	48.37 (48.36 , 48.38)	-34.51 (-34.53 , -34.50)
	Eye_L	77.08 (77.02 , 77.14)	77.07 (76.97 , 77.14)	-0.01 (-0.16 , 0.26)	30.93 (30.85 , 31.01)	-59.88 (-59.98 , -59.76)
	Eye_R	72.14 (72.08 , 72.18)	72.12 (72.05 , 72.14)	-0.02 (-0.15 , 0.16)	21.12 (21.07 , 21.20)	-70.72 (-70.80 , -70.61)
Near Field	Thyroid	1.48E-03 (1.47E-03 , 1.48E-03)	1.47E-03 (1.45E-03 , 1.51E-03)	-0.34 (-2.24 , 4.00)	1.72E-03 (1.69E-03 , 1.75E-03)	16.26 (14.11 , 18.28)
Far Field	Lungs	5.98E-02 (5.95E-02 , 5.99E-02)	6.25E-02 (6.22E-02 , 6.29E-02)	4.53 (3.77 , 5.94)	5.48E-02 (5.45E-02 , 5.51E-02)	-8.36 (-8.98 , -7.85)
	Liver	1.73E-02 (1.71E-02 , 1.74E-02)	1.30E-02 (1.29E-02 , 1.31E-02)	-24.47 (-25.56 , -22.60)	1.24E-02 (1.23E-02 , 1.25E-02)	-28.30 (-29.05 , -27.22)
	Kidneys	1.28E-02 (1.23E-02 , 1.37E-02)	1.36E-02 (1.32E-02 , 1.42E-02)	6.58 (1.50 , 20.86)	1.25E-02 (1.21E-02 , 1.32E-02)	-2.21 (-7.14 , 7.04)
	Bladder	3.18E-04 (2.85E-04 , 3.66E-04)	2.89E-04 (2.53E-04 , 3.27E-04)	-8.98 (-23.88 , 27.21)	2.62E-04 (2.35E-04 , 2.89E-04)	-17.60 (-29.70 , 0.25)

Excess Relative Risk using Fluence-Weighted Neutron Energy

		WBCT	Hybrid		Scaled MRCP	
	Organ	ERR	ERR	% Difference	ERR	% Difference
In Field	Brain	2.04 (2.04 , 2.04)	2.04 (2.04 , 2.04)	-0.01 (-0.02 , 0.03)	1.33 (1.33 , 1.33)	-34.82 (-34.83 , -34.81)
	Eye_L	2.13 (2.13 , 2.13)	2.13 (2.13 , 2.13)	0.00 (-0.12 , 0.25)	8.42E-01 (8.41E-01 , 8.44E-01)	-60.47 (-60.52 , -60.40)
	Eye_R	1.99 (1.99 , 1.99)	1.99 (1.99 , 1.99)	-0.03 (-0.14 , 0.15)	5.70E-01 (5.69E-01 , 5.72E-01)	-71.40 (-71.46 , -71.29)
Near Field	Thyroid	1.02E-02 (9.99E-03 , 1.04E-02)	1.02E-02 (1.00E-02 , 1.03E-02)	-0.46 (-3.28 , 4.54)	1.08E-02 (1.06E-02 , 1.10E-02)	5.08 (2.08 , 7.82)
Far Field	Lungs	3.33E-03 (3.31E-03 , 3.35E-03)	3.51E-03 (3.49E-03 , 3.53E-03)	5.40 (4.48 , 7.13)	3.23E-03 (3.21E-03 , 3.25E-03)	-3.15 (-4.10 , -2.27)
	Liver	1.21E-03 (1.20E-03 , 1.22E-03)	9.46E-04 (9.39E-04 , 9.51E-04)	-21.55 (-22.35 , -19.86)	9.50E-04 (9.43E-04 , 9.57E-04)	-21.23 (-22.00 , -20.21)
	Kidneys	3.03E-04 (2.92E-04 , 3.18E-04)	3.25E-04 (3.14E-04 , 3.37E-04)	7.24 (1.65 , 19.66)	3.11E-04 (2.98E-04 , 3.25E-04)	2.53 (-3.44 , 9.60)
	Bladder	6.94E-05 (6.08E-05 , 8.12E-05)	6.69E-05 (5.79E-05 , 7.58E-05)	-3.59 (-21.07 , 39.64)	6.00E-05 (5.24E-05 , 7.14E-05)	-13.50 (-28.74 , 13.67)

Excess Relative Risk using KERMA-Weighted Neutron Energy

		WBCT	Hybrid		Scaled MRCP	
	Organ	ERR	ERR	% Difference	ERR	% Difference
In Field	Brain	2.05 (2.05 , 2.05)	2.05 (2.05 , 2.05)	0.00 (-0.02 , 0.02)	1.35 (1.35 , 1.35)	-34.51 (-34.53 , -34.50)
	Eye_L	2.14 (2.14 , 2.15)	2.14 (2.14 , 2.15)	-0.01 (-0.16 , 0.26)	8.60E-01 (8.58E-01 , 8.63E-01)	-59.88 (-59.98 , -59.76)
	Eye_R	2.01 (2.01 , 2.01)	2.01 (2.00 , 2.01)	-0.02 (-0.15 , 0.16)	5.87E-01 (5.86E-01 , 5.90E-01)	-70.72 (-70.80 , -70.61)
Near Field	Thyroid	1.60E-02 (1.56E-02 , 1.63E-02)	1.60E-02 (1.57E-02 , 1.63E-02)	-0.20 (-3.36 , 5.53)	1.58E-02 (1.55E-02 , 1.61E-02)	-1.57 (-4.56 , 1.20)
Far Field	Lungs	4.90E-03 (4.88E-03 , 4.92E-03)	5.13E-03 (5.10E-03 , 5.16E-03)	4.53 (3.77 , 5.94)	4.49E-03 (4.47E-03 , 4.52E-03)	-8.36 (-8.98 , -7.85)
	Liver	1.62E-03 (1.60E-03 , 1.63E-03)	1.22E-03 (1.21E-03 , 1.23E-03)	-24.47 (-25.56 , -22.60)	1.16E-03 (1.15E-03 , 1.17E-03)	-28.30 (-29.05 , -27.22)
	Kidneys	3.56E-04 (3.43E-04 , 3.81E-04)	3.79E-04 (3.68E-04 , 3.95E-04)	6.58 (1.50 , 20.86)	3.48E-04 (3.36E-04 , 3.68E-04)	-2.21 (-7.14 , 7.04)
	Bladder	7.33E-05 (6.57E-05 , 8.42E-05)	6.67E-05 (5.82E-05 , 7.54E-05)	-8.98 (-23.88 , 27.21)	6.04E-05 (5.41E-05 , 6.65E-05)	-17.60 (-29.70 , 0.25)

D.2.4 Pat 4

Table D.23: EAR and ERR in Pat 4 using the LNT model and both neutron energy scorers

LNT

Excess Absolute Risk using Fluence-Weighted Neutron Energy

		WBCT	Hybrid		Scaled MRCP	
	Organ	EAR per 10k PY	EAR per 10k PY	% Difference	EAR per 10k PY	% Difference
In Field	Brain	111.00 (110.97, 111.01)	111.02 (110.98, 111.07)	0.02 (-0.02, 0.11)	120.78 (120.76, 120.81)	8.81 (8.79, 8.85)
	Eye_L	875.20 (874.36, 875.71)	875.04 (874.25, 875.89)	-0.02 (-0.15, 0.22)	895.41 (893.85, 896.93)	2.31 (2.11, 2.49)
	Eye_R	871.24 (870.46, 871.35)	870.61 (869.79, 871.30)	-0.07 (-0.20, 0.13)	965.15 (964.44, 965.89)	10.78 (10.65, 10.85)
Near Field	Thyroid	4.50 (4.50, 4.50)	4.50 (4.50, 4.50)	0.01 (-0.06, 0.17)	4.81 (4.81, 4.82)	6.92 (6.81, 7.05)
Far Field	Lungs	2.13 (2.13, 2.13)	1.99 (1.98, 1.99)	-6.86 (-6.98, -6.58)	4.77E-01 (4.76E-01, 4.78E-01)	-77.61 (-77.67, -77.57)
	Liver	5.42E-02 (5.40E-02, 5.44E-02)	5.35E-02 (5.29E-02, 5.40E-02)	-1.39 (-2.54, 0.73)	4.70E-02 (4.66E-02, 4.74E-02)	-13.24 (-14.09, -12.45)
	Kidneys	5.44E-02 (5.28E-02, 5.63E-02)	5.66E-02 (5.47E-02, 5.74E-02)	4.03 (-0.59, 12.62)	4.86E-02 (4.69E-02, 5.05E-02)	-10.59 (-14.72, -5.78)
	Bladder	3.85E-03 (3.70E-03, 3.93E-03)	3.24E-03 (2.99E-03, 3.65E-03)	-15.86 (-23.32, 2.86)	2.95E-03 (2.76E-03, 3.12E-03)	-23.55 (-29.18, -18.49)

Excess Absolute Risk using KERMA-Weighted Neutron Energy

		WBCT	Hybrid		Scaled MRCP	
	Organ	EAR per 10k PY	EAR per 10k PY	% Difference	EAR per 10k PY	% Difference
In Field	Brain	112.37 (112.35, 112.39)	112.39 (112.34, 112.43)	0.02 (-0.03, 0.10)	122.31 (122.29, 122.32)	8.84 (8.81, 8.87)
	Eye_L	877.36 (876.59, 877.88)	877.15 (876.42, 878.06)	-0.02 (-0.15, 0.21)	897.90 (896.18, 899.42)	2.34 (2.13, 2.52)
	Eye_R	873.49 (872.80, 873.80)	872.85 (872.18, 873.52)	-0.07 (-0.18, 0.12)	967.78 (967.26, 968.44)	10.80 (10.69, 10.87)
Near Field	Thyroid	4.50 (4.50, 4.50)	4.50 (4.50, 4.50)	0.01 (-0.06, 0.17)	4.81 (4.81, 4.82)	6.92 (6.81, 7.05)
Far Field	Lungs	2.24 (2.23, 2.24)	2.10 (2.10, 2.11)	-5.95 (-6.14, -5.58)	5.66E-01 (5.64E-01, 5.68E-01)	-74.68 (-74.80, -74.60)
	Liver	8.05E-02 (7.99E-02, 8.09E-02)	7.91E-02 (7.84E-02, 7.99E-02)	-1.70 (-2.94, 0.60)	6.61E-02 (6.55E-02, 6.68E-02)	-17.88 (-18.88, -16.95)
	Kidneys	7.93E-02 (7.74E-02, 8.17E-02)	8.21E-02 (7.97E-02, 8.39E-02)	3.56 (-0.32, 11.40)	6.49E-02 (6.22E-02, 6.77E-02)	-18.14 (-22.10, -13.67)
	Bladder	4.25E-03 (4.03E-03, 4.39E-03)	3.58E-03 (3.21E-03, 3.91E-03)	-15.65 (-25.36, 2.90)	3.02E-03 (2.75E-03, 3.21E-03)	-29.02 (-36.17, -23.39)

Excess Relative Risk using Fluence-Weighted Neutron Energy

		WBCT	Hybrid		Scaled MRCP	
	Organ	ERR	ERR	% Difference	ERR	% Difference
In Field	Brain	3.09 (3.09, 3.09)	3.09 (3.09, 3.09)	0.02 (-0.02, 0.11)	3.36 (3.36, 3.36)	8.81 (8.79, 8.85)
	Eye_L	24.35 (24.32, 24.36)	24.34 (24.32, 24.36)	-0.02 (-0.15, 0.22)	24.91 (24.86, 24.95)	2.31 (2.11, 2.49)
	Eye_R	24.23 (24.21, 24.24)	24.22 (24.19, 24.24)	-0.07 (-0.20, 0.13)	26.85 (26.83, 26.87)	10.78 (10.65, 10.85)
Near Field	Thyroid	9.05 (9.04, 9.05)	9.05 (9.05, 9.05)	0.02 (-0.06, 0.18)	9.67 (9.67, 9.68)	6.94 (6.83, 7.07)
Far Field	Lungs	1.75E-01 (1.75E-01, 1.75E-01)	1.63E-01 (1.63E-01, 1.63E-01)	-6.86 (-6.98, -6.58)	3.92E-02 (3.91E-02, 3.92E-02)	-77.61 (-77.67, -77.57)
	Liver	5.08E-03 (5.05E-03, 5.09E-03)	5.01E-03 (4.95E-03, 5.05E-03)	-1.39 (-2.54, 0.73)	4.41E-03 (4.37E-03, 4.44E-03)	-13.24 (-14.09, -12.45)
	Kidneys	1.51E-03 (1.47E-03, 1.57E-03)	1.57E-03 (1.52E-03, 1.60E-03)	4.03 (-0.59, 12.62)	1.35E-03 (1.30E-03, 1.40E-03)	-10.59 (-14.72, -5.78)
	Bladder	8.88E-04 (8.53E-04, 9.05E-04)	7.47E-04 (6.88E-04, 8.42E-04)	-15.86 (-23.32, 2.86)	6.79E-04 (6.37E-04, 7.19E-04)	-23.55 (-29.18, -18.49)

Excess Relative Risk using KERMA-Weighted Neutron Energy

		WBCT	Hybrid		Scaled MRCP	
	Organ	ERR	ERR	% Difference	ERR	% Difference
In Field	Brain	3.13 (3.13, 3.13)	3.13 (3.13, 3.13)	0.02 (-0.03, 0.10)	3.40 (3.40, 3.40)	8.84 (8.81, 8.87)
	Eye_L	24.41 (24.38, 24.42)	24.40 (24.38, 24.42)	-0.02 (-0.15, 0.21)	24.98 (24.93, 25.02)	2.34 (2.13, 2.52)
	Eye_R	24.30 (24.28, 24.31)	24.28 (24.26, 24.30)	-0.07 (-0.18, 0.12)	26.92 (26.91, 26.94)	10.80 (10.69, 10.87)
Near Field	Thyroid	9.08 (9.07, 9.09)	9.08 (9.08, 9.08)	0.03 (-0.08, 0.22)	9.71 (9.71, 9.72)	6.99 (6.86, 7.12)
Far Field	Lungs	1.83E-01 (1.83E-01, 1.84E-01)	1.73E-01 (1.72E-01, 1.73E-01)	-5.95 (-6.14, -5.58)	4.64E-02 (4.62E-02, 4.66E-02)	-74.68 (-74.80, -74.60)
	Liver	7.54E-03 (7.48E-03, 7.58E-03)	7.41E-03 (7.34E-03, 7.48E-03)	-1.70 (-2.94, 0.60)	6.19E-03 (6.13E-03, 6.25E-03)	-17.88 (-18.88, -16.95)
	Kidneys	2.21E-03 (2.15E-03, 2.27E-03)	2.28E-03 (2.22E-03, 2.33E-03)	3.56 (-0.32, 11.40)	1.81E-03 (1.73E-03, 1.88E-03)	-18.14 (-22.10, -13.67)
	Bladder	9.79E-04 (9.29E-04, 1.01E-03)	8.26E-04 (7.41E-04, 9.00E-04)	-15.65 (-25.36, 2.90)	6.95E-04 (6.35E-04, 7.39E-04)	-29.02 (-36.17, -23.39)

Table D.24: EAR and ERR in Pat 4 using the linear plateau model with a 10 Sv inflection point and both neutron energy scorers

Linear-Plateau 10 Sv

Excess Absolute Risk using Fluence-Weighted Neutron Energy

		WBCT	Hybrid		Scaled MRCP	
	Organ	EAR per 10k PY	EAR per 10k PY	% Difference	EAR per 10k PY	% Difference
In Field	Brain	36.32 (36.32, 36.32)	36.32 (36.32, 36.32)	0.00 (0.00, 0.01)	36.67 (36.67, 36.67)	0.97 (0.97, 0.97)
	Eye_L	37.72 (37.72, 37.72)	37.72 (37.72, 37.72)	0.00 (0.00, 0.00)	37.72 (37.72, 37.72)	0.00 (0.00, 0.00)
	Eye_R	37.72 (37.72, 37.72)	37.72 (37.72, 37.72)	0.00 (0.00, 0.00)	37.72 (37.72, 37.72)	0.00 (0.00, 0.00)
Near Field	Thyroid	7.41E-01 (7.41E-01, 7.41E-01)	7.41E-01 (7.41E-01, 7.41E-01)	0.00 (0.00, 0.00)	7.41E-01 (7.41E-01, 7.41E-01)	0.04 (0.04, 0.04)
Far Field	Lungs	2.23 (2.22, 2.23)	2.08 (2.08, 2.09)	-6.42 (-6.53, -6.15)	5.26E-01 (5.25E-01, 5.27E-01)	-76.38 (-76.43, -76.33)
	Liver	6.06E-02 (6.03E-02, 6.08E-02)	5.97E-02 (5.91E-02, 6.03E-02)	-1.39 (-2.54, 0.73)	5.26E-02 (5.21E-02, 5.30E-02)	-13.22 (-14.07, -12.43)
	Kidneys	6.08E-02 (5.91E-02, 6.30E-02)	6.33E-02 (6.12E-02, 6.42E-02)	4.02 (-0.59, 12.61)	5.44E-02 (5.25E-02, 5.64E-02)	-10.58 (-14.71, -5.77)
	Bladder	4.31E-03 (4.14E-03, 4.40E-03)	3.63E-03 (3.34E-03, 4.09E-03)	-15.86 (-23.32, 2.86)	3.30E-03 (3.09E-03, 3.49E-03)	-23.54 (-29.18, -18.49)

Excess Absolute Risk using KERMA-Weighted Neutron Energy

		WBCT	Hybrid		Scaled MRCP	
	Organ	EAR per 10k PY	EAR per 10k PY	% Difference	EAR per 10k PY	% Difference
In Field	Brain	36.38 (36.37, 36.38)	36.38 (36.37, 36.38)	0.00 (0.00, 0.01)	36.72 (36.72, 36.72)	0.94 (0.94, 0.95)
	Eye_L	37.72 (37.72, 37.72)	37.72 (37.72, 37.72)	0.00 (0.00, 0.00)	37.72 (37.72, 37.72)	0.00 (0.00, 0.00)
	Eye_R	37.72 (37.72, 37.72)	37.72 (37.72, 37.72)	0.00 (0.00, 0.00)	37.72 (37.72, 37.72)	0.00 (0.00, 0.00)
Near Field	Thyroid	7.41E-01 (7.41E-01, 7.41E-01)	7.41E-01 (7.41E-01, 7.41E-01)	0.00 (0.00, 0.00)	7.41E-01 (7.41E-01, 7.41E-01)	0.04 (0.04, 0.04)
Far Field	Lungs	2.33 (2.32, 2.33)	2.20 (2.20, 2.20)	-5.55 (-5.72, -5.20)	6.22E-01 (6.19E-01, 6.24E-01)	-73.27 (-73.39, -73.18)
	Liver	8.99E-02 (8.92E-02, 9.03E-02)	8.83E-02 (8.75E-02, 8.92E-02)	-1.69 (-2.93, 0.59)	7.38E-02 (7.31E-02, 7.46E-02)	-17.84 (-18.84, -16.91)
	Kidneys	8.87E-02 (8.66E-02, 9.13E-02)	9.18E-02 (8.92E-02, 9.38E-02)	3.56 (-0.32, 11.39)	7.26E-02 (6.96E-02, 7.57E-02)	-18.13 (-22.07, -13.66)
	Bladder	4.76E-03 (4.51E-03, 4.91E-03)	4.01E-03 (3.60E-03, 4.37E-03)	-15.65 (-25.36, 2.90)	3.38E-03 (3.08E-03, 3.59E-03)	-29.02 (-36.17, -23.38)

Excess Relative Risk using Fluence-Weighted Neutron Energy

		WBCT	Hybrid		Scaled MRCP	
	Organ	ERR	ERR	% Difference	ERR	% Difference
In Field	Brain	1.01 (1.01, 1.01)	1.01 (1.01, 1.01)	0.00 (0.00, 0.01)	1.02 (1.02, 1.02)	0.97 (0.97, 0.97)
	Eye_L	1.05 (1.05, 1.05)	1.05 (1.05, 1.05)	0.00 (0.00, 0.00)	1.05 (1.05, 1.05)	0.00 (0.00, 0.00)
	Eye_R	1.05 (1.05, 1.05)	1.05 (1.05, 1.05)	0.00 (0.00, 0.00)	1.05 (1.05, 1.05)	0.00 (0.00, 0.00)
Near Field	Thyroid	7.42E-01 (7.42E-01, 7.42E-01)	7.42E-01 (7.42E-01, 7.42E-01)	0.00 (0.00, 0.00)	7.42E-01 (7.42E-01, 7.42E-01)	0.00 (0.00, 0.00)
Far Field	Lungs	1.83E-01 (1.83E-01, 1.83E-01)	1.71E-01 (1.71E-01, 1.71E-01)	-6.42 (-6.53, -6.15)	4.32E-02 (4.31E-02, 4.32E-02)	-76.38 (-76.43, -76.33)
	Liver	5.67E-03 (5.65E-03, 5.69E-03)	5.59E-03 (5.53E-03, 5.65E-03)	-1.39 (-2.54, 0.73)	4.92E-03 (4.88E-03, 4.97E-03)	-13.22 (-14.07, -12.43)
	Kidneys	1.69E-03 (1.64E-03, 1.75E-03)	1.76E-03 (1.70E-03, 1.79E-03)	4.02 (-0.59, 12.61)	1.51E-03 (1.46E-03, 1.57E-03)	-10.58 (-14.71, -5.77)
	Bladder	9.94E-04 (9.55E-04, 1.01E-03)	8.37E-04 (7.70E-04, 9.43E-04)	-15.86 (-23.32, 2.86)	7.60E-04 (7.13E-04, 8.05E-04)	-23.54 (-29.18, -18.49)

Excess Relative Risk using KERMA-Weighted Neutron Energy

		WBCT	Hybrid		Scaled MRCP	
	Organ	ERR	ERR	% Difference	ERR	% Difference
In Field	Brain	1.01 (1.01, 1.01)	1.01 (1.01, 1.01)	0.00 (0.00, 0.01)	1.02 (1.02, 1.02)	0.94 (0.94, 0.95)
	Eye_L	1.05 (1.05, 1.05)	1.05 (1.05, 1.05)	0.00 (0.00, 0.00)	1.05 (1.05, 1.05)	0.00 (0.00, 0.00)
	Eye_R	1.05 (1.05, 1.05)	1.05 (1.05, 1.05)	0.00 (0.00, 0.00)	1.05 (1.05, 1.05)	0.00 (0.00, 0.00)
Near Field	Thyroid	7.42E-01 (7.42E-01, 7.42E-01)	7.42E-01 (7.42E-01, 7.42E-01)	0.00 (0.00, 0.00)	7.42E-01 (7.42E-01, 7.42E-01)	0.00 (0.00, 0.00)
Far Field	Lungs	1.91E-01 (1.91E-01, 1.91E-01)	1.80E-01 (1.80E-01, 1.81E-01)	-5.55 (-5.72, -5.20)	5.10E-02 (5.08E-02, 5.12E-02)	-73.27 (-73.39, -73.18)
	Liver	8.42E-03 (8.35E-03, 8.46E-03)	8.27E-03 (8.19E-03, 8.35E-03)	-1.69 (-2.93, 0.59)	6.91E-03 (6.85E-03, 6.98E-03)	-17.84 (-18.84, -16.91)
	Kidneys	2.47E-03 (2.41E-03, 2.54E-03)	2.55E-03 (2.48E-03, 2.61E-03)	3.56 (-0.32, 11.39)	2.02E-03 (1.93E-03, 2.11E-03)	-18.13 (-22.07, -13.66)
	Bladder	1.10E-03 (1.04E-03, 1.13E-03)	9.24E-04 (8.29E-04, 1.01E-03)	-15.65 (-25.36, 2.90)	7.78E-04 (7.10E-04, 8.28E-04)	-29.02 (-36.17, -23.38)

Table D.25: EAR and ERR in Pat 4 using the linear plateau model with a 40 Sv inflection point and both neutron energy scorers

Linear-Plateau 40 Sv

Excess Absolute Risk using Fluence-Weighted Neutron Energy

		WBCT	Hybrid		Scaled MRCP	
	Organ	EAR per 10k PY	EAR per 10k PY	% Difference	EAR per 10k PY	% Difference
In Field	Brain	77.82 (77.81 , 77.83)	77.83 (77.81 , 77.85)	0.01 (-0.01 , 0.07)	82.08 (82.07 , 82.10)	5.48 (5.46 , 5.50)
	Eye_L	138.47 (138.47 , 138.47)	138.47 (138.47 , 138.47)	0.00 (0.00 , 0.00)	138.50 (138.50 , 138.50)	0.02 (0.02 , 0.02)
	Eye_R	138.46 (138.46 , 138.46)	138.46 (138.46 , 138.46)	0.00 (0.00 , 0.00)	138.57 (138.57 , 138.57)	0.08 (0.08 , 0.08)
Near Field	Thyroid	2.23 (2.23 , 2.23)	2.23 (2.23 , 2.23)	0.01 (-0.02 , 0.06)	2.28 (2.28 , 2.28)	2.49 (2.45 , 2.53)
Far Field	Lungs	2.16 (2.15 , 2.16)	2.01 (2.01 , 2.01)	-6.75 (-6.86 , -6.47)	4.89E-01 (4.88E-01 , 4.90E-01)	-77.31 (-77.36 , -77.26)
	Liver	5.58E-02 (5.55E-02 , 5.59E-02)	5.50E-02 (5.44E-02 , 5.55E-02)	-1.39 (-2.54 , 0.73)	4.84E-02 (4.80E-02 , 4.88E-02)	-13.23 (-14.09 , -12.44)
	Kidneys	5.60E-02 (5.43E-02 , 5.79E-02)	5.82E-02 (5.63E-02 , 5.91E-02)	4.03 (-0.59 , 12.62)	5.00E-02 (4.83E-02 , 5.19E-02)	-10.59 (-14.72 , -5.78)
	Bladder	3.97E-03 (3.81E-03 , 4.04E-03)	3.34E-03 (3.07E-03 , 3.76E-03)	-15.86 (-23.32 , 2.86)	3.03E-03 (2.84E-03 , 3.21E-03)	-23.55 (-29.18 , -18.49)

Excess Absolute Risk using KERMA-Weighted Neutron Energy

		WBCT	Hybrid		Scaled MRCP	
	Organ	EAR per 10k PY	EAR per 10k PY	% Difference	EAR per 10k PY	% Difference
In Field	Brain	78.44 (78.43 , 78.45)	78.45 (78.43 , 78.47)	0.01 (-0.02 , 0.07)	82.72 (82.71 , 82.73)	5.46 (5.44 , 5.47)
	Eye_L	138.47 (138.47 , 138.47)	138.47 (138.47 , 138.47)	0.00 (0.00 , 0.00)	138.50 (138.50 , 138.50)	0.02 (0.02 , 0.02)
	Eye_R	138.47 (138.46 , 138.47)	138.46 (138.46 , 138.47)	0.00 (0.00 , 0.00)	138.57 (138.57 , 138.57)	0.08 (0.08 , 0.08)
Near Field	Thyroid	2.23 (2.23 , 2.23)	2.23 (2.23 , 2.23)	0.01 (-0.02 , 0.06)	2.28 (2.28 , 2.28)	2.49 (2.45 , 2.53)
Far Field	Lungs	2.26 (2.26 , 2.26)	2.13 (2.13 , 2.13)	-5.85 (-6.03 , -5.49)	5.80E-01 (5.77E-01 , 5.82E-01)	-74.33 (-74.45 , -74.25)
	Liver	8.28E-02 (8.21E-02 , 8.32E-02)	8.14E-02 (8.06E-02 , 8.21E-02)	-1.70 (-2.94 , 0.60)	6.80E-02 (6.74E-02 , 6.87E-02)	-17.87 (-18.87 , -16.94)
	Kidneys	8.16E-02 (7.96E-02 , 8.40E-02)	8.45E-02 (8.20E-02 , 8.63E-02)	3.56 (-0.32 , 11.40)	6.68E-02 (6.40E-02 , 6.97E-02)	-18.14 (-22.09 , -13.67)
	Bladder	4.37E-03 (4.15E-03 , 4.52E-03)	3.69E-03 (3.31E-03 , 4.02E-03)	-15.65 (-25.36 , 2.90)	3.10E-03 (2.83E-03 , 3.30E-03)	-29.02 (-36.17 , -23.38)

Excess Relative Risk using Fluence-Weighted Neutron Energy

		WBCT	Hybrid		Scaled MRCP	
	Organ	ERR	ERR	% Difference	ERR	% Difference
In Field	Brain	2.16 (2.16 , 2.16)	2.17 (2.16 , 2.17)	0.01 (-0.01 , 0.07)	2.28 (2.28 , 2.28)	5.48 (5.46 , 5.50)
	Eye_L	3.85 (3.85 , 3.85)	3.85 (3.85 , 3.85)	0.00 (0.00 , 0.00)	3.85 (3.85 , 3.85)	0.02 (0.02 , 0.02)
	Eye_R	3.85 (3.85 , 3.85)	3.85 (3.85 , 3.85)	0.00 (0.00 , 0.00)	3.85 (3.85 , 3.85)	0.08 (0.08 , 0.08)
Near Field	Thyroid	2.64 (2.64 , 2.64)	2.64 (2.64 , 2.64)	0.00 (-0.01 , 0.02)	2.66 (2.66 , 2.66)	0.72 (0.71 , 0.73)
Far Field	Lungs	1.77E-01 (1.77E-01 , 1.77E-01)	1.65E-01 (1.65E-01 , 1.65E-01)	-6.75 (-6.86 , -6.47)	4.01E-02 (4.01E-02 , 4.02E-02)	-77.31 (-77.36 , -77.26)
	Liver	5.22E-03 (5.20E-03 , 5.24E-03)	5.15E-03 (5.09E-03 , 5.20E-03)	-1.39 (-2.54 , 0.73)	4.53E-03 (4.49E-03 , 4.57E-03)	-13.23 (-14.09 , -12.44)
	Kidneys	1.56E-03 (1.51E-03 , 1.61E-03)	1.62E-03 (1.57E-03 , 1.64E-03)	4.03 (-0.59 , 12.62)	1.39E-03 (1.34E-03 , 1.44E-03)	-10.59 (-14.72 , -5.78)
	Bladder	9.14E-04 (8.78E-04 , 9.31E-04)	7.69E-04 (7.08E-04 , 8.67E-04)	-15.86 (-23.32 , 2.86)	6.99E-04 (6.55E-04 , 7.40E-04)	-23.55 (-29.18 , -18.49)

Excess Relative Risk using KERMA-Weighted Neutron Energy

		WBCT	Hybrid		Scaled MRCP	
	Organ	ERR	ERR	% Difference	ERR	% Difference
In Field	Brain	2.18 (2.18 , 2.18)	2.18 (2.18 , 2.18)	0.01 (-0.02 , 0.07)	2.30 (2.30 , 2.30)	5.46 (5.44 , 5.47)
	Eye_L	3.85 (3.85 , 3.85)	3.85 (3.85 , 3.85)	0.00 (0.00 , 0.00)	3.85 (3.85 , 3.85)	0.02 (0.02 , 0.02)
	Eye_R	3.85 (3.85 , 3.85)	3.85 (3.85 , 3.85)	0.00 (0.00 , 0.00)	3.85 (3.85 , 3.85)	0.08 (0.08 , 0.08)
Near Field	Thyroid	2.64 (2.64 , 2.64)	2.64 (2.64 , 2.64)	0.00 (-0.01 , 0.03)	2.66 (2.66 , 2.66)	0.72 (0.70 , 0.73)
Far Field	Lungs	1.85E-01 (1.85E-01 , 1.86E-01)	1.74E-01 (1.74E-01 , 1.75E-01)	-5.85 (-6.03 , -5.49)	4.76E-02 (4.74E-02 , 4.77E-02)	-74.33 (-74.45 , -74.25)
	Liver	7.75E-03 (7.69E-03 , 7.79E-03)	7.62E-03 (7.55E-03 , 7.69E-03)	-1.70 (-2.94 , 0.60)	6.37E-03 (6.31E-03 , 6.43E-03)	-17.87 (-18.87 , -16.94)
	Kidneys	2.27E-03 (2.22E-03 , 2.34E-03)	2.35E-03 (2.28E-03 , 2.40E-03)	3.56 (-0.32 , 11.40)	1.86E-03 (1.78E-03 , 1.94E-03)	-18.14 (-22.09 , -13.67)
	Bladder	1.01E-03 (9.56E-04 , 1.04E-03)	8.50E-04 (7.62E-04 , 9.26E-04)	-15.65 (-25.36 , 2.90)	7.15E-04 (6.53E-04 , 7.61E-04)	-29.02 (-36.17 , -23.38)

Table D.26: EAR and ERR in Pat 4 using the linear exponential model with a 10 Sv inflection point and both neutron energy scorers

Linear-Exponential 10 Sv

Excess Absolute Risk using Fluence-Weighted Neutron Energy

		WBCT	Hybrid		Scaled MRCP	
	Organ	EAR per 10k PY	EAR per 10k PY	% Difference	EAR per 10k PY	% Difference
In Field	Brain	29.33 (29.33, 29.33)	29.33 (29.33, 29.32)	-0.01 (-0.03, 0.03)	28.14 (28.14, 28.13)	-4.08 (-4.09, -4.06)
	Eye_L	1.22E-02 (1.23E-02, 1.21E-02)	1.22E-02 (1.23E-02, 1.21E-02)	0.19 (-1.18, 2.66)	9.61E-03 (9.79E-03, 9.44E-03)	-21.16 (-22.82, -19.72)
	Eye_R	1.28E-02 (1.29E-02, 1.28E-02)	1.29E-02 (1.30E-02, 1.28E-02)	0.75 (-0.59, 2.79)	4.22E-03 (4.25E-03, 4.18E-03)	-66.98 (-67.39, -66.74)
Near Field	Thyroid	2.61E-01 (2.61E-01, 2.60E-01)	2.61E-01 (2.61E-01, 2.61E-01)	-0.03 (-0.17, 0.27)	2.27E-01 (2.28E-01, 2.27E-01)	-12.81 (-12.99, -12.59)
Far Field	Lungs	2.22 (2.21, 2.22)	2.07 (2.07, 2.08)	-6.47 (-6.58, -6.20)	5.20E-01 (5.19E-01, 5.21E-01)	-76.53 (-76.58, -76.48)
	Liver	5.98E-02 (5.95E-02, 6.00E-02)	5.90E-02 (5.84E-02, 5.95E-02)	-1.39 (-2.54, 0.73)	5.19E-02 (5.15E-02, 5.23E-02)	-13.22 (-14.07, -12.43)
	Kidneys	6.01E-02 (5.83E-02, 6.22E-02)	6.25E-02 (6.04E-02, 6.34E-02)	4.02 (-0.59, 12.61)	5.37E-02 (5.18E-02, 5.57E-02)	-10.59 (-14.71, -5.78)
	Bladder	4.26E-03 (4.09E-03, 4.34E-03)	3.58E-03 (3.30E-03, 4.04E-03)	-15.86 (-23.32, 2.86)	3.26E-03 (3.05E-03, 3.45E-03)	-23.54 (-29.18, -18.49)

Excess Absolute Risk using KERMA-Weighted Neutron Energy

		WBCT	Hybrid		Scaled MRCP	
	Organ	EAR per 10k PY	EAR per 10k PY	% Difference	EAR per 10k PY	% Difference
In Field	Brain	29.17 (29.18, 29.17)	29.17 (29.18, 29.17)	-0.01 (-0.03, 0.03)	27.94 (27.94, 27.93)	-4.24 (-4.25, -4.23)
	Eye_L	1.19E-02 (1.20E-02, 1.18E-02)	1.19E-02 (1.20E-02, 1.18E-02)	0.25 (-1.02, 2.68)	9.33E-03 (9.52E-03, 9.17E-03)	-21.46 (-23.22, -20.02)
	Eye_R	1.24E-02 (1.25E-02, 1.24E-02)	1.25E-02 (1.26E-02, 1.24E-02)	0.75 (-0.40, 2.70)	4.09E-03 (4.11E-03, 4.05E-03)	-67.14 (-67.48, -66.89)
Near Field	Thyroid	2.61E-01 (2.61E-01, 2.60E-01)	2.61E-01 (2.61E-01, 2.61E-01)	-0.03 (-0.17, 0.27)	2.27E-01 (2.28E-01, 2.27E-01)	-12.81 (-12.99, -12.59)
Far Field	Lungs	2.32 (2.31, 2.32)	2.19 (2.19, 2.19)	-5.59 (-5.77, -5.24)	6.16E-01 (6.13E-01, 6.17E-01)	-73.44 (-73.56, -73.35)
	Liver	8.87E-02 (8.81E-02, 8.92E-02)	8.72E-02 (8.64E-02, 8.80E-02)	-1.69 (-2.93, 0.59)	7.29E-02 (7.22E-02, 7.36E-02)	-17.85 (-18.84, -16.92)
	Kidneys	8.75E-02 (8.55E-02, 9.02E-02)	9.07E-02 (8.80E-02, 9.26E-02)	3.56 (-0.32, 11.39)	7.17E-02 (6.87E-02, 7.48E-02)	-18.13 (-22.08, -13.66)
	Bladder	4.70E-03 (4.46E-03, 4.85E-03)	3.96E-03 (3.55E-03, 4.32E-03)	-15.65 (-25.36, 2.90)	3.33E-03 (3.04E-03, 3.55E-03)	-29.02 (-36.17, -23.38)

Excess Relative Risk using Fluence-Weighted Neutron Energy

		WBCT	Hybrid		Scaled MRCP	
	Organ	ERR	ERR	% Difference	ERR	% Difference
In Field	Brain	8.16E-01 (8.16E-01, 8.16E-01)	8.16E-01 (8.16E-01, 8.16E-01)	-0.01 (-0.03, 0.03)	7.83E-01 (7.83E-01, 7.83E-01)	-4.08 (-4.09, -4.06)
	Eye_L	3.39E-04 (3.42E-04, 3.37E-04)	3.40E-04 (3.43E-04, 3.36E-04)	0.19 (-1.18, 2.66)	2.67E-04 (2.72E-04, 2.63E-04)	-21.16 (-22.82, -19.72)
	Eye_R	3.55E-04 (3.58E-04, 3.55E-04)	3.58E-04 (3.61E-04, 3.55E-04)	0.75 (-0.59, 2.79)	1.17E-04 (1.18E-04, 1.16E-04)	-66.98 (-67.39, -66.74)
Near Field	Thyroid	2.66E-02 (2.67E-02, 2.65E-02)	2.66E-02 (2.66E-02, 2.66E-02)	-0.12 (-0.54, 0.67)	1.89E-02 (1.89E-02, 1.88E-02)	-29.14 (-29.53, -28.70)
Far Field	Lungs	1.82E-01 (1.82E-01, 1.82E-01)	1.70E-01 (1.70E-01, 1.70E-01)	-6.47 (-6.58, -6.20)	4.27E-02 (4.26E-02, 4.28E-02)	-76.53 (-76.58, -76.48)
	Liver	5.60E-03 (5.58E-03, 5.62E-03)	5.52E-03 (5.46E-03, 5.58E-03)	-1.39 (-2.54, 0.73)	4.86E-03 (4.82E-03, 4.90E-03)	-13.22 (-14.07, -12.43)
	Kidneys	1.67E-03 (1.62E-03, 1.73E-03)	1.74E-03 (1.68E-03, 1.76E-03)	4.02 (-0.59, 12.61)	1.49E-03 (1.44E-03, 1.55E-03)	-10.59 (-14.71, -5.78)
	Bladder	9.81E-04 (9.42E-04, 1.00E-03)	8.26E-04 (7.60E-04, 9.31E-04)	-15.86 (-23.32, 2.86)	7.50E-04 (7.04E-04, 7.95E-04)	-23.54 (-29.18, -18.49)

Excess Relative Risk using KERMA-Weighted Neutron Energy

		WBCT	Hybrid		Scaled MRCP	
	Organ	ERR	ERR	% Difference	ERR	% Difference
In Field	Brain	8.12E-01 (8.12E-01, 8.11E-01)	8.11E-01 (8.12E-01, 8.11E-01)	-0.01 (-0.03, 0.03)	7.77E-01 (7.77E-01, 7.77E-01)	-4.24 (-4.25, -4.23)
	Eye_L	3.30E-04 (3.33E-04, 3.28E-04)	3.31E-04 (3.34E-04, 3.28E-04)	0.25 (-1.02, 2.68)	2.60E-04 (2.65E-04, 2.55E-04)	-21.46 (-23.22, -20.02)
	Eye_R	3.46E-04 (3.49E-04, 3.45E-04)	3.48E-04 (3.51E-04, 3.46E-04)	0.75 (-0.40, 2.70)	1.14E-04 (1.14E-04, 1.13E-04)	-67.14 (-67.48, -66.89)
Near Field	Thyroid	2.62E-02 (2.63E-02, 2.61E-02)	2.61E-02 (2.62E-02, 2.61E-02)	-0.14 (-0.69, 0.79)	1.85E-02 (1.85E-02, 1.84E-02)	-29.41 (-29.85, -28.97)
Far Field	Lungs	1.90E-01 (1.90E-01, 1.90E-01)	1.80E-01 (1.79E-01, 1.80E-01)	-5.59 (-5.77, -5.24)	5.05E-02 (5.03E-02, 5.07E-02)	-73.44 (-73.56, -73.35)
	Liver	8.31E-03 (8.25E-03, 8.36E-03)	8.17E-03 (8.09E-03, 8.25E-03)	-1.69 (-2.93, 0.59)	6.83E-03 (6.77E-03, 6.90E-03)	-17.85 (-18.84, -16.92)
	Kidneys	2.44E-03 (2.38E-03, 2.51E-03)	2.52E-03 (2.45E-03, 2.58E-03)	3.56 (-0.32, 11.39)	1.99E-03 (1.91E-03, 2.08E-03)	-18.13 (-22.08, -13.66)
	Bladder	1.08E-03 (1.03E-03, 1.12E-03)	9.13E-04 (8.18E-04, 9.95E-04)	-15.65 (-25.36, 2.90)	7.68E-04 (7.01E-04, 8.17E-04)	-29.02 (-36.17, -23.38)

Table D.27: EAR and ERR in Pat 4 using the linear exponential model with a 40 Sv inflection point and both neutron energy scorers

Linear-Exponential 40 Sv

Excess Absolute Risk using Fluence-Weighted Neutron Energy

		WBCT	Hybrid		Scaled MRCP	
	Organ	EAR per 10k PY	EAR per 10k PY	% Difference	EAR per 10k PY	% Difference
In Field	Brain	79.58 (79.57 , 79.59)	79.59 (79.57 , 79.61)	0.01 (-0.01 , 0.07)	83.91 (83.90 , 83.92)	5.44 (5.42 , 5.46)
	Eye_L	53.46 (53.56 , 53.41)	53.48 (53.57 , 53.39)	0.03 (-0.21 , 0.47)	51.25 (51.42 , 51.08)	-4.14 (-4.50 , -3.82)
	Eye_R	53.90 (53.99 , 53.89)	53.97 (54.07 , 53.90)	0.13 (-0.10 , 0.49)	44.12 (44.19 , 44.05)	-18.15 (-18.33 , -18.03)
Near Field	Thyroid	2.21 (2.21 , 2.21)	2.21 (2.21 , 2.21)	0.00 (-0.02 , 0.04)	2.24 (2.24 , 2.24)	1.60 (1.58 , 1.63)
Far Field	Lungs	2.15 (2.15 , 2.16)	2.01 (2.01 , 2.01)	-6.76 (-6.88 , -6.48)	4.88E-01 (4.87E-01 , 4.89E-01)	-77.35 (-77.40 , -77.30)
	Liver	5.56E-02 (5.53E-02 , 5.57E-02)	5.48E-02 (5.42E-02 , 5.53E-02)	-1.39 (-2.54 , 0.73)	4.82E-02 (4.78E-02 , 4.86E-02)	-13.24 (-14.09 , -12.44)
	Kidneys	5.58E-02 (5.41E-02 , 5.77E-02)	5.80E-02 (5.61E-02 , 5.89E-02)	4.03 (-0.59 , 12.62)	4.99E-02 (4.81E-02 , 5.17E-02)	-10.59 (-14.72 , -5.78)
	Bladder	3.95E-03 (3.79E-03 , 4.03E-03)	3.33E-03 (3.06E-03 , 3.75E-03)	-15.86 (-23.32 , 2.86)	3.02E-03 (2.83E-03 , 3.20E-03)	-23.55 (-29.18 , -18.49)

Excess Absolute Risk using KERMA-Weighted Neutron Energy

		WBCT	Hybrid		Scaled MRCP	
	Organ	EAR per 10k PY	EAR per 10k PY	% Difference	EAR per 10k PY	% Difference
In Field	Brain	80.21 (80.20 , 80.22)	80.22 (80.20 , 80.24)	0.01 (-0.02 , 0.07)	84.55 (84.55 , 84.56)	5.41 (5.39 , 5.43)
	Eye_L	53.22 (53.31 , 53.16)	53.25 (53.33 , 53.15)	0.04 (-0.18 , 0.48)	50.98 (51.17 , 50.82)	-4.21 (-4.59 , -3.89)
	Eye_R	53.65 (53.73 , 53.62)	53.72 (53.80 , 53.65)	0.13 (-0.07 , 0.48)	43.87 (43.92 , 43.80)	-18.24 (-18.39 , -18.12)
Near Field	Thyroid	2.21 (2.21 , 2.21)	2.21 (2.21 , 2.21)	0.00 (-0.02 , 0.04)	2.24 (2.24 , 2.24)	1.60 (1.58 , 1.63)
Far Field	Lungs	2.26 (2.25 , 2.26)	2.12 (2.12 , 2.13)	-5.86 (-6.04 , -5.50)	5.78E-01 (5.76E-01 , 5.80E-01)	-74.38 (-74.50 , -74.29)
	Liver	8.25E-02 (8.18E-02 , 8.29E-02)	8.11E-02 (8.03E-02 , 8.18E-02)	-1.70 (-2.94 , 0.60)	6.78E-02 (6.71E-02 , 6.84E-02)	-17.88 (-18.87 , -16.95)
	Kidneys	8.13E-02 (7.93E-02 , 8.37E-02)	8.42E-02 (8.17E-02 , 8.60E-02)	3.56 (-0.32 , 11.40)	6.65E-02 (6.37E-02 , 6.94E-02)	-18.14 (-22.09 , -13.67)
	Bladder	4.36E-03 (4.13E-03 , 4.50E-03)	3.67E-03 (3.30E-03 , 4.00E-03)	-15.65 (-25.36 , 2.90)	3.09E-03 (2.82E-03 , 3.29E-03)	-29.02 (-36.17 , -23.39)

Excess Relative Risk using Fluence-Weighted Neutron Energy

		WBCT	Hybrid		Scaled MRCP	
	Organ	ERR	ERR	% Difference	ERR	% Difference
In Field	Brain	2.21 (2.21 , 2.21)	2.21 (2.21 , 2.21)	0.01 (-0.01 , 0.07)	2.33 (2.33 , 2.33)	5.44 (5.42 , 5.46)
	Eye_L	1.49 (1.49 , 1.49)	1.49 (1.49 , 1.49)	0.03 (-0.21 , 0.47)	1.43 (1.43 , 1.42)	-4.14 (-4.50 , -3.82)
	Eye_R	1.50 (1.50 , 1.50)	1.50 (1.50 , 1.50)	0.13 (-0.10 , 0.49)	1.23 (1.23 , 1.23)	-18.15 (-18.33 , -18.03)
Near Field	Thyroid	2.11 (2.11 , 2.11)	2.11 (2.11 , 2.11)	-0.01 (-0.05 , 0.07)	2.03 (2.03 , 2.03)	-3.51 (-3.57 , -3.45)
Far Field	Lungs	1.77E-01 (1.76E-01 , 1.77E-01)	1.65E-01 (1.65E-01 , 1.65E-01)	-6.76 (-6.88 , -6.48)	4.00E-02 (3.99E-02 , 4.01E-02)	-77.35 (-77.40 , -77.30)
	Liver	5.20E-03 (5.18E-03 , 5.22E-03)	5.13E-03 (5.08E-03 , 5.18E-03)	-1.39 (-2.54 , 0.73)	4.52E-03 (4.48E-03 , 4.55E-03)	-13.24 (-14.09 , -12.44)
	Kidneys	1.55E-03 (1.51E-03 , 1.61E-03)	1.61E-03 (1.56E-03 , 1.64E-03)	4.03 (-0.59 , 12.62)	1.39E-03 (1.34E-03 , 1.44E-03)	-10.59 (-14.72 , -5.78)
	Bladder	9.11E-04 (8.74E-04 , 9.28E-04)	7.66E-04 (7.06E-04 , 8.63E-04)	-15.86 (-23.32 , 2.86)	6.96E-04 (6.53E-04 , 7.38E-04)	-23.55 (-29.18 , -18.49)

Excess Relative Risk using KERMA-Weighted Neutron Energy

		WBCT	Hybrid		Scaled MRCP	
	Organ	ERR	ERR	% Difference	ERR	% Difference
In Field	Brain	2.23 (2.23 , 2.23)	2.23 (2.23 , 2.23)	0.01 (-0.02 , 0.07)	2.35 (2.35 , 2.35)	5.41 (5.39 , 5.43)
	Eye_L	1.48 (1.48 , 1.48)	1.48 (1.48 , 1.48)	0.04 (-0.18 , 0.48)	1.42 (1.42 , 1.41)	-4.21 (-4.59 , -3.89)
	Eye_R	1.49 (1.49 , 1.49)	1.49 (1.50 , 1.49)	0.13 (-0.07 , 0.48)	1.22 (1.22 , 1.22)	-18.24 (-18.39 , -18.12)
Near Field	Thyroid	2.10 (2.10 , 2.10)	2.10 (2.10 , 2.10)	-0.01 (-0.07 , 0.08)	2.03 (2.03 , 2.03)	-3.57 (-3.63 , -3.51)
Far Field	Lungs	1.85E-01 (1.85E-01 , 1.85E-01)	1.74E-01 (1.74E-01 , 1.75E-01)	-5.86 (-6.04 , -5.50)	4.74E-02 (4.72E-02 , 4.76E-02)	-74.38 (-74.50 , -74.29)
	Liver	7.73E-03 (7.67E-03 , 7.77E-03)	7.60E-03 (7.52E-03 , 7.66E-03)	-1.70 (-2.94 , 0.60)	6.35E-03 (6.29E-03 , 6.41E-03)	-17.88 (-18.87 , -16.95)
	Kidneys	2.26E-03 (2.21E-03 , 2.33E-03)	2.34E-03 (2.27E-03 , 2.39E-03)	3.56 (-0.32 , 11.40)	1.85E-03 (1.77E-03 , 1.93E-03)	-18.14 (-22.09 , -13.67)
	Bladder	1.00E-03 (9.53E-04 , 1.04E-03)	8.47E-04 (7.59E-04 , 9.23E-04)	-15.65 (-25.36 , 2.90)	7.13E-04 (6.51E-04 , 7.58E-04)	-29.02 (-36.17 , -23.39)

D.2.5 Pat 5

Table D.28: EAR and ERR in Pat 5 using the LNT model and both neutron energy scorers

LNT

Excess Absolute Risk using Fluence-Weighted Neutron Energy

		WBCT	Hybrid		Scaled MRCP	
	Organ	EAR per 10k PY	EAR per 10k PY	% Difference	EAR per 10k PY	% Difference
In Field	Brain	102.81 (102.79 , 102.82)	102.85 (102.82 , 102.88)	0.04 (0.00 , 0.11)	107.78 (107.76 , 107.80)	4.84 (4.81 , 4.86)
	Eye_L	104.12 (103.95 , 104.13)	104.35 (104.15 , 104.59)	0.22 (-0.03 , 0.68)	70.39 (70.25 , 70.52)	-32.40 (-32.57 , -32.28)
	Eye_R	89.60 (89.44 , 89.73)	89.59 (89.43 , 89.78)	-0.01 (-0.26 , 0.49)	58.58 (58.44 , 58.68)	-34.62 (-34.81 , -34.47)
Near Field	Thyroid	8.86 (8.85 , 8.87)	8.88 (8.87 , 8.89)	0.26 (0.11 , 0.57)	10.02 (10.01 , 10.02)	13.12 (12.98 , 13.26)
Far Field	Lungs	7.55 (7.55E+00 , 7.56E+00	9.32 (9.32E+00 , 9.32E+00	23.48 (23.44 , 23.57)	4.53 (4.53E+00 , 4.53E+00	-40.01 (-40.05 , -39.97)
	Liver	1.91E-02 (1.90E-02 , 1.93E-02)	1.84E-02 (1.83E-02 , 1.86E-02)	-3.55 (-4.65 , -1.19)	1.99E-02 (1.97E-02 , 2.01E-02)	4.15 (3.09 , 5.57)
	Kidneys	3.67E-02 (3.59E-02 , 3.74E-02)	3.25E-02 (3.19E-02 , 3.32E-02)	-11.37 (-14.02 , -6.05)	3.63E-02 (3.47E-02 , 3.75E-02)	-1.19 (-5.98 , 2.74)
	Bladder	2.08E-03 (1.92E-03 , 2.23E-03)	1.82E-03 (1.77E-03 , 1.89E-03)	-12.49 (-19.57 , 3.29)	1.73E-03 (1.55E-03 , 1.85E-03)	-16.75 (-27.60 , -7.34)

Excess Absolute Risk using KERMA-Weighted Neutron Energy

		WBCT	Hybrid		Scaled MRCP	
	Organ	EAR per 10k PY	EAR per 10k PY	% Difference	EAR per 10k PY	% Difference
In Field	Brain	103.69 (103.67 , 103.71)	103.73 (103.71 , 103.77)	0.04 (0.01 , 0.11)	108.76 (108.73 , 108.78)	4.89 (4.85 , 4.91)
	Eye_L	105.03 (104.82 , 105.06)	105.26 (105.03 , 105.51)	0.22 (-0.07 , 0.73)	71.00 (70.87 , 71.11)	-32.40 (-32.58 , -32.30)
	Eye_R	90.47 (90.31 , 90.64)	90.45 (90.29 , 90.63)	-0.02 (-0.27 , 0.51)	59.21 (59.05 , 59.34)	-34.56 (-34.77 , -34.37)
Near Field	Thyroid	8.86 (8.85 , 8.87)	8.88 (8.87 , 8.89)	0.26 (0.11 , 0.57)	10.02 (10.01 , 10.02)	13.12 (12.98 , 13.26)
Far Field	Lungs	7.64 (7.64 , 7.65)	9.46 (9.46 , 9.46)	23.79 (23.74 , 23.92)	4.68 (4.68 , 4.68)	-38.73 (-38.77 , -38.68)
	Liver	2.75E-02 (2.72E-02 , 2.76E-02)	2.65E-02 (2.65E-02 , 2.67E-02)	-3.51 (-4.60 , -1.75)	2.80E-02 (2.78E-02 , 2.83E-02)	1.91 (0.57 , 2.93)
	Kidneys	5.35E-02 (5.32E-02 , 5.42E-02)	4.73E-02 (4.68E-02 , 4.80E-02)	-11.61 (-12.60 , -8.74)	4.99E-02 (4.82E-02 , 5.17E-02)	-6.63 (-9.90 , -3.20)
	Bladder	2.29E-03 (2.15E-03 , 2.46E-03)	2.00E-03 (1.88E-03 , 2.13E-03)	-13.01 (-20.57 , 4.52)	1.81E-03 (1.64E-03 , 1.95E-03)	-21.02 (-29.98 , -11.68)

Excess Relative Risk using Fluence-Weighted Neutron Energy

		WBCT	Hybrid		Scaled MRCP	
	Organ	ERR	ERR	% Difference	ERR	% Difference
In Field	Brain	6.16 (6.16 , 6.16)	6.16 (6.16 , 6.16)	0.04 (0.00 , 0.11)	6.45 (6.45 , 6.46)	4.84 (4.81 , 4.86)
	Eye_L	6.23 (6.22 , 6.24)	6.25 (6.24 , 6.26)	0.22 (-0.03 , 0.68)	4.21 (4.21 , 4.22)	-32.40 (-32.57 , -32.28)
	Eye_R	5.37 (5.36 , 5.37)	5.36 (5.36 , 5.38)	-0.01 (-0.26 , 0.49)	3.51 (3.50 , 3.51)	-34.62 (-34.81 , -34.47)
Near Field	Thyroid	17.78 (17.77 , 17.80)	17.83 (17.81 , 17.84)	0.25 (0.10 , 0.55)	20.12 (20.11 , 20.13)	13.16 (13.03 , 13.30)
Far Field	Lungs	1.83 (1.83 , 1.83)	2.26 (2.26 , 2.26)	23.48 (23.44 , 23.57)	1.10 (1.10 , 1.10)	-40.01 (-40.05 , -39.97)
	Liver	3.94E-03 (3.92E-03 , 3.98E-03)	3.80E-03 (3.76E-03 , 3.83E-03)	-3.55 (-4.65 , -1.19)	4.10E-03 (4.07E-03 , 4.14E-03)	4.15 (3.09 , 5.57)
	Kidneys	2.20E-03 (2.15E-03 , 2.24E-03)	1.95E-03 (1.91E-03 , 1.99E-03)	-11.37 (-14.02 , -6.05)	2.17E-03 (2.08E-03 , 2.24E-03)	-1.19 (-5.98 , 2.74)
	Bladder	2.53E-03 (2.34E-03 , 2.71E-03)	2.22E-03 (2.16E-03 , 2.30E-03)	-12.49 (-19.57 , 3.29)	2.11E-03 (1.89E-03 , 2.26E-03)	-16.75 (-27.60 , -7.34)

Excess Relative Risk using KERMA-Weighted Neutron Energy

		WBCT	Hybrid		Scaled MRCP	
	Organ	ERR	ERR	% Difference	ERR	% Difference
In Field	Brain	6.21 (6.21 , 6.21)	6.21 (6.21 , 6.21)	0.04 (0.01 , 0.11)	6.51 (6.51 , 6.51)	4.89 (4.85 , 4.91)
	Eye_L	6.29 (6.28 , 6.29)	6.30 (6.29 , 6.32)	0.22 (-0.07 , 0.73)	4.25 (4.24 , 4.26)	-32.40 (-32.58 , -32.30)
	Eye_R	5.42 (5.41 , 5.43)	5.42 (5.41 , 5.43)	-0.02 (-0.27 , 0.51)	3.55 (3.54 , 3.55)	-34.56 (-34.77 , -34.37)
Near Field	Thyroid	17.84 (17.82 , 17.86)	17.88 (17.86 , 17.90)	0.25 (0.11 , 0.52)	20.20 (20.19 , 20.21)	13.25 (13.13 , 13.38)
Far Field	Lungs	1.86 (1.85 , 1.86)	2.30 (2.30 , 2.30)	23.79 (23.74 , 23.92)	1.14 (1.14 , 1.14)	-38.73 (-38.77 , -38.68)
	Liver	5.66E-03 (5.60E-03 , 5.69E-03)	5.46E-03 (5.45E-03 , 5.50E-03)	-3.51 (-4.60 , -1.75)	5.77E-03 (5.73E-03 , 5.82E-03)	1.91 (0.57 , 2.93)
	Kidneys	3.20E-03 (3.19E-03 , 3.25E-03)	2.83E-03 (2.80E-03 , 2.88E-03)	-11.61 (-12.60 , -8.74)	2.99E-03 (2.89E-03 , 3.09E-03)	-6.63 (-9.90 , -3.20)
	Bladder	2.79E-03 (2.61E-03 , 3.00E-03)	2.43E-03 (2.29E-03 , 2.59E-03)	-13.01 (-20.57 , 4.52)	2.20E-03 (2.00E-03 , 2.37E-03)	-21.02 (-29.98 , -11.68)

Table D.29: EAR and ERR in Pat 5 using the linear plateau model with a 10 Sv inflection point and both neutron energy scorers

Linear-Plateau 10 Sv

Excess Absolute Risk using Fluence-Weighted Neutron Energy

		WBCT	Hybrid		Scaled MRCP	
	Organ	EAR per 10k PY	EAR per 10k PY	% Difference	EAR per 10k PY	% Difference
In Field	Brain	28.63 (28.63, 28.63)	28.63 (28.63, 28.64)	0.00 (0.00, 0.01)	28.73 (28.73, 28.73)	0.34 (0.34, 0.35)
	Eye_L	28.66 (28.66, 28.66)	28.67 (28.66, 28.67)	0.02 (0.00, 0.05)	27.24 (27.23, 27.25)	-4.98 (-5.01, -4.94)
	Eye_R	28.26 (28.25, 28.26)	28.26 (28.25, 28.27)	0.00 (-0.03, 0.06)	26.11 (26.09, 26.12)	-7.60 (-7.67, -7.56)
Near Field	Thyroid	1.47 (1.47, 1.47)	1.47 (1.47, 1.47)	0.00 (0.00, 0.00)	1.47 (1.47, 1.47)	0.07 (0.07, 0.07)
Far Field	Lungs	7.18 (7.18, 7.18)	8.54 (8.54, 8.54)	18.98 (18.95, 19.05)	4.59 (4.59, 4.59)	-36.01 (-36.05, -35.98)
	Liver	2.14E-02 (2.13E-02, 2.16E-02)	2.06E-02 (2.04E-02, 2.08E-02)	-3.55 (-4.64, -1.19)	2.23E-02 (2.21E-02, 2.25E-02)	4.14 (3.08, 5.56)
	Kidneys	4.11E-02 (4.01E-02, 4.18E-02)	3.64E-02 (3.57E-02, 3.72E-02)	-11.36 (-14.01, -6.05)	4.06E-02 (3.88E-02, 4.19E-02)	-1.19 (-5.97, 2.74)
	Bladder	2.33E-03 (2.15E-03, 2.49E-03)	2.04E-03 (1.98E-03, 2.12E-03)	-12.49 (-19.57, 3.29)	1.94E-03 (1.74E-03, 2.07E-03)	-16.74 (-27.59, -7.34)

Excess Absolute Risk using KERMA-Weighted Neutron Energy

		WBCT	Hybrid		Scaled MRCP	
	Organ	EAR per 10k PY	EAR per 10k PY	% Difference	EAR per 10k PY	% Difference
In Field	Brain	28.65 (28.65, 28.65)	28.65 (28.65, 28.65)	0.00 (0.00, 0.01)	28.75 (28.75, 28.75)	0.34 (0.34, 0.34)
	Eye_L	28.68 (28.68, 28.68)	28.68 (28.68, 28.69)	0.02 (-0.01, 0.05)	27.28 (27.27, 27.29)	-4.88 (-4.91, -4.85)
	Eye_R	28.29 (28.29, 28.30)	28.29 (28.28, 28.30)	0.00 (-0.03, 0.06)	26.18 (26.17, 26.20)	-7.45 (-7.52, -7.39)
Near Field	Thyroid	1.47 (1.47, 1.47)	1.47 (1.47, 1.47)	0.00 (0.00, 0.00)	1.47 (1.47, 1.47)	0.07 (0.07, 0.07)
Far Field	Lungs	7.25 (7.25, 7.25)	8.64 (8.63, 8.64)	19.17 (19.13, 19.28)	4.73 (4.73, 4.73)	-34.74 (-34.78, -34.69)
	Liver	3.07E-02 (3.03E-02, 3.08E-02)	2.96E-02 (2.96E-02, 2.98E-02)	-3.50 (-4.59, -1.74)	3.13E-02 (3.11E-02, 3.16E-02)	1.90 (0.57, 2.93)
	Kidneys	5.98E-02 (5.95E-02, 6.07E-02)	5.29E-02 (5.24E-02, 5.37E-02)	-11.60 (-12.59, -8.73)	5.59E-02 (5.39E-02, 5.78E-02)	-6.62 (-9.89, -3.20)
	Bladder	2.57E-03 (2.40E-03, 2.76E-03)	2.23E-03 (2.10E-03, 2.39E-03)	-13.01 (-20.57, 4.52)	2.03E-03 (1.84E-03, 2.18E-03)	-21.02 (-29.97, -11.68)

Excess Relative Risk using Fluence-Weighted Neutron Energy

		WBCT	Hybrid		Scaled MRCP	
	Organ	ERR	ERR	% Difference	ERR	% Difference
In Field	Brain	1.71 (1.71, 1.71)	1.71 (1.71, 1.71)	0.00 (0.00, 0.01)	1.72 (1.72, 1.72)	0.34 (0.34, 0.35)
	Eye_L	1.72 (1.72, 1.72)	1.72 (1.72, 1.72)	0.02 (0.00, 0.05)	1.63 (1.63, 1.63)	-4.98 (-5.01, -4.94)
	Eye_R	1.69 (1.69, 1.69)	1.69 (1.69, 1.69)	0.00 (-0.03, 0.06)	1.56 (1.56, 1.56)	-7.60 (-7.67, -7.56)
Near Field	Thyroid	1.47 (1.47, 1.47)	1.47 (1.47, 1.47)	0.00 (0.00, 0.00)	1.47 (1.47, 1.47)	0.00 (0.00, 0.00)
Far Field	Lungs	1.74 (1.74, 1.74)	2.07 (2.07, 2.07)	18.98 (18.95, 19.05)	1.11 (1.11, 1.12)	-36.01 (-36.05, -35.98)
	Liver	4.40E-03 (4.38E-03, 4.45E-03)	4.25E-03 (4.20E-03, 4.29E-03)	-3.55 (-4.64, -1.19)	4.59E-03 (4.55E-03, 4.63E-03)	4.14 (3.08, 5.56)
	Kidneys	2.46E-03 (2.40E-03, 2.51E-03)	2.18E-03 (2.14E-03, 2.23E-03)	-11.36 (-14.01, -6.05)	2.43E-03 (2.33E-03, 2.51E-03)	-1.19 (-5.97, 2.74)
	Bladder	2.84E-03 (2.62E-03, 3.03E-03)	2.48E-03 (2.41E-03, 2.57E-03)	-12.49 (-19.57, 3.29)	2.36E-03 (2.11E-03, 2.52E-03)	-16.74 (-27.59, -7.34)

Excess Relative Risk using KERMA-Weighted Neutron Energy

		WBCT	Hybrid		Scaled MRCP	
	Organ	ERR	ERR	% Difference	ERR	% Difference
In Field	Brain	1.72 (1.72, 1.72)	1.72 (1.72, 1.72)	0.00 (0.00, 0.01)	1.72 (1.72, 1.72)	0.34 (0.34, 0.34)
	Eye_L	1.72 (1.72, 1.72)	1.72 (1.72, 1.72)	0.02 (-0.01, 0.05)	1.63 (1.63, 1.63)	-4.88 (-4.91, -4.85)
	Eye_R	1.69 (1.69, 1.69)	1.69 (1.69, 1.69)	0.00 (-0.03, 0.06)	1.57 (1.57, 1.57)	-7.45 (-7.52, -7.39)
Near Field	Thyroid	1.47 (1.47, 1.47)	1.47 (1.47, 1.47)	0.00 (0.00, 0.00)	1.47 (1.47, 1.47)	0.00 (0.00, 0.00)
Far Field	Lungs	1.76 (1.76, 1.76)	2.10 (2.10, 2.10)	19.17 (19.13, 19.28)	1.15 (1.15, 1.15)	-34.74 (-34.78, -34.69)
	Liver	6.32E-03 (6.25E-03, 6.35E-03)	6.10E-03 (6.09E-03, 6.14E-03)	-3.50 (-4.59, -1.74)	6.44E-03 (6.40E-03, 6.50E-03)	1.90 (0.57, 2.93)
	Kidneys	3.58E-03 (3.57E-03, 3.63E-03)	3.17E-03 (3.13E-03, 3.22E-03)	-11.60 (-12.59, -8.73)	3.35E-03 (3.23E-03, 3.46E-03)	-6.62 (-9.89, -3.20)
	Bladder	3.12E-03 (2.92E-03, 3.36E-03)	2.72E-03 (2.56E-03, 2.90E-03)	-13.01 (-20.57, 4.52)	2.47E-03 (2.24E-03, 2.66E-03)	-21.02 (-29.97, -11.68)

Table D.30: EAR and ERR in Pat 5 using the linear plateau model with a 40 Sv inflection point and both neutron energy scorers

Linear-Plateau 40 Sv

Excess Absolute Risk using Fluence-Weighted Neutron Energy

		WBCT	Hybrid		Scaled MRCP	
	Organ	EAR per 10k PY	EAR per 10k PY	% Difference	EAR per 10k PY	% Difference
In Field	Brain	67.29 (67.28 , 67.29)	67.30 (67.29 , 67.31)	0.02 (0.00 , 0.06)	69.15 (69.14 , 69.16)	2.77 (2.75 , 2.78)
	Eye_L	67.78 (67.72 , 67.79)	67.87 (67.80 , 67.96)	0.13 (-0.02 , 0.40)	52.68 (52.60 , 52.75)	-22.28 (-22.42 , -22.19)
	Eye_R	61.88 (61.81 , 61.93)	61.87 (61.80 , 61.96)	-0.01 (-0.17 , 0.31)	46.13 (46.05 , 46.19)	-25.45 (-25.61 , -25.34)
Near Field	Thyroid	4.40 (4.40 , 4.41)	4.41 (4.41 , 4.41)	0.10 (0.04 , 0.22)	4.60 (4.60 , 4.60)	4.51 (4.46 , 4.56)
Far Field	Lungs	7.45 (7.45 , 7.46)	9.11 (9.11 , 9.11)	22.28 (22.24 , 22.37)	4.55 (4.54 , 4.55)	-39.00 (-39.04 , -38.96)
	Liver	1.97E-02 (1.96E-02 , 1.99E-02)	1.90E-02 (1.88E-02 , 1.91E-02)	-3.55 (-4.65 , -1.19)	2.05E-02 (2.03E-02 , 2.07E-02)	4.15 (3.09 , 5.57)
	Kidneys	3.78E-02 (3.69E-02 , 3.85E-02)	3.35E-02 (3.28E-02 , 3.42E-02)	-11.36 (-14.02 , -6.05)	3.73E-02 (3.57E-02 , 3.86E-02)	-1.19 (-5.98 , 2.74)
	Bladder	2.14E-03 (1.98E-03 , 2.29E-03)	1.88E-03 (1.82E-03 , 1.95E-03)	-12.49 (-19.57 , 3.29)	1.78E-03 (1.60E-03 , 1.91E-03)	-16.75 (-27.60 , -7.34)

Excess Absolute Risk using KERMA-Weighted Neutron Energy

		WBCT	Hybrid		Scaled MRCP	
	Organ	EAR per 10k PY	EAR per 10k PY	% Difference	EAR per 10k PY	% Difference
In Field	Brain	67.62 (67.62 , 67.63)	67.64 (67.63 , 67.65)	0.02 (0.00 , 0.06)	69.51 (69.50 , 69.52)	2.79 (2.77 , 2.80)
	Eye_L	68.13 (68.05 , 68.14)	68.22 (68.13 , 68.31)	0.13 (-0.04 , 0.42)	53.00 (52.93 , 53.06)	-22.21 (-22.34 , -22.13)
	Eye_R	62.25 (62.18 , 62.33)	62.25 (62.18 , 62.33)	-0.01 (-0.17 , 0.32)	46.49 (46.40 , 46.57)	-25.32 (-25.49 , -25.16)
Near Field	Thyroid	4.40 (4.40 , 4.41)	4.41 (4.41 , 4.41)	0.10 (0.04 , 0.22)	4.60 (4.60 , 4.60)	4.51 (4.46 , 4.56)
Far Field	Lungs	7.54 (7.54 , 7.54)	9.24 (9.23 , 9.24)	22.56 (22.51 , 22.68)	4.69 (4.69 , 4.70)	-37.72 (-37.76 , -37.67)
	Liver	2.83E-02 (2.79E-02 , 2.84E-02)	2.73E-02 (2.72E-02 , 2.74E-02)	-3.50 (-4.60 , -1.75)	2.88E-02 (2.86E-02 , 2.91E-02)	1.91 (0.57 , 2.93)
	Kidneys	5.50E-02 (5.48E-02 , 5.58E-02)	4.86E-02 (4.82E-02 , 4.94E-02)	-11.61 (-12.60 , -8.74)	5.14E-02 (4.96E-02 , 5.32E-02)	-6.63 (-9.90 , -3.20)
	Bladder	2.36E-03 (2.21E-03 , 2.54E-03)	2.05E-03 (1.93E-03 , 2.19E-03)	-13.01 (-20.57 , 4.52)	1.86E-03 (1.69E-03 , 2.01E-03)	-21.02 (-29.97 , -11.68)

Excess Relative Risk using Fluence-Weighted Neutron Energy

		WBCT	Hybrid		Scaled MRCP	
	Organ	ERR	ERR	% Difference	ERR	% Difference
In Field	Brain	4.03 (4.03 , 4.03)	4.03 (4.03 , 4.03)	0.02 (0.00 , 0.06)	4.14 (4.14 , 4.14)	2.77 (2.75 , 2.78)
	Eye_L	4.06 (4.06 , 4.06)	4.06 (4.06 , 4.07)	0.13 (-0.02 , 0.40)	3.15 (3.15 , 3.16)	-22.28 (-22.42 , -22.19)
	Eye_R	3.71 (3.70 , 3.71)	3.71 (3.70 , 3.71)	-0.01 (-0.17 , 0.31)	2.76 (2.76 , 2.77)	-25.45 (-25.61 , -25.34)
Near Field	Thyroid	5.22 (5.22 , 5.22)	5.22 (5.22 , 5.22)	0.03 (0.01 , 0.06)	5.29 (5.29 , 5.29)	1.26 (1.25 , 1.27)
Far Field	Lungs	1.81 (1.81 , 1.81)	2.21 (2.21 , 2.21)	22.28 (22.24 , 22.37)	1.10 (1.10 , 1.10)	-39.00 (-39.04 , -38.96)
	Liver	4.05E-03 (4.03E-03 , 4.09E-03)	3.91E-03 (3.87E-03 , 3.94E-03)	-3.55 (-4.65 , -1.19)	4.22E-03 (4.18E-03 , 4.26E-03)	4.15 (3.09 , 5.57)
	Kidneys	2.26E-03 (2.21E-03 , 2.30E-03)	2.00E-03 (1.97E-03 , 2.05E-03)	-11.36 (-14.02 , -6.05)	2.24E-03 (2.14E-03 , 2.31E-03)	-1.19 (-5.98 , 2.74)
	Bladder	2.61E-03 (2.41E-03 , 2.79E-03)	2.28E-03 (2.22E-03 , 2.37E-03)	-12.49 (-19.57 , 3.29)	2.17E-03 (1.94E-03 , 2.32E-03)	-16.75 (-27.60 , -7.34)

Excess Relative Risk using KERMA-Weighted Neutron Energy

		WBCT	Hybrid		Scaled MRCP	
	Organ	ERR	ERR	% Difference	ERR	% Difference
In Field	Brain	4.05 (4.05 , 4.05)	4.05 (4.05 , 4.05)	0.02 (0.00 , 0.06)	4.16 (4.16 , 4.16)	2.79 (2.77 , 2.80)
	Eye_L	4.08 (4.08 , 4.08)	4.08 (4.08 , 4.09)	0.13 (-0.04 , 0.42)	3.17 (3.17 , 3.18)	-22.21 (-22.34 , -22.13)
	Eye_R	3.73 (3.72 , 3.73)	3.73 (3.72 , 3.73)	-0.01 (-0.17 , 0.32)	2.78 (2.78 , 2.79)	-25.32 (-25.49 , -25.16)
Near Field	Thyroid	5.22 (5.22 , 5.22)	5.23 (5.22 , 5.23)	0.03 (0.01 , 0.06)	5.29 (5.29 , 5.29)	1.26 (1.24 , 1.27)
Far Field	Lungs	1.83 (1.83 , 1.83)	2.24 (2.24 , 2.24)	22.56 (22.51 , 22.68)	1.14 (1.14 , 1.14)	-37.72 (-37.76 , -37.67)
	Liver	5.82E-03 (5.76E-03 , 5.85E-03)	5.62E-03 (5.61E-03 , 5.65E-03)	-3.50 (-4.60 , -1.75)	5.93E-03 (5.89E-03 , 5.99E-03)	1.91 (0.57 , 2.93)
	Kidneys	3.30E-03 (3.28E-03 , 3.34E-03)	2.91E-03 (2.88E-03 , 2.96E-03)	-11.61 (-12.60 , -8.74)	3.08E-03 (2.97E-03 , 3.18E-03)	-6.63 (-9.90 , -3.20)
	Bladder	2.87E-03 (2.69E-03 , 3.09E-03)	2.50E-03 (2.35E-03 , 2.67E-03)	-13.01 (-20.57 , 4.52)	2.27E-03 (2.06E-03 , 2.44E-03)	-21.02 (-29.97 , -11.68)

Table D.31: EAR and ERR in Pat 5 using the linear exponential model with a 10 Sv inflection point and both neutron energy scorers

Linear-Exponential 10 Sv

Excess Absolute Risk using Fluence-Weighted Neutron Energy

		WBCT	Hybrid		Scaled MRCP	
	Organ	EAR per 10k PY	EAR per 10k PY	% Difference	EAR per 10k PY	% Difference
In Field	Brain	20.51 (20.52, 20.51)	20.51 (20.51, 20.50)	-0.03 (-0.05, 0.02)	19.80 (19.80, 19.79)	-3.49 (-3.52, -3.48)
	Eye_L	20.33 (20.35, 20.32)	20.29 (20.32, 20.26)	-0.16 (-0.35, 0.17)	24.10 (24.10, 24.09)	18.54 (18.40, 18.57)
	Eye_R	22.28 (22.29, 22.26)	22.28 (22.30, 22.25)	0.01 (-0.12, 0.26)	24.41 (24.41, 24.41)	9.59 (9.49, 9.66)
Near Field	Thyroid	5.23E-01 (5.24E-01, 5.22E-01)	5.21E-01 (5.22E-01, 5.19E-01)	-0.50 (-0.77, 0.10)	4.03E-01 (4.04E-01, 4.03E-01)	-22.97 (-23.16, -22.78)
Far Field	Lungs	7.21 (7.21, 7.21)	8.60 (8.60, 8.60)	19.30 (19.27, 19.38)	4.59 (4.58, 4.59)	-36.39 (-36.42, -36.35)
	Liver	2.11E-02 (2.10E-02, 2.13E-02)	2.04E-02 (2.01E-02, 2.05E-02)	-3.55 (-4.64, -1.19)	2.20E-02 (2.18E-02, 2.22E-02)	4.14 (3.08, 5.56)
	Kidneys	4.05E-02 (3.96E-02, 4.13E-02)	3.59E-02 (3.52E-02, 3.67E-02)	-11.36 (-14.01, -6.05)	4.01E-02 (3.84E-02, 4.14E-02)	-1.19 (-5.97, 2.74)
	Bladder	2.30E-03 (2.13E-03, 2.46E-03)	2.01E-03 (1.96E-03, 2.09E-03)	-12.49 (-19.57, 3.29)	1.92E-03 (1.71E-03, 2.05E-03)	-16.74 (-27.59, -7.34)

Excess Absolute Risk using KERMA-Weighted Neutron Energy

		WBCT	Hybrid		Scaled MRCP	
	Organ	EAR per 10k PY	EAR per 10k PY	% Difference	EAR per 10k PY	% Difference
In Field	Brain	20.39 (20.39, 20.38)	20.38 (20.38, 20.38)	-0.03 (-0.05, 0.02)	19.65 (19.66, 19.65)	-3.60 (-3.63, -3.58)
	Eye_L	20.20 (20.23, 20.19)	20.16 (20.20, 20.13)	-0.17 (-0.38, 0.21)	24.06 (24.07, 24.05)	19.13 (18.95, 19.17)
	Eye_R	22.17 (22.19, 22.15)	22.17 (22.19, 22.15)	0.01 (-0.12, 0.28)	24.42 (24.41, 24.42)	10.14 (10.04, 10.24)
Near Field	Thyroid	5.23E-01 (5.24E-01, 5.22E-01)	5.21E-01 (5.22E-01, 5.19E-01)	-0.50 (-0.77, 0.10)	4.03E-01 (4.04E-01, 4.03E-01)	-22.97 (-23.16, -22.78)
Far Field	Lungs	7.28 (7.28, 7.29)	8.70 (8.70, 8.70)	19.50 (19.46, 19.61)	4.73 (4.72, 4.73)	-35.11 (-35.14, -35.06)
	Liver	3.03E-02 (3.00E-02, 3.05E-02)	2.92E-02 (2.92E-02, 2.94E-02)	-3.50 (-4.59, -1.74)	3.09E-02 (3.07E-02, 3.12E-02)	1.90 (0.57, 2.93)
	Kidneys	5.91E-02 (5.88E-02, 5.99E-02)	5.22E-02 (5.17E-02, 5.31E-02)	-11.60 (-12.59, -8.73)	5.52E-02 (5.32E-02, 5.70E-02)	-6.62 (-9.89, -3.20)
	Bladder	2.53E-03 (2.37E-03, 2.72E-03)	2.21E-03 (2.08E-03, 2.36E-03)	-13.01 (-20.57, 4.52)	2.00E-03 (1.82E-03, 2.16E-03)	-21.02 (-29.97, -11.68)

Excess Relative Risk using Fluence-Weighted Neutron Energy

		WBCT	Hybrid		Scaled MRCP	
	Organ	ERR	ERR	% Difference	ERR	% Difference
In Field	Brain	1.23 (1.23, 1.23)	1.23 (1.23, 1.23)	-0.03 (-0.05, 0.02)	1.19 (1.19, 1.19)	-3.49 (-3.52, -3.48)
	Eye_L	1.22 (1.22, 1.22)	1.22 (1.22, 1.21)	-0.16 (-0.35, 0.17)	1.44 (1.44, 1.44)	18.54 (18.40, 18.57)
	Eye_R	1.33 (1.34, 1.33)	1.33 (1.34, 1.33)	0.01 (-0.12, 0.26)	1.46 (1.46, 1.46)	9.59 (9.49, 9.66)
Near Field	Thyroid	5.48E-02 (5.51E-02, 5.45E-02)	5.42E-02 (5.44E-02, 5.39E-02)	-1.22 (-1.93, 0.18)	2.86E-02 (2.87E-02, 2.85E-02)	-47.82 (-48.13, -47.52)
Far Field	Lungs	1.75 (1.75, 1.75)	2.09 (2.09, 2.09)	19.30 (19.27, 19.38)	1.11 (1.11, 1.11)	-36.39 (-36.42, -36.35)
	Liver	4.35E-03 (4.33E-03, 4.39E-03)	4.19E-03 (4.15E-03, 4.23E-03)	-3.55 (-4.64, -1.19)	4.53E-03 (4.49E-03, 4.57E-03)	4.14 (3.08, 5.56)
	Kidneys	2.43E-03 (2.37E-03, 2.47E-03)	2.15E-03 (2.11E-03, 2.20E-03)	-11.36 (-14.01, -6.05)	2.40E-03 (2.30E-03, 2.48E-03)	-1.19 (-5.97, 2.74)
	Bladder	2.80E-03 (2.59E-03, 2.99E-03)	2.45E-03 (2.38E-03, 2.54E-03)	-12.49 (-19.57, 3.29)	2.33E-03 (2.08E-03, 2.49E-03)	-16.74 (-27.59, -7.34)

Excess Relative Risk using KERMA-Weighted Neutron Energy

		WBCT	Hybrid		Scaled MRCP	
	Organ	ERR	ERR	% Difference	ERR	% Difference
In Field	Brain	1.22 (1.22, 1.22)	1.22 (1.22, 1.22)	-0.03 (-0.05, 0.02)	1.18 (1.18, 1.18)	-3.60 (-3.63, -3.58)
	Eye_L	1.21 (1.21, 1.21)	1.21 (1.21, 1.21)	-0.17 (-0.38, 0.21)	1.44 (1.44, 1.44)	19.13 (18.95, 19.17)
	Eye_R	1.33 (1.33, 1.33)	1.33 (1.33, 1.33)	0.01 (-0.12, 0.28)	1.46 (1.46, 1.46)	10.14 (10.04, 10.24)
Near Field	Thyroid	5.40E-02 (5.42E-02, 5.37E-02)	5.33E-02 (5.36E-02, 5.32E-02)	-1.23 (-1.92, 0.05)	2.80E-02 (2.81E-02, 2.79E-02)	-48.17 (-48.43, -47.87)
Far Field	Lungs	1.77 (1.77, 1.77)	2.11 (2.11, 2.11)	19.50 (19.46, 19.61)	1.15 (1.15, 1.15)	-35.11 (-35.14, -35.06)
	Liver	6.24E-03 (6.17E-03, 6.28E-03)	6.03E-03 (6.02E-03, 6.06E-03)	-3.50 (-4.59, -1.74)	6.36E-03 (6.32E-03, 6.42E-03)	1.90 (0.57, 2.93)
	Kidneys	3.54E-03 (3.52E-03, 3.59E-03)	3.13E-03 (3.10E-03, 3.18E-03)	-11.60 (-12.59, -8.73)	3.30E-03 (3.19E-03, 3.42E-03)	-6.62 (-9.89, -3.20)
	Bladder	3.08E-03 (2.88E-03, 3.31E-03)	2.68E-03 (2.53E-03, 2.87E-03)	-13.01 (-20.57, 4.52)	2.44E-03 (2.21E-03, 2.62E-03)	-21.02 (-29.97, -11.68)

Table D.32: EAR and ERR in Pat 5 using the linear exponential model with a 40 Sv inflection point and both neutron energy scorers

Linear-Exponential 40 Sv

Excess Absolute Risk using Fluence-Weighted Neutron Energy

		WBCT	Hybrid		Scaled MRCP	
	Organ	EAR per 10k PY	EAR per 10k PY	% Difference	EAR per 10k PY	% Difference
In Field	Brain	31.35 (31.34 , 31.35)	31.53 (31.52 , 31.54)	0.59 (0.55 , 0.66)	35.42 (35.42 , 35.43)	13.01 (12.98 , 13.04)
	Eye_L	21.82 (21.78 , 21.89)	21.88 (21.84 , 21.96)	0.28 (0.02 , 1.01)	30.97 (30.90 , 31.02)	41.92 (41.50 , 42.39)
	Eye_R	61.20 (61.16 , 61.22)	61.72 (61.65 , 61.77)	0.84 (0.71 , 1.06)	61.79 (61.75 , 61.84)	0.97 (0.87 , 1.05)
Near Field	Thyroid	5.68E-01 (5.67E-01 , 5.69E-01)	5.69E-01 (5.68E-01 , 5.71E-01)	0.26 (-0.03 , 0.83)	4.78E-01 (4.78E-01 , 4.78E-01)	-15.78 (-15.94 , -15.67)
Far Field	Lungs	1.37E-01 (1.36E-01 , 1.37E-01)	1.55E-01 (1.55E-01 , 1.56E-01)	13.55 (13.11 , 14.25)	1.06E-01 (2.36E-01 , 2.37E-01)	-22.16 (-117.19 , -116.32)
	Liver	1.52E-02 (1.52E-02 , 1.53E-02)	1.40E-02 (1.38E-02 , 1.41E-02)	-8.12 (-9.26 , -5.94)	1.38E-02 (3.49E-02 , 3.54E-02)	-9.19 (-147.69 , -143.97)
	Kidneys	1.84E-02 (1.83E-02 , 1.86E-02)	1.67E-02 (1.65E-02 , 1.69E-02)	-9.23 (-10.48 , -6.58)	1.61E-02 (1.59E-02 , 1.63E-02)	-12.66 (-14.07 , -11.02)
	Bladder	7.40E-04 (6.96E-04 , 7.96E-04)	8.65E-04 (8.18E-04 , 9.37E-04)	16.94 (7.57 , 41.03)	7.89E-04 (3.02E-03 , 3.38E-03)	6.65 (-295.51 , -214.45)

Excess Absolute Risk using KERMA-Weighted Neutron Energy

		WBCT	Hybrid		Scaled MRCP	
	Organ	EAR per 10k PY	EAR per 10k PY	% Difference	EAR per 10k PY	% Difference
In Field	Brain	31.74 (31.74 , 31.75)	31.92 (31.91 , 31.93)	0.57 (0.53 , 0.62)	35.80 (35.80 , 35.81)	12.80 (12.77 , 12.84)
	Eye_L	22.12 (22.09 , 22.18)	22.19 (22.15 , 22.27)	0.32 (0.07 , 1.02)	31.33 (31.25 , 31.39)	41.63 (41.18 , 42.08)
	Eye_R	61.50 (61.45 , 61.51)	62.00 (61.92 , 62.06)	0.82 (0.67 , 1.06)	62.11 (62.05 , 62.18)	1.00 (0.88 , 1.11)
Near Field	Thyroid	5.68E-01 (5.67E-01 , 5.69E-01)	5.69E-01 (5.68E-01 , 5.71E-01)	0.26 (-0.03 , 0.83)	4.78E-01 (4.78E-01 , 4.78E-01)	-15.78 (-15.94 , -15.67)
Far Field	Lungs	1.64E-01 (1.64E-01 , 1.64E-01)	1.88E-01 (1.87E-01 , 1.89E-01)	14.49 (13.98 , 15.41)	1.33E-01 (1.33E-01 , 1.33E-01)	-19.04 (-19.40 , -18.81)
	Liver	2.45E-02 (2.45E-02 , 2.46E-02)	2.12E-02 (2.10E-02 , 2.15E-02)	-13.40 (-14.32 , -11.33)	2.01E-02 (1.99E-02 , 2.04E-02)	-17.94 (-19.00 , -16.95)
	Kidneys	2.80E-02 (2.78E-02 , 2.86E-02)	2.52E-02 (2.47E-02 , 2.57E-02)	-10.29 (-12.00 , -6.20)	2.26E-02 (2.21E-02 , 2.31E-02)	-19.51 (-21.17 , -17.10)
	Bladder	8.16E-04 (7.35E-04 , 8.87E-04)	9.50E-04 (8.80E-04 , 1.06E-03)	16.40 (1.98 , 51.41)	8.30E-04 (7.94E-04 , 8.81E-04)	1.70 (-9.32 , 15.92)

Excess Relative Risk using Fluence-Weighted Neutron Energy

		WBCT	Hybrid		Scaled MRCP	
	Organ	ERR	ERR	% Difference	ERR	% Difference
In Field	Brain	8.72E-01 (8.72E-01 , 8.72E-01)	8.77E-01 (8.77E-01 , 8.77E-01)	0.59 (0.55 , 0.66)	9.85E-01 (9.85E-01 , 9.86E-01)	13.01 (12.98 , 13.04)
	Eye_L	6.07E-01 (6.06E-01 , 6.09E-01)	6.09E-01 (6.08E-01 , 6.11E-01)	0.28 (0.02 , 1.01)	8.61E-01 (8.59E-01 , 8.63E-01)	41.92 (41.50 , 42.39)
	Eye_R	1.70 (1.70 , 1.70)	1.72 (1.71 , 1.72)	0.84 (0.71 , 1.06)	1.72 (1.72 , 1.72)	0.97 (0.87 , 1.05)
Near Field	Thyroid	1.03 (1.03 , 1.04)	1.04 (1.04 , 1.04)	0.24 (0.00 , 0.72)	8.87E-01 (8.86E-01 , 8.87E-01)	-14.24 (-14.40 , -14.14)
Far Field	Lungs	1.12E-02 (1.12E-02 , 1.12E-02)	1.27E-02 (1.27E-02 , 1.28E-02)	13.55 (13.11 , 14.25)	8.73E-03 (8.71E-03 , 8.75E-03)	-22.16 (-22.37 , -21.98)
	Liver	1.43E-03 (1.42E-03 , 1.43E-03)	1.31E-03 (1.29E-03 , 1.32E-03)	-8.12 (-9.26 , -5.94)	1.29E-03 (1.29E-03 , 1.31E-03)	-9.19 (-9.78 , -8.32)
	Kidneys	5.12E-04 (5.09E-04 , 5.18E-04)	4.65E-04 (4.60E-04 , 4.71E-04)	-9.23 (-10.48 , -6.58)	4.48E-04 (4.41E-04 , 4.55E-04)	-12.66 (-14.07 , -11.02)
	Bladder	1.70E-04 (1.60E-04 , 1.83E-04)	1.99E-04 (1.89E-04 , 2.16E-04)	16.94 (7.57 , 41.03)	1.82E-04 (1.74E-04 , 1.95E-04)	6.65 (-1.10 , 19.17)

Excess Relative Risk using KERMA-Weighted Neutron Energy

		WBCT	Hybrid		Scaled MRCP	
	Organ	ERR	ERR	% Difference	ERR	% Difference
In Field	Brain	8.83E-01 (8.83E-01 , 8.83E-01)	8.88E-01 (8.88E-01 , 8.88E-01)	0.57 (0.53 , 0.62)	9.96E-01 (9.96E-01 , 9.96E-01)	12.80 (12.77 , 12.84)
	Eye_L	6.15E-01 (6.14E-01 , 6.17E-01)	6.17E-01 (6.16E-01 , 6.20E-01)	0.32 (0.07 , 1.02)	8.72E-01 (8.69E-01 , 8.73E-01)	41.63 (41.18 , 42.08)
	Eye_R	1.71 (1.71 , 1.71)	1.72 (1.72 , 1.73)	0.82 (0.67 , 1.06)	1.73 (1.73 , 1.73)	1.00 (0.88 , 1.11)
Near Field	Thyroid	1.04 (1.04 , 1.04)	1.04 (1.04 , 1.05)	0.26 (0.03 , 0.74)	8.93E-01 (8.91E-01 , 8.93E-01)	-14.21 (-14.36 , -14.12)
Far Field	Lungs	1.35E-02 (1.34E-02 , 1.35E-02)	1.54E-02 (1.54E-02 , 1.55E-02)	14.49 (13.98 , 15.41)	1.09E-02 (1.09E-02 , 1.09E-02)	-19.04 (-19.40 , -18.81)
	Liver	2.30E-03 (2.29E-03 , 2.30E-03)	1.99E-03 (1.97E-03 , 2.02E-03)	-13.40 (-14.32 , -11.33)	1.89E-03 (1.86E-03 , 1.91E-03)	-17.94 (-19.00 , -16.95)
	Kidneys	7.80E-04 (7.74E-04 , 7.94E-04)	7.00E-04 (6.88E-04 , 7.14E-04)	-10.29 (-12.00 , -6.20)	6.28E-04 (6.16E-04 , 6.43E-04)	-19.51 (-21.17 , -17.10)
	Bladder	1.88E-04 (1.69E-04 , 2.04E-04)	2.19E-04 (2.03E-04 , 2.45E-04)	16.40 (1.98 , 51.41)	1.91E-04 (1.83E-04 , 2.03E-04)	1.70 (-9.32 , 15.92)

D.2.6 Pat 6

Table D.33: EAR and ERR in Pat 6 using the LNT model and both neutron energy scorers

LNT

Excess Absolute Risk using Fluence-Weighted Neutron Energy

		WBCT	Hybrid		Scaled MRCP	
	Organ	EAR per 10k PY	EAR per 10k PY	% Difference	EAR per 10k PY	% Difference
In Field	Brain	13.07 (13.07, 13.08)	13.08 (13.07, 13.08)	0.01 (0.00, 0.07)	11.50 (11.50, 11.51)	-12.01 (-12.04, -11.98)
	Eye_L	61.01 (60.87, 61.19)	61.04 (60.94, 61.15)	0.05 (-0.24, 0.68)	24.97 (24.93, 25.01)	-59.08 (-59.19, -58.94)
	Eye_R	1.80 (1.79, 1.81)	1.79 (1.76, 1.82)	-0.71 (-2.72, 3.02)	7.03E-01 (6.90E-01, 7.10E-01)	-60.99 (-61.78, -60.51)
Near Field	Thyroid	3.66E-01 (3.64E-01, 3.68E-01)	3.68E-01 (3.67E-01, 3.69E-01)	0.34 (-0.33, 1.58)	6.62E-02 (6.60E-02, 6.65E-02)	-81.92 (-82.05, -81.81)
Far Field	Lungs	5.85E-02 (5.84E-02, 5.88E-02)	6.62E-02 (6.62E-02, 6.65E-02)	13.21 (12.92, 14.12)	5.73E-02 (5.70E-02, 5.77E-02)	-2.06 (-2.60, -1.25)
	Liver	4.69E-03 (4.63E-03, 4.72E-03)	4.92E-03 (4.88E-03, 5.01E-03)	4.89 (3.39, 8.41)	5.00E-03 (4.99E-03, 5.05E-03)	6.58 (5.25, 7.85)
	Kidneys	1.66E-02 (1.61E-02, 1.70E-02)	1.59E-02 (1.54E-02, 1.65E-02)	-4.10 (-8.95, 4.87)	1.69E-02 (1.60E-02, 1.76E-02)	1.86 (-4.88, 6.63)
	Bladder	1.11E-03 (9.70E-04, 1.23E-03)	1.11E-03 (1.04E-03, 1.17E-03)	0.06 (-13.55, 31.98)	1.18E-03 (1.12E-03, 1.24E-03)	6.68 (-7.61, 25.92)

Excess Absolute Risk using KERMA-Weighted Neutron Energy

		WBCT	Hybrid		Scaled MRCP	
	Organ	EAR per 10k PY	EAR per 10k PY	% Difference	EAR per 10k PY	% Difference
In Field	Brain	13.22 (13.22, 13.22)	13.22 (13.22, 13.22)	0.02 (-0.01, 0.08)	11.64 (11.64, 11.65)	-11.90 (-11.94, -11.86)
	Eye_L	61.19 (61.03, 61.35)	61.22 (61.10, 61.33)	0.05 (-0.27, 0.69)	25.08 (25.05, 25.12)	-59.01 (-59.13, -58.89)
	Eye_R	1.92 (1.90, 1.94)	1.91 (1.88, 1.94)	-0.63 (-2.46, 3.17)	7.83E-01 (7.72E-01, 8.01E-01)	-59.21 (-59.88, -58.15)
Near Field	Thyroid	3.66E-01 (3.64E-01, 3.68E-01)	3.68E-01 (3.67E-01, 3.69E-01)	0.34 (-0.33, 1.58)	6.62E-02 (6.60E-02, 6.65E-02)	-81.92 (-82.05, -81.81)
Far Field	Lungs	7.66E-02 (7.64E-02, 7.71E-02)	8.95E-02 (8.94E-02, 9.00E-02)	16.88 (16.50, 18.23)	7.96E-02 (7.92E-02, 8.02E-02)	3.92 (3.35, 4.96)
	Liver	6.93E-03 (6.87E-03, 7.00E-03)	7.24E-03 (7.16E-03, 7.39E-03)	4.37 (2.94, 8.13)	6.99E-03 (6.95E-03, 7.05E-03)	0.82 (-0.23, 2.08)
	Kidneys	2.37E-02 (2.31E-02, 2.44E-02)	2.31E-02 (2.19E-02, 2.43E-02)	-2.61 (-8.38, 8.88)	2.31E-02 (2.20E-02, 2.40E-02)	-2.78 (-8.08, 2.23)
	Bladder	1.23E-03 (1.14E-03, 1.33E-03)	1.26E-03 (1.16E-03, 1.34E-03)	1.83 (-9.60, 25.40)	1.30E-03 (1.24E-03, 1.37E-03)	5.45 (-4.23, 17.28)

Excess Relative Risk using Fluence-Weighted Neutron Energy

		WBCT	Hybrid		Scaled MRCP	
	Organ	ERR	ERR	% Difference	ERR	% Difference
In Field	Brain	7.83E-01 (7.83E-01, 7.83E-01)	7.83E-01 (7.83E-01, 7.83E-01)	0.01 (0.00, 0.07)	6.89E-01 (6.89E-01, 6.89E-01)	-12.01 (-12.04, -11.98)
	Eye_L	3.65 (3.64, 3.66)	3.66 (3.65, 3.66)	0.05 (-0.24, 0.68)	1.50 (1.49, 1.50)	-59.08 (-59.19, -58.94)
	Eye_R	1.08E-01 (1.07E-01, 1.09E-01)	1.07E-01 (1.05E-01, 1.09E-01)	-0.71 (-2.72, 3.02)	4.21E-02 (4.13E-02, 4.25E-02)	-60.99 (-61.78, -60.51)
Near Field	Thyroid	7.43E-01 (7.38E-01, 7.45E-01)	7.45E-01 (7.42E-01, 7.48E-01)	0.34 (-0.41, 1.66)	1.40E-01 (1.40E-01, 1.41E-01)	-81.09 (-81.23, -80.98)
Far Field	Lungs	1.42E-02 (1.42E-02, 1.43E-02)	1.61E-02 (1.61E-02, 1.61E-02)	13.21 (12.92, 14.12)	1.39E-02 (1.38E-02, 1.40E-02)	-2.06 (-2.60, -1.25)
	Liver	9.66E-04 (9.54E-04, 9.73E-04)	1.01E-03 (1.01E-03, 1.03E-03)	4.89 (3.39, 8.41)	1.03E-03 (1.03E-03, 1.04E-03)	6.58 (5.25, 7.85)
	Kidneys	9.96E-04 (9.61E-04, 1.02E-03)	9.55E-04 (9.19E-04, 9.85E-04)	-4.10 (-8.95, 4.87)	1.01E-03 (9.57E-04, 1.05E-03)	1.86 (-4.88, 6.63)
	Bladder	1.35E-03 (1.18E-03, 1.50E-03)	1.35E-03 (1.27E-03, 1.43E-03)	0.06 (-13.55, 31.98)	1.44E-03 (1.36E-03, 1.51E-03)	6.68 (-7.61, 25.92)

Excess Relative Risk using KERMA-Weighted Neutron Energy

		WBCT	Hybrid		Scaled MRCP	
	Organ	ERR	ERR	% Difference	ERR	% Difference
In Field	Brain	7.91E-01 (7.91E-01, 7.92E-01)	7.92E-01 (7.91E-01, 7.92E-01)	0.02 (-0.01, 0.08)	6.97E-01 (6.97E-01, 6.98E-01)	-11.90 (-11.94, -11.86)
	Eye_L	3.66 (3.65, 3.67)	3.67 (3.66, 3.67)	0.05 (-0.27, 0.69)	1.50 (1.50, 1.50)	-59.01 (-59.13, -58.89)
	Eye_R	1.15E-01 (1.14E-01, 1.16E-01)	1.14E-01 (1.12E-01, 1.16E-01)	-0.63 (-2.46, 3.17)	4.69E-02 (4.62E-02, 4.80E-02)	-59.21 (-59.88, -58.15)
Near Field	Thyroid	7.50E-01 (7.46E-01, 7.53E-01)	7.53E-01 (7.49E-01, 7.56E-01)	0.33 (-0.44, 1.65)	1.46E-01 (1.45E-01, 1.47E-01)	-80.53 (-80.67, -80.39)
Far Field	Lungs	1.86E-02 (1.85E-02, 1.87E-02)	2.17E-02 (2.17E-02, 2.19E-02)	16.88 (16.50, 18.23)	1.93E-02 (1.92E-02, 1.95E-02)	3.92 (3.35, 4.96)
	Liver	1.43E-03 (1.42E-03, 1.44E-03)	1.49E-03 (1.48E-03, 1.52E-03)	4.37 (2.94, 8.13)	1.44E-03 (1.43E-03, 1.45E-03)	0.82 (-0.23, 2.08)
	Kidneys	1.42E-03 (1.38E-03, 1.46E-03)	1.38E-03 (1.31E-03, 1.45E-03)	-2.61 (-8.38, 8.88)	1.38E-03 (1.32E-03, 1.44E-03)	-2.78 (-8.08, 2.23)
	Bladder	1.50E-03 (1.38E-03, 1.61E-03)	1.53E-03 (1.41E-03, 1.64E-03)	1.83 (-9.60, 25.40)	1.58E-03 (1.51E-03, 1.67E-03)	5.45 (-4.23, 17.28)

Table D.34: EAR and ERR in Pat 6 using the linear plateau model with a 10 Sv inflection point and both neutron energy scorers

Linear-Plateau 10 Sv

Excess Absolute Risk using Fluence-Weighted Neutron Energy

		WBCT	Hybrid		Scaled MRCP	
	Organ	EAR per 10k PY	EAR per 10k PY	% Difference	EAR per 10k PY	% Difference
In Field	Brain	11.51 (11.51, 11.51)	11.51 (11.51, 11.51)	0.01 (0.00, 0.05)	10.41 (10.41, 10.42)	-9.53 (-9.56, -9.51)
	Eye_L	26.39 (26.37, 26.40)	26.39 (26.38, 26.40)	0.01 (-0.06, 0.17)	17.99 (17.97, 18.01)	-31.82 (-31.90, -31.74)
	Eye_R	1.95 (1.93, 1.96)	1.94 (1.90, 1.97)	-0.69 (-2.63, 2.92)	7.76E-01 (0.76, 0.78)	-60.16 (-60.96, -59.69)
Near Field	Thyroid	3.58E-01 (3.56E-01, 3.59E-01)	3.59E-01 (3.58E-01, 3.60E-01)	0.29 (-0.28, 1.37)	7.23E-02 (7.20E-02, 7.26E-02)	-79.79 (-79.92, -79.68)
Far Field	Lungs	6.54E-02 (6.53E-02, 6.57E-02)	7.40E-02 (7.40E-02, 7.43E-02)	13.19 (12.90, 14.10)	6.41E-02 (6.37E-02, 6.45E-02)	-2.06 (-2.60, -1.25)
	Liver	5.25E-03 (5.18E-03, 5.29E-03)	5.50E-03 (5.46E-03, 5.61E-03)	4.89 (3.39, 8.41)	5.59E-03 (5.58E-03, 5.65E-03)	6.58 (5.25, 7.84)
	Kidneys	1.86E-02 (1.80E-02, 1.91E-02)	1.78E-02 (1.72E-02, 1.84E-02)	-4.10 (-8.94, 4.87)	1.90E-02 (1.79E-02, 1.96E-02)	1.86 (-4.88, 6.63)
	Bladder	1.24E-03 (1.09E-03, 1.38E-03)	1.24E-03 (1.17E-03, 1.31E-03)	0.06 (-13.55, 31.98)	1.32E-03 (1.25E-03, 1.39E-03)	6.68 (-7.60, 25.92)

Excess Absolute Risk using KERMA-Weighted Neutron Energy

		WBCT	Hybrid		Scaled MRCP	
	Organ	EAR per 10k PY	EAR per 10k PY	% Difference	EAR per 10k PY	% Difference
In Field	Brain	11.61 (11.61, 11.61)	11.61 (11.61, 11.61)	0.01 (0.00, 0.07)	10.51 (10.51, 10.52)	-9.42 (-9.45, -9.39)
	Eye_L	26.40 (26.39, 26.42)	26.41 (26.40, 26.42)	0.01 (-0.07, 0.17)	18.04 (18.02, 18.05)	-31.69 (-31.76, -31.61)
	Eye_R	2.07 (2.06, 2.09)	2.06 (2.03, 2.09)	-0.60 (-2.37, 3.05)	8.64E-01 (8.52E-01, 8.84E-01)	-58.32 (-58.99, -57.26)
Near Field	Thyroid	3.58E-01 (3.56E-01, 3.59E-01)	3.59E-01 (3.58E-01, 3.60E-01)	0.29 (-0.28, 1.37)	7.23E-02 (7.20E-02, 7.26E-02)	-79.79 (-79.92, -79.68)
Far Field	Lungs	8.56E-02 (8.54E-02, 8.61E-02)	1.00E-01 (9.99E-02, 1.01E-01)	16.84 (16.47, 18.19)	8.90E-02 (8.85E-02, 8.96E-02)	3.91 (3.34, 4.95)
	Liver	7.76E-03 (7.69E-03, 7.83E-03)	8.10E-03 (8.01E-03, 8.26E-03)	4.36 (2.94, 8.12)	7.82E-03 (7.78E-03, 7.89E-03)	0.82 (-0.23, 2.08)
	Kidneys	2.66E-02 (2.58E-02, 2.73E-02)	2.59E-02 (2.45E-02, 2.71E-02)	-2.61 (-8.38, 8.87)	2.58E-02 (2.46E-02, 2.69E-02)	-2.78 (-8.07, 2.23)
	Bladder	1.38E-03 (1.27E-03, 1.48E-03)	1.41E-03 (1.29E-03, 1.51E-03)	1.83 (-9.60, 25.39)	1.46E-03 (1.39E-03, 1.54E-03)	5.45 (-4.22, 17.27)

Excess Relative Risk using Fluence-Weighted Neutron Energy

		WBCT	Hybrid		Scaled MRCP	
	Organ	ERR	ERR	% Difference	ERR	% Difference
In Field	Brain	6.89E-01 (6.89E-01, 6.89E-01)	6.89E-01 (6.89E-01, 6.90E-01)	0.01 (0.00, 0.05)	6.24E-01 (6.23E-01, 6.24E-01)	-9.53 (-9.56, -9.51)
	Eye_L	1.58 (1.58, 1.58)	1.58 (1.58, 1.58)	0.01 (-0.06, 0.17)	1.08 (1.08, 1.08)	-31.82 (-31.90, -31.74)
	Eye_R	1.17E-01 (1.16E-01, 1.17E-01)	1.16E-01 (1.14E-01, 1.18E-01)	-0.69 (-2.63, 2.92)	4.65E-02 (4.56E-02, 4.70E-02)	-60.16 (-60.96, -59.69)
Near Field	Thyroid	6.35E-01 (6.32E-01, 6.37E-01)	6.37E-01 (6.35E-01, 6.38E-01)	0.26 (-0.31, 1.23)	1.49E-01 (1.49E-01, 1.50E-01)	-76.52 (-76.65, -76.40)
Far Field	Lungs	1.59E-02 (1.58E-02, 1.59E-02)	1.80E-02 (1.80E-02, 1.80E-02)	13.19 (12.90, 14.10)	1.56E-02 (1.55E-02, 1.57E-02)	-2.06 (-2.60, -1.25)
	Liver	1.08E-03 (1.07E-03, 1.09E-03)	1.13E-03 (1.13E-03, 1.16E-03)	4.89 (3.39, 8.41)	1.15E-03 (1.15E-03, 1.16E-03)	6.58 (5.25, 7.84)
	Kidneys	1.11E-03 (1.08E-03, 1.14E-03)	1.07E-03 (1.03E-03, 1.10E-03)	-4.10 (-8.94, 4.87)	1.14E-03 (1.07E-03, 1.18E-03)	1.86 (-4.88, 6.63)
	Bladder	1.51E-03 (1.32E-03, 1.68E-03)	1.51E-03 (1.42E-03, 1.60E-03)	0.06 (-13.55, 31.98)	1.61E-03 (1.52E-03, 1.69E-03)	6.68 (-7.60, 25.92)

Excess Relative Risk using KERMA-Weighted Neutron Energy

		WBCT	Hybrid		Scaled MRCP	
	Organ	ERR	ERR	% Difference	ERR	% Difference
In Field	Brain	6.95E-01 (6.95E-01, 6.95E-01)	6.95E-01 (6.95E-01, 6.95E-01)	0.01 (0.00, 0.07)	6.30E-01 (6.29E-01, 6.30E-01)	-9.42 (-9.45, -9.39)
	Eye_L	1.58 (1.58, 1.58)	1.58 (1.58, 1.58)	0.01 (-0.07, 0.17)	1.08 (1.08, 1.08)	-31.69 (-31.76, -31.61)
	Eye_R	1.24E-01 (1.23E-01, 1.25E-01)	1.23E-01 (1.21E-01, 1.25E-01)	-0.60 (-2.37, 3.05)	5.17E-02 (5.10E-02, 5.29E-02)	-58.32 (-58.99, -57.26)
Near Field	Thyroid	6.40E-01 (6.37E-01, 6.42E-01)	6.41E-01 (6.39E-01, 6.43E-01)	0.24 (-0.33, 1.22)	1.55E-01 (1.54E-01, 1.56E-01)	-75.82 (-75.95, -75.65)
Far Field	Lungs	2.08E-02 (2.07E-02, 2.09E-02)	2.43E-02 (2.43E-02, 2.44E-02)	16.84 (16.47, 18.19)	2.16E-02 (2.15E-02, 2.18E-02)	3.91 (3.34, 4.95)
	Liver	1.60E-03 (1.58E-03, 1.61E-03)	1.67E-03 (1.65E-03, 1.70E-03)	4.36 (2.94, 8.12)	1.61E-03 (1.60E-03, 1.63E-03)	0.82 (-0.23, 2.08)
	Kidneys	1.59E-03 (1.55E-03, 1.63E-03)	1.55E-03 (1.47E-03, 1.63E-03)	-2.61 (-8.38, 8.87)	1.55E-03 (1.47E-03, 1.61E-03)	-2.78 (-8.07, 2.23)
	Bladder	1.68E-03 (1.55E-03, 1.81E-03)	1.71E-03 (1.58E-03, 1.83E-03)	1.83 (-9.60, 25.39)	1.77E-03 (1.69E-03, 1.87E-03)	5.45 (-4.22, 17.27)

Table D.35: EAR and ERR in Pat 6 using the linear plateau model with a 40 Sv inflection point and both neutron energy scorers

Linear-Plateau 40 Sv

Excess Absolute Risk using Fluence-Weighted Neutron Energy

		WBCT	Hybrid		Scaled MRCP	
	Organ	EAR per 10k PY	EAR per 10k PY	% Difference	EAR per 10k PY	% Difference
In Field	Brain	12.64 (12.64 , 12.65)	12.65 (12.65 , 12.65)	0.01 (0.00 , 0.06)	11.21 (11.20 , 11.21)	-11.36 (-11.39 , -11.33)
	Eye_L	47.54 (47.45 , 47.64)	47.56 (47.50 , 47.62)	0.04 (-0.18 , 0.50)	22.85 (22.82 , 22.88)	-51.93 (-52.04 , -51.81)
	Eye_R	1.84 (1.82 , 1.85)	1.83 (1.79 , 1.85)	-0.70 (-2.70 , 3.00)	7.21E-01 (7.07E-01 , 7.28E-01)	-60.78 (-61.58 , -60.31)
Near Field	Thyroid	3.64E-01 (3.62E-01 , 3.66E-01)	3.65E-01 (3.64E-01 , 3.67E-01)	0.33 (-0.31 , 1.52)	6.77E-02 (0.00E+00 , 0.00E+00)	-81.40 (-81.53 , -81.29)
Far Field	Lungs	6.02E-02 (6.00E-02 , 6.04E-02)	6.81E-02 (6.81E-02 , 6.84E-02)	13.20 (12.91 , 14.11)	5.89E-02 (5.87E-02 , 5.94E-02)	-2.06 (-2.60 , -1.25)
	Liver	4.82E-03 (4.76E-03 , 4.86E-03)	5.06E-03 (5.02E-03 , 5.16E-03)	4.89 (3.39 , 8.41)	5.14E-03 (5.13E-03 , 5.20E-03)	6.58 (5.25 , 7.85)
	Kidneys	1.71E-02 (1.65E-02 , 1.75E-02)	1.64E-02 (1.58E-02 , 1.69E-02)	-4.10 (-8.95 , 4.87)	1.74E-02 (1.64E-02 , 1.81E-02)	1.86 (-4.88 , 6.63)
	Bladder	1.14E-03 (9.98E-04 , 1.27E-03)	1.14E-03 (1.07E-03 , 1.21E-03)	0.06 (-13.55 , 31.98)	1.21E-03 (1.15E-03 , 1.28E-03)	6.68 (-7.61 , 25.92)

Excess Absolute Risk using KERMA-Weighted Neutron Energy

		WBCT	Hybrid		Scaled MRCP	
	Organ	EAR per 10k PY	EAR per 10k PY	% Difference	EAR per 10k PY	% Difference
In Field	Brain	12.77 (12.77 , 12.78)	12.78 (12.77 , 12.78)	0.01 (-0.01 , 0.08)	11.34 (11.33 , 11.34)	-11.25 (-11.28 , -11.21)
	Eye_L	47.64 (47.55 , 47.73)	47.66 (47.59 , 47.72)	0.04 (-0.20 , 0.51)	22.94 (22.91 , 22.97)	-51.84 (-51.95 , -51.73)
	Eye_R	1.96 (1.94 , 1.98)	1.95 (1.91 , 1.98)	-0.62 (-2.44 , 3.14)	8.03E-01 (7.92E-01 , 8.22E-01)	-58.99 (-59.66 , -57.93)
Near Field	Thyroid	3.64E-01 (3.62E-01 , 3.66E-01)	3.65E-01 (3.64E-01 , 3.67E-01)	0.33 (-0.31 , 1.52)	6.77E-02 (6.75E-02 , 6.80E-02)	-81.40 (-81.53 , -81.29)
Far Field	Lungs	7.88E-02 (7.86E-02 , 7.93E-02)	9.21E-02 (9.20E-02 , 9.26E-02)	16.87 (16.50 , 18.22)	8.19E-02 (8.15E-02 , 8.25E-02)	3.92 (3.35 , 4.96)
	Liver	7.13E-03 (7.07E-03 , 7.20E-03)	7.45E-03 (7.37E-03 , 7.60E-03)	4.37 (2.94 , 8.13)	7.19E-03 (7.16E-03 , 7.25E-03)	0.82 (-0.23 , 2.08)
	Kidneys	2.44E-02 (2.37E-02 , 2.51E-02)	2.38E-02 (2.25E-02 , 2.50E-02)	-2.61 (-8.38 , 8.88)	2.37E-02 (2.26E-02 , 2.47E-02)	-2.78 (-8.08 , 2.23)
	Bladder	1.27E-03 (1.17E-03 , 1.36E-03)	1.29E-03 (1.19E-03 , 1.38E-03)	1.83 (-9.60 , 25.40)	1.34E-03 (1.28E-03 , 1.41E-03)	5.45 (-4.22 , 17.28)

Excess Relative Risk using Fluence-Weighted Neutron Energy

		WBCT	Hybrid		Scaled MRCP	
	Organ	ERR	ERR	% Difference	ERR	% Difference
In Field	Brain	7.57E-01 (7.57E-01 , 7.57E-01)	7.57E-01 (7.57E-01 , 7.57E-01)	0.01 (0.00 , 0.06)	6.71E-01 (6.71E-01 , 6.71E-01)	-11.36 (-11.39 , -11.33)
	Eye_L	2.85 (2.84 , 2.85)	2.85 (2.84 , 2.85)	0.04 (-0.18 , 0.50)	1.37 (1.37 , 1.37)	-51.93 (-52.04 , -51.81)
	Eye_R	1.10E-01 (1.09E-01 , 1.11E-01)	1.09E-01 (1.07E-01 , 1.11E-01)	-0.70 (-2.70 , 3.00)	4.32E-02 (4.24E-02 , 4.36E-02)	-60.78 (-61.58 , -60.31)
Near Field	Thyroid	7.13E-01 (7.08E-01 , 7.15E-01)	7.15E-01 (7.12E-01 , 7.17E-01)	0.32 (-0.39 , 1.54)	1.43E-01 (1.42E-01 , 1.43E-01)	-79.99 (-80.13 , -79.88)
Far Field	Lungs	1.46E-02 (1.46E-02 , 1.47E-02)	1.65E-02 (1.65E-02 , 1.66E-02)	13.20 (12.91 , 14.11)	1.43E-02 (1.42E-02 , 1.44E-02)	-2.06 (-2.60 , -1.25)
	Liver	9.94E-04 (9.82E-04 , 1.00E-03)	1.04E-03 (1.03E-03 , 1.06E-03)	4.89 (3.39 , 8.41)	1.06E-03 (1.06E-03 , 1.07E-03)	6.58 (5.25 , 7.85)
	Kidneys	1.02E-03 (9.89E-04 , 1.05E-03)	9.83E-04 (9.46E-04 , 1.01E-03)	-4.10 (-8.95 , 4.87)	1.04E-03 (9.85E-04 , 1.08E-03)	1.86 (-4.88 , 6.63)
	Bladder	1.38E-03 (1.21E-03 , 1.54E-03)	1.39E-03 (1.30E-03 , 1.47E-03)	0.06 (-13.55 , 31.98)	1.48E-03 (1.40E-03 , 1.56E-03)	6.68 (-7.61 , 25.92)

Excess Relative Risk using KERMA-Weighted Neutron Energy

		WBCT	Hybrid		Scaled MRCP	
	Organ	ERR	ERR	% Difference	ERR	% Difference
In Field	Brain	7.65E-01 (7.65E-01 , 7.65E-01)	7.65E-01 (7.65E-01 , 7.65E-01)	0.01 (-0.01 , 0.08)	6.79E-01 (6.79E-01 , 6.79E-01)	-11.25 (-11.28 , -11.21)
	Eye_L	2.85 (2.85 , 2.86)	2.85 (2.85 , 2.86)	0.04 (-0.20 , 0.51)	1.37 (1.37 , 1.38)	-51.84 (-51.95 , -51.73)
	Eye_R	1.17E-01 (1.16E-01 , 1.19E-01)	1.17E-01 (1.15E-01 , 1.18E-01)	-0.62 (-2.44 , 3.14)	4.81E-02 (4.74E-02 , 4.92E-02)	-58.99 (-59.66 , -57.93)
Near Field	Thyroid	7.19E-01 (7.16E-01 , 7.22E-01)	7.22E-01 (7.18E-01 , 7.24E-01)	0.31 (-0.41 , 1.54)	1.48E-01 (1.48E-01 , 1.49E-01)	-79.40 (-79.53 , -79.25)
Far Field	Lungs	1.91E-02 (1.91E-02 , 1.92E-02)	2.24E-02 (2.23E-02 , 2.25E-02)	16.87 (16.50 , 18.22)	1.99E-02 (1.98E-02 , 2.00E-02)	3.92 (3.35 , 4.96)
	Liver	1.47E-03 (1.46E-03 , 1.48E-03)	1.53E-03 (1.52E-03 , 1.57E-03)	4.37 (2.94 , 8.13)	1.48E-03 (1.47E-03 , 1.49E-03)	0.82 (-0.23 , 2.08)
	Kidneys	1.46E-03 (1.42E-03 , 1.50E-03)	1.42E-03 (1.35E-03 , 1.49E-03)	-2.61 (-8.38 , 8.88)	1.42E-03 (1.36E-03 , 1.48E-03)	-2.78 (-8.08 , 2.23)
	Bladder	1.55E-03 (1.42E-03 , 1.66E-03)	1.57E-03 (1.45E-03 , 1.68E-03)	1.83 (-9.60 , 25.40)	1.63E-03 (1.55E-03 , 1.72E-03)	5.45 (-4.22 , 17.28)

Table D.36: EAR and ERR in Pat 6 using the linear exponential model with a 10 Sv inflection point and both neutron energy scorers

Linear-Exponential 10 Sv

Excess Absolute Risk using Fluence-Weighted Neutron Energy

		WBCT	Hybrid		Scaled MRCP	
	Organ	EAR per 10k PY	EAR per 10k PY	% Difference	EAR per 10k PY	% Difference
In Field	Brain	11.62 (11.62 , 11.62)	11.62 (11.62 , 11.63)	0.01 (0.00 , 0.05)	10.50 (10.49 , 10.50)	-9.68 (-9.70 , -9.65)
	Eye_L	24.41 (24.42 , 24.41)	24.41 (24.42 , 24.41)	0.00 (-0.01 , 0.01)	18.21 (18.19 , 18.22)	-25.42 (-25.49 , -25.35)
	Eye_R	1.93 (1.92 , 1.94)	1.92 (1.88 , 1.95)	-0.69 (-2.64 , 2.93)	7.68E-01 (7.54E-01 , 7.76E-01)	-60.27 (-61.07 , -59.79)
Near Field	Thyroid	3.59E-01 (3.57E-01 , 3.60E-01)	3.60E-01 (3.59E-01 , 3.61E-01)	0.30 (-0.29 , 1.38)	7.16E-02 (7.13E-02 , 7.19E-02)	-80.03 (-80.16 , -79.92)
Far Field	Lungs	6.46E-02 (6.44E-02 , 6.49E-02)	7.31E-02 (7.30E-02 , 7.34E-02)	13.19 (12.90 , 14.10)	6.33E-02 (6.29E-02 , 6.37E-02)	-2.06 (-2.60 , -1.25)
	Liver	5.18E-03 (5.12E-03 , 5.22E-03)	5.43E-03 (5.39E-03 , 5.54E-03)	4.89 (3.39 , 8.41)	5.52E-03 (5.51E-03 , 5.58E-03)	6.58 (5.25 , 7.84)
	Kidneys	1.84E-02 (1.77E-02 , 1.88E-02)	1.76E-02 (1.70E-02 , 1.82E-02)	-4.10 (-8.94 , 4.87)	1.87E-02 (1.77E-02 , 1.94E-02)	1.86 (-4.88 , 6.63)
	Bladder	1.22E-03 (1.07E-03 , 1.36E-03)	1.22E-03 (1.15E-03 , 1.30E-03)	0.06 (-13.55 , 31.98)	1.30E-03 (1.23E-03 , 1.37E-03)	6.68 (-7.60 , 25.92)

Excess Absolute Risk using KERMA-Weighted Neutron Energy

		WBCT	Hybrid		Scaled MRCP	
	Organ	EAR per 10k PY	EAR per 10k PY	% Difference	EAR per 10k PY	% Difference
In Field	Brain	11.72 (11.72 , 11.72)	11.72 (11.72 , 11.73)	0.01 (0.00 , 0.07)	10.60 (10.60 , 10.60)	-9.57 (-9.59 , -9.53)
	Eye_L	24.41 (24.41 , 24.41)	24.41 (24.41 , 24.41)	0.00 (-0.01 , 0.01)	18.26 (18.24 , 18.27)	-25.22 (-25.28 , -25.16)
	Eye_R	2.06 (2.04 , 2.08)	2.04 (2.01 , 2.07)	-0.61 (-2.38 , 3.07)	8.54E-01 (8.42E-01 , 8.74E-01)	-58.43 (-59.10 , -57.37)
Near Field	Thyroid	3.59E-01 (3.57E-01 , 3.60E-01)	3.60E-01 (3.59E-01 , 3.61E-01)	0.30 (-0.29 , 1.38)	7.16E-02 (7.13E-02 , 7.19E-02)	-80.03 (-80.16 , -79.92)
Far Field	Lungs	8.45E-02 (8.43E-02 , 8.51E-02)	9.88E-02 (9.86E-02 , 9.93E-02)	16.85 (16.48 , 18.20)	8.78E-02 (8.74E-02 , 8.85E-02)	3.91 (3.34 , 4.95)
	Liver	7.66E-03 (7.59E-03 , 7.73E-03)	7.99E-03 (7.91E-03 , 8.16E-03)	4.36 (2.94 , 8.12)	7.72E-03 (7.68E-03 , 7.79E-03)	0.82 (-0.23 , 2.08)
	Kidneys	2.62E-02 (2.55E-02 , 2.69E-02)	2.55E-02 (2.42E-02 , 2.68E-02)	-2.61 (-8.38 , 8.87)	2.55E-02 (2.43E-02 , 2.66E-02)	-2.78 (-8.08 , 2.23)
	Bladder	1.36E-03 (1.26E-03 , 1.46E-03)	1.39E-03 (1.28E-03 , 1.49E-03)	1.83 (-9.60 , 25.39)	1.44E-03 (1.37E-03 , 1.52E-03)	5.45 (-4.22 , 17.27)

Excess Relative Risk using Fluence-Weighted Neutron Energy

		WBCT	Hybrid		Scaled MRCP	
	Organ	ERR	ERR	% Difference	ERR	% Difference
In Field	Brain	6.96E-01 (6.96E-01 , 6.96E-01)	6.96E-01 (6.96E-01 , 6.96E-01)	0.01 (0.00 , 0.05)	6.29E-01 (6.28E-01 , 6.29E-01)	-9.68 (-9.70 , -9.65)
	Eye_L	1.46 (1.46 , 1.46)	1.46 (1.46 , 1.46)	0.00 (-0.01 , 0.01)	1.09 (1.09 , 1.09)	-25.42 (-25.49 , -25.35)
	Eye_R	1.16E-01 (1.15E-01 , 1.16E-01)	1.15E-01 (1.13E-01 , 1.17E-01)	-0.69 (-2.64 , 2.93)	4.60E-02 (4.51E-02 , 4.64E-02)	-60.27 (-61.07 , -59.79)
Near Field	Thyroid	6.42E-01 (6.39E-01 , 6.44E-01)	6.44E-01 (6.42E-01 , 6.45E-01)	0.26 (-0.31 , 1.25)	1.48E-01 (1.48E-01 , 1.49E-01)	-76.92 (-77.05 , -76.81)
Far Field	Lungs	1.57E-02 (1.56E-02 , 1.57E-02)	1.77E-02 (1.77E-02 , 1.78E-02)	13.19 (12.90 , 14.10)	1.54E-02 (1.53E-02 , 1.55E-02)	-2.06 (-2.60 , -1.25)
	Liver	1.07E-03 (1.05E-03 , 1.08E-03)	1.12E-03 (1.11E-03 , 1.14E-03)	4.89 (3.39 , 8.41)	1.14E-03 (1.13E-03 , 1.15E-03)	6.58 (5.25 , 7.84)
	Kidneys	1.10E-03 (1.06E-03 , 1.13E-03)	1.06E-03 (1.02E-03 , 1.09E-03)	-4.10 (-8.94 , 4.87)	1.12E-03 (1.06E-03 , 1.16E-03)	1.86 (-4.88 , 6.63)
	Bladder	1.49E-03 (1.30E-03 , 1.65E-03)	1.49E-03 (1.40E-03 , 1.58E-03)	0.06 (-13.55 , 31.98)	1.59E-03 (1.50E-03 , 1.67E-03)	6.68 (-7.60 , 25.92)

Excess Relative Risk using KERMA-Weighted Neutron Energy

		WBCT	Hybrid		Scaled MRCP	
	Organ	ERR	ERR	% Difference	ERR	% Difference
In Field	Brain	7.02E-01 (7.02E-01 , 7.02E-01)	7.02E-01 (7.02E-01 , 7.02E-01)	0.01 (0.00 , 0.07)	6.35E-01 (6.35E-01 , 6.35E-01)	-9.57 (-9.59 , -9.53)
	Eye_L	1.46 (1.46 , 1.46)	1.46 (1.46 , 1.46)	0.00 (-0.01 , 0.01)	1.09 (1.09 , 1.09)	-25.22 (-25.28 , -25.16)
	Eye_R	1.23E-01 (1.22E-01 , 1.24E-01)	1.22E-01 (1.20E-01 , 1.24E-01)	-0.61 (-2.38 , 3.07)	5.12E-02 (5.04E-02 , 5.23E-02)	-58.43 (-59.10 , -57.37)
Near Field	Thyroid	6.47E-01 (6.44E-01 , 6.49E-01)	6.49E-01 (6.46E-01 , 6.50E-01)	0.25 (-0.33 , 1.24)	1.54E-01 (1.53E-01 , 1.55E-01)	-76.23 (-76.36 , -76.07)
Far Field	Lungs	2.05E-02 (2.05E-02 , 2.07E-02)	2.40E-02 (2.39E-02 , 2.41E-02)	16.85 (16.48 , 18.20)	2.13E-02 (2.12E-02 , 2.15E-02)	3.91 (3.34 , 4.95)
	Liver	1.58E-03 (1.56E-03 , 1.59E-03)	1.65E-03 (1.63E-03 , 1.68E-03)	4.36 (2.94 , 8.12)	1.59E-03 (1.58E-03 , 1.60E-03)	0.82 (-0.23 , 2.08)
	Kidneys	1.57E-03 (1.53E-03 , 1.61E-03)	1.53E-03 (1.45E-03 , 1.60E-03)	-2.61 (-8.38 , 8.87)	1.53E-03 (1.46E-03 , 1.59E-03)	-2.78 (-8.08 , 2.23)
	Bladder	1.66E-03 (1.53E-03 , 1.78E-03)	1.69E-03 (1.55E-03 , 1.81E-03)	1.83 (-9.60 , 25.39)	1.75E-03 (1.67E-03 , 1.85E-03)	5.45 (-4.22 , 17.27)

Table D.37: EAR and ERR in Pat 6 using the linear exponential model with a 40 Sv inflection point and both neutron energy scorers

Linear-Exponential 40 Sv

Excess Absolute Risk using Fluence-Weighted Neutron Energy

	Organ	WBCT EAR per 10k PY	Hybrid EAR per 10k PY	Hybrid % Difference	Scaled MRCP EAR per 10k PY	Scaled MRCP % Difference
In Field	Brain	12.69 (12.69 , 12.70)	12.70 (12.69 , 12.70)	0.01 (0.00 , 0.06)	11.24 (11.24 , 11.25)	-11.43 (-11.46 , -11.40)
	Eye_L	48.53 (48.44 , 48.63)	48.54 (48.48 , 48.61)	0.04 (-0.18 , 0.51)	23.07 (23.04 , 23.11)	-52.45 (-52.56 , -52.33)
	Eye_R	1.83 (1.82 , 1.84)	1.82 (1.79 , 1.85)	-0.71 (-2.70 , 3.00)	7.19E-01 (7.05E-01 , 7.26E-01)	-60.81 (-61.61 , -60.33)
Near Field	Thyroid	3.64E-01 (3.62E-01 , 3.66E-01)	3.66E-01 (3.65E-01 , 3.67E-01)	0.33 (-0.32 , 1.53)	6.76E-02 (6.73E-02 , 6.78E-02)	-81.46 (-81.59 , -81.36)
Far Field	Lungs	6.00E-02 (5.98E-02 , 6.02E-02)	6.79E-02 (6.78E-02 , 6.81E-02)	13.20 (12.91 , 14.11)	5.87E-02 (5.84E-02 , 5.92E-02)	-2.06 (-2.60 , -1.25)
	Liver	4.81E-03 (4.75E-03 , 4.84E-03)	5.04E-03 (5.00E-03 , 5.14E-03)	4.89 (3.39 , 8.41)	5.12E-03 (5.11E-03 , 5.18E-03)	6.58 (5.25 , 7.85)
	Kidneys	1.70E-02 (1.65E-02 , 1.75E-02)	1.63E-02 (1.57E-02 , 1.69E-02)	-4.10 (-8.95 , 4.87)	1.74E-02 (1.64E-02 , 1.80E-02)	1.86 (-4.88 , 6.63)
	Bladder	1.13E-03 (9.94E-04 , 1.26E-03)	1.13E-03 (1.07E-03 , 1.20E-03)	0.06 (-13.55 , 31.98)	1.21E-03 (1.15E-03 , 1.27E-03)	6.68 (-7.61 , 25.92)

Excess Absolute Risk using KERMA-Weighted Neutron Energy

	Organ	WBCT EAR per 10k PY	Hybrid EAR per 10k PY	Hybrid % Difference	Scaled MRCP EAR per 10k PY	Scaled MRCP % Difference
In Field	Brain	12.83 (12.83 , 12.83)	12.83 (12.83 , 12.83)	0.01 (-0.01 , 0.08)	11.37 (11.37 , 11.38)	-11.33 (-11.36 , -11.29)
	Eye_L	48.63 (48.54 , 48.72)	48.65 (48.58 , 48.72)	0.04 (-0.20 , 0.52)	23.17 (23.14 , 23.20)	-52.36 (-52.47 , -52.25)
	Eye_R	1.95 (1.94 , 1.97)	1.94 (1.91 , 1.97)	-0.62 (-2.44 , 3.14)	8.00E-01 (7.89E-01 , 8.19E-01)	-59.02 (-59.68 , -57.95)
Near Field	Thyroid	3.64E-01 (3.62E-01 , 3.66E-01)	3.66E-01 (3.65E-01 , 3.67E-01)	0.33 (-0.32 , 1.53)	6.76E-02 (6.73E-02 , 6.78E-02)	-81.46 (-81.59 , -81.36)
Far Field	Lungs	7.85E-02 (7.83E-02 , 7.90E-02)	9.18E-02 (9.16E-02 , 9.23E-02)	16.87 (16.50 , 18.22)	8.16E-02 (8.12E-02 , 8.22E-02)	3.92 (3.35 , 4.96)
	Liver	7.11E-03 (7.04E-03 , 7.17E-03)	7.42E-03 (7.34E-03 , 7.57E-03)	4.37 (2.94 , 8.13)	7.17E-03 (7.13E-03 , 7.23E-03)	0.82 (-0.23 , 2.08)
	Kidneys	2.43E-02 (2.36E-02 , 2.50E-02)	2.37E-02 (2.25E-02 , 2.49E-02)	-2.61 (-8.38 , 8.88)	2.37E-02 (2.26E-02 , 2.46E-02)	-2.78 (-8.08 , 2.23)
	Bladder	1.27E-03 (1.17E-03 , 1.36E-03)	1.29E-03 (1.19E-03 , 1.38E-03)	1.83 (-9.60 , 25.40)	1.33E-03 (1.27E-03 , 1.41E-03)	5.45 (-4.23 , 17.28)

Excess Relative Risk using Fluence-Weighted Neutron Energy

	Organ	WBCT ERR	Hybrid ERR	Hybrid % Difference	Scaled MRCP ERR	Scaled MRCP % Difference
In Field	Brain	7.60E-01 (7.60E-01 , 7.60E-01)	7.60E-01 (0.76 , 0.76)	0.01 (0.00 , 0.06)	6.73E-01 (0.67 , 0.67)	-11.43 (-11.46 , -11.40)
	Eye_L	2.91 (2.90 , 2.91)	2.91 (2.90 , 2.91)	0.04 (-0.18 , 0.51)	1.38 (1.38 , 1.38)	-52.45 (-52.56 , -52.33)
	Eye_R	1.10E-01 (1.09E-01 , 1.10E-01)	1.09E-01 (0.11 , 0.11)	-0.71 (-2.70 , 3.00)	4.30E-02 (0.04 , 0.04)	-60.81 (-61.61 , -60.33)
Near Field	Thyroid	7.16E-01 (7.12E-01 , 7.19E-01)	7.18E-01 (7.16E-01 , 7.21E-01)	0.32 (-0.39 , 1.55)	1.42E-01 (1.42E-01 , 1.43E-01)	-80.13 (-80.26 , -80.01)
Far Field	Lungs	1.46E-02 (1.45E-02 , 1.46E-02)	1.65E-02 (1.65E-02 , 1.65E-02)	13.20 (12.91 , 14.11)	1.43E-02 (1.42E-02 , 1.44E-02)	-2.06 (-2.60 , -1.25)
	Liver	9.90E-04 (9.78E-04 , 9.98E-04)	1.04E-03 (1.03E-03 , 1.06E-03)	4.89 (3.39 , 8.41)	1.06E-03 (1.05E-03 , 1.07E-03)	6.58 (5.25 , 7.85)
	Kidneys	1.02E-03 (9.86E-04 , 1.05E-03)	9.79E-04 (9.43E-04 , 1.01E-03)	-4.10 (-8.95 , 4.87)	1.04E-03 (9.81E-04 , 1.08E-03)	1.86 (-4.88 , 6.63)
	Bladder	1.38E-03 (1.21E-03 , 1.53E-03)	1.38E-03 (1.30E-03 , 1.46E-03)	0.06 (-13.55 , 31.98)	1.47E-03 (1.39E-03 , 1.55E-03)	6.68 (-7.61 , 25.92)

Excess Relative Risk using KERMA-Weighted Neutron Energy

	Organ	WBCT ERR	Hybrid ERR	Hybrid % Difference	Scaled MRCP ERR	Scaled MRCP % Difference
In Field	Brain	7.68E-01 (7.68E-01 , 7.68E-01)	7.68E-01 (7.68E-01 , 7.68E-01)	0.01 (-0.01 , 0.08)	6.81E-01 (6.81E-01 , 6.81E-01)	-11.33 (-11.36 , -11.29)
	Eye_L	2.91 (2.91 , 2.92)	2.91 (2.91 , 2.92)	0.04 (-0.20 , 0.52)	1.39 (1.39 , 1.39)	-52.36 (-52.47 , -52.25)
	Eye_R	1.17E-01 (1.16E-01 , 1.18E-01)	1.16E-01 (1.14E-01 , 1.18E-01)	-0.62 (-2.44 , 3.14)	4.79E-02 (4.73E-02 , 4.90E-02)	-59.02 (-59.68 , -57.95)
Near Field	Thyroid	7.23E-01 (7.19E-01 , 7.26E-01)	7.25E-01 (7.22E-01 , 7.28E-01)	0.31 (-0.42 , 1.55)	1.48E-01 (1.47E-01 , 1.49E-01)	-79.54 (-79.67 , -79.39)
Far Field	Lungs	1.91E-02 (1.90E-02 , 1.92E-02)	2.23E-02 (2.22E-02 , 2.24E-02)	16.87 (16.50 , 18.22)	1.98E-02 (1.97E-02 , 2.00E-02)	3.92 (3.35 , 4.96)
	Liver	1.46E-03 (1.45E-03 , 1.48E-03)	1.53E-03 (1.51E-03 , 1.56E-03)	4.37 (2.94 , 8.13)	1.48E-03 (1.47E-03 , 1.49E-03)	0.82 (-0.23 , 2.08)
	Kidneys	1.46E-03 (1.42E-03 , 1.50E-03)	1.42E-03 (1.34E-03 , 1.49E-03)	-2.61 (-8.38 , 8.88)	1.42E-03 (1.35E-03 , 1.48E-03)	-2.78 (-8.08 , 2.23)
	Bladder	1.54E-03 (1.42E-03 , 1.65E-03)	1.57E-03 (1.44E-03 , 1.68E-03)	1.83 (-9.60 , 25.40)	1.62E-03 (1.55E-03 , 1.71E-03)	5.45 (-4.23 , 17.28)

D.2.7 Pat 7

Table D.38: EAR and ERR in Pat 7 using the LNT model and both neutron energy scorers

LNT

Excess Absolute Risk using Fluence-Weighted Neutron Energy

		WBCT	Hybrid		Scaled MRCP	
	Organ	EAR per 10k PY	EAR per 10k PY	% Difference	EAR per 10k PY	% Difference
In Field	Brain	110.36 (110.35 , 110.36)	110.36 (110.35 , 110.37)	0.00 (-0.01 , 0.02)	86.44 (86.43 , 86.45)	-21.67 (-21.68 , -21.67)
	Eye_L	15.66 (15.62 , 15.70)	15.64 (15.61 , 15.70)	-0.13 (-0.50 , 0.65)	12.44 (12.39 , 12.49)	-20.58 (-20.94 , -20.21)
	Eye_R	4.33 (4.30 , 4.36)	4.32 (4.32 , 4.33)	-0.14 (-0.76 , 1.23)	2.93 (2.91 , 2.94)	-32.30 (-32.90 , -31.83)
Near Field	Thyroid	3.93E-03 (3.88E-03 , 3.97E-03)	3.88E-03 (3.81E-03 , 3.92E-03)	-1.47 (-3.52 , 2.10)	5.25E-03 (5.15E-03 , 5.31E-03)	33.43 (30.35 , 35.34)
Far Field	Lungs	3.09E-02 (3.07E-02 , 3.10E-02)	4.23E-02 (4.21E-02 , 4.26E-02)	37.16 (36.07 , 39.22)	4.86E-02 (4.83E-02 , 4.88E-02)	57.49 (56.13 , 58.35)
	Liver	3.44E-03 (3.42E-03 , 3.45E-03)	4.33E-03 (4.27E-03 , 4.38E-03)	26.06 (24.23 , 29.26)	4.83E-03 (4.81E-03 , 4.87E-03)	40.69 (39.62 , 41.78)
	Kidneys	1.13E-02 (1.09E-02 , 1.15E-02)	1.01E-02 (9.88E-03 , 1.04E-02)	-10.50 (-14.09 , -3.47)	1.13E-02 (1.08E-02 , 1.17E-02)	0.21 (-5.21 , 4.97)
	Bladder	4.47E-04 (4.32E-04 , 4.61E-04)	4.48E-04 (4.23E-04 , 4.71E-04)	0.21 (-6.28 , 13.16)	4.27E-04 (4.09E-04 , 4.46E-04)	-4.36 (-9.64 , 1.07)

Excess Absolute Risk using KERMA-Weighted Neutron Energy

		WBCT	Hybrid		Scaled MRCP	
	Organ	EAR per 10k PY	EAR per 10k PY	% Difference	EAR per 10k PY	% Difference
In Field	Brain	110.97 (110.97 , 110.98)	110.97 (110.97 , 110.98)	0.00 (-0.01 , 0.02)	87.00 (87.00 , 87.01)	-21.60 (-21.60 , -21.59)
	Eye_L	15.98 (15.93 , 16.02)	15.96 (15.91 , 15.99)	-0.14 (-0.58 , 0.64)	12.73 (12.69 , 12.79)	-20.30 (-20.68 , -19.92)
	Eye_R	4.60 (4.57 , 4.63)	4.59 (4.58 , 4.61)	-0.17 (-0.75 , 1.17)	3.17 (3.15 , 3.20)	-30.94 (-31.60 , -30.19)
Near Field	Thyroid	3.93E-03 (3.88E-03 , 3.97E-03)	3.88E-03 (3.81E-03 , 3.92E-03)	-1.47 (-3.52 , 2.10)	5.25E-03 (5.15E-03 , 5.31E-03)	33.43 (30.35 , 35.34)
Far Field	Lungs	4.63E-02 (4.62E-02 , 4.65E-02)	6.58E-02 (6.51E-02 , 6.62E-02)	42.08 (40.54 , 44.62)	7.40E-02 (7.38E-02 , 7.41E-02)	59.84 (59.14 , 60.43)
	Liver	5.51E-03 (5.45E-03 , 5.57E-03)	6.69E-03 (6.59E-03 , 6.79E-03)	21.35 (19.08 , 25.87)	7.58E-03 (7.52E-03 , 7.63E-03)	37.54 (35.70 , 39.32)
	Kidneys	1.78E-02 (1.73E-02 , 1.84E-02)	1.54E-02 (1.50E-02 , 1.57E-02)	-13.45 (-16.84 , -6.71)	1.73E-02 (1.66E-02 , 1.80E-02)	-2.68 (-7.55 , 2.44)
	Bladder	5.54E-04 (5.35E-04 , 5.78E-04)	5.56E-04 (5.20E-04 , 5.86E-04)	0.47 (-6.89 , 14.96)	4.97E-04 (4.71E-04 , 5.19E-04)	-10.27 (-15.87 , -4.46)

Excess Relative Risk using Fluence-Weighted Neutron Energy

		WBCT	Hybrid		Scaled MRCP	
	Organ	ERR	ERR	% Difference	ERR	% Difference
In Field	Brain	6.61 (6.61 , 6.61)	6.61 (6.61 , 6.61)	0.00 (-0.01 , 0.02)	5.18 (5.18 , 5.18)	-21.67 (-21.68 , -21.67)
	Eye_L	9.38E-01 (9.35E-01 , 9.40E-01)	9.37E-01 (9.34E-01 , 9.40E-01)	-0.13 (-0.50 , 0.65)	7.45E-01 (7.42E-01 , 7.48E-01)	-20.58 (-20.94 , -20.21)
	Eye_R	2.59E-01 (2.58E-01 , 2.61E-01)	2.59E-01 (2.59E-01 , 2.59E-01)	-0.14 (-0.76 , 1.23)	1.76E-01 (1.74E-01 , 1.76E-01)	-32.30 (-32.90 , -31.83)
Near Field	Thyroid	1.68E-02 (1.67E-02 , 1.72E-02)	1.67E-02 (1.64E-02 , 1.69E-02)	-0.88 (-2.80 , 3.28)	2.03E-02 (1.99E-02 , 2.05E-02)	20.24 (17.60 , 22.75)
Far Field	Lungs	7.49E-03 (7.45E-03 , 7.52E-03)	1.03E-02 (1.02E-02 , 1.03E-02)	37.16 (36.07 , 39.22)	1.18E-02 (1.17E-02 , 1.18E-02)	57.49 (56.13 , 58.35)
	Liver	7.08E-04 (7.04E-04 , 7.10E-04)	8.92E-04 (8.81E-04 , 9.02E-04)	26.06 (24.23 , 29.26)	9.96E-04 (9.92E-04 , 1.00E-03)	40.69 (39.62 , 41.78)
	Kidneys	6.75E-04 (6.52E-04 , 6.91E-04)	6.04E-04 (5.92E-04 , 6.21E-04)	-10.50 (-14.09 , -3.47)	6.77E-04 (6.48E-04 , 7.03E-04)	0.21 (-5.21 , 4.97)
	Bladder	5.44E-04 (5.25E-04 , 5.61E-04)	5.45E-04 (5.15E-04 , 5.73E-04)	0.21 (-6.28 , 13.16)	5.20E-04 (4.97E-04 , 5.43E-04)	-4.36 (-9.64 , 1.07)

Excess Relative Risk using KERMA-Weighted Neutron Energy

		WBCT	Hybrid		Scaled MRCP	
	Organ	ERR	ERR	% Difference	ERR	% Difference
In Field	Brain	6.65 (6.65 , 6.65)	6.65 (6.65 , 6.65)	0.00 (-0.01 , 0.02)	5.21 (5.21 , 5.21)	-21.60 (-21.60 , -21.59)
	Eye_L	9.57E-01 (9.54E-01 , 9.59E-01)	9.55E-01 (9.53E-01 , 9.58E-01)	-0.14 (-0.58 , 0.64)	7.63E-01 (7.60E-01 , 7.66E-01)	-20.30 (-20.68 , -19.92)
	Eye_R	2.75E-01 (2.74E-01 , 2.77E-01)	2.75E-01 (2.74E-01 , 2.76E-01)	-0.17 (-0.75 , 1.17)	1.90E-01 (1.89E-01 , 1.92E-01)	-30.94 (-31.60 , -30.19)
Near Field	Thyroid	2.32E-02 (2.28E-02 , 2.37E-02)	2.32E-02 (2.30E-02 , 2.36E-02)	0.02 (-1.74 , 4.65)	2.62E-02 (2.55E-02 , 2.67E-02)	12.84 (9.36 , 16.03)
Far Field	Lungs	1.12E-02 (1.12E-02 , 1.13E-02)	1.60E-02 (1.58E-02 , 1.61E-02)	42.08 (40.54 , 44.62)	1.80E-02 (1.79E-02 , 1.80E-02)	59.84 (59.14 , 60.43)
	Liver	1.14E-03 (1.12E-03 , 1.15E-03)	1.38E-03 (1.36E-03 , 1.40E-03)	21.35 (19.08 , 25.87)	1.56E-03 (1.55E-03 , 1.57E-03)	37.54 (35.70 , 39.32)
	Kidneys	1.07E-03 (1.03E-03 , 1.10E-03)	9.22E-04 (8.98E-04 , 9.37E-04)	-13.45 (-16.84 , -6.71)	1.04E-03 (9.94E-04 , 1.08E-03)	-2.68 (-7.55 , 2.44)
	Bladder	6.74E-04 (6.52E-04 , 7.03E-04)	6.77E-04 (6.33E-04 , 7.13E-04)	0.47 (-6.89 , 14.96)	6.05E-04 (5.73E-04 , 6.31E-04)	-10.27 (-15.87 , -4.46)

Table D.39: EAR and ERR in Pat 7 using the linear plateau model with a 10 Sv inflection point and both neutron energy scorers

Linear-Plateau 10 Sv

Excess Absolute Risk using Fluence-Weighted Neutron Energy

		WBCT	Hybrid		Scaled MRCP	
	Organ	EAR per 10k PY	EAR per 10k PY	% Difference	EAR per 10k PY	% Difference
In Field	Brain	28.78 (28.78, 28.78)	28.78 (28.78, 28.78)	0.00 (0.00, 0.00)	28.14 (28.14, 28.14)	-2.22 (-2.22, -2.21)
	Eye_L	13.18 (13.16, 13.20)	13.17 (13.15, 13.21)	-0.10 (-0.37, 0.48)	11.08 (11.04, 11.11)	-15.98 (-16.28, -15.68)
	Eye_R	4.47 (4.44, 4.50)	4.46 (4.46, 4.47)	-0.13 (-0.70, 1.13)	3.10 (3.09, 3.11)	-30.51 (-31.07, -30.06)
Near Field	Thyroid	4.40E-03 (4.34E-03, 4.44E-03)	4.33E-03 (4.26E-03, 4.39E-03)	-1.47 (-3.51, 2.10)	5.86E-03 (5.75E-03, 5.93E-03)	33.37 (30.30, 35.26)
Far Field	Lungs	3.45E-02 (3.43E-02, 3.47E-02)	4.74E-02 (4.71E-02, 4.76E-02)	37.13 (36.04, 39.18)	5.44E-02 (5.40E-02, 5.46E-02)	57.42 (56.07, 58.29)
	Liver	3.85E-03 (3.82E-03, 3.86E-03)	4.85E-03 (4.78E-03, 4.90E-03)	26.05 (24.22, 29.25)	5.41E-03 (5.39E-03, 5.45E-03)	40.68 (39.61, 41.77)
	Kidneys	1.26E-02 (1.22E-02, 1.29E-02)	1.13E-02 (1.11E-02, 1.16E-02)	-10.49 (-14.09, -3.47)	1.26E-02 (1.21E-02, 1.31E-02)	0.21 (-5.21, 4.97)
	Bladder	5.00E-04 (4.83E-04, 5.16E-04)	5.01E-04 (4.74E-04, 5.28E-04)	0.21 (-6.28, 13.16)	4.79E-04 (4.58E-04, 4.99E-04)	-4.36 (-9.64, 1.07)

Excess Absolute Risk using KERMA-Weighted Neutron Energy

		WBCT	Hybrid		Scaled MRCP	
	Organ	EAR per 10k PY	EAR per 10k PY	% Difference	EAR per 10k PY	% Difference
In Field	Brain	28.79 (28.79, 28.79)	28.79 (28.79, 28.79)	0.00 (0.00, 0.00)	28.16 (28.16, 28.16)	-2.17 (-2.17, -2.17)
	Eye_L	13.38 (13.34, 13.40)	13.36 (13.33, 13.38)	-0.10 (-0.42, 0.46)	11.28 (11.25, 11.32)	-15.67 (-15.97, -15.36)
	Eye_R	4.72 (4.70, 4.74)	4.71 (4.70, 4.73)	-0.16 (-0.68, 1.07)	3.35 (3.32, 3.38)	-29.08 (-29.72, -28.36)
Near Field	Thyroid	4.40E-03 (4.34E-03, 4.44E-03)	4.33E-03 (4.26E-03, 4.39E-03)	-1.47 (-3.51, 2.10)	5.86E-03 (5.75E-03, 5.93E-03)	33.37 (30.30, 35.26)
Far Field	Lungs	5.18E-02 (5.17E-02, 5.20E-02)	7.36E-02 (7.28E-02, 7.40E-02)	42.02 (40.48, 44.55)	8.28E-02 (8.25E-02, 8.29E-02)	59.74 (59.04, 60.33)
	Liver	6.17E-03 (6.10E-03, 6.23E-03)	7.48E-03 (7.37E-03, 7.59E-03)	21.34 (19.07, 25.86)	8.48E-03 (8.42E-03, 8.54E-03)	37.52 (35.67, 39.30)
	Kidneys	1.99E-02 (1.93E-02, 2.06E-02)	1.72E-02 (1.68E-02, 1.75E-02)	-13.44 (-16.83, -6.71)	1.94E-02 (1.86E-02, 2.01E-02)	-2.68 (-7.55, 2.44)
	Bladder	6.20E-04 (5.99E-04, 6.47E-04)	6.23E-04 (5.82E-04, 6.56E-04)	0.47 (-6.89, 14.96)	5.56E-04 (5.27E-04, 5.81E-04)	-10.27 (-15.87, -4.46)

Excess Relative Risk using Fluence-Weighted Neutron Energy

		WBCT	Hybrid		Scaled MRCP	
	Organ	EAR per 10k PY	EAR per 10k PY	% Difference	EAR per 10k PY	% Difference
In Field	Brain	1.72 (1.72, 1.72)	1.72 (1.72, 1.72)	0.00 (0.00, 0.00)	1.69 (1.69, 1.69)	-2.22 (-2.22, -2.21)
	Eye_L	7.89E-01 (7.88E-01, 7.91E-01)	7.89E-01 (7.87E-01, 7.91E-01)	-0.10 (-0.37, 0.48)	6.63E-01 (6.61E-01, 6.65E-01)	-15.98 (-16.28, -15.68)
	Eye_R	2.67E-01 (2.66E-01, 2.69E-01)	2.67E-01 (2.67E-01, 2.68E-01)	-0.13 (-0.70, 1.13)	1.86E-01 (1.85E-01, 1.86E-01)	-30.51 (-31.07, -30.06)
Near Field	Thyroid	1.87E-02 (1.85E-02, 1.91E-02)	1.86E-02 (1.83E-02, 1.88E-02)	-0.88 (-2.79, 3.26)	2.25E-02 (2.21E-02, 2.27E-02)	20.08 (17.47, 22.57)
Far Field	Lungs	8.38E-03 (8.33E-03, 8.42E-03)	1.15E-02 (1.14E-02, 1.16E-02)	37.13 (36.04, 39.18)	1.32E-02 (1.31E-02, 1.33E-02)	57.42 (56.07, 58.29)
	Liver	7.92E-04 (7.88E-04, 7.95E-04)	9.99E-04 (9.86E-04, 1.01E-03)	26.05 (24.22, 29.25)	1.11E-03 (1.11E-03, 1.12E-03)	40.68 (39.61, 41.77)
	Kidneys	7.56E-04 (7.30E-04, 7.73E-04)	6.77E-04 (6.62E-04, 6.96E-04)	-10.49 (-14.09, -3.47)	7.58E-04 (7.26E-04, 7.87E-04)	0.21 (-5.21, 4.97)
	Bladder	6.09E-04 (5.88E-04, 6.28E-04)	6.10E-04 (5.76E-04, 6.42E-04)	0.21 (-6.28, 13.16)	5.82E-04 (5.57E-04, 6.08E-04)	-4.36 (-9.64, 1.07)

Excess Relative Risk using KERMA-Weighted Neutron Energy

		WBCT	Hybrid		Scaled MRCP	
	Organ	EAR per 10k PY	EAR per 10k PY	% Difference	EAR per 10k PY	% Difference
In Field	Brain	1.72 (1.72, 1.72)	1.72 (1.72, 1.72)	0.00 (0.00, 0.00)	1.69 (1.69, 1.69)	-2.17 (-2.17, -2.17)
	Eye_L	8.01E-01 (7.99E-01, 8.02E-01)	8.00E-01 (7.98E-01, 8.01E-01)	-0.10 (-0.42, 0.46)	6.75E-01 (6.74E-01, 6.78E-01)	-15.67 (-15.97, -15.36)
	Eye_R	2.83E-01 (2.81E-01, 2.84E-01)	2.82E-01 (2.81E-01, 2.83E-01)	-0.16 (-0.68, 1.07)	2.00E-01 (1.99E-01, 2.02E-01)	-29.08 (-29.72, -28.36)
Near Field	Thyroid	2.57E-02 (2.54E-02, 2.63E-02)	2.57E-02 (2.55E-02, 2.62E-02)	0.02 (-1.72, 4.60)	2.90E-02 (2.82E-02, 2.96E-02)	12.71 (9.26, 15.87)
Far Field	Lungs	1.26E-02 (1.25E-02, 1.26E-02)	1.79E-02 (1.77E-02, 1.80E-02)	42.02 (40.48, 44.55)	2.01E-02 (2.00E-02, 2.01E-02)	59.74 (59.04, 60.33)
	Liver	1.27E-03 (1.26E-03, 1.28E-03)	1.54E-03 (1.52E-03, 1.56E-03)	21.34 (19.07, 25.86)	1.75E-03 (1.73E-03, 1.76E-03)	37.52 (35.67, 39.30)
	Kidneys	1.19E-03 (1.16E-03, 1.23E-03)	1.03E-03 (1.00E-03, 1.05E-03)	-13.44 (-16.83, -6.71)	1.16E-03 (1.11E-03, 1.20E-03)	-2.68 (-7.55, 2.44)
	Bladder	7.54E-04 (7.29E-04, 7.87E-04)	7.58E-04 (7.08E-04, 7.98E-04)	0.47 (-6.89, 14.96)	6.77E-04 (6.41E-04, 7.07E-04)	-10.27 (-15.87, -4.46)

Table D.40: EAR and ERR in Pat 7 using the linear plateau model with a 40 Sv inflection point and both neutron energy scorers

Linear-Plateau 40 Sv

Excess Absolute Risk using Fluence-Weighted Neutron Energy

		WBCT	Hybrid		Scaled MRCP	
	Organ	EAR per 10k PY	EAR per 10k PY	% Difference	EAR per 10k PY	% Difference
In Field	Brain	70.08 (70.08 , 70.08)	70.08 (70.08 , 70.09)	0.00 (0.00 , 0.01)	60.48 (60.47 , 60.48)	-13.70 (-13.71 , -13.70)
	Eye_L	14.97 (14.93 , 15.00)	14.95 (14.92 , 15.00)	-0.12 (-0.46 , 0.60)	12.07 (12.03 , 12.11)	-19.37 (-19.72 , -19.02)
	Eye_R	4.36 (4.34 , 4.40)	4.36 (4.35 , 4.37)	-0.14 (-0.75 , 1.20)	2.97 (2.96 , 2.98)	-31.85 (-32.44 , -31.38)
Near Field	Thyroid	4.05E-03 (3.99E-03 , 4.08E-03)	3.99E-03 (3.92E-03 , 4.04E-03)	-1.47 (-3.52 , 2.10)	5.40E-03 (5.30E-03 , 5.46E-03)	33.42 (30.34 , 35.32)
Far Field	Lungs	3.18E-02 (3.16E-02 , 3.19E-02)	4.36E-02 (4.33E-02 , 4.38E-02)	37.16 (36.06 , 39.21)	5.00E-02 (4.97E-02 , 5.02E-02)	57.47 (56.11 , 58.34)
	Liver	3.54E-03 (3.51E-03 , 3.55E-03)	4.46E-03 (4.40E-03 , 4.50E-03)	26.05 (24.23 , 29.26)	4.97E-03 (4.95E-03 , 5.01E-03)	40.69 (39.62 , 41.78)
	Kidneys	1.16E-02 (1.12E-02 , 1.19E-02)	1.04E-02 (1.02E-02 , 1.07E-02)	-10.49 (-14.09 , -3.47)	1.16E-02 (1.11E-02 , 1.21E-02)	0.21 (-5.21 , 4.97)
	Bladder	4.60E-04 (4.44E-04 , 4.74E-04)	4.61E-04 (4.35E-04 , 4.85E-04)	0.21 (-6.28 , 13.16)	4.40E-04 (4.21E-04 , 4.59E-04)	-4.36 (-9.64 , 1.07)

Excess Absolute Risk using KERMA-Weighted Neutron Energy

		WBCT	Hybrid		Scaled MRCP	
	Organ	EAR per 10k PY	EAR per 10k PY	% Difference	EAR per 10k PY	% Difference
In Field	Brain	70.30 (70.30 , 70.30)	70.30 (70.30 , 70.31)	0.00 (0.00 , 0.01)	60.73 (60.73 , 60.73)	-13.62 (-13.62 , -13.61)
	Eye_L	15.25 (15.20 , 15.28)	15.23 (15.18 , 15.26)	-0.13 (-0.54 , 0.59)	12.34 (12.30 , 12.39)	-19.08 (-19.44 , -18.71)
	Eye_R	4.63 (4.61 , 4.66)	4.62 (4.61 , 4.64)	-0.17 (-0.73 , 1.15)	3.22 (3.19 , 3.25)	-30.47 (-31.13 , -29.73)
Near Field	Thyroid	4.05E-03 (3.99E-03 , 4.08E-03)	3.99E-03 (3.92E-03 , 4.04E-03)	-1.47 (-3.52 , 2.10)	5.40E-03 (5.30E-03 , 5.46E-03)	33.42 (30.34 , 35.32)
Far Field	Lungs	4.77E-02 (4.75E-02 , 4.78E-02)	6.77E-02 (6.70E-02 , 6.81E-02)	42.07 (40.52 , 44.60)	7.62E-02 (7.59E-02 , 7.63E-02)	59.82 (59.12 , 60.41)
	Liver	5.67E-03 (5.61E-03 , 5.73E-03)	6.88E-03 (6.78E-03 , 6.98E-03)	21.34 (19.08 , 25.87)	7.80E-03 (7.74E-03 , 7.85E-03)	37.53 (35.69 , 39.32)
	Kidneys	1.83E-02 (1.78E-02 , 1.89E-02)	1.58E-02 (1.54E-02 , 1.61E-02)	-13.45 (-16.84 , -6.71)	1.78E-02 (1.71E-02 , 1.85E-02)	-2.68 (-7.55 , 2.44)
	Bladder	5.70E-04 (5.51E-04 , 5.95E-04)	5.73E-04 (5.35E-04 , 6.03E-04)	0.47 (-6.89 , 14.96)	5.11E-04 (4.84E-04 , 5.34E-04)	-10.27 (-15.87 , -4.46)

Excess Relative Risk using Fluence-Weighted Neutron Energy

		WBCT	Hybrid		Scaled MRCP	
	Organ	ERR	ERR	% Difference	ERR	% Difference
In Field	Brain	4.20 (4.20 , 4.20)	4.20 (4.20 , 4.20)	0.00 (0.00 , 0.01)	3.62 (3.62 , 3.62)	-13.70 (-13.71 , -13.70)
	Eye_L	8.96E-01 (8.94E-01 , 8.98E-01)	8.95E-01 (8.93E-01 , 8.98E-01)	-0.12 (-0.46 , 0.60)	7.23E-01 (7.20E-01 , 7.25E-01)	-19.37 (-19.72 , -19.02)
	Eye_R	2.61E-01 (2.60E-01 , 2.63E-01)	2.61E-01 (2.61E-01 , 2.61E-01)	-0.14 (-0.75 , 1.20)	1.78E-01 (1.77E-01 , 1.78E-01)	-31.85 (-32.44 , -31.38)
Near Field	Thyroid	1.73E-02 (1.71E-02 , 1.76E-02)	1.72E-02 (1.69E-02 , 1.74E-02)	-0.88 (-2.80 , 3.28)	2.08E-02 (2.04E-02 , 2.10E-02)	20.20 (17.57 , 22.71)
Far Field	Lungs	7.71E-03 (7.66E-03 , 7.74E-03)	1.06E-02 (1.05E-02 , 1.06E-02)	37.16 (36.06 , 39.21)	1.21E-02 (1.21E-02 , 1.22E-02)	57.47 (56.11 , 58.34)
	Liver	7.29E-04 (7.24E-04 , 7.31E-04)	9.18E-04 (9.06E-04 , 9.28E-04)	26.05 (24.23 , 29.26)	1.02E-03 (1.02E-03 , 1.03E-03)	40.69 (39.62 , 41.78)
	Kidneys	6.95E-04 (6.71E-04 , 7.11E-04)	6.22E-04 (6.09E-04 , 6.40E-04)	-10.49 (-14.09 , -3.47)	6.96E-04 (6.67E-04 , 7.23E-04)	0.21 (-5.21 , 4.97)
	Bladder	5.60E-04 (5.41E-04 , 5.77E-04)	5.61E-04 (5.30E-04 , 5.90E-04)	0.21 (-6.28 , 13.16)	5.35E-04 (5.12E-04 , 5.58E-04)	-4.36 (-9.64 , 1.07)

Excess Relative Risk using KERMA-Weighted Neutron Energy

		WBCT	Hybrid		Scaled MRCP	
	Organ	ERR	ERR	% Difference	ERR	% Difference
In Field	Brain	4.21 (4.21 , 4.21)	4.21 (4.21 , 4.21)	0.00 (0.00 , 0.01)	3.64 (3.64 , 3.64)	-13.62 (-13.62 , -13.61)
	Eye_L	9.13E-01 (9.10E-01 , 9.15E-01)	9.12E-01 (9.09E-01 , 9.14E-01)	-0.13 (-0.54 , 0.59)	7.39E-01 (7.36E-01 , 7.42E-01)	-19.08 (-19.44 , -18.71)
	Eye_R	2.77E-01 (2.76E-01 , 2.79E-01)	2.77E-01 (2.76E-01 , 2.78E-01)	-0.17 (-0.73 , 1.15)	1.93E-01 (1.91E-01 , 1.94E-01)	-30.47 (-31.13 , -29.73)
Near Field	Thyroid	2.38E-02 (2.35E-02 , 2.43E-02)	2.38E-02 (2.36E-02 , 2.43E-02)	0.02 (-1.73 , 4.64)	2.69E-02 (2.61E-02 , 2.74E-02)	12.81 (9.33 , 15.99)
Far Field	Lungs	1.16E-02 (1.15E-02 , 1.16E-02)	1.64E-02 (1.63E-02 , 1.65E-02)	42.07 (40.52 , 44.60)	1.85E-02 (1.84E-02 , 1.85E-02)	59.82 (59.12 , 60.41)
	Liver	1.17E-03 (1.16E-03 , 1.18E-03)	1.42E-03 (1.40E-03 , 1.44E-03)	21.34 (19.08 , 25.87)	1.61E-03 (1.59E-03 , 1.62E-03)	37.53 (35.69 , 39.32)
	Kidneys	1.10E-03 (1.06E-03 , 1.13E-03)	9.49E-04 (9.24E-04 , 9.64E-04)	-13.45 (-16.84 , -6.71)	1.07E-03 (1.02E-03 , 1.11E-03)	-2.68 (-7.55 , 2.44)
	Bladder	6.93E-04 (6.70E-04 , 7.24E-04)	6.97E-04 (6.51E-04 , 7.33E-04)	0.47 (-6.89 , 14.96)	6.22E-04 (5.89E-04 , 6.50E-04)	-10.27 (-15.87 , -4.46)

Table D.41: EAR and ERR in Pat 7 using the linear exponential model with a 10 Sv inflection point and both neutron energy scorers

Linear-Exponential 10 Sv

Excess Absolute Risk using Fluence-Weighted Neutron Energy

		WBCT	Hybrid		Scaled MRCP	
	Organ	EAR per 10k PY	EAR per 10k PY	% Difference	EAR per 10k PY	% Difference
In Field	Brain	19.42 (19.42, 19.42)	19.42 (19.42, 19.42)	0.00 (-0.01, 0.01)	22.65 (22.65, 22.65)	16.64 (16.64, 16.65)
	Eye_L	13.34 (13.31, 13.36)	13.32 (13.30, 13.36)	-0.10 (-0.37, 0.48)	11.18 (11.14, 11.21)	-16.20 (-16.50, -15.90)
	Eye_R	4.45 (4.43, 4.48)	4.45 (4.44, 4.45)	-0.13 (-0.71, 1.14)	3.09 (3.07, 3.09)	-30.71 (-31.28, -30.26)
Near Field	Thyroid	4.34E-03 (4.28E-03, 4.38E-03)	4.28E-03 (4.21E-03, 4.33E-03)	-1.47 (-3.51, 2.10)	5.79E-03 (5.68E-03, 5.85E-03)	33.37 (30.30, 35.27)
Far Field	Lungs	3.41E-02 (3.39E-02, 3.42E-02)	4.68E-02 (4.65E-02, 4.70E-02)	37.13 (36.04, 39.18)	5.37E-02 (5.34E-02, 5.39E-02)	57.43 (56.08, 58.30)
	Liver	3.80E-03 (3.77E-03, 3.81E-03)	4.79E-03 (4.72E-03, 4.84E-03)	26.05 (24.23, 29.26)	5.34E-03 (5.32E-03, 5.38E-03)	40.68 (39.61, 41.77)
	Kidneys	1.25E-02 (1.20E-02, 1.27E-02)	1.12E-02 (1.09E-02, 1.15E-02)	-10.49 (-14.09, -3.47)	1.25E-02 (1.20E-02, 1.30E-02)	0.21 (-5.21, 4.97)
	Bladder	4.94E-04 (4.77E-04, 5.09E-04)	4.95E-04 (4.68E-04, 5.21E-04)	0.21 (-6.28, 13.16)	4.72E-04 (4.52E-04, 4.93E-04)	-4.36 (-9.64, 1.07)

Excess Absolute Risk using KERMA-Weighted Neutron Energy

		WBCT	Hybrid		Scaled MRCP	
	Organ	EAR per 10k PY	EAR per 10k PY	% Difference	EAR per 10k PY	% Difference
In Field	Brain	19.33 (19.33, 19.33)	19.33 (19.33, 19.33)	0.00 (-0.01, 0.01)	22.59 (22.59, 22.58)	16.86 (16.85, 16.86)
	Eye_L	13.53 (13.50, 13.56)	13.52 (13.49, 13.54)	-0.10 (-0.43, 0.47)	11.38 (11.35, 11.42)	-15.88 (-16.18, -15.56)
	Eye_R	4.71 (4.68, 4.73)	4.70 (4.69, 4.72)	-0.16 (-0.69, 1.08)	3.33 (3.30, 3.36)	-29.29 (-29.92, -28.56)
Near Field	Thyroid	4.34E-03 (4.28E-03, 4.38E-03)	4.28E-03 (4.21E-03, 4.33E-03)	-1.47 (-3.51, 2.10)	5.79E-03 (5.68E-03, 5.85E-03)	33.37 (30.30, 35.27)
Far Field	Lungs	5.11E-02 (5.10E-02, 5.13E-02)	7.26E-02 (7.19E-02, 7.31E-02)	42.03 (40.49, 44.56)	8.17E-02 (8.14E-02, 8.18E-02)	59.75 (59.05, 60.35)
	Liver	6.09E-03 (6.02E-03, 6.15E-03)	7.39E-03 (7.27E-03, 7.50E-03)	21.34 (19.07, 25.86)	8.37E-03 (8.31E-03, 8.43E-03)	37.52 (35.68, 39.30)
	Kidneys	1.97E-02 (1.91E-02, 2.03E-02)	1.70E-02 (1.66E-02, 1.73E-02)	-13.44 (-16.83, -6.71)	1.91E-02 (1.83E-02, 1.99E-02)	-2.68 (-7.55, 2.44)
	Bladder	6.12E-04 (5.92E-04, 6.39E-04)	6.15E-04 (5.75E-04, 6.47E-04)	0.47 (-6.89, 14.96)	5.49E-04 (5.20E-04, 5.73E-04)	-10.27 (-15.87, -4.46)

Excess Relative Risk using Fluence-Weighted Neutron Energy

		WBCT	Hybrid		Scaled MRCP	
	Organ	EAR per 10k PY	EAR per 10k PY	% Difference	EAR per 10k PY	% Difference
In Field	Brain	1.16 (1.16, 1.16)	1.16 (1.16, 1.16)	0.00 (-0.01, 0.01)	1.36 (1.36, 1.36)	16.64 (16.64, 16.65)
	Eye_L	7.99E-01 (0.80, 0.80)	7.98E-01 (0.80, 0.80)	-0.10 (-0.37, 0.48)	6.69E-01 (0.67, 0.67)	-16.20 (-16.50, -15.90)
	Eye_R	2.67E-01 (0.27, 0.27)	2.66E-01 (0.27, 0.27)	-0.13 (-0.71, 1.14)	1.85E-01 (0.18, 0.19)	-30.71 (-31.28, -30.26)
Near Field	Thyroid	1.85E-02 (1.83E-02, 1.89E-02)	1.84E-02 (1.81E-02, 1.86E-02)	-0.88 (-2.79, 3.26)	2.22E-02 (2.18E-02, 2.25E-02)	20.10 (17.48, 22.60)
Far Field	Lungs	8.28E-03 (8.23E-03, 8.31E-03)	1.14E-02 (1.13E-02, 1.14E-02)	37.13 (36.04, 39.18)	1.30E-02 (1.30E-02, 1.31E-02)	57.43 (56.08, 58.30)
	Liver	7.82E-04 (7.78E-04, 7.85E-04)	9.86E-04 (9.73E-04, 9.96E-04)	26.05 (24.23, 29.26)	1.10E-03 (1.10E-03, 1.11E-03)	40.68 (39.61, 41.77)
	Kidneys	7.46E-04 (7.21E-04, 7.63E-04)	6.68E-04 (6.54E-04, 6.87E-04)	-10.49 (-14.09, -3.47)	7.48E-04 (7.17E-04, 7.77E-04)	0.21 (-5.21, 4.97)
	Bladder	6.01E-04 (5.81E-04, 6.20E-04)	6.02E-04 (5.69E-04, 6.34E-04)	0.21 (-6.28, 13.16)	5.75E-04 (5.50E-04, 6.00E-04)	-4.36 (-9.64, 1.07)

Excess Relative Risk using KERMA-Weighted Neutron Energy

		WBCT	Hybrid		Scaled MRCP	
	Organ	EAR per 10k PY	EAR per 10k PY	% Difference	EAR per 10k PY	% Difference
In Field	Brain	1.16 (1.16, 1.16)	1.16 (1.16, 1.16)	0.00 (-0.01, 0.01)	1.35 (1.35, 1.35)	16.86 (16.85, 16.86)
	Eye_L	8.10E-01 (0.81, 0.81)	8.10E-01 (0.81, 0.81)	-0.10 (-0.43, 0.47)	6.82E-01 (0.68, 0.68)	-15.88 (-16.18, -15.56)
	Eye_R	2.82E-01 (0.28, 0.28)	2.81E-01 (0.28, 0.28)	-0.16 (-0.69, 1.08)	1.99E-01 (0.20, 0.20)	-29.29 (-29.92, -28.56)
Near Field	Thyroid	2.54E-02 (2.51E-02, 2.60E-02)	2.54E-02 (2.52E-02, 2.59E-02)	0.02 (-1.72, 4.61)	2.87E-02 (2.79E-02, 2.92E-02)	12.73 (9.28, 15.89)
Far Field	Lungs	1.24E-02 (1.24E-02, 1.25E-02)	1.76E-02 (1.75E-02, 1.77E-02)	42.03 (40.49, 44.56)	1.98E-02 (1.98E-02, 1.99E-02)	59.75 (59.05, 60.35)
	Liver	1.25E-03 (1.24E-03, 1.27E-03)	1.52E-03 (1.50E-03, 1.54E-03)	21.34 (19.07, 25.86)	1.72E-03 (1.71E-03, 1.74E-03)	37.52 (35.68, 39.30)
	Kidneys	1.18E-03 (1.14E-03, 1.22E-03)	1.02E-03 (9.92E-04, 1.04E-03)	-13.44 (-16.83, -6.71)	1.15E-03 (1.10E-03, 1.19E-03)	-2.68 (-7.55, 2.44)
	Bladder	7.45E-04 (7.20E-04, 7.77E-04)	7.48E-04 (6.99E-04, 7.87E-04)	0.47 (-6.89, 14.96)	6.68E-04 (6.33E-04, 6.98E-04)	-10.27 (-15.87, -4.46)

Table D.42: EAR and ERR in Pat 7 using the linear exponential model with a 40 Sv inflection point and both neutron energy scorers

Linear-Exponential 40 Sv

Excess Absolute Risk using Fluence-Weighted Neutron Energy

		WBCT	Hybrid		Scaled MRCP	
	Organ	EAR per 10k PY	EAR per 10k PY	% Difference	EAR per 10k PY	% Difference
In Field	Brain	71.48 (71.47 , 71.48)	71.48 (71.47 , 71.48)	0.00 (0.00 , 0.01)	61.85 (61.84 , 61.85)	-13.47 (-13.48 , -13.47)
	Eye_L	15.05 (15.01 , 15.08)	15.03 (14.99 , 15.08)	-0.12 (-0.47 , 0.61)	12.11 (12.07 , 12.16)	-19.51 (-19.86 , -19.15)
	Eye_R	4.36 (4.33 , 4.39)	4.35 (4.35 , 4.36)	-0.14 (-0.75 , 1.21)	2.97 (2.95 , 2.98)	-31.91 (-32.50 , -31.44)
Near Field	Thyroid	4.03E-03 (3.98E-03 , 4.07E-03)	3.97E-03 (3.91E-03 , 4.02E-03)	-1.47 (-3.52 , 2.10)	5.38E-03 (5.28E-03 , 5.44E-03)	33.42 (30.34 , 35.32)
Far Field	Lungs	3.16E-02 (3.15E-02 , 3.18E-02)	4.34E-02 (4.32E-02 , 4.37E-02)	37.16 (36.07 , 39.21)	4.98E-02 (4.95E-02 , 5.00E-02)	57.47 (56.12 , 58.34)
	Liver	3.52E-03 (3.50E-03 , 3.53E-03)	4.44E-03 (4.38E-03 , 4.49E-03)	26.05 (24.23 , 29.26)	4.96E-03 (4.93E-03 , 4.99E-03)	40.69 (39.62 , 41.78)
	Kidneys	1.16E-02 (1.12E-02 , 1.18E-02)	1.03E-02 (1.01E-02 , 1.06E-02)	-10.49 (-14.09 , -3.47)	1.16E-02 (1.11E-02 , 1.20E-02)	0.21 (-5.21 , 4.97)
	Bladder	4.58E-04 (4.43E-04 , 4.73E-04)	4.59E-04 (4.34E-04 , 4.83E-04)	0.21 (-6.28 , 13.16)	4.38E-04 (4.19E-04 , 4.57E-04)	-4.36 (-9.64 , 1.07)

Excess Absolute Risk using KERMA-Weighted Neutron Energy

		WBCT	Hybrid		Scaled MRCP	
	Organ	EAR per 10k PY	EAR per 10k PY	% Difference	EAR per 10k PY	% Difference
In Field	Brain	71.69 (71.69 , 71.69)	71.69 (71.69 , 71.69)	0.00 (0.00 , 0.01)	62.10 (62.10 , 62.11)	-13.37 (-13.38 , -13.37)
	Eye_L	15.33 (15.28 , 15.36)	15.31 (15.26 , 15.34)	-0.13 (-0.54 , 0.60)	12.38 (12.34 , 12.43)	-19.22 (-19.57 , -18.85)
	Eye_R	4.62 (4.60 , 4.65)	4.62 (4.60 , 4.64)	-0.17 (-0.73 , 1.15)	3.21 (3.19 , 3.24)	-30.53 (-31.19 , -29.78)
Near Field	Thyroid	4.03E-03 (3.98E-03 , 4.07E-03)	3.97E-03 (3.91E-03 , 4.02E-03)	-1.47 (-3.52 , 2.10)	5.38E-03 (5.28E-03 , 5.44E-03)	33.42 (30.34 , 35.32)
Far Field	Lungs	4.75E-02 (4.73E-02 , 4.77E-02)	6.75E-02 (6.68E-02 , 6.79E-02)	42.07 (40.52 , 44.61)	7.59E-02 (7.56E-02 , 7.60E-02)	59.82 (59.12 , 60.41)
	Liver	5.65E-03 (5.59E-03 , 5.71E-03)	6.85E-03 (6.75E-03 , 6.96E-03)	21.34 (19.08 , 25.87)	7.77E-03 (7.71E-03 , 7.83E-03)	37.53 (35.69 , 39.32)
	Kidneys	1.82E-02 (1.77E-02 , 1.88E-02)	1.58E-02 (1.54E-02 , 1.60E-02)	-13.45 (-16.84 , -6.71)	1.77E-02 (1.70E-02 , 1.84E-02)	-2.68 (-7.55 , 2.44)
	Bladder	5.68E-04 (5.49E-04 , 5.93E-04)	5.70E-04 (5.33E-04 , 6.00E-04)	0.47 (-6.89 , 14.96)	5.09E-04 (4.83E-04 , 5.32E-04)	-10.27 (-15.87 , -4.46)

Excess Relative Risk using Fluence-Weighted Neutron Energy

		WBCT	Hybrid		Scaled MRCP	
	Organ	ERR	ERR	% Difference	ERR	% Difference
In Field	Brain	4.28 (4.28 , 4.28)	4.28 (4.28 , 4.28)	0.00 (0.00 , 0.01)	3.70 (3.70 , 3.70)	-13.47 (-13.48 , -13.47)
	Eye_L	9.01E-01 (8.99E-01 , 9.03E-01)	9.00E-01 (8.98E-01 , 9.03E-01)	-0.12 (-0.47 , 0.61)	7.25E-01 (7.23E-01 , 7.28E-01)	-19.51 (-19.86 , -19.15)
	Eye_R	2.61E-01 (2.60E-01 , 2.63E-01)	2.61E-01 (2.60E-01 , 2.61E-01)	-0.14 (-0.75 , 1.21)	1.78E-01 (1.77E-01 , 1.78E-01)	-31.91 (-32.50 , -31.44)
Near Field	Thyroid	1.72E-02 (1.71E-02 , 1.76E-02)	1.71E-02 (1.68E-02 , 1.73E-02)	-0.88 (-2.80 , 3.28)	2.07E-02 (2.03E-02 , 2.10E-02)	20.21 (17.57 , 22.71)
Far Field	Lungs	7.68E-03 (7.64E-03 , 7.71E-03)	1.05E-02 (1.05E-02 , 1.06E-02)	37.16 (36.07 , 39.21)	1.21E-02 (1.20E-02 , 1.21E-02)	57.47 (56.12 , 58.34)
	Liver	7.26E-04 (7.22E-04 , 7.28E-04)	9.15E-04 (9.03E-04 , 9.25E-04)	26.05 (24.23 , 29.26)	1.02E-03 (1.02E-03 , 1.03E-03)	40.69 (39.62 , 41.78)
	Kidneys	6.92E-04 (6.69E-04 , 7.08E-04)	6.20E-04 (6.07E-04 , 6.37E-04)	-10.49 (-14.09 , -3.47)	6.94E-04 (6.65E-04 , 7.21E-04)	0.21 (-5.21 , 4.97)
	Bladder	5.58E-04 (5.39E-04 , 5.75E-04)	5.59E-04 (5.28E-04 , 5.88E-04)	0.21 (-6.28 , 13.16)	5.33E-04 (5.10E-04 , 5.56E-04)	-4.36 (-9.64 , 1.07)

Excess Relative Risk using KERMA-Weighted Neutron Energy

		WBCT	Hybrid		Scaled MRCP	
	Organ	ERR	ERR	% Difference	ERR	% Difference
In Field	Brain	4.29 (4.29 , 4.29)	4.29 (4.29 , 4.29)	0.00 (0.00 , 0.01)	3.72 (3.72 , 3.72)	-13.37 (-13.38 , -13.37)
	Eye_L	9.18E-01 (9.15E-01 , 9.20E-01)	9.17E-01 (9.14E-01 , 9.19E-01)	-0.13 (-0.54 , 0.60)	7.41E-01 (7.39E-01 , 7.44E-01)	-19.22 (-19.57 , -18.85)
	Eye_R	2.77E-01 (2.76E-01 , 2.79E-01)	2.76E-01 (2.76E-01 , 2.78E-01)	-0.17 (-0.73 , 1.15)	1.92E-01 (1.91E-01 , 1.94E-01)	-30.53 (-31.19 , -29.78)
Near Field	Thyroid	2.37E-02 (2.34E-02 , 2.42E-02)	2.37E-02 (2.35E-02 , 2.42E-02)	0.02 (-1.73 , 4.64)	2.68E-02 (2.61E-02 , 2.73E-02)	12.81 (9.34 , 15.99)
Far Field	Lungs	1.15E-02 (1.15E-02 , 1.16E-02)	1.64E-02 (1.62E-02 , 1.65E-02)	42.07 (40.52 , 44.61)	1.84E-02 (1.84E-02 , 1.84E-02)	59.82 (59.12 , 60.41)
	Liver	1.16E-03 (1.15E-03 , 1.18E-03)	1.41E-03 (1.39E-03 , 1.43E-03)	21.34 (19.08 , 25.87)	1.60E-03 (1.59E-03 , 1.61E-03)	37.53 (35.69 , 39.32)
	Kidneys	1.09E-03 (1.06E-03 , 1.13E-03)	9.45E-04 (9.21E-04 , 9.61E-04)	-13.45 (-16.84 , -6.71)	1.06E-03 (1.02E-03 , 1.10E-03)	-2.68 (-7.55 , 2.44)
	Bladder	6.91E-04 (6.68E-04 , 7.21E-04)	6.94E-04 (6.49E-04 , 7.31E-04)	0.47 (-6.89 , 14.96)	6.20E-04 (5.87E-04 , 6.47E-04)	-10.27 (-15.87 , -4.46)

Bibliography

[1] Mayo Clinic of Rochester. *Departments and Facilities* (2021). https://college.mayo.edu/academics/residencies-and-fellowships/radiation-oncology-clinical-medical-physics-residency-minnesota/department-and-facilities/.

[2] National Cancer Institute. *Second Primary Cancers* (2021). https://dceg.cancer.gov/research/what-we-study/second-cancers.

[3] Particle Therapy Co-Operative Group. *Particle therapy facilities in clinical operation* (2021). https://www.ptcog.ch/index.php/facilities-in-operation.

[4] University of Pennsylvania. *Program Overview* (2021). https://www.med.upenn.edu/medicalphysicsresidency/.

[5] World Heath Organization. *Cancer Overview* (2021). https://www.who.int/health-topics/cancer#tab=tab_1.

[6] D. Adam, T. Liu, P. Caracappa, B. Bednarz und X.G. Xu, *Medical Physics* **47** (2020), 2537.

[7] S. Agostinelli, J. Allison, K. Amako, J. Apostolakis, H. Arauji, P. Arce, M. Asai, D. Axen, S. Banerjee, G. Barrang, F. Behner, L. Bellagamba, J. Boudreau, L. Broglia, A. Brunengo, H. Bukhardt, S. Chauvie, J. Chuma, R. Chytacek, G. Cooperman, G. Cosmo, P. Degtyarenko, A. Dell'Acqua, G. Depaola, D. Dietrich, R. Enami, A. Feliciello, C. Ferguson, H. Fesefeldt, G. Folger, F. Foppiano, A. Forti, S. Garelli, S. Giani, R. Giannitrapani, D. Gibin, J.J. Gómez Cadenas, I. González, G.G. a G Greeniaus, W. Greiner, V. Grichine, A. Grossheim, S. Guatelli, P. Gumplinger, R. Hamatsu, K. Hashimoto, H. Hasui, A. Heikkinen, A. Howard, V. Ivanchenko, A. Johnson, F.W. Jones, J. Kallenbach, N. Kanaya, M. Kawabata, Y. Kawabata, M. Kawaguti, S. Kelner, P. Kent, A. Kimura, T. Kodama, R. Kokoulin, M. Kossov, H. Kurashige, E. Lamanna, T. Lampén, V. Lara, M. Maire, E. Medernach, K. Minamimoto, P. Mora de Freitas, Y. Morita, K. Murakami, M. Nagamatu, R. Nartallo, P. Nieminen, T. Nishimura, K. Ohtsubo, M. Okamura, S. O'Neale, Y. Oohata, K. Paech, J. Perl, A. Pfeiffer, M.G. Pia, F. Ranjard, S. Scherer, S. Sei, V. Sirotenko, D. Smith, N. Starkov, H. Stoecker, J. Sulkimo, M. Takahata, S. Tanaka, E. Tcherniaev, S. Safai

Tehrani, M. Tropeano, P. Truscott, H. Uno, L. Urban, M. Verderi, A. Walkden, W. Wander, H. Weber, J.P. Wellisch, T. Wenaus, D.C. Williams, D. Wright, T. Yamada, H. Yoshida und D. Zschiesche, *Nuclear Instruments and Methods in Physics Research Section A: Accelerators, Spectrometers, Detectors and Associated Equipment* **506** (2003), 250.

[8] F. Alongi, S. Arcangeli, A.R. Filippi, U. Ricardi und M. Scorsetti, *Oncologist* **17** (2012), 1100.

[9] P. Andreo, *Radiation Oncology* **13** (2018).

[10] C.J. Anker und J.Y. Wo, *International Journal of Radiation Oncology, Biology, Physics* **92** (2015), 843.

[11] L. Archambault, L. Beaulieu und V. Hubert-Tremblay. *DICOM Geant4 Example*. Github, 2007.

[12] C. Aristei, E. Perrucci, E. Ali, F. Marazzi, V. Masiello, S. Saldi und G. Ingrosso, *Frontiers in Oncology* **11** (2021), 461.

[13] K.M. Atkins, I.M. Pashtan, M.R. Bussière, K.H. Kang, A. Niemierko, J.E. Daly, T.M. Botticello, M.C. Hurd, P.H. Chapman, K. Oh, J.S. Loeffler und H.A. Shih, *International Journal of Radiation Oncology, Biology, Physics* **101** (2018), 820.

[14] A. Berrington de Gonzales, E. Gilbert, R. Curtis, P. Inskip, R. Kleinerman, L. Morton, P. Rajaraman und M.P. Litte, *International Journal of Radiation Oncology, Biology, Physics* **86** (2013), 224.

[15] A. Berrington de Gonzalez, R.E. Curtiz, S.F. Kry, E. Gilbert, S. Lamart, C.D. Berg, M. Stovall und E. Ron, *Lancet Oncology* **12** (2011), 353.

[16] H. Bethe, *Annalen der Physik* **5** (1930), 324.

[17] F. Bloch, *Annalen der Physik* **16** (1933), 285.

[18] D. Bodensteiner, *Medical Dosimetry* **43** (2018), 168.

[19] W.E. Bolch, C. Lee, M. Wayson und P. Johnson, *Radiation and Environmental Biophysics* **49** (2010), 155.

[20] J. Borras, Y. Lievens, M. Barton, J. Corral, J. Ferlay und F. Bray, *Radiotherapy and Oncology* **119** (2016), 5.

[21] D. Brenner und E. Hall, *Radiotherapy and Oncology* **86** (2008), 165.

[22] N.P. Brodin und W.A. Tomé, *Oral Oncology* **86** (2019), 8.

[23] A. Bryant, M. Banegas, M. Martinez, L. Mell und J. Murphy, *Cancer Epidemiology, Biomarkers and Prevention* **26** (2017), 963.

[24] J. Cardarelli und B. Ulsh, *Dose Response* **16** (2018).

[25] Center for Innovation in Radiation Oncology. *Contouring Atlases, Templates Tools*. NRG Oncology and RTOG, 2019.

[26] C. Chargari, E. Deutsch, P. Blanchard, S. Gouy, H. Martelli, F. Géurin, I. Dumas, A. Bossi, P. Morice, A.N. Viswanathan und C. Haie-Meder, *CA: A Cancer Journal for Clinicians* **69** (2019), 386.

[27] K.P. Chatzipapas, P. Papadimitroulas, D. Emfietzoglou, S.A. Kalospyros, M. Hada, A.G. Georgakilas und G.C. Kagadis, *Cancers (Basel)* **12** (2020), 799.

[28] A.M. Chen, M.E. Daly, J. Cui, H.O. Wooten, D.G. Farwell und J.A. Purdy, *British Journal of Radiology* **87** (2014).

[29] A.M. Chen, W.H. Hall, B. Li, M. Guiou, C. Wright, M. Mathai, A. Dublin und J.A. Purdy, *British Journal of Radiology* **84** (2011), 58.

[30] C. Choi, B. Shin, Y.S. Yeom, H. Han, S. Ha, S. Moon, G. Son, T.T. Nguyen, C.H. Kim, B.S. Chung und W.E. Bolch, *Journal of Radiological Protection* (2021).

[31] C. Choi, Y.S. Yeom, H. Lee, H. Han, B. Shin, T.T. Nguyen und C.H. Kim, *Physics in Medicine and Biology* **65** (2020).

[32] C.S. Chui und S.V. Spirou, *Medical Dosimetry* **26** (2001), 189.

[33] C. Chung, T. Yock, K. Nelson, Y. Xu, N. Keating und N. Tarbell, *International Journal of Radiation Oncology, Biology, Physics* **87** (2013), 46.

[34] S.E. Combs, B.G. Baumert, M. Bandszus, A. Bozzao, M. Brada, L. Fariselli, A. Fiorentino, U. Ganswindt, A.L. Grosu, F.L. Lagerwaard, M. Niyazi, T. Nyholm, I. Paddick, D.C. Weber, C. Belka und G. Minniti, *Radiotherapy and Oncology* **156** (2020), 80.

[35] B.O. Community. *Blender - a 3D modelling and rendering package*. Blender Foundation, Stichting Blender Foundation, Amsterdam (2018).

[36] N.R. Council, *Washington D.C.: The National Academies Press* (2006).

[37] A. Dasu und I. Toma-Dasu, *Physica Medica* **42** (2017), 232.

[38] L.A. Dawson und D.A. Jaffray, *Journal of Clinical Oncology* **25** (2016).

[39] D. De Ruysscher, E. Sterpin, K. Haustermans und T. Depuydt, *Cancers* **7** (2015), 1143.

[40] G. Delaney, S. Jacob, C. Featherstone und M. Barton, *Cancer* **104** (2005), 1129.

[41] S.F. Deus und J.W. Poston, *Proc. of the Symp. on Radiopharmaceutical Dosimetry HEW Publication 768044* (1976).

[42] I. Diallo, N. Haddy, E. Adjadj, A. Samand, J.C. E Quiniou, I. Alziar, N. Perret, S. Guérin, D. Lefkopoulos und F. de Vathaire, *International Journal of Radiation Oncology, Biology, Physics* **74** (2009), 876.

[43] M. Doss, *Journal of Nuclear Medicine* **59** (2018), 1786.

[44] T.N. Eade, A.L. Hanlon, E.M. Horwitz, M.K. Buyyounouski, G.E. Hanks und A. Pollack, *International Journal of Radiation Oncology, Biology, Physics* **68** (2007), 682.

[45] F.S. Englbrecht, S. Trinkl, V. Mares, W. Rühm, M. Wielunski, J.J. Wilkens, M. Hillbrand und K. Parodi, *Zeitschrift für Medizinische Physik* **31** (2021), 215.

[46] M. Feng, G. Valdes, N. Dixit und T.D. Solberg, *Frontiers in Oncology* **8** (2018), 110.

[47] A. Ferrari, P.R. Sala, A. Fassò und J. Ranft, *CERN-2005-10 (2005), INFN/TC*$_0$5/11, $SLAC - R - 773$(2005).

[48] J. Fontenot, C. Bloch, D. Followill, U. Titt und W.D. Newhauser, *Physics in Medicine and Biology* **55** (2010), 6987.

[49] J. Fontenot, A. Lee und W. Newhauser, *International Journal of Radiation Oncology, Biology, Physics* **74** (2009), 616.

[50] J. Fontenot, A. Lee und W. Newhauser, *Frontiers in Oncology* (2020).

[51] F. Foroudi, L. Wilson, M. Bresel, A. Haworth, C. Hornby, D. Pham, J. Cramb, S. Gill, K.H. Tai und T. Kron, *Radiation Oncology* **7** (2012), 111.

[52] N. Fukunaga-Johnson, H.M. Sandler, R. Marsh und M.K. Martel, *Clinical Investigations* **1** (1998), 77.

[53] G. Giovannini, T. Böhlen, G. Cabal, J. Bauer, T. Tessonnier, K. Frey, J. Debus, A. Mairani und K. Parodi, *Radiation Oncology* **11** (2016).

[54] C. Grassberger, S. Dowdell, A. Lomax, G. Sharp, J. Shackleford, N. Choi, H. Willers und H. Paganetti, *International Journal of Radiation Oncology, Biology, Physics* **86** (2013), 380.

[55] R. Hälg und U. Schneider, *The British Journal of Radiology* **93** (2020).

[56] A. Halloran, W. Newhauser, C. Chu und W. Donahue, *Physics in Medicine and Biology* **Accepted Online** (2021).

[57] H. Han, Y.S. Yeom, C. Choi, S. Moon, B. Shin, S. Ha und C.H. Kim, *Journal of Radiological Protection* **40** (2020), 962.

[58] S. Hashimoto, Y. Shibamoto, H. Iwata, H. Ogino, H. Shibata, T. Toshito, C. Sugie und J. Mizoe, *Journal of Radiation Research* **57** (2016), 524.

[59] N. Howlader, A. Noone, M. Krapcho, D. Miller, A. Brest, M. Yu, J. Ruhl, Z. Tatalovich, A. Mariotto, D. Lewis, H. Chen, E. Feuer und K. Cronin, *National Cancer Institute* (2021).

[60] J.L. Hurtado, C. Lee, D. Lodwick, T. Goede, J.L. Williams und W.E. Bolch, *Health Physics* **102** (2012), 292.

[61] J.L. Hwang, R.L. Shoup und J.W. Poston, *Oak Ridge National Laboratory* **Report ORNL/TM-5453** (1976).

[62] ICRP, *Annals of the ICRP* **92** (2003).

[63] ICRP, *Annals of the ICRP* **103** (2007).

[64] ICRP, *Annals of the ICRP* **110** (2009).

[65] ICRU, *Oxford University Press* **ICRU Report 59** (1998).

[66] L. Jagetic und W. Newhauser, *Physics in Medicine and Biology* **60** (2015), 4753.

[67] C.Z. Jarlskog und H. Paganetti, *International Journal of Radiation Oncology, Biology, Physics* **72** (2008), 228.

[68] H.C. Jenkinson, M.M. Hawkins, C.A. Stiller, D.L. Winter, H.B. Marsden und M.C. Stevens, *British Journal of Cancer* **91** (2004), 1905.

[69] D.T.L. Jones und A.N. Schreuder, *Radiation Physics and Chemistry* **61** (2001), 615.

[70] R.M. Jones, J.W. Poston, J.L. Hwang, T.D. Jones und G.G. Warner, *Oak Ridge National Laboratory* **Report ORNL/TM-5278** (1976).

[71] A. Kaiser, J.G. Eley, N.E. Onyeuku, S.R. Rice, C.C. Wright, N.E. McGovern, M. Sank, M. Zhu, Z. Vujaskovic, C.B. Simone 2nd und A. Hussain, *Journal of Visualized Experiments - Medicine* **144** (2019).

[72] A.B. Keener, *Nature* **585** (2020).

[73] C.H. Kim, J.H. Jeong, W.E. Bolch, K.W. Cho und S.B. Hwang, *Physics in Medicine and Biology* **56** (2011), 3137.

[74] C.H. Kim, J.H. Jeong, W.E. Bolch, K.W. Cho und S.B. Hwang, *Physics in Medicine and Biology* **59** (2014), 3173.

[75] C.H. Kim, Y.S. Yeom, T.T. Nguyen, M.C. Han, C. Choi, H. Lee, H. Han, B. Shin, J.K. Lee, H.S. Kim, M. Zankl, N. Petoussi-Henss, W.E. Bolch, C. Lee, B.S. Chung, R. Qiu und K. Eckerman, *Annals of the ICRP* **47** (2018), 45.

[76] C.H. Kim, Y.S. Yeom, T.T. Nguyen, Z.J. Wang, H.S. Kim, M.C. Han, J.K. Lee, M. Zankl, N. Petoussi-Henss, W.E. Bolch, C. Lee und B.S. Chung, *Annals of the ICRP* **45** (2016), 188.

[77] E. Kollitz, H. Han, C.H. Kim, M. Pinto, M. Schwarz, M. Riboldi, F. Kamp, C. Belka, W.D. Newhauser, G. Dedes und K. Parodi, *Physics in Medicine and Biology* **67** (2022), 035005.

[78] A.C. Kraan, N. Depauw, B. Clasie, M. Giunta, T. Madden und H.M. Kooy, *Medical Physics* **45** (2017), 60.

[79] R. Kramer, M. Zankl, G. Williams und G. Drexler, *Gesellschaft für Strahlen- und Umweltforschung* **GSF-Report S-885** (1982).

[80] D.J. Kroon. *Wavefront OBJ Toolbox*. MATLAB Central File Exchange, 2011.

[81] G.A. Kuzmin, M.M. Mille, J.W. Jung, C. Lee, C. Pelletier, G. Akabani und C. Lee, *Radiation Research* **189** (2018), 618.

[82] R. Lamba, J. McGahan, M. Corwin, C.S. Li, T. Tran, J.A. Seibert und J. Boone, *American Journal of Roentgenology* **203** (2016), 1013.

[83] A.W. Lee, W.T. Ng, J.J. Pan, C. Chiang, S.S. Poh, H.C. Choi, Y.C. Ahn, H. Al-Hussain, J. Corry, C. Grau, V. Grégoire, K.J. Harrington, C.S. Hu, D.L. Kwong, J.A. Langendijk, Q.T. Le, N.Y. Lee, J.C. Lin, T.X. Lu, W.M. Mendenhall, B. O'Sullivan, E. Ozyar, L.J. Peters, D.I. Rosenthal, G. Sanguineti, Y.L. Soong, Y. Tao, S.S. Yom und J.T. Wee, *International Journal of Radiation Oncology, Biology, Physics* **105** (2019), 567.

[84] C. Lee, D. Lodwick, D. Hasenauer, J.L. Williams, C. Lee und W.E. Bolch, *Physics in Medicine and Biology* **52** (2007), 3309.

[85] H. Li, L. Dong, L. Zhang, J.N. Yang, M.T. Gillin und X.R. Zhu, *Medical Physics* **38** (2011), 6730.

[86] G. Lim, L. Kardar, S. Ebrahimi und W. Cao, *European Journal of Operational Research* **280** (2020), 266.

[87] K. Lim, W. Small Jr, L. Portelance, C. Creutzberg, I.M. Jürgenliemk-Schulz, A. Mundt, L.K. Mell, N. Mayr, A. Viswanathan, A. Jhingran, B. Erickson, J. De los Santos, D. Gaffney, C. Yashar, S. Beriwal, A. Wolfson, A. Taylor, W. Bosch, I. El Naqa, A. Fyles und Gyn IMRT Consortium, *International Journal of Radiation Oncology, Biology, Physics* **79** (2011), 348.

[88] L.L. Lin, M. Kirk, J. Scholey, N. Taku, J. Kiely, B. White und S. Both, *International Journal of Radiation Oncology, Biology, Physics* **95** (2016), 181.

[89] Y.C. Liu, H.M. Chang, H.H. Lin, C.C. Lu und L.H. Lai, *Journal of Clinical Medicine* **9** (2020), 3884.

[90] A.R. Mahal und J.B. Yu, *Physicians' Education Resources* **13** (2017), 11.

[91] A. Mairani, S. Brons, F. Cerutti, A. Fassò, A. Ferrari, M. Krämer, K. Parodi, M. Scholz und F. Sommerer, *Cancers (Basel)* **12** (2020), 799.

[92] D. Mansur, *Expert Review of Anticancer Therapy* **14** (2014), 1001.

[93] S. Marnitz, W. Wlodarczyk, O. Neumann, C. Koehler, M. Weihrauch, V. Budach und L. Cozzi, *Radiation Oncology* **10** (2015).

[94] S. McMahon, H. Paganetti und K. Prise, *Physics in Medicine and Biology* **63** (2018).

[95] G. Meijer, J. de Klerk, K. Bzdusek, H. van den Berg, R. Janssen, M. Kaus, P. Rodrigus und P. van der Toorn, *International Journal of Radiation Oncology, Biology, Physics* **72** (2008), 1416.

[96] K. Miller, L. Nogueira, A.B. Mariotto, J. Rowland, K.R. Yabroff, C.M. Alfano, A. Jemal, J.L. Kramer und R.L. Siegel, *CA: A Cancer Journal for Clinicians* **69** (2019), 363.

[97] L.E. Molière, *Zeitschrift für Naturforschung A* **3A** (1948), 78.

[98] J. Molitoris, T. Diwanji, J. Snider III, S. Mossahebi, S. Samanta, S. Badiyan, C. Simone II und P. Mohindra, *Journal of Thoracic Disease* **10** (2018), S2437.

[99] K. Mossman, *Dose Response* **10** (2012).

[100] S. Muraro, G. Battistoni und A. Kraan, *Frontiers in Physics* **8** (2020), 391.

[101] N. Nabavizadeh, D.A. Elliott, Y. Chen, A.S. Kusano, T. Mitin, C.R. Thomas Jr. und J.M. Holland, *International Journal of Radiation Oncology, Biology, Physics* **94** (2016), 850.

[102] W. Newhauser und M. Durante, *Nature Reviews Cancer* **11** (2011), 438.

[103] W. Newhauser, J. Fontenot, A. Mahajan, D. Kornguth, M. Stovall, Y. Zheng, P. Taddei, D. Mirkovic, R. Mohan, J. Cox und S. Woo, *Physics in Medicine and Biology* **54** (2009), 2277.

[104] W. Newhauser und R. Zhang, *Physics in Medicine and Biology* **60** (2015).

[105] W.D. Newhauser, C. Schneider, L. Wilson, S. Shreshtha und W. Donahue, *Radiation Protection Dosimetry* **180** (2018), 245.

[106] C. Nieder, A.L. Grosu und L.E. Gaspar, *Radiation Oncology* **9** (2014).

[107] C. Oehler, S. Lang, P. Dimmerling, C. Bolesch, S. Kloeck, A. Tini, C. Glanzmann, Y. Najafi, G. Studer, und D.R. Zwahlen, *Radiation Oncology* **9** (2014), 229.

[108] J.T. Olesen und U.T. Landberg. *dicomrt2matlab*. Github, 2019.

[109] openREGGUI. *Image processing open-source platform for adaptive proton therapy in cancer treatment*. https://openreggui.org/, 2016.

[110] K. Ozasa, Y. Shimizu, A. Suyama, F. Kasagi, M. Soda, E. Grant, R. Sakata, H. Sugiyama und K. Kodama, *Radiation Research* **177** (2012), 229.

[111] H. Paganetti, *Physics in Medicine and Biology* **47** (2002), 747.

[112] H. Paganetti, T. Bortfeld und H. Kooy, *Medical Physics* **32** (2005), 2048.

[113] H. Paganetti, A. Niemierko, M. Ancukiewicz, L.E. Gerweck, M. Goitein, J.S. Loeffler und H.D. Suit, *International Journal of Radiation Oncology, Biology, Physics* **53** (2002), 407.

[114] F. Pajonk, E. Vlashi und W.H. McBride, *Stem Cells* **28** (2010), 639.

[115] N.M. Patel, *Clinical Chemistry* **63** (2017), 791.

[116] P.R. Patel, Y. Lei, T. Wang, Y. Fu, J.R. Roper, A. Jani, J.D. Bradley, T. Liu und X. Yang, *International Journal of Radiation Oncology, Biology, Physics* **111** (2021), e290.

[117] D.B. Pelowitz, *Los Alamos National Laboratory* **LA-CP-11-00438** (2011).

[118] N. Qin, M. Pinto, Z. Tian, G. Dedes, A. Pompos, S.B. Jiang, K. Parodi und X. Jia, *Physics in Medicine and Biology* **62** (2017), 3682.

[119] N. Qin, C. Shen, M.Y. Tsai, M. Pinto, Z. Tian, G. Dedes, A. Pompos, S.B. Jiang, K. Parodi und X. Jia, *International Journal of Radiation Oncology, Biology, Physics* **100** (2018), 235.

[120] L. Rechner, J. Eley, R. Howell, R. Zhang, D. Mirkovic und W. Newhauser, *Physics in Medicine and Biology* **60** (2015), 3999.

[121] L.A. Rechner, R.M. Howell, R. Zhang, C. Etzel, A.K. Lee und W.D. Newhauser, *Physics in Medicine and Biology* **57** (2012), 7117.

[122] E. Roelofs, M. Engelsman, C. Rasch, L. Persoon, S. Qamhiyeh, D. de Ruysscher, F. Verhaegen, M. Pijls-Johannesma und P. Lambin, *Journal of Thoracic Oncology* **7** (2012), 165.

[123] L. Roger, P. Zhang, M. Vogelbaum, A. Perry, J.M.M. L S Ashby, A.M. Alleman, J. Galvin, D. Brachman, J.M. Jenrette, J. De Groot, J.A. Bovi, M. Werner-Wasik, J.P.S. Knisley und M.P. Mehta, *Journal of Neurosurgery* (2017).

[124] J. Ruben, S. Davis, C. Evans, P. Jones, F. Gagliardi, M. Haynes und A. Hunter, *International Journal of Radiation Oncology, Biology, Physics* **70** (2008), 1530.

[125] R.K. Sachs und D.J. Brenner, *Proceedings of the National Academy of Sciences of the United States of America* **102** (2005), 13040.

[126] A. Schipler und G. Iliakis, *Nucleic Acids Research* **41** (2013), 7589.

[127] S. Schmid, G. Landry, C. Thieke, F. Verhaegen, U. Ganswindt, C. Belka, K. Parodi und G. Dedes, *Physics in Medicine and Biology* **60** (2015), 9329.

[128] U. Schneider, S. Agosteo, E. Pedroni und J. Besserer, *International Journal of Radiation Oncology, Biology, Physics* **53** (2002), 244.

[129] U. Schneider und R. Hälg, *Frontiers in Oncology* **5** (2015), 235.

[130] U. Schneider, M. Sumila und J. Robotka, *Theoretical Biology and Medical Modelling* (2011).

[131] W. Schneider, T. Bortfeld und W. Schlegel, *Physics in Medicine and Biology* **45** (2000), 459.

[132] S. Scoccianti, M. Krengli, L. Marrazzo, S.M. Magrini, B. Detti, V. Fusco, L. Pirtoli, D. Doino, A. Fiorentino, L. Masini, D. Greto, M. Buglione, G. Rubino, F. Lonardi, F. Migliaccio, S. Marzano, R. Santoni, U. Ricardi und L. Livi, *Radiologia Medica* **123** (2018), 48.

[133] W.P. Segars, J. Bond, J. Frush, S. Hon, C. Eckersley, C.H. Williams, J. Feng, D.J. Tward, J.T. Ratnanather, M.I. Miller, D. Frush und E. Samei, *Medical Physics* **40** (2013).

[134] H. Seim, D. Kainmueller, M. Heller, H. Lamecker, S. Zachow und H.C. Hege, *Eurographics Workshop on Visual Computing for Biomedicine* (2008).

[135] H. Shu, C. Yin, H. Zhang, M. Liu, M. Zhang, L. Zhao, K. Chu, X. Dai und M.F. Moyers, *MethodsX* **6** (2019), 1933.

[136] I. Shuryak, P. Hahnfeldt, L.H. nd Rainer K Sachs und D.J. Brenner, *Radiation and Environmental Biophysics* **48** (2009), 263.

[137] I. Shuryak, P. Hahnfeldt, L.H. nd Rainer K Sachs und D.J. Brenner, *Radiation and Environmental Biophysics* **48** (2009), 275.

[138] R. Siegel, K. Miller, H. Fuchs und A. Jemal, *CA: A Cancer Journal for Clinicians* **671** (2021), 7.

[139] A.J. Sigurdson, C.M. Ronckers, A.C. Mertens, M. Stovall, S.A. Smith, Y. Liu, R.L. Berkow, S. Hammond, J.P. Neglia, A.T. Meadows, C.A. Sklar, L.L. Robison und P.D. Inskip, *The Lancet* **365** (2005), 2014.

[140] W. Smith, M. Kim, C. Holdsworth, J. Liao und M. Phillips, *Radiation Oncology* **11** (2016).

[141] W.S. Snyder, H.L. Fisher Jr, M.R. Ford und G.G. Warner, *Journal of Nuclear Medicine* **3** (1969), 7.

[142] J. Son, S.B. Lee, Y. Lim, S.Y. Park, K. Cho, M. Yoon und D. Shin, *Sensors* **18** (2018), 227.

[143] S. St. James, C. Grassberger und H.M. Lu, *Translational Lung Cancer Research* **7** (2018), 210.

[144] M.G. Stabin, E.E. Watson, M. Cristy, J.C. Ryman, K.F. Eckerman, J.L. Davis, D. Marshall und M.K. Gehlen, *Oak Ridge National Laboratory* **Report ORNL/TM-12907** (1995).

[145] C. Stokkevåg, M. Fukahori, T. Nomiya, N. Matsufuji, G.M. Engeseth, L.B. Hysing, K.S. Ytre-Hauge, E. Rørvik, A. Szostak und L.P. Muren, *Radiotherapy and Oncology* **120** (2016), 300.

[146] I. Stroud: *Boundary Representation Modelling Techniques*. Springer, 2006.

[147] J. Sveistrup, P.M. af Rosenschöld, J.O. Deasy, J.H. Oh, T. Pommer, P.M. Petersen und S.A. Engelholm, *Radiation Oncology* **9** (2014).

[148] G.P. Swanson und S. Stathakis, *American Journal of Clinical Oncology* **34** (2010), 188.

[149] P. Sykes, *Dose Response* **18** (2020).

[150] B.S. Teh, M.D. Bastasch, T.M. Wheeler, W.Y. Mai, A. Frolov, B.M. Uhl, H.H. Lu, L.S. Carpenter, J.K. Chiu, J. McGary, S.Y. Woo, W.H. Grant 3rd und E.B. Butler, *International Journal of Radiation Oncology, Biology, Physics* **56** (2003), 184.

[151] M. Teoh, C.H. Clark, K. Wood, S. Whitaker und A. Nisbet, *The British Journal of Radiology* **84** (2011), 967.

[152] I. Toma-Dasu, A. Dasu, A. Vestergaard, P.W. Nyström und H. Nyström, *Acta Oncologica* **10** (2020).

[153] A. Tran, J. Zhang, K. Woods, V. Yu, D. Nguyen, G. Gustafson, L. Rosen und K. Sheng, *Radiation Oncology* **12** (2017).

[154] H. Tsujii und T. Kamada, *Japanese Journal of Clinical Oncology* **42** (2012), 670.

[155] J. Van Dyk, R.B. Barnett, J.E. Cygler und P.C. Shragge, *International Journal of Radiation Oncology, Biology, Physics* **26** (1993), 261.

[156] M. Vania, D. Mureja und D. Lee, *Journal of Computational Design and Engineering* **6** (2019), 224.

[157] V. Verma, M. Mishra und M. Mehta, *Cancer* **122** (2016), 1483.

[158] A. Vogt, S. Schmid, K. Heinimann, H. Frick, C. Herrmann, T. Cerny und A. Omlin, *ESMO Open - Cancer Horizons* **2** (2017).

[159] F. Wang, C. Jiang, L. Wang, F. Yan, Y. Piao, Z. Ye, M. Xu, J. Liu, Z. Fu und Y. Jiang, *Journal of Cancer* **11** (2020), 5210.

[160] L. Wang und C. Ma: *Encyclopedia of Radiation Oncology*. Springer, 2013.

[161] Y. Wang, C. Jiang, C. Schroeder und J. Teran, *An adaptive virtual node algorithm with robust mesh cutting* (2015), 77.

[162] L.J. Wilson und W.D. Newhauser, *Physics in Medicine and Biology* **66** (2021).

[163] X.G. Xu, *Physics in Medicine and Biology* **59** (2014).

[164] Y.S. Yeom, C. Choi, H. Han, H. Lee, B. Shin, T.T. Nguyen, M.C. Han, C. Lee und C.H. Kim, *Nuclear Engineering and Technology* **51** (2018), 843.

[165] P. Yepes, A. Adair, S.J. Frank, D.R. Grosshans, Z. Liao, A. Liu, D. Mirkovic, F. Poenisch, U. Titt, Q. Wang und R. Mohan, *Advances in Radiation Oncology* **4** (2019), 156.

[166] H. Zaidi und X.G. Xu, *Annual Review of Biomedical Engineering* **9** (2007), 471.

[167] J. Zhang, Y.H. Na, P.F. Caracappa und X.G. Xu, *Physics in Medicine and Biology* **54** (2009), 5885.

[168] A. Zvereva, H. Schlattl, M. Zankl, J. Becker, N. Petoussi-Henss, Y.S. Yeom, C.H. Kim, C. Hoeschen und K. Parodi, *Physica Medica: European Journal of Medical Physics* **39** (2017), 100.